

Phase Extraction of Non-Stationary Signals Produced in Dynamic Interferometry Involving Speckle Waves

THÈSE N° 4514 (2009)

PRÉSENTÉE LE 13 NOVEMBRE 2009

À LA FACULTÉ SCIENCES ET TECHNIQUES DE L'INGÉNIEUR
LABORATOIRE DE NANOPHOTONIQUE ET MÉTROLOGIE
PROGRAMME DOCTORAL EN PHOTONIQUE

ÉCOLE POLYTECHNIQUE FÉDÉRALE DE LAUSANNE

POUR L'OBTENTION DU GRADE DE DOCTEUR ÈS SCIENCES

PAR

Sébastien EQUIS

acceptée sur proposition du jury:

Prof. M. Chergui, président du jury
Prof. P. Jacquot, directeur de thèse
Dr X. Colonna De Lega, rapporteur
Prof. C. Depeursinge, rapporteur
Prof. P. Flandrin, rapporteur



ÉCOLE POLYTECHNIQUE
FÉDÉRALE DE LAUSANNE

Suisse
2009

Abstract

It is now widely acknowledged, among communities of researchers and engineers of very different horizons, that speckle interferometry (SI) offers powerful techniques to characterize mechanical rough surfaces with a submicronic accuracy in static or quasi-static regime, when small displacements are involved (typically several microns or tens of microns). The issue of dynamic regimes with possibly large deformations (typically several hundreds of microns) is still topical and prevents an even more widespread use of speckle techniques. This is essentially due to the lack of efficient processing schemes able to cope with non-stationary AM-FM interferometric signals. In addition, decorrelation-induced phase errors represent an hindrance to accurate measurement when such large displacements and classical fringe analysis techniques are considered. This work is an attempt to address those issues and to endeavor to make the most of speckle interferometry signals.

Our answers to those problems are located on two different levels. First of all, we adopt the temporal analysis approach, *i.e.* the analysis of the temporal signal of each pixel of the sensor area used to record the interferograms. A return to basics of phase extraction is operated to properly identify the conditions under which the computed phase is meaningful and thus give some insight on the physical phenomenon under analysis. Due to their intrinsic non-stationary nature, a preprocessing tool is missing to put the SI temporal signals in a shape which ensures an accurate phase computation, whichever technique is chosen. This is where the Empirical Mode Decomposition (EMD) intervenes. This technique, somehow equivalent to an adaptive filtering technique, has been studied and tailored to fit with our expectations. The EMD has shown a great ability to remove efficiently the random fluctuating background intensity and to evaluate the modulation intensity. The Hilbert tranform (HT) is the natural quadrature operator. Its use to build an analytical signal from the so-detrended SI signal, for subsequent phase computation, has been studied and assessed. Other phase extraction techniques have been considered as well for comparison purposes .

Finally, our answer to the decorrelation-induced phase error relies on the well-known result that the higher the pixel modulation intensity, the lower the random phase error. We took benefit from this result - not only linked to basic SNR considerations, but more

specifically to the intrinsic phase structure of speckle fields - with a novel approach. The regions within the pixel signal history classified as unreliable because under-modulated, are purely and simply discarded. An interpolation step with the Delaunay triangulation is carried out with the so-obtained non-uniformly sampled phase maps to recover a smooth phase which relies on the most reliable available data. Our schemes have been tested and discussed with simulated and experimental SI signals.

We eventually have developed a versatile, accurate and efficient phase extraction procedure, perfectly able to tackle the challenge of dynamic behaviors characterization, even for displacements and/or deformations beyond the classical limit of the correlation dimensions.

Keywords:

Dynamic speckle interferometry, Instantaneous frequency/phase estimation/tracking, Non-stationary signals processing, Fringe analysis, Full-field measurements, Diffraction patterns calculation, Speckle fields statistics, Delaunay triangulation, Scattered data interpolation.

Résumé

Il est unanimement reconnu, parmi les chercheurs et ingénieurs provenant d'horizons très différents, que l'interférométrie speckle (SI) permet, par un ensemble de techniques puissantes, la caractérisation de surfaces mécaniques rugueuses en régime statique et quasi-statique, lorsque de faibles déplacements sont en jeu (typiquement de l'ordre du micron ou de la dizaine de microns). Le problème des régimes dynamiques avec de potentiels grands déplacements (typiquement de l'ordre de la centaine de microns) reste à ce jour d'actualité, et empêche un usage encore plus répandu qu'il ne l'est déjà des techniques speckle. Ceci s'explique essentiellement par le manque de techniques de calcul capables de traiter efficacement les signaux interférométriques non-stationnaires modulés en amplitude et en fréquence. En outre, les erreurs de phase dues aux décorrelations entravent sérieusement l'obtention de mesures précises lorsque l'on a affaire à de grands déplacements et que l'on considère des techniques classiques d'analyse de franges. Ces problématiques sont au coeur de ce travail de thèse, avec pour objectif de s'efforcer d'exploiter au mieux les signaux d'interférométrie speckle.

Nos solutions à ces problèmes se situent sur deux niveaux. Tout d'abord, nous avons adopté l'approche de l'analyse temporelle des signaux, *i.e.* l'analyse des signaux enregistrés sur chaque pixel du capteur matriciel au cours du temps. Nous avons effectué un retour aux principes de base de l'extraction de phase de façon à clairement identifier les conditions *sine qua non* sous lesquelles la phase extraite a un sens physique et peut être de manière univoque reliée au phénomène physique analysé. A cause de leur nature non-stationnaire intrinsèque, les signaux temporels provenant de techniques speckle ne permettent pas un calcul direct de la phase et il manque un outil de pré-traitement pour mettre ces signaux dans la forme *ad hoc*, quelle que soit d'ailleurs la technique de calcul de phase choisie. C'est ici qu'intervient la décomposition modale empirique (EMD). Cet outil, qui est en somme équivalent à une technique de filtrage adaptatif, a été étudié et adapté à nos besoins. Nous avons démontré que grâce à l'EMD l'intensité aléatoire du fond continu peut être efficacement éliminée et l'intensité de modulation, elle aussi aléatoire, précisément calculée. La transformée de Hilbert (HT) est l'opérateur de quadrature naturel. Son usage pour construire le signal analytique à partir du signal précédemment centré, et duquel sera tiré la phase, a été étudié, évalué et enfin

comparé à d'autres méthodes telles que la transformée en ondelettes et le décalage de phase dynamique

Enfin, nous avons apporté une solution originale au problème des erreurs de phase aléatoires. Nous sommes partis du constat bien connu, que l'extraction de phase est d'autant plus précise que le signal du pixel est bien modulé. Ces erreurs de phases aléatoires sont plus liées à la structure profonde des champs speckle qu'à de simples considérations de rapport signal sur bruit. Les régions sous-modulées du signal temporel du pixel sont considérées comme non fiables et sont par conséquent purement et simplement éliminées. Les cartes de phases qui résultent de cette classification sont ainsi échantillonnées de manière non uniforme, et une étape d'interpolation doit être menée pour retrouver des cartes de phases uniformes, où seules les données les plus fiables ont été conservées. Cette interpolation fait intervenir la triangulation de Delaunay. Nos algorithmes de traitement ont été testés avec des signaux issus de simulations et d'expériences, et les résultats obtenus discutés.

Nous avons finalement développé une procédure de calcul de la phase, précise, efficace et souple, en mesure de relever le challenge de la caractérisation des régimes dynamiques en mécanique expérimentale, pour des déplacements et/ou déformations allant au-delà de la limite classique des dimensions de corrélation.

Mots clés:

Interférométrie speckle dynamique, Estimation/suivi de fréquence et phase instantanées, Traitement des signaux non-stationnaires, Analyse de franges, Mesure optique plein-champ, Calcul de figures de diffraction, Statistiques de champs speckle, Triangulation de Delaunay, Interpolation de données diffuses.

Si sa [de l'Homme] vie entière n'avait pas été consacrée à la recherche du superflu, il n'eût jamais pu, d'une façon aussi inexpugnable, s'entourer du nécessaire.

William James

tiré du livre *L'Homme Sauvage et l'Enfant* de Robert Bly

Contents

Contents	7
I Foreword	15
1 Background and goal of the thesis	15
2 Original contribution of this work	16
3 Layout of the dissertation	16
II Interferometric measurement methods	19
1 Smooth wave interferometry	19
1.1 Theoretical background	19
1.1.1 The notion of optical path	19
1.1.2 Interferences: the 2-beam equation	20
1.1.3 Interferences in partially coherent light	21
1.2 Quantitative measurement in smooth-wave interferometry and basic setups	21
2 Speckle wave interferometry	22
2.1 Where does speckle come from?	22
2.2 What defines SI?	23
2.3 The 2-beam equation with at least one speckle wave	23
2.4 The interferometer sensitivity: what can we measure in SI?	24
2.5 Fringe formation in SI	25
2.6 Experimental setups	26
2.6.1 Out-of-plane speckle interferometer	26
2.6.2 In-plane speckle interferometer	27
2.6.3 Shearing speckle interferometer	29
2.6.4 Contouring speckle interferometer	30
3 Imaging versus interferometric methods	31

III	Theoretical description of speckle fields and speckle interferometry	35
1	The central limit theorem and basic first order statistics	35
1.1	The perfectly resolved case	35
1.2	The integrated case: the box-car approximation	36
2	The notion of speckle grain and second order statistics	38
2.1	The perfectly resolved case	38
2.2	The correlation cell of integrated speckle fields	40
3	Intensity and phase maps topology: phase saddles, vortices and bright spots	41
3.1	Phase singularities	41
3.1.1	Existence and basic properties	41
3.1.2	Singularities density, motion, birth and annihilation	43
3.1.3	Phase singularities: nuisance or useful feature?	44
3.2	Are bright speckle grains the location of stationary phase?	46
4	Optimization of SI measurements with unresolved speckles	48
5	Decorrelations and their impact on the achievable phase extraction accuracy	49
IV	Phase extraction from SI signals in dynamic regime: still a topical issue	51
1	Phase-shifting interferometry (PSI): the choicest method in terms of measurement accuracy	53
1.1	Principle of the phase extraction from several intensity maps	53
1.2	General approaches to design PSI algorithms	54
1.2.1	A general formulation with Fourier series	54
1.2.2	A general formulation with the concept of data-sampling window	54
1.2.3	A general formulation for non-sinusoidal waveforms	56
1.3	Some basic algorithms	56
1.3.1	The five-frame algorithm	56
1.3.2	The Carré algorithm	57
1.4	Improved phase-shifting methods for dynamic regimes	57
1.4.1	The temporal phase-unwrapping algorithm	58
1.4.2	The object induced dynamic phase-shifting method	58
1.4.3	The one bucket algorithm	59

2	The main streams in single frame based techniques	59
2.1	Mathematical transform based methods	59
2.1.1	Fourier transform based methods	59
2.1.2	The Spiral Phase Quadrature Transform (SPQT)	60
2.1.3	Time-frequency and Time-scale distributions	62
2.2	Morphological methods	64
3	Phase map filtering and unwrapping	65
3.1	Filtering methods for wrapped phase maps	65
3.2	2D phase unwrapping	66
4	State of the art of the temporal analysis approach	66
5	The analytic signal and the analytic method: back to basics	68
5.1	Stationarity and non-stationarity in practice	68
5.2	Definition of instantaneous quantities of an arbitrary signal	69
5.2.1	What is wrong with Fourier analysis?	69
5.2.2	Defining and interpreting instantaneous quantities of a signal	70
5.3	Which operator to build the quadrature signal?	71
5.3.1	General requirements on the quadrature operator	71
5.3.2	Reminder on the Hilbert transform	72
5.3.3	Conditions for a meaningful use of the HT as the quadrature operator	72
5.4	How to compute the HT?	75
5.5	Behavior of the analytic method with different types of signals	76
5.5.1	Frequency modulated signal	76
5.5.2	Signal with phase or frequency step	78
5.5.3	Noise sensitivity	78
5.6	A preprocessing tool is missing for detrending SI signals	80
V	The Empirical Mode Decomposition dedicated to SI	81
1	Basic principles of the decomposition	81
1.1	Algorithm	82
1.1.1	The concept of the intrinsic mode function	82

1.1.2	The way the decomposition works	82
1.2	Applications	92
1.3	Strengths and weaknesses of the method	92
2	Deeper analysis of the decomposition	93
2.1	The <i>extrema</i> finding and the sampling influence	93
2.2	The sifting process influence	96
2.3	The boundaries ending	100
2.4	Orthogonality	101
3	A fast implementation of the EMD for SI signals processing	103
3.1	Advocating the fast implementation	103
3.2	Additional free features of the EMD	103
3.3	Algorithm and evaluation	104
3.4	Outlook: construction of an hybrid mode	107
VI A novel approach to address the modulation drops issue with the Delaunay triangulation		109
1	Data classification and the concept of pixel reliability	110
1.1	The dynamic regime	110
1.2	The static regime	111
2	The Delaunay triangulation: a new approach to the modulation loss issue .	112
2.1	Convex hull, Delaunay triangulation and Voronoi diagram	112
2.1.1	Definition and computation of the convex hull of a data set	112
2.1.2	The DT and its dual graph: the Voronoi diagram	114
2.2	The Quickhull algorithm	115
3	The 3DPP procedure	116
3.1	Description of the method	116
3.2	Assessment of the 3DPP method	117
3.3	Choice of the modulation threshold	118
3.4	Computation load reduction with the sparse-3DPP	118
3.5	Definition of convex hull with constraints	118
3.6	Outlook: an improved 3DPP procedure for phase discontinuities management	119

VII Application of the EMD-HT-3DPP to experimental signals	121
1 Experimental setup	121
1.1 Experiment I: rigid body translation	123
1.2 Experiment II: rigid body rotation	124
1.3 Experiment III: rubber compression	125
2 Acquisition and processing chain	125
2.1 Acquisition system	125
2.1.1 Hardware	125
2.1.2 Acquisition software	127
2.2 Processing scheme	127
3 Results and discussion	129
3.1 Experiment I: rigid body translation	129
3.1.1 Accurate computation of the temporal carrier frequency . .	129
3.1.2 Phase extraction and discussion of the results	129
3.2 Experiment II: rigid body rotation	138
3.2.1 Result of EMD + HT	138
3.2.2 Result of 3DPP	139
3.2.3 Discussion	140
3.2.4 Results for the total displacement	146
3.3 Experiment III: rubber compression	149
3.3.1 Results and discussion	149
3.3.2 Results of sparse-3DPP	152
4 Evaluation of the sine-cosine DT filter	153
VIII The stochastic signal processing world: a mine of phase extraction methods within reach thanks to the EMD	157
1 Estimation or tracking techniques?	157
2 Example: Linear predictive filtering for signal modeling	158
IX Conclusion	161
1 Achievements	161
2 Further work	162

A	A reminder on Fourier analysis	165
1	The continuous Fourier transform (FT)	165
1.1	Definition	165
1.2	Basic theorems	165
1.2.1	Similarity theorem	165
1.2.2	Shift theorem	166
1.2.3	Modulation theorem	166
1.2.4	Convolution theorem	166
2	The discrete Fourier transform (DFT)	166
2.1	Definition and theorems	166
2.2	The Shannon's sampling theorem	167
2.3	FT of finite sequences	167
2.3.1	Definition	167
2.3.2	Windowing and DFT	168
2.3.3	Zero-padding	168
B	Diffraction patterns computation	169
1	In which way a numerical model is valuable?	169
2	Diffraction theory: from Rayleigh-Sommerfeld to Fresnel	170
3	Computation of diffraction patterns: sampling considerations	172
4	The fractional FT: a versatile tool for near-field and far-field diffraction computation	174
5	Which computation method for speckle and SI signals computation?	176
6	Potentials, limits and applications of the model	176
7	Matlab program	177
C	Fast-EMD algorithm	179
	Bibliography	189
	Curriculum vitae	205
	List of publications	209

Acknowledgements

The realization of this thesis work has been made possible thanks to the support of the Swiss National Science Foundation. The allocated grants were respectively entitled "Phase extraction of 3D SI signals" (200021 – 109364/1) and "Phase extraction of 3D SI signals: final investigations" (200020 – 121513/1), and respectively covered the periods 2006-2008 and 2009.

First of all, I wish to thank Professor Pierre Jacquot who welcome me in his group and supervised me during this thesis work. His unanimously acknowledged scientific skills and his rigorousness have been a constant source of teaching and inspiration. I want to thank him also for his trust, his availability and his understanding for things that went far beyond this PhD work strictly speaking. A PhD is a real life experience, and as far as I am concerned, it would have never been as enriching - on many levels - as it was without him. I want to show him my heartfelt gratitude for everything.

Thanks to Prof. M. Chergui, Dr. X. Colonna De Lega, Prof. C. Depeursinge and Prof. P. Flandrin for having kindly accepted to be on my thesis committee. As an aside, I want to warmly thank Prof. G.H. Kaufmann for interesting interactions and I wish him a prompt recovery.

I want also to thank Prof. P. Chavel and Prof. J.M. Jonathan from I.O.T.A in Orsay and Prof. J.-M. Fournier from EPFL for precious insights and sound advice, which eventually led me to start this PhD.

This work has been done in the Nanophotonics and Metrology laboratory, directed by Professor Olivier Martin.

I want also to sincerely thank Pierrette Paulou, the administrative assistant of the nanophotonics and metrology laboratory and of the doctoral school in photonics. She was the heart of the lab and I cannot count the number of times she helped me. Many thanks Pierrette for your kindness, your daily good mood, - whatever happened, and we cannot say that this good mood has not been challenged - and your availability!

I want to thank Pascal et Fredo, who have been of sound advice, especially for mechanical design.

Thank you also to Sébastien Halouze-Lamy, the system manager of the laboratory, who has always been available and of precious help for anything related to computers and

motorbikes.

I want also to thank Gaëtan Lévêque, André Christ and Holger Fisher, with whom I spent very special time riding, skiing, running, chatting, in any order and not separately.

Thank you also to Chin, Lina, Weihua and more recently Andreas, Daniele, José, Benjamin and Christian to contribute to the good atmosphere of the lab among PhD students and post-docs. I spent and keep spending great time with Dani, "awesome" Andi - who has also been of precious help with \LaTeX - and José.

In the "extra-work" difficulties I have been through, I found help and support next to Claire, Dani, José and Pili, Julien and Anne-Lise, not forgetting Marie-Elizabeth and Didier. I want to show them my deepest gratitude for their gesture, which meant a lot for me.

May my sister, Anne-Gaëlle, and her fiancé, Gwenaël, be thanked for their unfailing support. I am very grateful for what they have been able to give me along those three and half years. Je tiens enfin à remercier mes parents du fond du coeur. Sans eux, je n'aurais certainement pas trouvé les ressources nécessaires pour accomplir ce travail de thèse. Un immense merci à eux!

I cannot find the correct words to thank Sophie for the priceless and most prestigious title that I have received one month and half after the beginning of my thesis: the one of father. Apart from a chronic lack of sleep, Louis has been and is still a constant source of joy and wonder. His inexhaustible energy is a daily source of putting in perspective and inspiration.

Chapter I

Foreword

1 Background and goal of the thesis

The full-field optical methods have proved huge capabilities and potentials in engineering and industrial areas and their use tends to be more and more widespread. Speckle interferometry (SI) considerably widened the horizon of classical interferometry, by offering the capability to characterize rough mechanical surfaces with a submicronic accuracy. Digital holography has been equivalently a huge step forward, notably in microscopy. Those methods require efficient and accurate processing schemes to meet the increasing demand for computation speed and measurement accuracy. If many experimental arrangements have been proposed to overcome the limitations that are most likely to exist in a real industrial environment, one bottleneck remains: the processing load. It is indeed easy to acquire a huge amount of data (typically dozens of GB or even more) from an experiment, but the computation tasks are still intensive. An additional constraint exists, and not the slightest, which is unavoidable as soon as speckle waves are involved: decorrelation and its impact on the achievable phase accuracy.

This project aims at improving the processing of interference patterns: it should be faster, more reliable and accurate, as well as less operator-dependent. The focus here is on SI signals: because of the intrinsic nature of speckle, those signals exhibit substantial intensity and phase fluctuations, and thus represent the worst case to be treated. This research work was organized along four principal directions:

- i) build an accurate and simple numerical tool to simulate complex speckle fields in order to assess and compare the performances of existing and new phase extraction algorithms,
- ii) gain knowledge of the processing schemes successfully applied in neighboring fields (speech and image processing, non-stationary signals study, acoustic and

- microwave interferometry),
- iii) imagine and combine efficient processing methods with the resources of optics to build a reliable procedure able to process full-field measurement signals,
- iv) test our processing procedures on well-controlled, reproducible and - it would be of great benefit for us and mechanics experts as well - relevant experiments.

2 Original contribution of this work

This thesis work addresses the processing of non-stationary interferometric signals stemming from dynamic experiments. The original contribution of this work is actually built on three main axes. The first one is the conception of a numerical model able to simulate complex speckle fields which reproduces with a high faithfulness physical speckle fields. A clear definition of the strengths and the limits of this numerical model has been provided and constitutes the first stone of this thesis. The second contribution is the clear statement of the phase extraction problem with non-stationary interferometric signals, which leads naturally to an adaptive filtering method, namely the Empirical Mode Decomposition. This latter technique has been thoroughly studied and tailored to make the SI signals in dynamic regimes amenable to a subsequent phase extraction step as reliable as possible. The phase computation method based on the Hilbert transform has been considered, theoretically studied, implemented, assessed and finally compared to other well-behaved methods, as dynamic phase-shifting and Morlet wavelet transform. The final contribution was an original answer to the under-modulation issue. The technique basically starts with the classification of the pixel signals, along time, according to their modulation. The pixels declared as irrelevant are then purely and simply discarded, and an interpolation step has then to take place so as to recover uniformly sampled phase maps. The interpolation scheme which has been considered is based on the Delaunay triangulation, followed by a cubic spline interpolation and a resampling step. This approach has the huge asset to discard pixels regions that are the most likely to generate the largest phase errors and thus to avoid having reliable data polluted by unreliable ones, which is never achieved with usual filtering techniques. *In fine*, we have a method at our disposal, which is robust, accurate and versatile to process flows of interferometric signals in order to reconstruct the temporal phase evolution. The techniques that have been developed can totally be applied to other full-field optical methods, like digital holography and fringe projection.

3 Layout of the dissertation

We give here some clues about the organization of this dissertation. Chapter 2 recalls some basics on interferometry and gives the fundamental definitions of speckle interfer-

ometry. We conclude the chapter by a short discussion on imaging methods, which we very briefly confront to interferometric methods. The reader familiar with speckle techniques might prefer to skip this chapter.

Chapter 3 is dedicated to a review of some fundamental statistics which rule speckle fields, both amplitude, intensity and phase. This is actually also the opportunity to conduct some more involved simulations, notably on the fine structure of speckle phase maps. The reader, again familiar with the theoretical description of speckle fields might prefer to skip the three first sections of this chapter, and jump to the last two sections, where we talk about the optimization of the interferometric signals with unresolved speckle and about decorrelations and the induced random phase errors.

Chapter 4 deals with the very core of this thesis, which is the phase extraction techniques, even if the bulk of this chapter is dedicated to a review of existing methods. We actually start with the phase-shifting techniques, which are acknowledged as the choicest methods in static regimes, and thus do not represent the ideal candidates to address the dynamic regime problem. We then present some single-frames techniques, to finally advocate the temporal approach which basically consists in analyzing the temporal history of the pixel signal. We finally come to the Hilbert transform and the concept of analytic signal. This non chronological way of introducing phase computation methods was motivated by the will to return to the fundamentals of phase extraction from non-stationary signals.

Chapter 5 is dedicated to the Empirical Mode Decomposition. We study this processing tool in details and advocate its use to make the speckle interferometry temporal signals in a suitable shape for accurate subsequent phase extraction. In concrete terms, we will show that the Empirical Mode Decomposition is a very accurate, versatile and efficient tool for detrending those non-stationary signals, *i.e.* remove their fluctuating mean intensity. This step is indeed mandatory to conduct a meaningful phase computation.

As already said and widely known, the temporal pixel signals are strongly non-stationary and the modulation is perfectly able to drop to zero, which leads to phase indeterminations. To solve this well-known issue, we propose, in chapter 6, a novel approach based on the Delaunay triangulation. The idea is to classify, in a binary manner, the pixels, based on a criterion and discard the ones found to be prone to the largest phase errors and thus irrelevant. The criterion used is the pixel modulation intensity, as it is acknowledged that the higher the modulation, the lower the phase error. We have then in hands some scattered data which have been found to be reliable, and an interpolation has to take place to fill in the gaps and rebuild phase maps sampled on a uniform grid. We also show a very similar method to filter wrapped phase maps obtained, for instance, with a phase-shifting algorithm.

Chapter 7 is dedicated to the experimental assessment of our processing schemes, while Chapter 8 is somehow an outlook chapter, with a glance to the stochastic world and its

mine of phase tracking and estimation techniques, originally developed for the radio-wave and the speech processing communities. We indeed think that interesting methods could be successfully applied to our field, especially after the Empirical Mode Decomposition pre-processing step. We think to autoregressive models, Kalman filters and so on.

The last chapter summarizes the main points of our work and also proposes some potential further developments of phase extraction techniques in dynamic regime.

Appendix A is a short reminder on Fourier analysis, Appendix B presents our speckle pattern diffraction model with a discussion on its potential and limits and our algorithm of the EMD is given in Appendix C.

Chapter II

Interferometric measurement methods

1 Smooth wave interferometry

1.1 Theoretical background

1.1.1 The notion of optical path

Pierre de Fermat put the cornerstone of the formulation of the light propagation in any medium with his famous principle, formulated in 1657, and historically known as the principle of the shortest optical path or the principle of least time and which can be stated in a more complete manner as:

The light follows the trajectory corresponding to a stationary optical path ([23, 82]).

Considering two points A and B in a given medium, characterized by its refractive index $n(s)$ depending on the location in space, the optical path is the length of the trajectory, weighted by $n(s)$, followed by the light between those two points and is defined by the curvilinear integral:

$$L = \int_A^B n(s) ds \quad (\text{II.1})$$

This path is said to be stationary if the quantity L varies slowly when the trajectory is slightly distorted. In other words, the light trajectory is shorter than any other curves lying in its neighborhood. In mathematical terms, along the light trajectory we have:

$$\partial L = 0 \text{ to the first order with } \partial M, \quad (\text{II.2})$$

M being any point of the trajectory except A and B . This principle implies, among other things, a straight trajectory of the light in an homogeneous medium. The optical path becomes simply in that case:

$$L = n\overline{AB} \quad (\text{II.3})$$

1.1.2 Interferences: the 2-beam equation

When two beams are separated with an *ad hoc* apparatus and recombined, geometrical optics is not able to explain the phenomenon that occurs. The light distribution in the region of superposition can have maxima, which exceed the sum of the intensities of the beams, and minima, which can be zero. This is the interference phenomenon, demonstrated by Thomas Young and his famous double-slit experiment at the very beginning of the XIXth century. In this section, we will limit ourselves to the case of interferences with strictly monochromatic waves. The case of real physical sources will be covered in the next section with the notion of coherence.

Let us consider two scalar waves of complex amplitude:

$$A_m(x, y) = E_m(x, y) \exp(i\phi_m) = E_m(x, y) \exp(ikz) \quad , \text{ with } k = \frac{2\pi}{\lambda} \quad , \quad (\text{II.4})$$

where E_m ($m=1,2$) is the real valued amplitude of the field, λ the light wavelength, z the coordinate along the propagation direction, x and y the coordinates in the transversal plane and $i^2 = -1$. The time dependence of the field has been skipped, and we assume that the fields are monochromatic, stem from the same source and propagate in air. In the overlapping region, the total complex field is (the spatial coordinates have been skipped to lighten the equations):

$$A_{tot} = A_1 + A_2 = E_1 \exp(i\phi_1) + E_2 \exp(i\phi_2) \quad , \quad (\text{II.5})$$

and the resulting intensity is:

$$I_{tot} = A_{tot} \cdot A_{tot}^* = I_1 + I_2 + I_{12} \quad , \quad (\text{II.6})$$

where \star denotes complex conjugate, and I_{12} is the interference term and equals to:

$$I_{12} = 2\sqrt{I_1 I_2} \cos \Delta\phi \quad , \text{ with } \Delta\phi = \phi_1 - \phi_2 = \frac{2\pi}{\lambda} OPD \quad (\text{II.7})$$

OPD is the optical path difference between the reference arm and the measurement arm, *i.e.* the quantity of interest in interferometry. This is the well-known 2-beam equation generally written as:

$$I_{tot} = I_o + I_m \cos \Delta\phi \quad , \quad (\text{II.8})$$

where I_o is the background intensity and I_m is the modulation intensity. The ratio I_m/I_o is the fringe visibility or fringe contrast ranging from 0 to 1. Optical sensors are sensitive to intensity and this fringe contrast becomes thus of primary importance as it is the determining factor of the measurement quality of the phase $\Delta\phi$, which is again the measurand.

1.1.3 Interferences in partially coherent light

The coherence theory deals with the consequences of the finite frequency bandwidth of light sources, and of their stability in terms of polarization, frequency and phase. The mathematics related to this field are rather intricate, and the addressed cases in the literature are usually the punctual source of finite frequency bandwidth and the pure monochromatic spatially extended source. We will even not treat those cases here and will simply recall how the 2-beam equation is affected by partial coherence between overlapping beams ([23, 123]):

$$I_{tot} = I_o + I_m |\gamma_{12}| \cos \Delta\phi, \quad (II.9)$$

where $|\gamma_{12}|$ is the normalized module of the cross-correlation of the complex amplitudes, also called the degree of coherence. This term, ranging from 0 to 1, will be taken equal to 1 in the following, as for fully coherent interfering beams. Some interferometric techniques exploit the partial temporal coherence of finite broad band light sources as the optical coherence tomography and the white-light interferometry.

1.2 Quantitative measurement in smooth-wave interferometry and basic setups

Albert Abraham Michelson, (1852-1931), Armand Hippolyte Louis Fizeau (1819-1896), Ludwig Louis Albert Zehnder (1854-1949) and Ludwig Mach (son of Ernst Mach), Franck Twymann and Arthur Green, Jules Celestin Jamin (1818-1886), Charles Fabry (1867-1945), Jean-Baptiste Perot (1863-1925), among others, all gave their name to interferometers ([23]), that are now well-known and widely used. Optical interferometers combine two or more light beams, created either by wavefront or amplitude division.

Since the CCD technology has become easily available directly from the shelf, the interferometric measurements, until then qualitative, became quantitative full-field measurements. As already mentioned, the phase $\Delta\phi$ in Eq.(II.8) is the sought-after quantity, and extracting this phase coded in intensity levels has received - and still receives nowadays - a considerable interest from the researchers. Classical interferometry is nonetheless confined to transparent media and optically smooth dioptries and surfaces. To deal with rough surfaces, phase extraction methods had to be refined and/or rethought. Before getting to the heart of the matter of this thesis work, *i.e.* the phase extraction from speckle interferometry signals in dynamic regimes, one must define several notions, and, speckle effect and speckle interferometry are two of them.

2 Speckle wave interferometry

2.1 Where does speckle come from?

In the early 1960s, the continuous-wave lasers became available, which gave a huge impetus to research and development in optics, and notably to interferometry. When a laser beam is pointed on a rough object ¹, this object is seen with a peculiar granular appearance. When the observer is moving, the distribution of speckle spots, which has no direct relationship with the macroscopic characteristics of the object, changes in the manner of the surface of boiling water. This type of granularity became known as speckle. If speckle has been observed in optics with coherent light sources for the first time at that time, analogous phenomena have been previously observed and studied in the radio-wave domain (see [77] and references therein). Speckle actually appears in a signal when it is composed by the addition of a multitude of independently phase shifted complex components (see Fig.II.1).

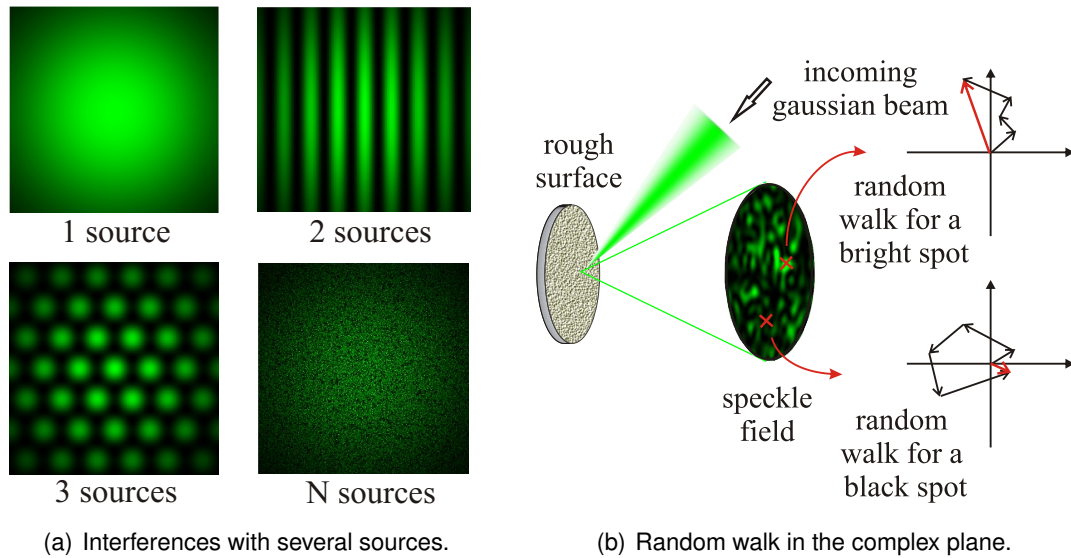


Figure II.1: Multiple independent phasors.

Depending on the statistics of the surface roughness, the created speckle field can be either partially or fully developed. The latter case is the usually encountered regime in SI. It is notably characterized by a contrast C ($C = \sigma_I / \langle I \rangle$, where σ_I is the standard deviation of the intensity and $\langle . \rangle$ denotes averaging) of the speckle field equal to 1.

¹The term roughness is always to be understood as compared to the scale of optical wavelength. There are actually an in-depth and an in-plane characteristic lengths. The first one is the determining factor for the speckle field to be fully developed or not, while the last one must be unresolved by the imaging system to give birth to a speckle field.

The case of partially developed speckle pattern has received some attentions, especially the dependance of this speckle contrast on the surface roughness ([67, 74, 91]). This dependance has been notably exploited to follow the temporal change of the state of a surface, as, for instance, the drying process of a painting.

2.2 What defines SI?

We recalled in the previous section some basic knowledge about interferometry involving smooth waves, which possess nearly constant amplitude and gently varying phase. Speckle interferometry (SI) is the time-honored expression to designate measurement interferometric methods involving at least one speckle wavefront. It is in contrast with smooth wave interferometry, where all components, including the object under analysis, have roughness extremely small compared to the light wavelength. Since its birth in the early 1970s ([30, 90, 104]), SI techniques arouse interest first in the holography community and later in the experimental mechanics circles, to finally assert themselves as major full-field optical methods. SI still attracts researchers interest and its range of applications is getting wider and wider. This success can be partly explained by the ease of use of those methods: the needed material (laser sources, sensor array, acquisition and storage system) is affordable and readily available in the market, and setups are less critical than in classical smooth-wave interferometry, especially if some arrangements are made (e.g. common path interferometers), and thus are well suited for reasonably disturbed environment. Another important asset is that the speckle grain does not need to be resolved as in speckle photography or holographic interferometry. It allows the use of large aperture objectives (frequently F/4 but up to F/2) and thus makes the characterization of broad objects possible with reasonable optical power. The counterpart lies in the phase extraction complexity, especially if the phenomenon under study is dynamic. Phase extraction constitutes the heart of the matter of the thesis and will be discussed in details starting from chapter 4.

2.3 The 2-beam equation with at least one speckle wave

SI signals follow the 2-beam equation, recalled below with the phase $\Delta\phi$ split into a random term representing the phase of the speckle field $\phi_{speckle}$ and the sought-after quantity ϕ_{OPD} :

$$I_{tot} = I_o + I_m \cos(\phi_{speckle} + \phi_{OPD}) \quad (II.10)$$

Now the background intensity I_o , the modulation intensity I_m and the phase $\phi_{speckle}$ are random variables. The intensity pattern recorded on a sensor array contains definitely the information but, on the contrary of smooth-wave interferometry, this information is

embedded in "noise" and its extraction is thus not straightforward. Applying classical phase extraction methods will not lead to any kind of usable information. SI techniques are actually differential, and to get rid of the random phase term $\phi_{speckle}$, a reference state is needed. In addition, the two states have to be correlated, which means that speckle grains of the two states must be at least partially superimposed. Impact of decorrelations on the achievable accuracy of the extracted phase will be discussed in Chapter 3 and 6. Depending on the sought information (deformation, displacement, shape), special experimental arrangements are required, and this will be the theme of the coming subsections.

2.4 The interferometer sensitivity: what can we measure in SI?

In SI setups, in contrast with classical interferometry, the link between the change of the physical quantity and the phase depends on both the illumination direction and the observation direction. We usually define the observation direction as the line joining any point M on the object surface to the pupil center of the recording device (CCD or CMOS camera). In a similar manner, we define the illumination direction as the propagation direction of the beam impinging the object at the same point M . We respectively associate the vectors \vec{K}_o and \vec{K}_i to those directions. We can then define the so-called sensitivity vector $\vec{S} = \vec{K}_o - \vec{K}_i$ of the speckle interferometer (Fig.II.2).

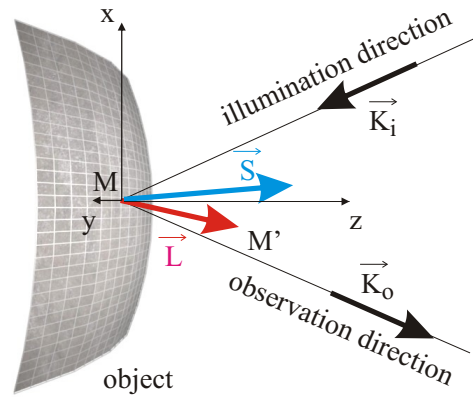


Figure II.2: Speckle interferometer sensitivity.

This leads to the very general formula which gives, for a certain displacement $\vec{L} = \overrightarrow{MM'}$, the corresponding phase change:

$$\Delta\phi = \frac{2\pi}{\lambda} \vec{S} \cdot \vec{L} \quad (\text{II.11})$$

In a system of axes (x, y, z) attached to the object surface, the projection of \vec{S} on the z axis defines the out-of-plane sensitivity, while its projection on the (x, y) plane defines the in-plane sensitivity. It is of primary importance to carefully design the interferometer to have the highest sensitivity along one preferential direction and the lowest one along other directions for the sake of interpretability of the observed correlation fringes and the extracted phase. The know-how of people using SI consists indeed in choosing properly an interferometer whose response is predominantly due to one of the components, to extract a meaningful phase. Measuring all the displacement components necessitates special and complex arrangements ([69, 78]), where several illumination and/or observation directions are successively selected and synchronized with the acquisition and storage system. Another matter of concern is the variations of \vec{K}_o and \vec{K}_i within the field of view, inducing a variable sensitivity vector. This issue is readily solved by a careful calibration step, with a well-controlled experiment (in general a rigid body motion along the average sensitivity vector).

2.5 Fringe formation in SI

As mentioned above, SI methods are differential, and both states (e.g. before and after deformation of the probed object) are specklegrams where no fringes appear directly. The first step consists in general in recording the reference state:

$$I_i = I_o + I_m \cos(\phi_{speckle}) \quad (\text{II.12})$$

A second pattern is recorded after application of a load to the object:

$$I_f = I_o + I_m \cos(\phi_{speckle} + \phi_{OPD}) \quad (\text{II.13})$$

ϕ_{OPD} is the phase change induced by the deformation of the object and is the wanted quantity. If no fringes can be seen at this stage, it is nonetheless possible to compute the square of the difference between the two recorded states to form the so-called correlation fringes - the two states must be correlated (see next chapter):

$$(I_f - I_i)^2 = 2I_m^2 \sin^2(\phi_{speckle} + \frac{\phi_{OPD}}{2}) \cdot (1 - \cos(\phi_{OPD})) \quad (\text{II.14})$$

We obtain a pattern whose envelope is a function of ϕ_{OPD} , showing thus locations of equal displacement as bright and dark fringes (ϕ_{OPD} being respectively equal to $2k\pi$ and $(2k + 1)\pi$, k being an integer). However, the bright fringes are modulated by a term depending on random quantities, *i.e.* the modulation intensity I_m and the speckle phase $\phi_{speckle}$. It gives this grainy aspect to the so-built fringes, which necessitate some filtering step before applying any kind of fringe analysis technique. Fig.II.3 shows a specklegram recorded in a SI setup with an in-plane sensitivity. After having recorded a second image,

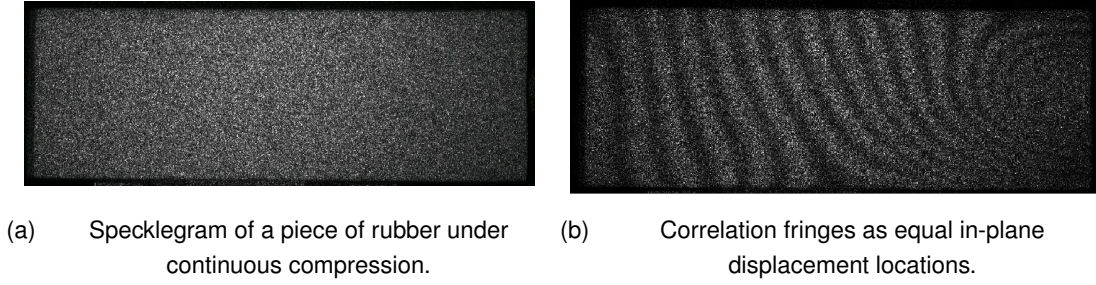


Figure II.3: An example of subtraction fringes experimentally obtained in an in-plane setup.

the two patterns are subtracted to form the correlation fringes shown in Fig.II.3(b).

Correlation fringes can also be observed by adding the two recorded patterns of Eq.(II.12) and Eq.(II.13):

$$I_f + I_i = 2I_o + 2I_m \cos(\phi_{speckle} + \frac{\phi_{OPD}}{2}) \cos(\frac{\phi_{OPD}}{2}) \quad (II.15)$$

The background is not removed, and the fringes visibility is thus reduced. However, it is possible to obtain directly such fringes patterns by performing double-exposure experiments, without recourse to photographic processing or plate relocation². Such arrangements have been proposed for the first time in the 1970s by Cookson *et al* for vibration analysis ([41]) using a vidicon TV camera and a pulsed ruby laser. Very high speed transients have been observed this way with laser pulse separation of a few tenths of μs . Some researchers have proposed since then techniques to enhance the poor contrast of addition fringes recorded by CCD sensors ([94, 131]).

2.6 Experimental setups

There are mainly two groups of interferometers: the external-referenced ones and the self-referenced ones. In usual operating conditions the first group is generally used for out-of-plane characterization and the second one for in-plane characterization and shearing measurements.

2.6.1 Out-of-plane speckle interferometer

This class of speckle interferometers features a sensitivity vector along the normal of the surface under analysis. Typical arrangements are shown in Fig.II.4.

²Butters and Leendertz proposed in [29] a double exposure speckle technique involving photographic plate in the very beginning of the 1970s.

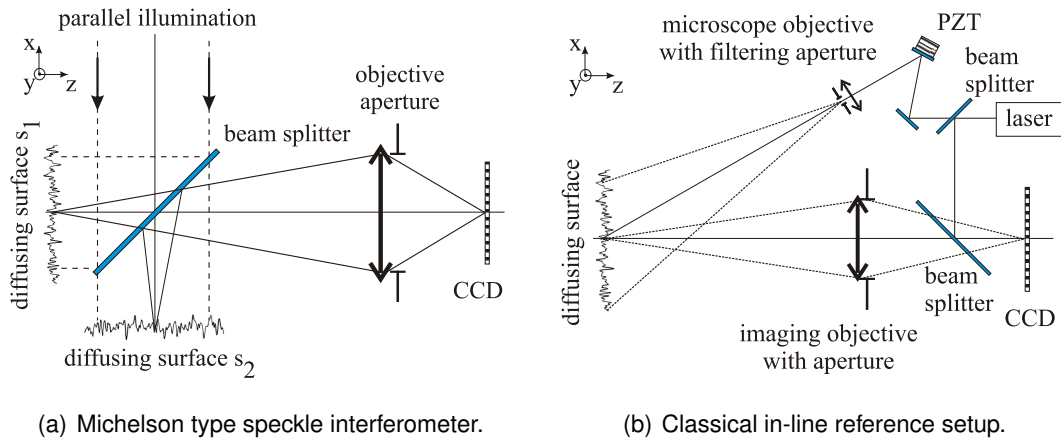


Figure II.4: Typical out-of-plane setups.

In Fig.II.4(a), a Michelson type setup, where the mirrors are replaced by diffusing surfaces, is shown. In addition, a temporal carrier can be easily added by implementing a PZT actuator on one arm.

Lately a new class of self-referenced interferometers has been proposed [27] for out-of-plane measurement. Those interferometers stand indeed apart from the general classification mentioned earlier. Those namely "double-focusing" interferometers have typically a Michelson structure with unbalanced arms, either it be by a longer optical path or by an additional optical element. The object beam is focused on the detector, while the reference beam is defocused. Those interferometers lead to compact and simple setups.

2.6.2 In-plane speckle interferometer

The probably most well-known arrangement used to perform in-plane measurement is the Leendertz configuration, also known as dual-illumination, single-observation direction method. The Duffy's - or single-illumination, dual-observation-direction method - method is also well-known but has been rather used in Moiré gauging. A schematic of the latter experimental arrangement is shown in Fig.II.5.

The wave coming from the two apertures interfere in the image plane with an angle. Hence, the speckle grains, whose size depends on the aperture diameter, are modulated by a straight fringe pattern. After deformation, the fringe are locally shifted and the addition of the two states - either through the use of a developed photographic plate, or numerically in a computer - create a Moiré-like fringe pattern.

Leendertz demonstrated in [104] the fringe formation in SI by superposition of speckle patterns coming from either two different scattering surfaces, or a single one. This latter case necessitates two directions of illumination (see Fig.II.6) making an angle θ_1 and θ_2 with the surface normal. We usually assume that the average directions of illumination

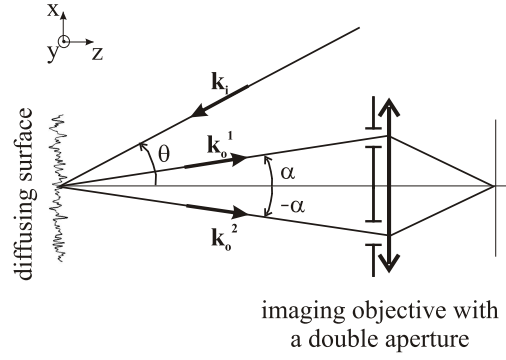


Figure II.5: Duffy's configuration for in-plane measurement.

are symmetrical, *i.e.* $\theta_1 = \theta_2$ for the chief rays. The recorded speckle pattern is the result of the coherent superposition of two speckle patterns.

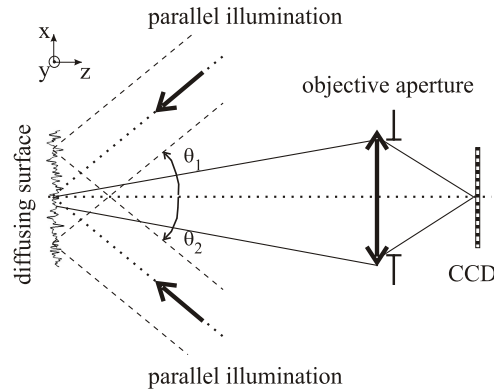


Figure II.6: Leendertz configuration for in-plane measurement.

With a parallel illumination, any displacement along the z or the y axis produces no relative phase change between the superposed speckle patterns. However, a surface movement δx in the x direction produces for one beam a phase change of $(2\pi/\lambda)\delta x \sin \theta$ and for the other one a phase change of $-(2\pi/\lambda)\delta x \sin \theta$ resulting in a relative phase change equal to:

$$\Delta\Phi = \frac{4\pi}{\lambda}\delta x \sin \theta = \mathcal{S}_x \delta x \quad (\text{II.16})$$

With a divergent illumination, the angles θ_1 and θ_2 will change across the field of view. For points where the illumination angles are no more symmetrical, the in-plane sensitivity

\mathcal{S}_x ³ will fluctuate whereas, there will be a residual out-of-plane sensitivity \mathcal{S}_z :

$$\begin{aligned}\mathcal{S}_x &= \frac{2\pi}{\lambda}(\sin \theta_1 - \sin \theta_2) \\ \mathcal{S}_z &= \frac{2\pi}{\lambda}(\cos \theta_1 - \cos \theta_2)\end{aligned}\tag{II.17}$$

A very nice feature of this kind of setups is that the wanted sensitivity \mathcal{S}_x is readily tunable by changing the illumination directions.

Lately, a new class of speckle interferometers with a radial in-plane sensitivity has been proposed in [5, 6]. Originally the radial in-plane sensitivity was obtained with two coaxial conical mirrors - one of the mirrors can be shifted along its axis with a PZT actuator to introduce a temporal carrier - illuminated by an annular collimated laser beam. The last development involved a circular diffractive element, and is somehow a Leendertz configuration with an axial symmetry. The nice feature of this arrangement is that its sensitivity, given by $\mathcal{S}_\rho = 2\pi/p$, depends only on the period of the grating p , which makes possible the use of cheap low coherence laser sources.

2.6.3 Shearing speckle interferometer

Experimental mechanics experts, and especially strain analysts, are often more interested in deformation, *i.e.* the derivative of the displacements, than in displacements. A straightforward way is to compute the displacement map and differentiate it. The differentiating operation is equivalent to high-pass filtering, and thus tends to enhance the noise, which is not negligible in phase maps stemming from SI measurements. It is thus preferable to obtain a phase map which is directly representative of the deformation field, and the numerous proposed techniques are well-known under the denomination shearography, or equivalently, speckle shearing interferometry. Leendertz, and shortly after Hung, imagined in the 1970s a setup based on a classical Michelson configuration with lateral shear (Fig. II.7), whereby derivative of displacements could be directly computed from the extracted phase ([86, 103]). Interested readers are invited to look into [168] for a pretty comprehensive review of setups with various sensitivities. It has to be said that the Duffy's arrangement for in-plane measurement can be easily adapted for shearing by simply adding a wedge in front of one aperture. As predictable, shearing arrangements have been widely used in experimental mechanics circles to compute strain fields ([2, 170]).

The phase change is now proportional to the difference of displacement of any point on the surface, realizing this way an optical differentiation:

$$\Delta\Phi = \frac{2\pi}{\lambda} \Delta x (1 + \cos \theta) \frac{\partial w(x, y)}{\partial x}, \tag{II.18}$$

³We set apart the component of the sensitivity vector \vec{S} along the x-axis S_x and the quantity \mathcal{S}_x which includes the term $2\pi/\lambda$. This latter quantity represents the amount of phase induced by a unitary deformation. We will call \mathcal{S}_x the in-plane sensitivity and likewise \mathcal{S}_z the out-of-plane sensitivity for the sake of simplicity.

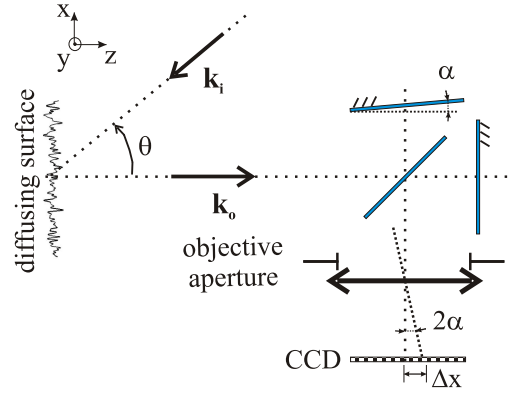


Figure II.7: Michelson arrangement for shearing.

where Δx is the lateral shear and $w(x, y)$ is the displacement of any point on the surface along the z -axis. This setup has some nice features, with notably a pretty good insensitivity to external perturbations as the two interfering beams are created very close to the detector⁴. In addition, the shearing amount Δx is easily tunable to adapt the interferometer sensitivity.

2.6.4 Contouring speckle interferometer

As already explained before, SI techniques necessitate two states. To perform shape measurements of rough objects, as no load is applied to the object, the two states are generated by changing one parameter of setup (wavelength, refractive index, illumination direction, object orientation) ([168]). The setup is usually the same configuration (see Fig.II.8) as the one used for in-plane measurement (Leendertz type). If the illumination direction change is small and designated by $\delta\theta$, then, using Eq.(II.17), the sensitivity to the surface height (along the z coordinate) is simply given by:

$$\mathcal{S}_z = \frac{2\pi}{\lambda} 2 \sin(\theta) \delta\theta \quad (\text{II.19})$$

This is the dual-beam shifted SI contouring technique ([196]). A technique using a Duffy like arrangement has been proposed in ([161]). Another approach is to use an out-of-plane setup and to generate the two required states with a slight shift of the illumination source wavelength, while keeping the geometrical parameters of the setup untouched. The subtraction correlation fringes represent the contour lines where the elevation difference between consecutive isohypsies is $\Lambda/2$, Λ being the synthetic wavelength, ranging

⁴We assume here that the illuminating beam wavefront does not experience perturbations that would be non-uniform across its propagation region. Otherwise, the shearing phase would include the derivative of those perturbations.

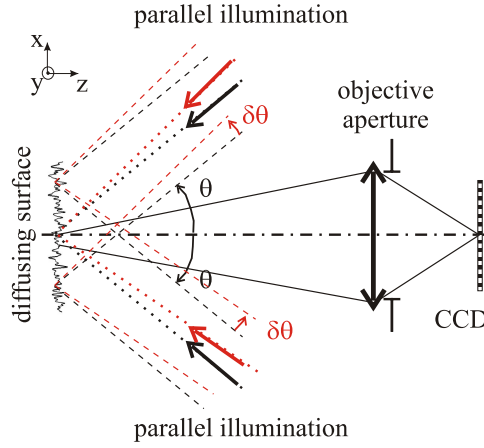


Figure II.8: Leendertz setup for surface contouring.

from microns to millimeters depending on the closeness of the wavelengths:

$$\Lambda = \frac{\lambda_1 \lambda_2}{|\lambda_1 - \lambda_2|} \quad (\text{II.20})$$

3 Imaging versus interferometric methods

The object of this section is to present an alternative to interferometric methods for full-field measurements and wavefront reconstruction, and methods involving a reference beam (interferometric methods) are thus not considered here. We will briefly adopt the general point of view of digital holography, of microscopy and finally of experimental mechanics end user. More precisely, these approaches are the wavefront reconstruction with the deconvolution problem, the phase retrieval from one or several intensity measurements with notably the Gerchberg-Saxton algorithm, and finally the digital image correlation. Wang *et al* introduced the optical vortex metrology ([187]) some years ago. We will come back to those techniques in the forthcoming chapter, as they involve topological objects of speckle fields, namely, the phase singularities.

Classical holography has, nowadays, unfortunately fallen out of favour with researchers and engineers who use and/or look for full-field measurements methods. However, digital holography (DH) has the wind in its sails since its feasibility has been established in the mid 1990s ([162])⁵. The idea is actually to replace the photosensitive substrate by an electronic sensor array, to perform the reconstruction process numerically, through the use of the Fresnel integral (see Appendix B), instead of optically. Schnars and Jüptner wrote a review article on the principles and the major applications of DH ([163]).

⁵The principle of numerically reconstructed images from electronically detected holograms was originally demonstrated by Goodman *et al* thirty years before ([73])

Reconstruction algorithms in DH ([112]) feature a valuable flexibility as they offer the opportunity to numerically compensate optical aberrations ([38]), a task which was originally done by well-designed and expensive optics. DH also lends perfectly itself to microscopy ([1]) and this way to the characterization of micrometric and submicrometric objects (MEMS/MOEMS, micro optics ([31]), living cells ([32]), etc). A theoretical formulation of digital Fresnel holography is available in [146], where the reconstruction process formulation follows the classical imaging theory, that is to say the reconstructed field (say in the +1 order) results from the convolution between the object field and the impulse response of a linear system. This latter function is composed by functions representing the reference wavefront aberrations, the focusing error, the finite extend of the pixel⁶ and of the sensor and finally the reconstructed image localization. The intrinsic spatial resolution in digital Fresnel holography is imposed by the finite size of the sensor, which is the recording zone. To extend the recording zone and thus the spatial resolution, solutions have been proposed with notably a shift of the sensor in the observation plane to make several recordings so as to record a synthetic hologram, larger than the sensor. An alternative approach has been proposed in order to increase the numerical aperture of the holographic system: the idea is to insert a grating in the path of the object beam so as to fold back parts of the diffracted beam by the object, corresponding to higher spatial frequencies, which otherwise would have fallen outside the sensor array. The method has been originally presented in [115] with a 1D grating, and substantially improved with a 2D grating in [143].

Apart from the classical reconstruction algorithms succinctly presented before, a different approach has been proposed by Skarman and improved by Yamaguchi ([193]), and is known as phase-shifting digital holography. The basic idea is to use a phase-shifting algorithm to compute the complex optical field in the electronic recording support plane. The wave field in another plane is then computed with the Rayleigh-Sommerfeld integral (see Appendix B). The bulk of this thesis is the phase extraction from SI signals in dynamic regime, but it is quite clear that DH can benefit from the techniques developed here for SI.

Another set of techniques exists, called sometimes in-line holography, allowing object reconstruction from a sequence of recorded diffraction pattern. The basic principle is shown in Fig.II.9 and was first proposed by Pedrini *et al* a couple of years ago ([144]) with transmitting apertures.

The reconstruction technique has been shown to perform well with diffusiving objects, transmitting or reflective [10]. Improved procedures have been proposed since then, no-

⁶The spatial resolution of electronic sensing devices is at least one order of magnitude lower than the one of usual argentic emulsions: 1000 lines per mm and up to 5000 for photographic emulsions, to compare to at most 100 lines per mm for an electronic sensing device ([163]). In DH, the maximum angle between the reference wave and the object wave is therefore limited to a few degrees.

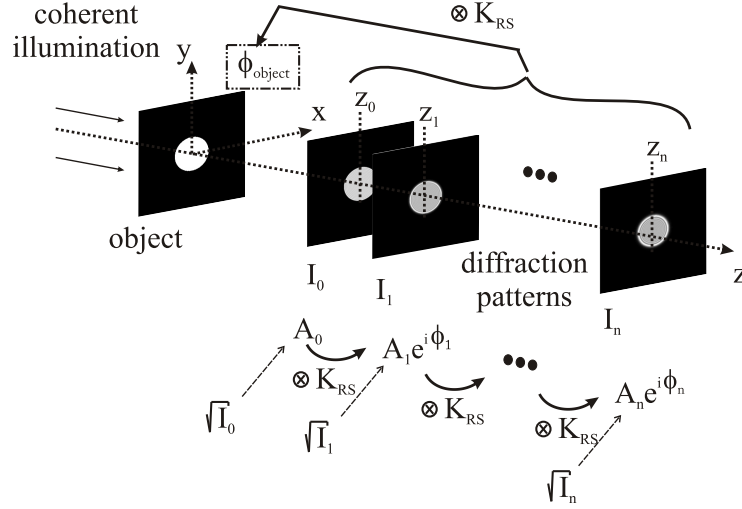


Figure II.9: Principle of object reconstruction from a sequence of diffraction patterns.

tably with the introduction of a random phase object right after or before the object, and are known under the terminology speckle-based phase retrieval technique ([9, 12]). The addition of the random diffuser allows the detection of very low frequencies with recording planes that are recorded at close locations, in comparison with what would be necessary in classical in-line holography without diffuser.

Let us now take the second point of view, the one of the microscopy expert. The only things that can be readily measured in optics are intensity maps and power spectrum, which means that some substantial knowledge about the object, carried by the phase, is lost. The Gerchberg-Saxton algorithm has been originally designed to address the problem of recovering the phase from two intensity measurements. The block diagram of the algorithm is recalled in Fig.II.10, where $g(x, y)$ and $G(u, v)$ designate complex quantities in real and Fourier domains respectively. The convergence of the algorithm is notably discussed in [59], where others algorithms are moreover proposed. A generalization of the Gerchberg-Saxton algorithm for nonunitary optical system, the Yang-Gu algorithm, can be found in [194].

The conventional Shack-Hartmann sensor is another well-known technique of wavefront sensing and has been - is still - used in astronomy. This sensor uses a microlenses array and its principle is basically to measure the deviation of the spot given by each lens from its optical axis, giving this way the average local slope of the wavefront. The use of such a device is still plagued with low spatial resolution.

To conclude this section, we can say some words on digital image correlation - DIC - ([141, 175, 176]), which took over classical gauge sensing in the experimental mechanics circles two decades ago. Without enlarging on the subject, the basic idea is to compare

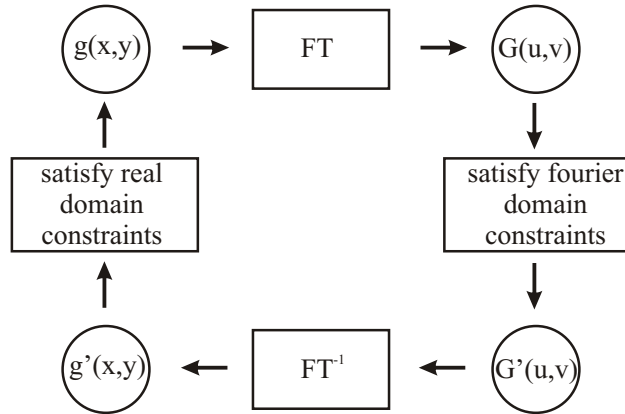


Figure II.10: Block-diagram of the Gerchberg-Saxton algorithm.

the two frames corresponding to the states of the probed surface before and after deformation and obtained by classical imaging with a white light illumination. The recorded frames are actually split into picturelets of usually 10×10 pixels, on which an interpolation procedure is performed. The correlation function is then computed between the smooth interpolated picturelets and its maximum gives the local averaged (due to the use of sub-windows) in-plane displacement of the surface between the two states. The interpolation step with efficient algorithm for the correlation function computation allow to achieve an accuracy in the displacement computation up to $1/100$ pixel. Though being a huge improvement with respect to gauge sensing, the DIC techniques present poor spatial resolution. In addition, a speckle-like structure is most of the time needed on the object surface if the sample does not present its own natural texture. Moreover the achievable accuracy for displacement computation of SI techniques is usually acknowledged to be submicrometric and, say, one order of magnitude smaller than DIC techniques in usual conditions. However, apart from the speckle-like structure which needs to be attached to the probed surface in some manner - which excludes DIC techniques from non destructive remote sensing techniques - , the setup is very simple and obviously much less sensitive to external disturbances than interferometric arrangements.

Chapter III

Theoretical description of speckle fields and speckle interferometry

1 The central limit theorem and basic first order statistics

1.1 The perfectly resolved case

We have seen in the previous chapter that speckle phenomenon arises each time a surface with a roughness scale of the same order of magnitude of the light wavelength is illuminated with a beam of coherent light. The Huygens principle stipulates that the surface can be seen as a certain number N of independent phasors, and at each point of the speckle pattern the electric field is the sum of their N contributions. Having no clue on the exact structure of the surface, a deterministic analysis of the resulting field is not possible. The central limit theorem is the starting point of all the statistical analysis of speckle fields. This fundamental theorem states that the probability density function (PDF) of the speckle electric field tends toward a gaussian distribution as soon as N tends to infinity. In practice, we observe a gaussian speckle pattern as soon as few tenths of elementary scatterers are involved.

Assuming having a large enough number of independent phasors, the joint PDF of the electric field real and imaginary part is Gaussian (see Fig.III.1(a)):

$$p(A_r, A_i) = \frac{1}{\sigma^2} \exp\left(-\frac{A_r^2 + A_i^2}{\sigma^2}\right) \quad (\text{III.1})$$

By applying a variable transformation from the couple (A_r, A_i) to (I, ϕ) on the previous gaussian distribution, we obtain a uniform distribution for the phase of the resultant phasor in the range $[-\pi, \pi]$, while the light intensity defined by $I = AA^*$ obeys the well-known negative exponential distribution:

$$\begin{aligned} p(I) &= \frac{1}{\langle I \rangle} \exp\left(-\frac{I}{\langle I \rangle}\right), \text{ for } I \geq 0 \text{ and } 0 \text{ elsewhere} \\ p(\phi) &= \frac{1}{2\pi}, \text{ for } \phi \in [-\pi, \pi], \end{aligned} \quad (\text{III.2})$$

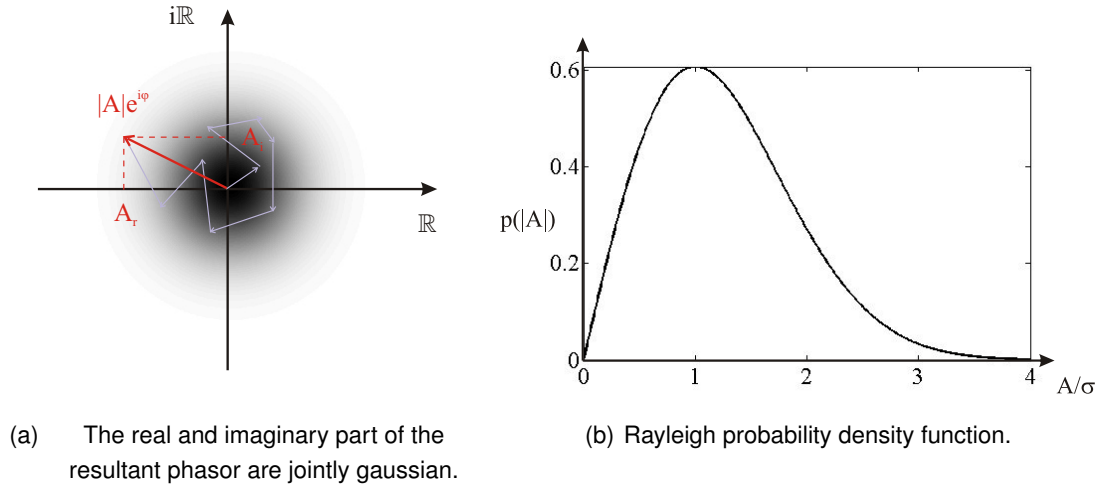


Figure III.1: First order statistics of (A_r, A_i) and $|A|$.

where $\langle . \rangle$ stands for the averaging operator. It is worthwhile to point out that the real and the imaginary parts are jointly gaussian but it is not the case for the amplitude of the electric field. The PDF of the amplitude is readily obtained by a direct-probability transformation of Eq.(III.1) ([77]) and is known as the Rayleigh density function (see Fig.III.1(b)):

$$p(|A|) = \frac{2|A|}{\sigma^2} \exp\left(-\frac{|A|^2}{\sigma^2}\right) \quad (\text{III.3})$$

1.2 The integrated case: the box-car approximation

What has been seen so far holds for the ideal case of an infinitely small detector. In the real world, the sensors are obviously of finite size and the statistics of integrated speckle fields are rather different from the ideal resolved case. The smooth resolved speckle intensity pattern can be approximated by a staircase function as shown in Fig.III.2. Within each individual sub-area, the assumption of a constant intensity $I(x, y)$ can be made. The intensity values of the sub-areas are in addition supposed to be statistically independent. In other words, the sub-areas must thus be small enough for the approximation of constant intensity to hold and large enough for the assumption of statistical independence to be valid. Under those assumptions which constitute the so-called box-car approximation, the integrated intensity PDF takes the following form ([77]):

$$p(I) = \frac{1}{\Gamma(m)} \left(\frac{m}{\langle I \rangle}\right)^m I^{m-1} \exp\left(-m \frac{I}{\langle I \rangle}\right), \quad (\text{III.4})$$

where $\Gamma(m)$ is the gamma function of argument m . m can be interpreted as the number of independent sub-areas within each elementary sensor. This interpretation holds for large values of m and fails as m becomes closer and closer to 1 which is the asymptotic

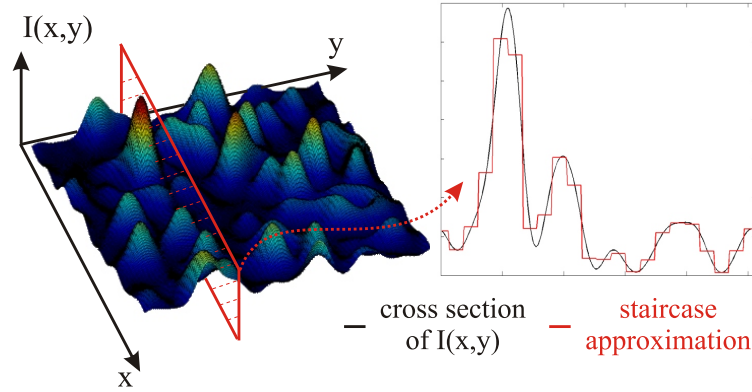


Figure III.2: The box-car approximation.

value of the resolved case ¹. The case $m = 1$ does certainly not correspond to one correlation cell per elementary sensor. It has been shown nonetheless that the negative exponential distribution can be obtained to a good confidence level for an aperture size ten times smaller than the average speckle size ([133]).

In Fig.III.3, a nearly resolved speckle pattern and an integrated one, both obtained by numerical simulation ², are shown with the corresponding values of m . The theoretical PDFs are depicted with respect to the variable $I / \langle I \rangle$, jointly with the computed histograms. The central limit theorem applies again here for large values of m . The PDF of a strongly integrated speckle pattern tends to follow a Gaussian law, centered on the mean intensity. The gamma distribution of Eq.(III.4) is pretty accurate for small and large values of m .

The first order statistics give insight in the energy fluctuations and second order statistics are necessary to get more knowledge on the spatial properties of the speckle pattern, or in other words on granularity of its spatial structure.

¹ m is the fitting parameter of the gamma distribution, and it is only in some cases that it can be connected to the number of speckle grains contained in the elementary sensor. Two different symbols are used in [75] to avoid the ambiguity, m and \mathcal{M} .

²All the simulations of complex speckle fields have been carried out based on the model described in Appendix B and [52].

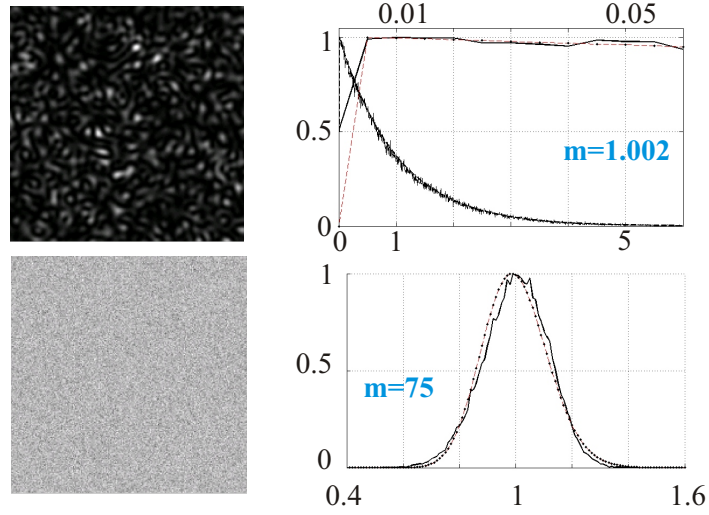


Figure III.3: Nearly resolved and integrated simulated speckle patterns and the corresponding PDFs.

2 The notion of speckle grain and second order statistics

2.1 The perfectly resolved case

Given a speckle pattern, the autocorrelation function of the intensity map provides a measure of the characteristic size of a speckle grain:

$$R_I(r) = \langle I(r_0)I(r_0 - r) \rangle, \quad (\text{III.5})$$

where $\langle . \rangle$ denotes an averaging over an ensemble of rough surfaces. The dimension of the objective impulse response is the resolution limit in the image plane, so we expect from the computation of R_I to retrieve this physical dimension for the average size of the speckle spot. For the usual case of a circular lens aperture of diameter D , the autocorrelation function takes the form of the Airy function and the average transversal width of the grain is thus ([110]):

$$\delta_t \approx \frac{\lambda z}{D}, \quad (\text{III.6})$$

where λ is the wavelength of light and z is the distance between the exit pupil of the lens and the image plane. For the case of objective speckle pattern, the same formula applies with D now corresponding to the dimension of the illuminated area and z the distance between the diffusing surface and the observation plane.

Along the z -axis, the average width is given by ([110]):

$$\delta_l \approx \frac{8\lambda z^2}{D^2} \quad (\text{III.7})$$

The first zero of the 3D autocorrelation function of the intensity map define a volume which has the famous cigar shape (see Fig.III.4).

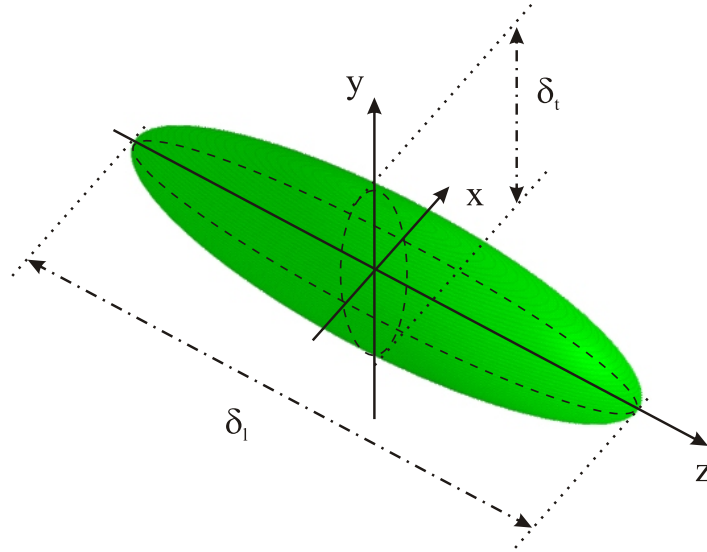


Figure III.4: The statistical dimensions of speckle grain in 3D.

A more detailed study of the 3D dimensions of the speckle cell outside of the Fresnel diffraction domain can be found in [110, 111]. For a free-space pattern, the speckles grains point away from the center of the illuminated area of the scattering surface. They tend to stretch along the observation direction and to have an elliptic profile in a transversal plane.

The 3D average dimensions of the speckle grain do not depend on the defocusing or on the geometrical aberrations ([77, 132]), insofar as aberrations correspond to an additional phase term in the pupil plane. The zeros of the autocorrelations functions are thus not affected. This is actually no more the case for partially developed speckle fields, and it turns out that, if the zeros of the power spectral density ([132]) remain unaffected by aberrations, the distribution of energy inside the main lobe changes³. In the following only the case of fully developed speckle fields will be considered. This cigar-shaped volume actually define the volume of correlation of the speckle field. This notion of correlation volume is of primary importance in SI and we will come back to this notion more thoroughly later on, especially when talking about decorrelations and random phase errors in SI.

³The power spectral density (PSD) of a speckle pattern is defined as the FT of the autocorrelation function of intensity, or in other words as the convolution of the coherent transfer function of the lens with itself. It represents the distribution of intensity fluctuations with respect to spatial frequencies. As an example, the PSD of a subjective speckle pattern involving a rectangular uniform aperture has triangular cross-sections along the axes in the frequencies plane ([77]).

2.2 The correlation cell of integrated speckle fields

We have quickly reviewed the box-car approximation, which provides the framework notably to easily compute some first-order statistics in integrated regimes. The integration of the array sensor has also an influence on the second-order statistics, *i.e.* on the correlation volume dimensions. The sensor cell integrates the intensity over a certain region of the speckle field. To understand what is happening within this elementary region, the box-car approximation combined with the random walk view in the complex plane is useful. We can indeed consider that the elementary sensor cell collects the contributions from K several independent phasor, to which a complex intensity is associated as follows (see Fig.III.5):

$$I_k = I_{o_k} + I_{m_k} e^{i\phi_k} \quad \text{with } 1 \leq k \leq K \quad (\text{III.8})$$

Each elementary sensor being independent, the correlation cell, in a transverse plane, is thus the pixel itself.

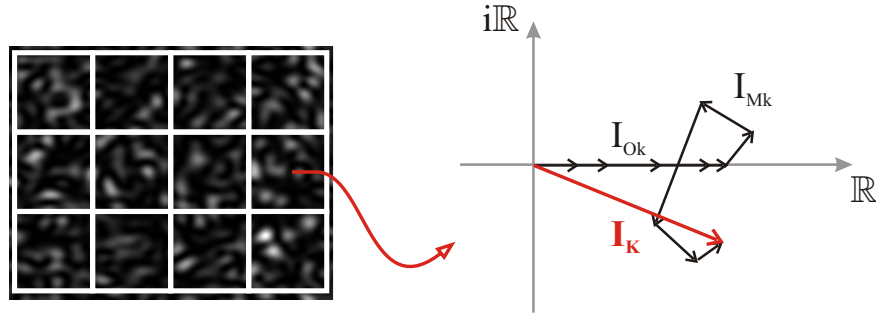


Figure III.5: Resulting intensity of a pixel in integrated regime.

Along the z -axis, the things are slightly different. The sensor cell integrates several speckle grains whose statistical dimension along the propagation axis is given by Eq.(III.7). In Fig.III.6, the contour of a simulated three-dimensional speckle field is jointly shown with different pixels sizes for different integration regimes (The point of computing the speckle cell dimensions by thresholding an intensity map is discussed in [7]. It is notably showed that the speckle grain size is correctly estimated with intensity threshold levels equal roughly to twice the mean value).

We carried out simulations for a nearly perfectly resolved, a weakly integrated and a strongly integrated regime. We know from Eq.(III.4) and common sense that the probability density function deviates from the negative exponential as the speckle field is more and more integrated and tends to a gaussian distribution centered around the mean value, with a narrower and narrower range of likely gray levels. Without conducting any mathematical derivation, we can imagine that the correlation coefficient along the z -axis

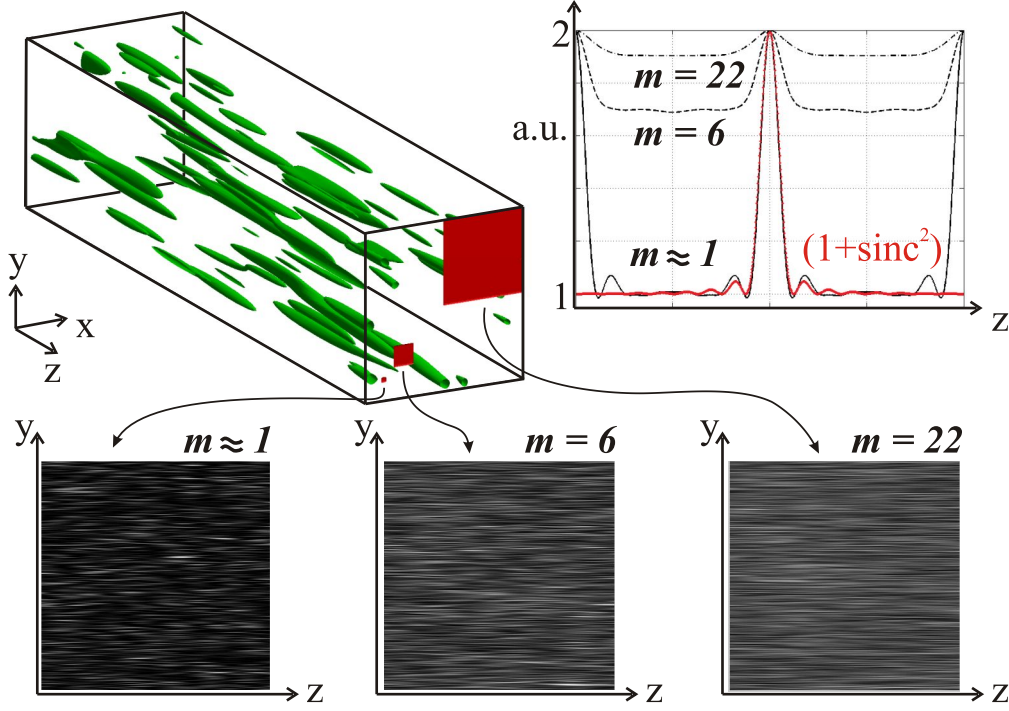


Figure III.6: Effect of the pixel size on the in-depth correlation length.

will deviate from the sinc^2 function as the number of speckle grains integrated in the elementary sensor increases, with a peak less and less sharp, as seen in FigIII.6. We observe from the simulations that the in-depth correlation length seems to increase as the speckle field is more and more integrated. This observation would definitely need a deeper analysis both theoretically and experimentally.

3 Intensity and phase maps topology: phase saddles, vortices and bright spots

3.1 Phase singularities

3.1.1 Existence and basic properties

The central limit theorem states that the real and imaginary part of the electric field resulting from the interference of independent phasors are themselves independent and jointly gaussian.

$$\begin{aligned} A(x, y) &= A_r(x, y) + A_i(x, y) = \rho(x, y) \exp(i\chi(x, y)) \\ \rho^2(x, y) &= A_r^2(x, y) + A_i^2(x, y) \\ \tan(\chi(x, y)) &= \frac{A_i(x, y)}{A_r(x, y)} \end{aligned} \quad (\text{III.9})$$

It is thus likely that $A_r(x, y)$ and $A_i(x, y)$ both vanish, and thus lead to an indeterminate phase $\chi(x, y)$. In their seminal work on phase vortices published in 1974, Nye and Berry ([138]) showed that points of zero complex amplitude exist in pulses diffracted by rough surfaces, and introduced the concept of phase dislocation, a key topological object of speckle fields. Nye and Berry, in [138], placed the emphasis on the dislocations in the non-monochromatic case (pulses of light), and the case of monochromatic speckled wavefront has been studied in [17] and [65].

$A_r(x, y)$ and $A_i(x, y)$ actually define surfaces in space which respectively intersect with the zero plane in a family of lines. The phase singularities are located where those family of lines intersect themselves.

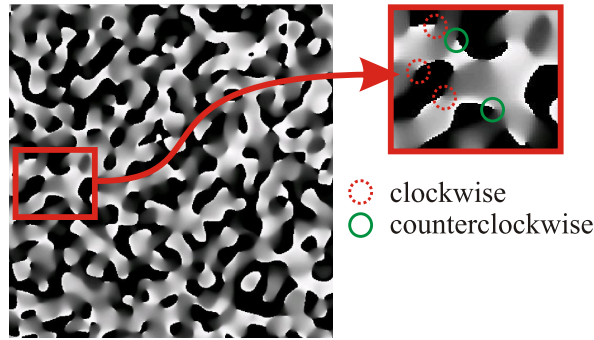


Figure III.7: Phase singularities in a simulated speckle field.

It can be seen in Fig.III.7 that walking around singularities makes the phase go through a full 2π loop clockwise or counterclockwise. In Fig.III.8, a cross-section along the z -axis of a simulated speckle pattern is shown.

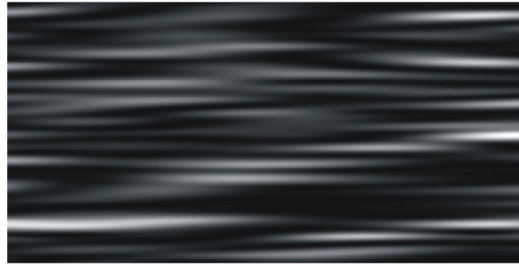


Figure III.8: Longitudinal simulated speckle pattern.

The raw phase of the field is shown in Fig.III.9, while the same phase map where the propagation phase term has been removed is shown in Fig.III.10.

We can see that when walking from A to B in Fig.III.9 the phase ranges from 0 to 2π , while the phase covers a range twice larger along the path $A'B'$. This is the signature of

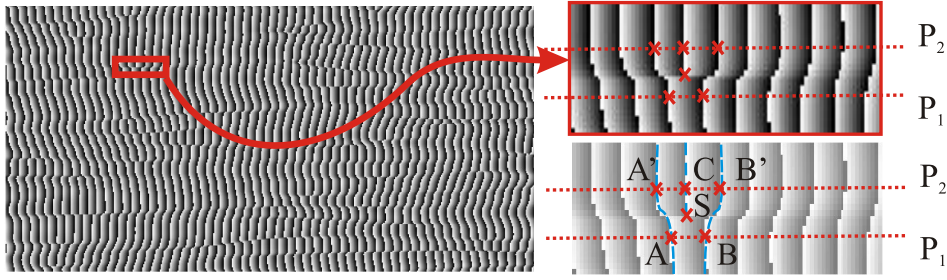


Figure III.9: Phase map of the longitudinal simulated speckle pattern.

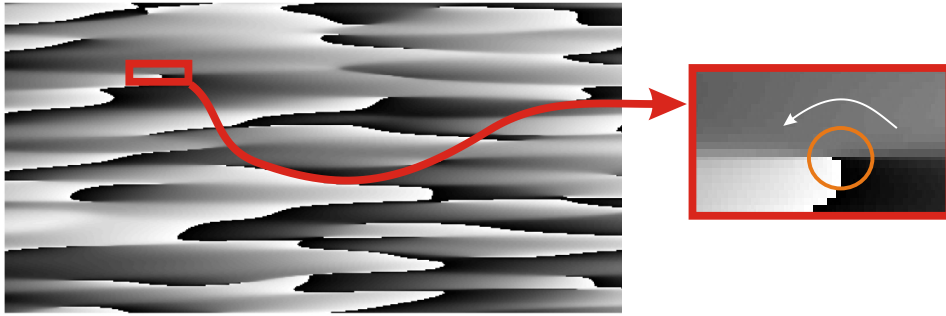


Figure III.10: Phase map of the longitudinal simulated speckle pattern without the propagation phase term.

a phase singularity enclosed in the circuit $A - A' - B' - B$. Moving from A to B in an Argand diagram⁴ simply means turning around the origin once. In the same diagram, two loops lie between A' to B' . It means that if we represent the field in the complex plane while we move smoothly from plane P_1 to plane P_2 , the curve $A(x, y)$ has to pass through the origin (point S in Fig.III.9).

Those simulations meant to show that the fine structure of the phase of a speckle field can faithfully be simulated, and it might be of use to study the connection between the phase map and the intensity map topologies, which has clearly important implications in practice in SI.

3.1.2 Singularities density, motion, birth and annihilation

It is known since the work of Berry in 1977 ([17]) that the phase singularities are in average as numerous as bright spots in a speckle pattern. They are moreover known to appear by pair and disappear as well by pair; a pair containing a counterclockwise (positive) and a clockwise (negative) vortice. Our numerical simulations confirmed that there

⁴An Argand diagram is a plot of complex numbers as points in the complex plane. It is also known as Fresnel diagram, which is used in electrical engineering.

is in average a pair of singularities of each speckle grain, a general result which has been somehow demonstrated in [65]. When we look at a typical speckle phase map (Fig.III.7), the analogy between singularities and electric charges comes naturally to mind, with the equiphases being similar to electric field lines. It is also very intuitive that the singularities can only appear and annihilate by pair, leaving the total charge conserved ([64]).

Singularities in wavefronts can be classified following some topological parameters: sign, isotropy (the constant phase gradient curve around a singularity is a circle in the isotropic case), orientation (it is the angle between the local coordinate system and the global one), amplitude scale factor (it denotes how fast the field increases away from the vortice), and degeneration factor (it denotes how many 2π intervals the phase circulates through in one cycle) ([65]). The analogy with electric field and charges is actually exact for the isotropic and non-degenerated singularities, which is generally the encountered case with circular aperture, symmetrical gaussian illumination beams and in the paraxial approximation.

In [77], the density of vortices is computed for a speckle pattern plus a coherent background. The condition to obtain a phase singularity changes now to obtain at the same point in space a null imaginary part of the field and a real part of the field canceling the background intensity. As might be expected, the stronger is the background intensity, the lower is the probability to form a vortex. The density of vortices is thus reduced by the addition of a coherent background and depends exponentially on the ratio $I_{background} / \langle I_{speckle} \rangle$.

3.1.3 Phase singularities: nuisance or useful feature?

The authors in [138] had already the intuition that phase dislocations may act as markers and thus be of interest in the field of remote sensing, and it is only thirty years later that optical vortex metrology has been introduced by Wang in [187]. The authors make profit of the fact that, without decorrelations, the displacement of each phase singularity is directly related to the local displacement of the object surface. However, extracting the real speckle phase implies an interferometric measurement with a well-calibrated reference beam, with all the usual attention that must be paid to all direct interferometric measurements. The idea of the authors was rather to build an analytic signal directly from the intensity speckle pattern and extract from it a pseudo-phase. The very good point of this approach is that a pseudo-phase can be computed from any structure containing enough randomness (printed or projected random pattern, random texture of an object *etc*). We will come back with details to the analytic method, originally introduced by Gabor in 1946, in one and two dimensions, later on in chapter 4. The analytic signal is thus computed for the original state and the final state as well, *i.e.* after displacement. A pseudo-phase map is computed from the multiplication of the complex signal corresponding to the initial state by the complex conjugate signal corresponding to final state. If the two complex

3. Intensity and phase maps topology: phase saddles, vortices and bright spots

patterns are shifted by the correct amount along both x and y directions, the singularities density within this new pseudo-phase map reach a minimum, as two vortices respectively positively and negatively charged annihilate. In the ideal case of a displacement of an integer number of pixels and sufficiently small to neglect decorrelations effects, all the singularities should be paired and thus annihilated. Looking for the smallest density of vortices yields an accurate measurement of the displacement. As we said before, the intuition of Nye proved to be true, but the method exposed in [187] is not really applicable to real situations, as it is limited to very small displacements - typically a couple of pixels - and also to pure rigid body translations. However, it is one of the very first work which shows that phase singularities are of use in optical sensing.

The method has been deeply revised in [188]. The analytic signal is now built from the original random pattern as follows:

$$I(\tilde{x}, \tilde{y}) = \mathcal{F}^{-1}[\mathcal{LG}(\nu_x, \nu_y) \cdot \mathcal{F}(I(x, y))] , \quad (\text{III.10})$$

where \mathcal{F} is the FT (see Appendix A) and \mathcal{LG} is the Laguerre-Gauss (LG) filter, and defined as a Riesz transform with a doughnut-like zero-phase bandpass filter. The Riesz transform is an isotropic HT and some words will be said about it in the next chapter, as it has been introduced in fringe analysis by Larkin *et al* in [100, 102]. To fix the ideas, the LG filter expression in the Fourier domain is defined by:

$$\mathcal{LG}(\nu_x, \nu_y) = \rho \exp(-\frac{\rho^2}{\omega^2}) \exp(i\theta) \quad (\text{III.11})$$

The spiral phase operator allows an isotropic implementation of the HT in 2D while the LG kernel allows to control, through ω , the density of singularities in the pseudo-phase map. To illustrate the effect of the LG transform, a $N \times N$ speckle pattern has been simulated (see Appendix B) with $N = 128$. From this pattern, a pseudo-phase map has been computed for different values of ω . The results are shown in Fig.III.11. We can clearly observe the impact of the zero-phase doughnut-like amplitude filter on the singularities density.

With the idea to extend the measurement range and to be able to characterize not only pure translation motion but also pure rotation, matching the singularities as before is not enough, and the last improvement of the method lies in the fact that the core structure of the singularities is considered: the topological charge (clock-wise or counterclock-wise singularity and number of 2π cycles around it), the vorticity (vorticity of the phase around the vortex), the eccentricity (ellipticity of the amplitude contour lines) and the zero-crossing angle (angle between the zero-crossing lines of the real and imaginary parts of the analytic pattern) are now computed for each singularities and matched so as to retrieve the object motion. Those features are the fingerprints of each singularity and thus allow its identification without ambiguity. The method has proven to be efficient *in vivo* to track living objects in their own environment (fugu fishes) ([189]).

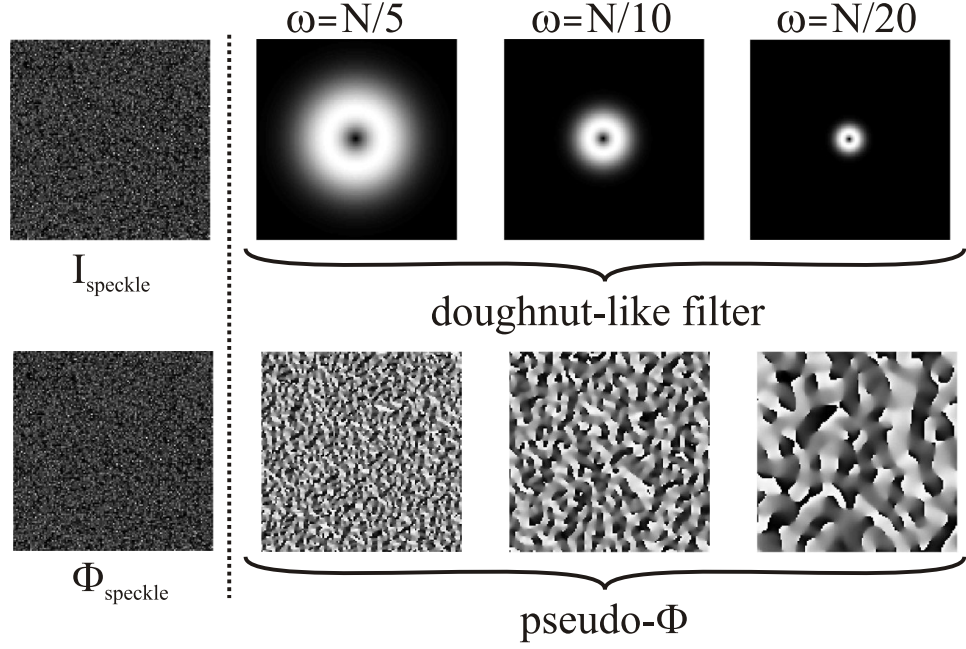


Figure III.11: Examples of pseudo-phase maps computed from a speckle pattern for different sizes of the doughnut-like filter.

3.2 Are bright speckle grains the location of stationary phase?

This section mostly relies on the work of Shvartsman and Freund ([167]). This work actually provided a wealth of insights in the speckle phase maps topology and notably shed new light on the connection between bright spots and stationary phase areas. It was indeed acknowledged that the correlation area of a speckle field is a region of nearly constant amplitude and phase ([65]). This statement might lead to think that the phase is nearly constant within speckle bright grains, which is actually refuted by the following short reasoning: let us consider that the complex-valued speckle field is written: $A(x, y) = B(x, y) + iC(x, y)$. The intensity is given by: $I = AA^* = B^2 + C^2$, while the phase is: $\phi = \arctan(C/B)$. With the convention $dF/dx = F_x$, maxima of amplitude and phase respectively imply the following equations:

$$\begin{aligned} \frac{\partial I}{\partial x} = \frac{\partial I}{\partial y} = 0 &\Rightarrow BB_x + CC_x = BB_y + CC_y = 0 \\ \frac{\partial \tan \phi}{\partial x} = \frac{\partial \tan \phi}{\partial y} = 0 &\Rightarrow CB_x + C_x B = CB_y + C_y B = 0 \end{aligned} \quad (\text{III.12})$$

Those conditions are jointly fulfilled if and only if B_x , B_y , C_x and C_y are equal to zero. B and C being independent random variables, the probability that their partial derivatives vanish together is minute. The phase is thus not stationary within bright grains. The authors observed that speckle spots actually lay on the borders of phase saddles, as shown in Fig.III.12. The authors reported an average phase gradient of 172° per corre-

3. Intensity and phase maps topology: phase saddles, vortices and bright spots

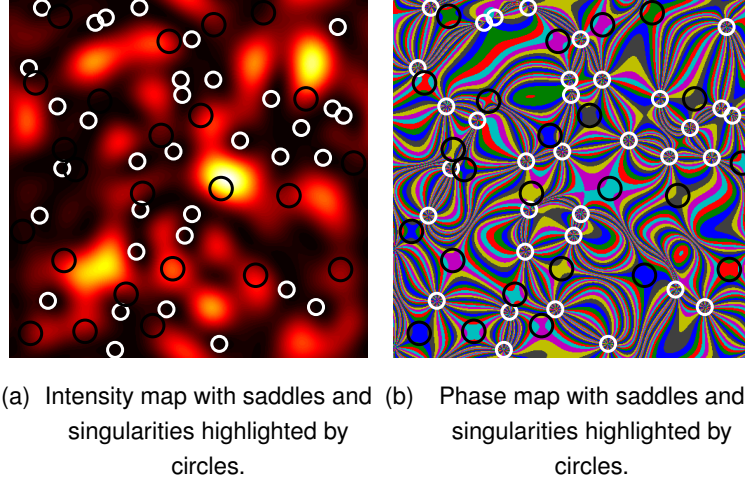


Figure III.12: Topology of phase and intensity in a complex speckle field.

lation length, while it is around 50° per correlation length within bright grains, so more than three times less than elsewhere in average. A theoretical value of 140° is reported in [108]. With the simulation model presented in Appendix B, we also computed the average phase gradient within a speckle phase map and obtained a typical value of $136^\circ \pm 2^\circ$. The small difference comes probably from different definition of the correlation length, but the order of magnitude is the same. As a little detail that it is worthwhile to mention, it is better to compute the gradient using the following trick than classically:

$$\nabla \phi = \sqrt{(\nabla(\cos \phi))^2 + (\nabla(\sin \phi))^2} = \sqrt{(\nabla \phi)^2 (\sin^2 \phi + \cos^2 \phi)} \quad (\text{III.13})$$

Around phase singularities the 2π step can lead to a gradient of $\sqrt{2} \times 2\pi$. The previous trick avoids this wrong estimation.

It is actually surprising that the phase gradient is not null or at least very small within regions of high intensity. Fresnel diagrams are actually of use to predict such behaviors of the complex field in the neighboring of such topological objects (see Fig.III.13). The diagram on the left of Fig.III.13 illustrates the case of a phase saddle. As previously stated, it clearly appears that a phase saddle and an intensity maximum cannot be situated at the same location⁵. In the diagram on the right, we present some likely situations around a maximum of intensity. The green line illustrates the case where a bright speckle grain rides a phase saddle ([167]).

The observations reported in [167] and the analytical derivation in [108]⁶ enable to conclude that the brightest pixels are not the ones to favor as they are the scene of a certain

⁵The speckle field is continuous and differentiable and the curve followed by the field in the complex plane has thus the same properties of differentiability. There is thus no singular point apart from the origin, which is the location of the phase vortices.

⁶It is reported in [88, 108] and acknowledged that the higher the modulation, the lower the random phase error induced by decorrelation.

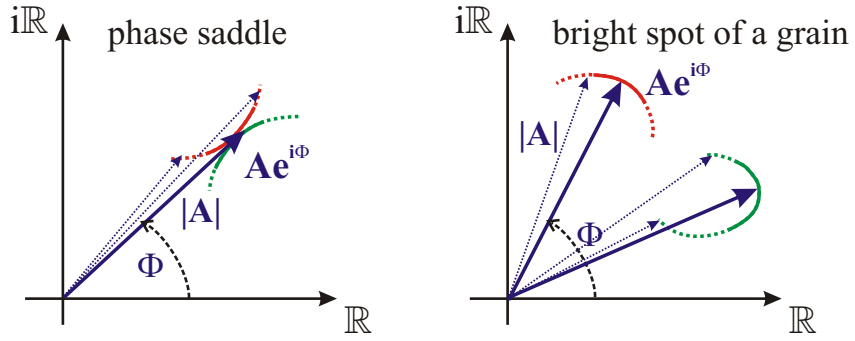


Figure III.13: Likely path followed by the speckle field in the complex plane around a phase saddle (left) and a bright spot in a grain (right).

phase error. The pixels in the neighborhood of a phase saddle, less bright, should thus be privileged. Those conclusions are valid in the resolved case. In the integrated regime, there are no more such topological objects - phase saddles and phase singularities -, especially for large values of m (see the section of the box-car approximation), but the same reasonings hold for the complex intensity of the "meta-speckles", and its path in the complex plane.

4 Optimization of SI measurements with unresolved speckles

Performing accurate measurements in SI requires a certain know-how, as it is less straightforward than in classical interferometry. We will not come to the inherent limitations of interferometric methods or let us rather say the precautions one must take to avoid the recorded signals depending on too many external parameters, degrading this way their quality and thus their reliability and their relevance. This is a well-known point which has received a lot of attention. Here we will rather speak about the parameters we can play on to maximize the measurement quality, which is usually quantified in SI by the amount of random phase errors. Lehmann studied the case in [106, 107] for the resolved and the unresolved regime. The setup parameters considered here are the beam intensity levels with respect to the camera dynamic and noise level, and the lens aperture. The interferometer sensitivity is of course of primary importance but rather for sampling considerations than for measurement quality considerations. The beam intensities, are in practice, limited by the available laser power, especially for large objects, and the lens aperture is thus adapted to match the illumination with the camera dynamic. It is now acknowledged that the speckle grains do not need to be resolved to perform SI measurements. Of course, the highest modulation is attained in the resolved case, but for obvious illumination considerations, performing SI in a resolved case is not realistic in practice.

5. Decorrelations and their impact on the achievable phase extraction accuracy

In addition, in the resolved, or nearly resolved, regime the grey levels that are the most likely are rather black, whereas the range of likely grey levels becomes narrower as and when more and more speckle grains are integrated in the pixel. Thus, in the integrated regime, there may not be pixels with the highest achievable quality, but there will be a higher number of pixels with reasonable quality.

In addition, it makes sense to think that saturation must be avoided. This is actually wrong in SI. Huntley showed indeed in [88] that the decorrelation-induced phase errors are lower when a certain amount of pixels are saturating the sensor. The saturating pixels are useless but their sacrifice allows to elevate the average modulation - and the average SNR - and thus the average reliability of the pixels.

It is reasonable to evaluate the quality of the measurement by attributing a quality index to the pixels of the probing sensor. The two solutions that are offered to us are:

- a binary classification of the pixels: valid and not valid, with respect to a certain criterion.
- a finer classification with continuous weights.

It is now well-known that the decorrelation-induced phase error is to a very good approximation inversely proportional to the modulation intensity, and pixel weights proportional to the square of its modulation represent theoretically an ideal choice ([106, 107]).

At a first glance, the binary classification might appear as a simplistic solution, as a pixel is neither fully good nor completely bad. More realistically, the higher the modulation, the more reliable the pixel, and thus the pixel reliability is gradually getting better and better, as its modulation is itself higher and higher. We chose nonetheless this classification strategy to offer a completely new approach to speckle phase maps filtering, which will be detailed in the chapter 6.

5 Decorrelations and their impact on the achievable phase extraction accuracy

Due to the intrinsic randomness of the intensity and the phase of a speckle field, the temporal SI signal will experience strong fluctuations of modulation and local mean (respectively I_m and I_o in Eq.(II.10)). In [55], we advocated the use of the Empirical Mode Decomposition (EMD) ([85]) to remove efficiently the local mean to give to the signals the required shape for a meaningful subsequent phase computation ([55]). However, when the modulation of the centered signal drops to zero, the derivative of the phase or instantaneous frequency (IF) ([19]) does not reflect the underlying physical phenomenon. In addition, in the vicinity of those areas of null modulation, noise - due to the electronic chain of acquisition, or to laser power fluctuations, or also to mechanical disturbances -

becomes preeminent and the EMD and, as a consequence, the phase extraction tend to be very inaccurate as any other method would be, by the way. Due to the 1D unwrapping operation, the error will propagate and corrupt the whole phase dataset. The statistics of these phase errors are actually quite complex ([77, 88, 109]). In [109], the standard deviation of this error is computed with respect to the decorrelation amount for different pixel modulations (see Fig.III.14).

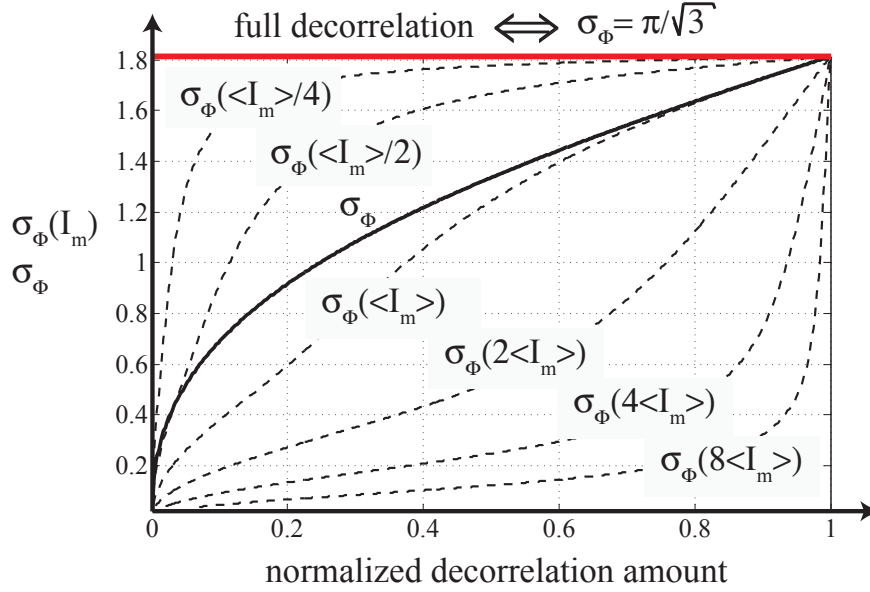


Figure III.14: Overall standard deviation (σ_Φ) and conditional standard deviation ($\sigma_\Phi(I_m)$) of the decorrelation-induced phase error as a function of the normalized decorrelation (0 for no decorrelation and 1 for total decorrelation). The curves of the conditional standard deviation are given for different pixel modulations ranging from $<I_m>/4$ to $8<I_m>$, $<I_m>$ being the mean pixel modulation.

The conclusion is that the higher the modulation, the lower the phase error, reaching of course the maximum value of $\pi/\sqrt{3}$ at total decorrelation (standard deviation of a random variable uniformly distributed in the range $[-\pi, \pi]$). Interestingly, the phase error does not depend on the number of speckle grains per pixel. Those results have been derived analytically for a smooth-reference-wave interferometer and the trickier case of speckle-reference-wave interferometer follows presumably the same trend.

Chapter IV

Phase extraction from SI signals in dynamic regime: still a topical issue

Drawing up a thorough review of the phase extraction techniques is clearly out of our scope, though this work can hardly be found in the literature ([89]). We provide in Fig.IV.1 an attempt of classification of the main techniques in fringe analysis divided in four main streams: morphological, phase probing, definite transforms based methods and stochastic methods.

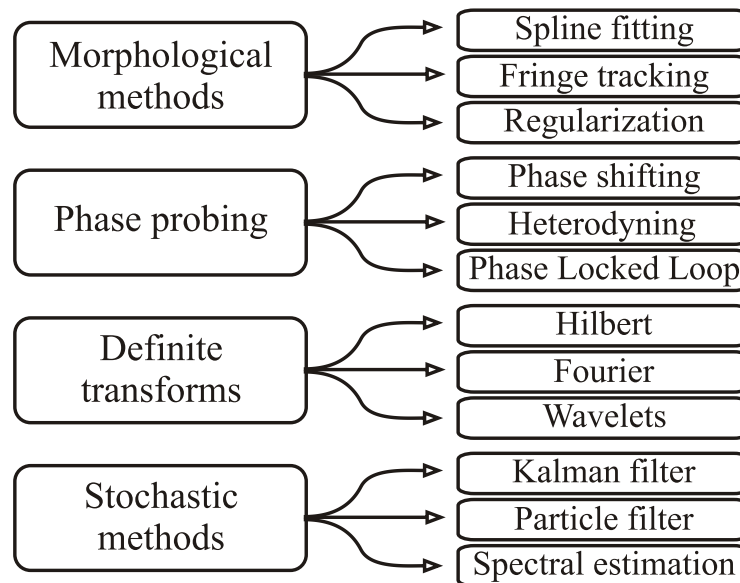


Figure IV.1: A tentative classification of phase extraction methods.

Among phase probing techniques, we found phase-locked loop (PLL) methods ([114]), where the basic idea is to build a system (either analogical or digital) which responds

to both the phase and the frequency of the signal under consideration, and provides, by adapting the frequency of an internal controlled oscillator, an output signal which matches the input signal both in phase and frequency. In fringe analysis, the idea is to analyze the interferogram column-wise or row-wise with a PLL algorithm. Only interferograms with a carrier can be processed this way and different techniques have been developed to increase the noise rejection power and compensate the locked-in time ([71, 165, 166]). The first section will deal with phase-shifting techniques. Those techniques have been massively used and substantially improved ([44, 45]). Though generally acknowledged as the choicest techniques in terms of measurement and spatial resolutions, they are not in essence good candidates for dynamic problems, despite attempts to adapt it to real time situations ([28, 40, 87]). Resorting to single-frame based techniques is then the natural trend, and it will be the matter of the next section. The mainstream techniques are here the Fourier transform (FT) method combined with spatial carrier fringes ([22, 177]), the spiral phase quadrature transform method ([102]), the latter being basically a convenient 2D isotropic Hilbert Transform (HT), the local interpolation of the intensity pattern using splines ([26, 158]), and regularization based methods ([127]). Most of the single-frame techniques need a 2D unwrapping step ([72]), and the task is not trivial with noisy wrapped phase maps, even if iterative filtering techniques have proven to be efficient and easy to implement ([3]). Besides the sign ambiguity that cannot be removed without a priori knowledge, single-image techniques depend on the quality of the correlation fringes. With standard apertures of usual systems, the correlation lengths are as small as a few tens of microns both in out-of-plane and in-plane measurements, and the fringes are not exploitable beyond this range.

Leaving aside computational considerations for the moment, a fruitful approach lies in the pixel history analysis, presented in a third section. It offers not only means to get rid of the intrinsic limit of correlation, but it reduces also greatly the complexity of the unwrapping step, as one deals from now on with 1D signals. The sign ambiguity is moreover easily cleared up by adding a temporal carrier, readily subtracted afterwards. The methods devoted to solve the 1D temporal problem include the Morlet wavelet transform ([35]) and the HT ([120]).

The need of increasing performances in terms of accuracy and computation speed is permanently demanding new efficient processing techniques, and convinced that the temporal approach has a lot to offer, we look for efficient and accurate techniques to compute the phase from the temporal signals of each pixel of the sensor array, which undergo strong intensity fluctuations. To this aim, we consider the problem from a general point of view with a return to the basics of defining the instantaneous quantities of a non-stationary signal. We will thus focus on those issues in the last section of the chapter. We will conclude by the fact that a pre-processing tool is missing to make the SI temporal signals amenable to a meaningful phase extraction step.

1 Phase-shifting interferometry (PSI): the choicest method in terms of measurement accuracy

1.1 Principle of the phase extraction from several intensity maps

Due to the sign ambiguity of the *arccos* function in Eq.(II.10) it is generally not possible to compute the phase distribution from one single interferogram without *a priori* knowledge. The general method to solve this ambiguity is to add a linear temporal carrier ([44]). To this aim, a phase shifter, properly calibrated, is inserted into one arm of the interferometer. Each interference pattern following the two beam equation (Eq.(II.10)), at least three states are necessary to solve the three unknowns equation.

$$I_k = I_o + I_m \cos(\Phi + k\delta\phi) , \quad (\text{IV.1})$$

where $\delta\phi$ is the phase-shift amount induced by the shifter device (e.g. a mirror mounted on a PZT actuator, a liquid crystal cell, *etc*), and Φ is the sought-after phase (it includes the speckle phase and the OPD phase denoted by ϕ_{speckle} and ϕ_{OPD} in Eq.(II.10)). Many algorithms have been designed with a different number of frames and different values for the phase shift. The phase-shifter miscalibrations are a matter of concern in phase-shifting interferometry, and numerous solutions have been proposed to solve this issue ([4, 173, 190]), either by making the algorithm more robust to random errors around the expected values of phase shifts, or by computing alternatively the phase based on *a priori* values of phase shifts and then recompute the phase shifts values based on this phase. The procedure is repeated several times to refine the computation, until some convergence criterions are met. A review and assessment of existing algorithms that are insensitive to linear phase shift errors has been conducted in [134].

The authors in [96] propose an iterative technique to adjust the voltage values applied to the PZT to perform the wanted phase-shifts. Interestingly, they showed that by selecting pairs of quadrature pixels in the array sensor, we can form Lissajous curves whose shape helps to compensate miscalibrations of the PZT actuator. As an example, if the K phase-shifts run over less or more than a 2π cycle, a gap or an overlap is respectively observed on the Lissajous display. The shape of the curve is strongly affected by PZT miscalibrations, mechanical disturbances, sensor non-linearities, thresholding or saturation, and can severely stray from the ideal circular shape. Adjusting iteratively the voltages for each phase-shift amount has a direct visual influence on the curve and it has been demonstrated that an almost circular Lissajous curve, *i.e* a proper phase-shifting voltage profile, can be obtained after say 5 iterations.

1.2 General approaches to design PSI algorithms

We present in this section some general approaches that allow to design and optimize PSI algorithms. We start with the Fourier series approach presented in [25]. We give some clues then on the more general approach presented in [49] which makes a neat connection between PSI algorithm design and the use of windows in Fourier analysis. We will end up the section with an even more general approach presented in [174], which is able to address the issue of non-sinusoidal intensity waveforms. Phillion came up in [145] with a family of algorithms that have been designed to be insensitive to various orders of PZT distortions, detector non-linearities and signal and background drifts.

1.2.1 A general formulation with Fourier series

Bruning *et al* proposed in [25] an alternative representation of Eq.(IV.1) with Fourier series:

$$I_k = a_o + a_1 \cos(k\delta\phi) + a_2 \sin(k\delta\phi) \quad (\text{IV.2})$$

We recall that $\delta\phi$ is the phase-shift amount between consecutive recorded intensity pattern and is equal to $2\pi/K$, K being the number of steps to run over a complete 2π cycle. The latter equation is the Fourier series decomposition of I_k with a dc term and the first harmonic. The Fourier coefficients are defined as following:

$$\begin{aligned} a_0 &= I_o \\ a_1 &= I_m \cos(\Phi) = \frac{2}{K} \sum_{k=1}^K I_k \cos(k\delta\phi) \\ a_2 &= I_m \sin(\Phi) = \frac{2}{K} \sum_{k=1}^K I_k \sin(k\delta\phi) \end{aligned} \quad (\text{IV.3})$$

The sought-after phase is thus readily obtained by:

$$\tan \Phi = \frac{a_2}{a_1} = \frac{\sum_{k=1}^K I_k \sin(k\delta\phi)}{\sum_{k=1}^K I_k \cos(k\delta\phi)} \quad (\text{IV.4})$$

Starting from this general formulation, Küchel designed algorithms able to make benefit of random phase shifts, caused for instance by mechanical vibrations, to measure deformations of very large optical mirrors dedicated to telescopes ([98]).

1.2.2 A general formulation with the concept of data-sampling window

So as to design algorithms able to compensate errors due to shifter miscalibrations or non-linearities, and also due to the likely presence of higher harmonics, the following approach has been proposed in [49]. The idea is to consider the recorded frames as a

1. Phase-shifting interferometry (PSI): the choicest method in terms of measurement accuracy

windowed and sampled version of the continuous frequency-modulated 2-beam equation. The 2-beam equation with a temporal carrier can be rewritten in the following way:

$$I(t) = I_o(1 + V \cos(\Phi + \phi(t))) , \quad (\text{IV.5})$$

where $\phi(t)$ is supposed to be continuous and linear, and thus of the form: $\phi(t) = 2\pi\nu_o t$. The FT of Eq.(IV.5) with the previous hypothesis is simply:

$$\hat{I}(t, \nu) = I_o[\hat{w}(\nu) + \frac{V}{2}(\hat{w}(\nu - \nu_o) \exp(i\Phi) + \hat{w}(\nu + \nu_o) \exp(-i\Phi))] , \quad (\text{IV.6})$$

where the hat denotes FT and $w(t)$ is the sampling window. If the window is such that its spectrum vanishes at ν_o and $2\nu_o$, then the phase Φ is readily available by:

$$\Phi(t) = \arctan\left[\frac{\text{Im}(\hat{I}(t, \nu_o))}{\text{Re}(\hat{I}(t, \nu_o))}\right] + \arg(\hat{w}(0)) \quad (\text{IV.7})$$

If we consider a rectangular sampling window, which is usually the case, the previous conditions on the window spectrum are fulfilled but the important variations of the *sinc* function on both sides of ν_o and $2\nu_o$ are responsible in practice for a high sensitivity to phase-shifter errors. It is thus highly preferable to give smoothness to the sampling window in real domain, so as to greatly reduce the spectral leakage in Fourier domain and thus lead to robust algorithms, tolerant to phase-shifter miscalibrations. In [49], the Hahn window is used and a seven-frame algorithm is designed with very interesting results. Of course, we have to deal with discrete signals in practical cases, that are formally written as Dirac combs:

$$w(\Phi, t) = \sum_j w_j \delta\left[t - \frac{\Phi_j}{2\pi\nu_o}\right] \quad (\text{IV.8})$$

The DFT of the sampled intensity is:

$$\hat{I}(t, \nu_o) = \sum_j \hat{I}_j w_j \exp(-i\Phi_j) \quad (\text{IV.9})$$

The previous derived equation for phase computation becomes then:

$$\Phi(t) = \arctan\left[\frac{\sum_j \text{Im}(w_j \exp(-i\Phi_j)) \hat{I}_j}{\sum_j \text{Re}(w_j \exp(-i\Phi_j)) \hat{I}_j}\right] \quad (\text{IV.10})$$

This way of writing has the asset to be a generalization of the previous formulation involving Fourier series ([25]) with the introduction of weights which are the window samples. In addition, this formulation is compliant with existing PSI algorithms as it is possible to know the window coefficients w_j if the algorithm coefficients are known. This general formulation provides actually a wealth of insights in the process of designing PSI algorithms, and permits to understand it with well-known tools of Fourier analysis.

1.2.3 A general formulation for non-sinusoidal waveforms

So far, we have considered the ideal case of sinusoidal waveforms. The case of non-sinusoidal waveforms can occur in practice if the intensity levels are not well adapted to the sensor dynamic, with thresholding and saturating effects. This case is also encountered in fringe projection with non-sinusoidal fringe profile. A general approach has been proposed in [174], and as it introduces the notion of characteristic polynomial in PSI algorithm design, it has the nice feature to cling to Z -transform theory. In this more general case, the algorithm is not only expected to be tolerant to shifter non-linearities but also to the harmonics. The starting point is the decomposition in Fourier series of the intensity, as what is presented in [25], but not limited to the sinewave case.

$$I(\Phi + k\delta) = \sum_{m=-\infty}^{\infty} \alpha_m \exp(im\Phi)(\exp(im\delta))^k \quad (\text{IV.11})$$

Eq.(IV.4) is equivalent to the computation of the argument of a signal which is a linear combination of the recorded intensities with complex weights.

$$\Phi = \arctan\left[\frac{\sum_{k=0}^{K-1} b_k I_k}{\sum_{k=0}^{K-1} a_k I_k}\right] = \arg\left[\sum_{k=0}^{K-1} c_k I_k\right] = \arg[S(\Phi)] , \quad (\text{IV.12})$$

where, $c_k = a_k + ib_k$, and $I_k = I(\Phi + k\delta)$. Injecting the decomposition in Fourier series of I_k into the expression of $S(\Phi)$, we get:

$$S(\Phi) = \sum_{m=-\infty}^{\infty} \alpha_m \exp(im\Phi) \sum_{k=0}^{K-1} c_k (\exp(im\delta))^k = \sum_{m=-\infty}^{\infty} \alpha_m \exp(im\Phi) P(e^{im\delta}) , \quad (\text{IV.13})$$

where P is the so-called characteristic polynomial of the algorithm. It is shown that, depending on quite simple rules applying to the location and the multiplicity of the characteristic polynomial roots, insensitivity of the algorithm to harmonics of arbitrary order, with or without phase-shifter miscalibrations, can be obtained.

1.3 Some basic algorithms

There is an impressive number of PSI algorithms and we simply recall below two of the most well-known standard algorithms, namely, the five-frame algorithm and the Carré method ([152]).

1.3.1 The five-frame algorithm

This algorithm is actually an improvement of an older procedure which needs four frames shifted by $\delta\phi = \pi/2$. Here also, the phase shift is equal to $\pi/2$, and the phase estimator

1. Phase-shifting interferometry (PSI): the choicest method in terms of measurement accuracy

is given by the following combination of the intensity patterns:

$$\hat{\Phi} = \arctan \frac{2(I_3 - I_1)}{I_4 + I_0 - 2I_2} \quad (\text{IV.14})$$

This algorithm belongs to a class of algorithms known as $N + 1$ algorithms, due to the fact that the last image is supposed to be the same as the first one. Here, the last recorded image I_4 is indeed supposed to be identical to the first one I_0 , and it has been shown that this redundancy makes the algorithm more tolerant to phase-shift non-linearities. This appreciated feature is exploited in the dynamic phase-shifting technique, whose spirit is briefly described in a coming paragraph.

1.3.2 The Carré algorithm

An alternative to the $N + 1$ algorithms class, is to consider the phase shift $\delta\phi$ as another unknown. In that case, four frames are sufficient to compute Φ :

$$\begin{aligned} I_1 &= I_o + I_m \cos(\Phi - \frac{3}{2}\delta\phi) \\ I_2 &= I_o + I_m \cos(\Phi - \frac{1}{2}\delta\phi) \\ I_3 &= I_o + I_m \cos(\Phi + \frac{1}{2}\delta\phi) \\ I_4 &= I_o + I_m \cos(\Phi + \frac{3}{2}\delta\phi) \end{aligned} \quad (\text{IV.15})$$

The phase-shift $\delta\phi$ is supposed to be unknown but linear. The phase-shift and the phase estimators are given below:

$$\begin{aligned} \widehat{\delta\phi} &= 2\arctan \sqrt{\frac{3(I_2 - I_3) - (I_1 - I_4)}{(I_2 - I_3) + (I_1 - I_4)}} \\ \hat{\Phi} &= \arctan \frac{\sqrt{[(I_1 - I_4) + (I_2 - I_3)][3(I_2 - I_3) - (I_1 - I_4)]}}{(I_2 + I_3) - (I_1 + I_4)} \end{aligned} \quad (\text{IV.16})$$

The phase is only computed *modulo* π . The sign ambiguity is readily solved, if the sign of $\delta\phi$ is known, by inspecting the quantities $I_2 + I_3$ and $I_2 - I_3$, respectively proportional to $\cos \Phi$ and $\sin \Phi$. One small drawback of the method is that the computed phase does not correspond to any of the recorded frame, but the algorithm allows to perfectly compensate linear phase-shift errors. For instance, if divergent beams are used for the illumination, the phase-shift will change across the field of view. The phase-shift computation following Eq.(IV.16) is pixelwise, and the method is thus perfectly able to compensate this kind of systematic error ([45]).

1.4 Improved phase-shifting methods for dynamic regimes

Usually, the phase-shifting method relies on the assumption that the phase is constant during the acquisition cycle of the N necessary images. One way to proceed is to design setups where the N frames can be acquired simultaneously with N synchronized, calibrated and perfectly aligned cameras ([169]). Some techniques have been proposed to circumvent such setups with prohibitive complexity and cost.

1.4.1 The temporal phase-unwrapping algorithm

This method, presented in [87], straddles the questions of unwrapping and dynamic event characterization. It has actually been proposed as a mean to obtain an unwrapped phase from several acquired interference patterns, without the drawbacks of usual unwrapping algorithms, and notably the propagation of phase errors outward from regions of low SNR. The technique exploits the fact that interferograms have been acquired at different times of a deformation process, and therefore the name of temporal unwrapping, in contrast with spatial unwrapping as generally considered ([72]). This approach is also very interesting also because it is one of the first work to introduce the temporal approach, which has many assets for dynamic regimes. The authors consider a four-frames algorithm:

$$\Phi(t) = \arctan\left[\frac{I_4(t) - I_2(t)}{I_1(t) - I_3(t)}\right] = \arctan\left[\frac{\Delta I_{42}(t)}{\Delta I_{13}(t)}\right], \quad (\text{IV.17})$$

where the I_i , ($i = 1..4$) are the recorded intensity frames. Considering a set of four frames corresponding to the instant $t - 1$, and another set of four frames recorded at instant t , the phase increment between the states $t - 1$ and t can be directly calculated by:

$$\Delta\Phi(t) = \arctan\left[\frac{\Delta I_{42}(t)\Delta I_{13}(t-1) - \Delta I_{13}(t)\Delta I_{42}(t-1)}{\Delta I_{13}(t)\Delta I_{13}(t-1) + \Delta I_{42}(t)\Delta I_{42}(t-1)}\right] \quad (\text{IV.18})$$

The final phase map is readily calculated afterwards by summing the phase increments obtained at the different instants. The temporal unwrapping method relies on a four-frames PSI algorithm, which is not the most tolerant to shifter non-linearities. In addition, the phase is supposed to be constant over the cycle of four frames, which limits the range of application of the method to quasi-static regimes. It would be probably worthwhile to combine a five-frame algorithm with the temporal unwrapping approach to extend the method to the characterization of dynamic events where the phase is no more piecewise constant but piecewise linear.

1.4.2 The object induced dynamic phase-shifting method

The basic idea is to take advantage of the phase change induced by the application of the load on the object under analysis ([40]). Indeed, with an appropriate sampling rate, the application of the load will yield interferograms which are naturally phase-shifted, comparable to interferograms artificially phase-shifted, created to compute the phase of a given static interferogram. For basic sampling considerations, it is required that the phase change at each pixel is less than π between successive frames, and it is also required for the phase evolution induced by the object to be locally linear, which is in general the case in practise. Once an appropriate sampling rate is set and a suitable temporal carrier is chosen, a phase extraction algorithm has to be chosen. A mandatory feature of the

algorithm is that it must include a step where the phase-shift is computed, as we have no clue - beside an upper bound - on the natural phase increment between successive frames acquired during the dynamic event. From this work, it turns out that the 5-frames algorithm is very stable for a phase-shift amount around $\pi/2$, and is thus well-adapted to dynamic events characterization. It is worthwhile to emphasize the fact that several PSI algorithms have been designed to compensate miscalibrations of the shifter and thus for unknown and even unequal phase-shift amounts, but which are the same within the field of view (irregularities being compensated during the calibration step). Here the phase-shift computation is performed pixelwise. The major limit of this method lies in the fact that errors occur as soon as the phase evolution fulfils no more the piecewise linear condition.

1.4.3 The one bucket algorithm

Another approach has been presented in [28]. The idea is to design a PSI algorithm able to retrieve the phase from one single frame acquired in a deformed state, provided that the reference state is perfectly known. Although, the mean intensity I_o and the modulation intensity I_m are supposed to be constant during the deformation of the investigated object, another requirement must be formulated to solve the sign ambiguity of the phase $\Delta\phi$. It is thus assumed that the sought-after phase is considered as being constant within a small neighborhood around each pixel. If an area constituted by two contiguous pixels is enough to solve the sign ambiguity, it is highly recommended to consider larger areas to minimize phase errors due to decorrelations. The phase is computed for each pixel within a sliding area containing N pixels by a least square method applied to the overdetermined linear system of two-beam equations written for each of the N pixels - keeping in mind that the modulation and the mean intensity at any point are known from the reference state. The major drawback of the method is that it is limited in terms of measurement range to the correlation cell, unless the reference state is somehow refreshed periodically.

2 The main streams in single frame based techniques

2.1 Mathematical transform based methods

2.1.1 Fourier transform based methods

Takeda proposed in the beginning of the 1980s a method which became a key technique in full-field measurement field ([177]). The method consists in, first, introducing a spatial carrier (grid projection, additional tilt in one arm of the interferogram), and then in demodulating the so-constituted pattern, which contains the sought-after phase (either it be a

true phase as in interferometric techniques or a synthetic one as in fringe projection techniques). The demodulating step makes benefit of the modulation theorem (see Appendix A). The principle is well-known and illustrated in Fig.IV.2.

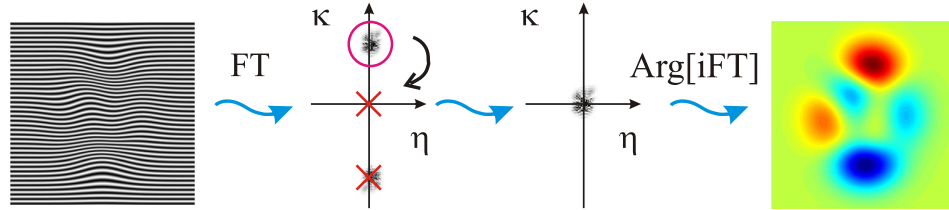


Figure IV.2: Principle of the Fourier-based method.

The method proposed in [177] analyzes originally the frame line after line with a 1D FT. It has been improved in [119] and has been proposed in its final version of Fig.IV.2 by Bone in [22], with the use of a 2D FT and the full-frame, instead of linewise, processing. The introduction of a spatial carrier shifts the object spectrum around the frequency of the carrier ν_o and $-\nu_o$. The idea is then to filter one part of the spectrum, say the one around ν_o , and shift it back to the origin to remove the carrier. The phase is retrieved by extracting the argument of the inverse FT of the so-filtered complex spectrum.

When the carrier frequency does not coincide with a discrete frequency $k/(N\delta x)$ in the Fourier domain, interpolating and resampling are mandatory to shift the filtered part of the spectrum by the *ad hoc* amount. To avoid the resampling part, one can consider rather to remove the carrier in the real domain once the carrier frequency has been computed accurately enough, either by removing a phase plane from the unwrapped argument, or by multiplying by the correct complex exponential. A best-fit plane in the real domain is also a good option. The band-pass filtering step is the most critical step of the method - the exact determination of the carrier frequency is not critical as an eventual remaining error can be compensated most of the time by a final best plane fit step. A trade-off must be found between removing the noise with a narrow filter, and keeping as many details as possible in the object phase. In addition, the final outcome of the method depends strongly not only on the size of the window but also on its "smoothness". The use of windows and FT is discussed in [81].

2.1.2 The Spiral Phase Quadrature Transform (SPQT)

A more detailed description of the Hilbert transform (HT) will be given in the third section dedicated to the analytic signal and its instantaneous quantities. The domain of validity of the analytic method will be defined and its use to process SI signals will be advocated. As another mathematical transform based method, the SPQT ([100, 102]) is a neat exten-

2. The main streams in single frame based techniques

sion of the HT to 2D. The HT reduces in the Fourier domain to a pure phase filter, shifting the phase of positive frequencies by $\pi/2$ and the phase of negative frequencies by $-\pi/2$ (signum function). The HT of a real-valued signal is thus a quadrature version of the signal itself. It is the natural way to build a complex signal and then to be able to compute the phase. To overcome the anisotropy of usual implementations of the HT in 2D, Larkin proposed in [100, 102] a new isotropic signum function defined as spiral phase function in the spatial frequency space (see Fig.IV.3(a)). The spiral phase operator exhibits a π step on any radius, but which is between $-\pi/2$ and $\pi/2$ only for one specific orientation (see Fig.IV.3(b)). An additional step is needed to readjust the radial phase step functions to $-\pi/2$ and $\pi/2$, to be an acceptable quadrature operator. The readjustment actually corresponds to the considered orientation angle in the Fourier domain, which is the local orientation of the fringe pattern (see Fig.IV.3(c)).

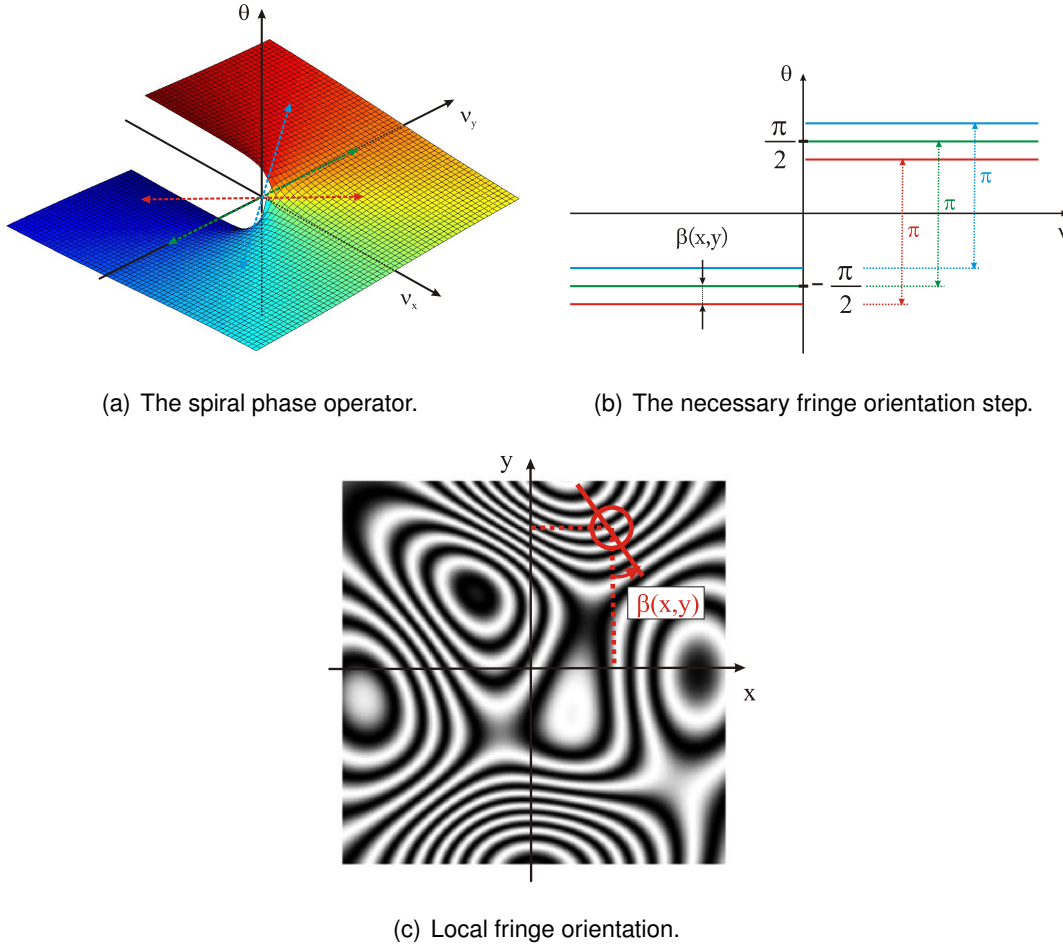


Figure IV.3: The spiral phase operator requires the computation of the fringe orientation.

In addition, the fringe orientation map has to be unwrapped, but of course, unlike the

classical case of phase unwrapping which aims at a final smooth phase distribution, here the orientation phase map cannot be continuous, as illustrated in FigIV.4 with experimental correlation fringe obtained with an out-of-plane sensitive speckle interferometer. The use of regular unwrapping algorithms is thus precluded.

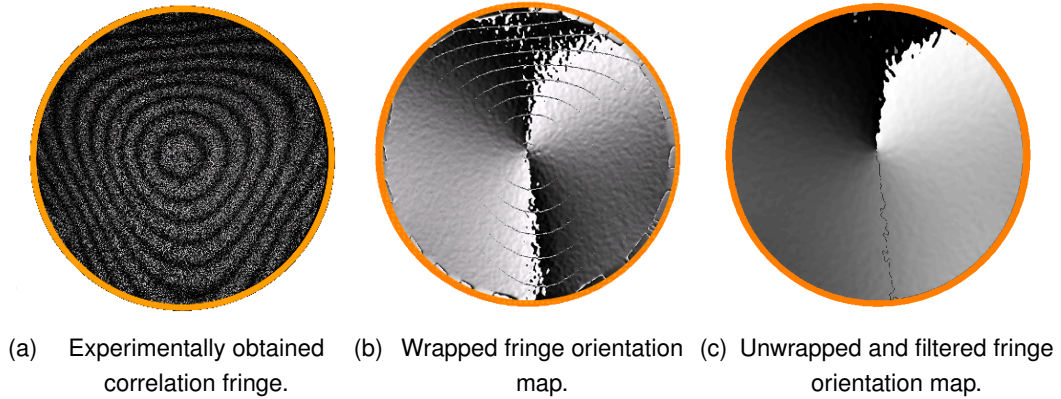


Figure IV.4: A practical case of fringe orientation computation with a gradient-based method.

Despite its neat formulation, the method suffers from the fact that the fringe orientation has to be computed ([101, 149]). The task is not easy especially when we have to deal with noisy fringe pattern, and notably speckle correlation fringe.

2.1.3 Time-frequency and Time-scale distributions

As discussed in the final section of this chapter, the FT is not well suited for processing non-stationary signals. The very fundamental goal of time-frequency analysis is to devise a function, that depends jointly on time and frequency - which are mixed together in classical Fourier analysis - and represents the energy distribution per time and frequency unit. Understanding what a time-varying spectrum is, and representing the varying properties of a signal simultaneously in time and frequency is indeed a huge challenge. There are many ways to design a proper time-frequency distributions (TFD) and the question of the TFD optimality is not solved yet, though it aroused the interest of mathematicians in the last few decades and continues to do so. Cohen reviews the fundamental ideas of time-frequency analysis in [36] for deterministic signals, and we will not give further details here, except mention some examples and give references of TFD applications in our field and more specifically for phase extraction.

The use of the windowed FT (WFT), or equivalently called short-time FT (STFT), has been investigated in [95] with a double view to denoise fringe patterns and to extract the

phase from them. The basic idea behind STFT is to limit the window of observation to a certain duration inside which the signal can be considered as stationary so that using the FT be meaningful. Kemaio *et al* extend this principle in 2D, leading to 4D distribution, to process interferograms with good-looking results.

Wavelets analysis is a widely used mathematical tool in a continuously growing number of fields. Daubechies, in a very interesting paper [47], suggests the image of the tree to represent both the numerous branching which contributed to the establishment of the wavelets analysis theory as we know them since the mid-1990s and the not less numerous communities of researchers and engineers of very different horizons branches (acoustics, optics, data compression *etc*) where wavelets are successfully used [35, 66, 70, 92]. Giving a faithful history, though interesting, is by far beyond the scope of this thesis work and our knowledge. The literature about the matter in hand is profuse, either it be about the synthesis of wavelets basis of compact support from FIR filters, or their connections with multiresolution analysis, subband coding, splines and so on ([121, 181, 184]). We will confine ourselves to recall what is known as the Morlet wavelet transform, because it remarkably fits with our application, as shown by the pioneering work of Colonna De Lega ([39]), and also because we will compare our algorithms with it and discuss the limits and assets of each method.

The mother Morlet wavelet is basically a sine wave whose support is limited by a smooth window, usually a Gaussian window. The daughter wavelets are then classically shifted and scaled versions of the mother wavelet (see Eq.(IV.19))

$$S(a, b) = \frac{1}{a} \int_{-\infty}^{\infty} s(t) m_{a,b}(t) dt, \quad (\text{IV.19})$$

where $s(t)$ is the signal under analysis and $m_{a,b}(t)$ is the daughter wavelet centered around instant b and scaled by the factor a (see Eq.(IV.20))

$$m_{a,b}(t) = m\left(\frac{t-b}{a}\right) = \exp\left(-\frac{(t-b)^2}{2a^2}\right) \exp\left(i\frac{\omega_0}{a}(t-b)\right) \quad (\text{IV.20})$$

It is then possible to compute the inner product of every daughter wavelet at scale a and at time b with the signal, resulting in a two-dimensional distribution or scalogram (see Fig.IV.5).

The sought-after IF is then computed by looking for the maximum of the so-built distribution at each instant. The wanted phase is then directly available by numerical integration, but this way of doing is neither reliable nor efficient. The computation of the wavelet coefficients is indeed performed over a certain range of scales and the whole duration of the signal. Detecting spurious peaks, which do not reflect the underlying phenomenon, is also very likely especially in the presence of noise. In addition it does not exploit the fact that, on the ridge, the wavelet phase is equal to the signal phase. Efficient ridge tracking algorithms follow from this observation ([50]), and proved to be well-suited for temporal

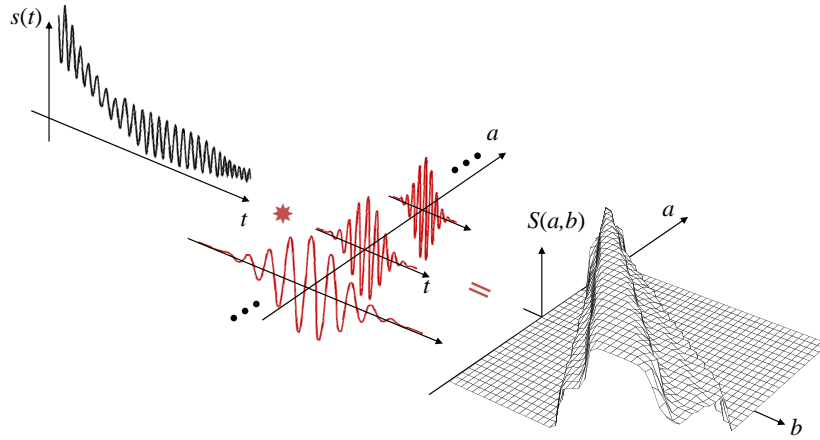


Figure IV.5: Computation of the scalogram of a given signal $s(t)$.

analysis of SI signals ([35, 39]), yielding smooth and reliable results (see Fig.IV.6).

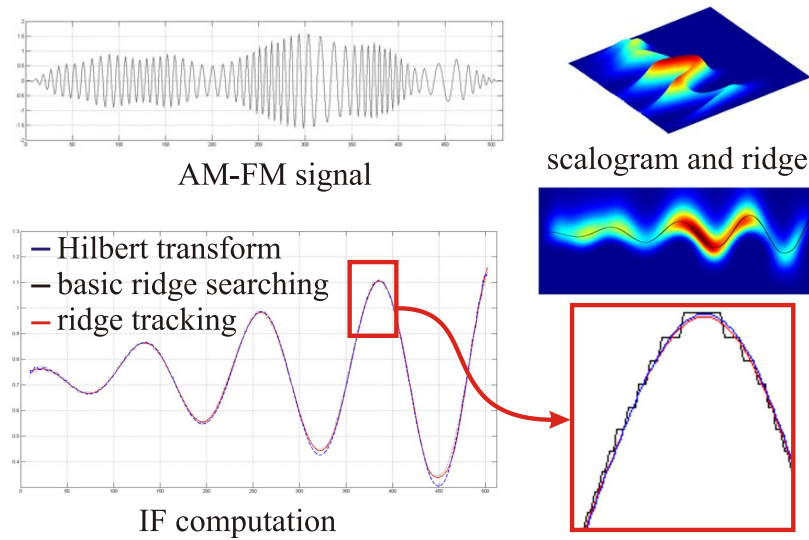


Figure IV.6: Ridge extraction.

2.2 Morphological methods

We now come to another class of fringe demodulation methods. It consists in a collection of techniques which aim at fitting the fringe pattern with smooth functions by minimizing a certain cost function (a process known as regularization).

In [157], the authors search locally for the maximum of similarity between the original fringe pattern and a straight fringe pattern. In other words, they want to locally match the

phase with a plane. The step of finding the minimum of the function of merit is greedy in terms of computation resources. The authors propose then an improved method in [158] where they use a polynomial as the mathematical model, and the maximum of correlation between the fringe pattern and the mathematical model is achieved through a steepest-descent algorithm.

Another fitting procedure is proposed in [26] based on a B-spline formulation. The surface is expressed as a linear combination of fitting functions defined as B-spline with different degrees in the two orthogonal directions, say x and y , centered on the knots of a predetermined grid (this grid is sparser than the sampling grid of the original data). The fitting procedure consists then in building and solving a linear over-determined system. In this way, a rectangular matrix is build with as many columns as the coefficients, and as many rows as the data points ($N \cdot M$ data points obtained with a $N \times M$ sensor).

Servin *et al* developed in [164] a regularization technique to demodulate interferograms with open and close fringe. The authors defined thus a cost function, classically composed by a "closeness" term and a "smoothness" term, that has to be minimized. The "closeness" term is here to keep the fringe model faithful to the data in a least-square sense. The purpose of the "smoothness" term is explicit and its weight in the final result is controlled by a regularization parameter, which can be adjusted by the reliability of the data. The regularization technique yields a phase which is smooth and unwrapped. The regularization framework has been shown to be well-suited to any fringe processing step ([127]), from demodulation to smoothing and fringe orientation computation. Those techniques have a high noise rejection power and a great immunity to border effects. However, the phase tracking is carried out pixelwise, which can be a problem for large amounts of data, and furthermore, it must be fed with normalized and background free fringe patterns. This latter point has been addressed in [105], by including in the original cost function new terms to regularize the background and the modulation with a plane model.

3 Phase map filtering and unwrapping

3.1 Filtering methods for wrapped phase maps

The phase map, extracted in $[-\pi, \pi]$, contains usually a lot of noise in SI, mainly due to decorrelations. Filtering out this noise while preserving the 2π sharp phase jumps, necessitates specific filtering techniques. One simple and very efficient technique is the iterative sine-cosine filter. The basic scheme is shown in Fig.IV.7. The novelty of the method in [3] is that the phase is computed each time a filtering step takes place. The spatial resolution is much less degraded this way. There is a large freedom in choosing the kernel. The authors in [3] showed the benefit of an anisotropic filter.

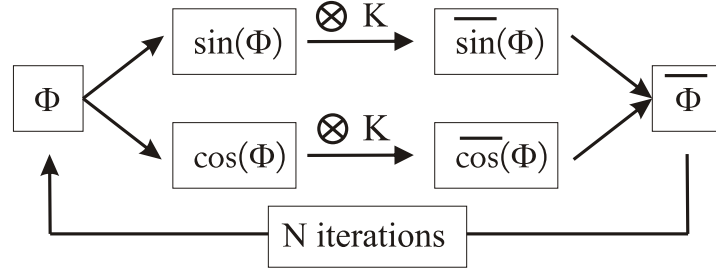


Figure IV.7: Iterative sine-cosine filter.

As the phase error due to decorrelation is to a good approximation inversely proportional to the pixel modulation, a good way to filter the wrapped phase map is to use a weighted kernel, whose weights depend on the pixel modulation. More precisely, the weights are chosen to be functions of the inverse of the square pixel modulation ([108]).

We will propose in Chapter 6 a completely new approach to filter noisy wrapped phase maps through the use of the Delaunay triangulation.

3.2 2D phase unwrapping

Once the phase map is obtained, it is generally wrapped in the range $[-\pi, \pi]$, which is neither pleasant to the eye, nor convenient for subsequent quantitative analysis. The unwrapping process consists in scanning the data set to detect and remove the 2π jumps. The operation is straightforward with noise-free 1-D signals, but it gains in complexity in 2-D and when the wrapped phase is highly corrupted by noise. Phase unwrapping accounts for a field of research in itself, and a comprehensive review of techniques with the corresponding codes is given in [72] (see also Chapter 6 in [159]). Mainly because we could escape this complex task as we focused on to the temporal approach, addressed in the forthcoming section, and also because some tools have been developed in our laboratory in the past ([183]), we did not concern ourselves with this thorny problem.

4 State of the art of the temporal analysis approach

To get rid of the intrinsic correlation length limitation and simplify the unwrapping step, a straightforward approach lies in the pixel history analysis. The idea is thus to reshape the stack of $N \times N$ frames recorded in the acquiring computer into $N \times N$ unidimensional signals (see Fig.IV.8).

The phase is extracted from those temporal signals and phase maps can then be rebuilt.

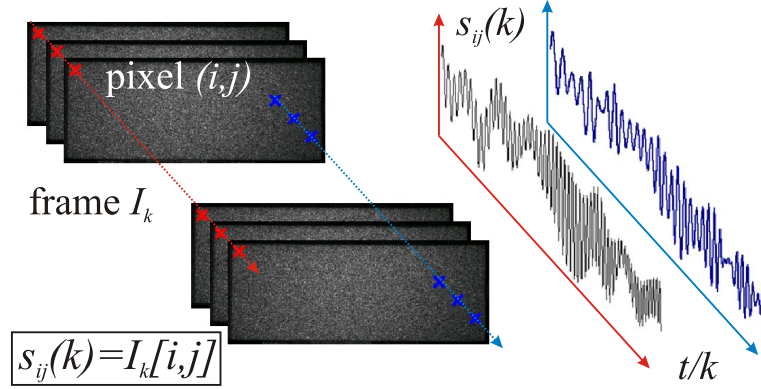


Figure IV.8: The temporal approach.

The phase extraction can be very efficient but the access to each of the so-built $N_x \times N_y$ signals followed by the saving of computed phase signal is quite time demanding. A straightforward and time-preserving solution is to gather the $N_x \times N_y$ temporal interferometric signals into N_x or N_y stacks of respectively N_y or N_x signals each (see Fig.IV.9).

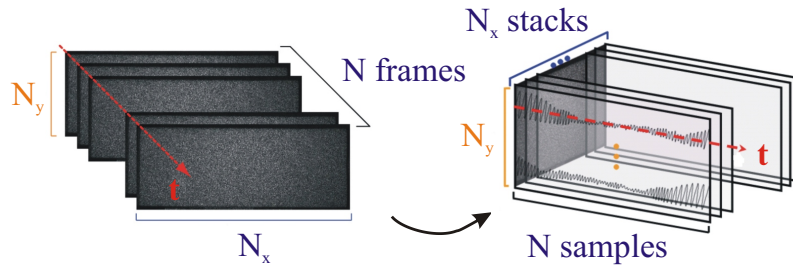


Figure IV.9: Data shaping for computation load reduction.

In the last decade, it became obvious that the ability to accurately characterize the dynamic behavior of a mechanical surface under stress was of great interest. Colonna De Lega ([39]) pioneered the domain with the use of the Morlet wavelet transform with a scalogram ridge tracking algorithm to avoid the heavy computation of the distribution over a fixed pre-determined grid. The obtained results were conclusive and demonstrated the potential of the temporal approach. As any tracking algorithm, the ridge tracking algorithm, originally proposed in [50], smooths the phase evolution, especially in low SNR areas. This case occurs, in SI, when the pixel is under-modulated, resulting in high phase variance. This crucial point will be discussed in details in chapter 6, where another approach to this issue is proposed.

A FT-based demodulation technique has also been proposed by Kaufmann *et al* in [93]. The

HT has been assessed in [120]. As it will be also seen in the last section of this chapter, the signal must be centered for a meaningful use of the HT as the quadrature operator. The authors thus cancelled the local mean of the temporal signal with a sliding window of a certain duration empirically set. The main drawback, and quite considerable, of the method is the lack of adaptiveness due to this mean cancellation step. This issue will be addressed in the next chapter through the use of the Empirical Mode Decomposition.

The authors in [160] proposed a method based on the computation of the WFT of the temporal signal and on searching for the ridge of the TFD, from which the phase is extracted (the ridge tracking can be found by classical iterative methods like Newton-Raphson algorithm). In the absence of object motion, *i.e.* the phase variations being only due to the temporal carrier, we retrieve the FT of the window (a Hanning window is used in [160]) around the carrier frequencies. The object motion, assumed to be piecewise linear, will result in a shift of the peaks at a speed proportional to the object motion speed. The benefit of the method is a high tracking ability of the phase fluctuations even in low SNR conditions.

5 The analytic signal and the analytic method: back to basics

5.1 Stationarity and non-stationarity in practice

A discrete time stochastic process is said to be stationary when its statistical properties do not vary in time ¹. Stationarity means thus that we have realizations of infinite duration in hands, something obviously unrealistic in practice. In the real world, stationarity is rather a relative concept linked to the observation scale ([61, 192]). A speckle field is theoretically a stationary stochastic process, at least in the wide sense. In practice, depending on the observation area, the stationarity is lost (IV.10). The authors in [61, 192] propose to generate surrogate signals from the signal under consideration, which actually share with this latter one the same marginal spectrum but which are known to be stationary. The set of surrogate signals are in practice built by destroying the phase structure of the signal (the signal is usually Fourier transformed and the phase of the FT is then replaced by a random one). The raw signal is then "compared" to the surrogates with a certain norm to finally determine if the signal is stationary or not within the analysis window.

¹The strict-sense stationarity implies that all the moments of the process are independent of time and the correlation function between a realization of the process and its time-shifted version by τ depends only on τ and not on the time. If we release the first condition by only a requirement on the first moment, we introduce the notion of wide-sense stationarity. The strict-sense stationarity implies the wide-sense stationarity.

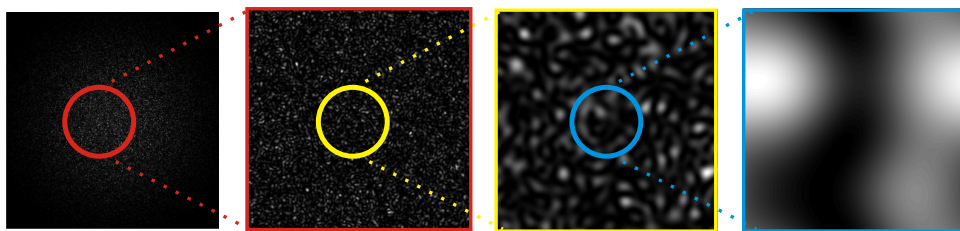


Figure IV.10: Depending on the observation scale, a speckle field, which is supposed to be a stationary process, appears non-stationary.

5.2 Definition of instantaneous quantities of an arbitrary signal

5.2.1 What is wrong with Fourier analysis?

Communication theory was first based on the two disjointed methods of signal analysis: one in time domain and the other in Fourier domain. The first one operates with sharp instants of time, while the second one deals with infinite harmonic waves. The necessity to represent a 1D signal in a 2D time-frequency space becomes obvious ahead of the inability of classical Fourier analysis to properly represent non-stationary signal. For instance, taking the FT of a musical track will provide a series of harmonic which enlarges upon the entire duration of the music, which is obviously not representative of the reality². The mathematical description is nonetheless correct, as the components of the decomposition have a certain phase so as to produce constructive and destructive interference when summing them up and thus recovering the original signal. Though mathematically unquestionable, Fourier analysis yields results that are not easy to reconcile with our physical intuition. It is much more intuitive and interpretable to decompose the signal under analysis in such a way that the spectral components are localized in time. This is the instantaneous spectrum. Hence, considering time and frequency as coordinates of a unique representation necessitates a novel paradigm. To this aim, the expression of the original signal, say $s(t)$, has to be somewhat changed, and here comes the analytic signal $\Psi(t)$ ([68, 186]):

$$\Psi(t) = s(t) + i\sigma(t) , \quad (\text{IV.21})$$

where $\sigma(t)$ represents the signal in quadrature of $s(t)$. Hence, from an oscillating signal, we obtain a rotating vector (see Fig. IV.11).

This is a mathematical operation to which an analogy can be found in Optics: this is indeed the effect of a quarter-wave plate on an optical field linearly polarized and whose polarization orientation is at 45° of the fast and slow axes of the plate.

²By paraphrasing P. Flandrin during a seminar, the time-frequency analysis quest is wonderfully described by the phrase of George Perec in "La vie, mode d'emploi": *Je cherche en même temps l'éternel et l'éphémère*.

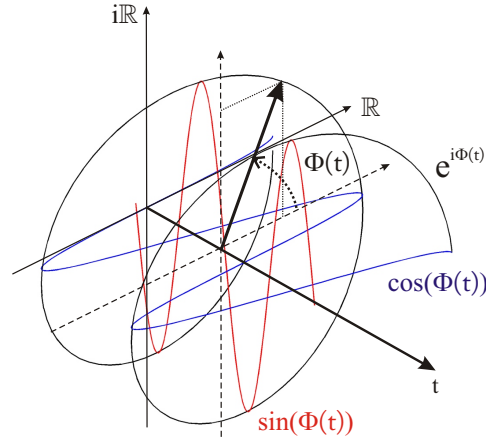


Figure IV.11: The analytic signal built from a sine wave.

The way to obtain the so-called analytic signal will be reviewed in a forthcoming paragraph. Now, having this complex signal in the hands, we are going to define its instantaneous quantities, *i.e.* its instantaneous phase, amplitude and frequency. In this section, we introduced the analytic signal without explicitly mentioning the HT, though the two are unequivocally linked by definition. The idea behind this intended omission is to see how the HT is the most natural quadrature operator (QO in the following) so as to vindicate its use, even if other solutions have been proposed ([118, 182]).

5.2.2 Defining and interpreting instantaneous quantities of a signal

We mentioned that the analytic signal is built from the real-valued signal so that we can write:

$$s(t) = \Re[|\Psi(t)| \exp(i \arg(\Psi))] , \quad (\text{IV.22})$$

where \Re stands for real part and \arg denotes the argument of a complex-valued function. $s(t)$ is thus an oscillating signal modulated by $|\Psi(t)|$. This latter quantity is the envelope of the signal at the instant of time t or the *instantaneous amplitude*, and the *instantaneous frequency* (IF) is defined by the derivative of the *instantaneous phase* $\arg(\Psi)$ ([186]):

$$\nu(t) = \frac{1}{2\pi} \frac{d}{dt}(\arg(\Psi)) = \frac{1}{4i\pi} \frac{\Psi^*}{\Psi} \frac{d}{dt} \frac{\Psi}{\Psi^*} , \quad (\text{IV.23})$$

where \star denotes the complex conjugate. We have seen that the concept of frequency is unambiguous but does not lend itself to a localization in time. The concept of IF is much more questionable, though the concept is intuitive. If the considered signal is monocomponent, the IF would be the frequency of the sine wave which locally fits with the original signal ([19]). The literature is profuse on the connection between the IF and the spectral components (see [19, 20, 118, 122]), and some words will be said when discussing on

the meaningful use of the analytic method to access the instantaneous quantities of the signal under analysis. The general case of multicomponents and wide-band signals will be left apart or only briefly mentioned through the two-tone case.

5.3 Which operator to build the quadrature signal?

5.3.1 General requirements on the quadrature operator

In this section, we discuss the choice of the quadrature operator, relying on [118, 182]. The notations adopted in Eq.(IV.21), Eq.(IV.22) and Eq.(IV.23) will be kept all along the section. The use of the HT as QO is a natural and intuitive choice, but even without recalling the proofs, it is worth to see that the HT is actually the choicest QO for physical and mathematical reasons. The author in [182] lists three reasonable physical conditions the QO (denoted by \mathcal{O} in the following equations) should fulfill:

- i) Amplitude continuity and differentiability: A small variation δs of the original signal $s(t)$ should imply a correspondingly small variation on the quadrature signal $\mathcal{O}[s(t)]$. It means that the QO must be continuous. The existence of the derivative of $\mathcal{O}[s(t)]$ is also required for the IF to exist (Eq.(IV.23)).
- ii) Phase independence of scaling: The phase should remain the same when the signal amplitude is scaled by any real number. It imposes for the operator \mathcal{O} to be homogeneous³, *i.e.* $\mathcal{O}[c.s(t)] = c.\mathcal{O}[s(t)]$ for any c in \mathbb{R} .
- iii) Harmonic correspondence: The instantaneous quantities of a simple sine-wave should be its constant amplitude and frequency.

It can be shown that the HT is the only QO that fulfils those conditions ([182]). So given few simple requirements, the choice of the QO is imposed and the complex-valued signal is thus uniquely defined. This uniqueness has been discussed and disputed notably in [37] and [80]. The authors in [118] have suggested other requirements for the QO to fulfill, which lead them to consider rather time-frequency distributions (TFD, see [36]) than the analytic method. They notably impose the QO to be bounded-input / bounded-output, which is an additional and more restrictive constraint on the amplitude than the simple amplitude continuity condition of Vakman ([182]). They suggest also that if the signal frequency content is limited to a certain range, then the extracted IF should likewise be limited to the same range. The HT is well-known to violate those two conditions. They moreover suggested to extend the three conditions cited before by a fourth condition on the continuity of the phase, which has been found irrelevant by Hahn in [80]. The HT

³a function f , between two vector spaces, is said to be homogeneous of degree α if: $f(\lambda x) = \lambda^\alpha f(x)$.
A linear function is thus homogeneous of degree 1.

is clearly a very natural choice for the QO despite some limits, and after recalling some definitions and properties of the HT, we will see which conditions the signal has to fulfil for a meaningful use of the HT, and thus a subsequent accurate phase extraction.

5.3.2 Reminder on the Hilbert transform

We remind here several definitions and basic properties of the HT. The HT of a function $s(t)$ is defined by the following convolution product ([24]):

$$\mathcal{H}[s(t)] = \frac{1}{\pi} \int_{-\infty}^{\infty} \frac{s(x)}{t-x} dx = \frac{-1}{\pi t} \otimes s(t) \quad (\text{IV.24})$$

It is well-known, that it is much more efficient to compute convolution products in the Fourier space, thanks to the Fast Fourier Transform (FFT) algorithm (see Annexes). We thus define the HT in the reciprocal space:

$$\mathcal{F}\{\mathcal{H}[s(t)]\} = \begin{cases} iS(\nu) & \text{for } \nu > 0 \\ -iS(\nu) & \text{for } \nu < 0, \end{cases} \quad (\text{IV.25})$$

where ν is the Fourier domain coordinate and $S(\nu)$ is the FT of $s(t)$. The HT reduces to a phase filter in the Fourier domain, adding $\pi/2$ to the phase of positive frequencies components and $-\pi/2$ to the phase of the negative ones, while leaving the amplitudes unimpaired (see Fig.IV.12(a) and Fig.IV.12(b) for a basic example, the cosine function). We recall below two useful basic results on HT:

$$\begin{aligned} \mathcal{H}[\cos t] &= -\sin t \\ \mathcal{H}[\alpha] &= 0, \quad \forall \alpha \in [-\infty, \infty] \end{aligned} \quad (\text{IV.26})$$

Once the quadrature signal is built and thus the analytic signal also, the phase $\Phi(t)$ is then extracted in the range $[-\pi, \pi]$ with the arctan function:

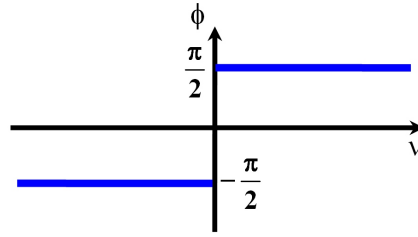
$$\Phi(t) = \arctan\left(\frac{-\mathcal{H}[s(t)]}{s(t)}\right) \quad (\text{IV.27})$$

The unwrapping operation is straightforward in one-dimension, provided that the noise level is low enough to detect only actual 2π phase jumps.

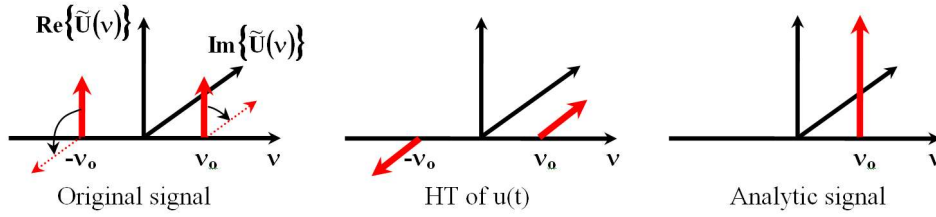
5.3.3 Conditions for a meaningful use of the HT as the quadrature operator

There are actually some restrictive conditions in a meaningful use of the HT to obtain the proper quadrature signal, or in other words, to extract a phase representative of the physical phenomena:

- i) amplitude and phase modulations spectra have to be well separated,



(a) The HT in the Fourier domain reduces to a phase filter.



(b) HT of a cosine

Figure IV.12: The HT: the natural quadrature operator

- ii) the mean has to be locally zero and
- iii) the signal has to be narrow-band.

After those general considerations, we will consider from now on the following signal:

$$s(t) = \beta(t) \cdot \cos(\Phi(t)) + \alpha(t) \quad (\text{IV.28})$$

5.3.3.1 Amplitude and phase spectra well separated The spectra of the amplitude $\beta(t)$ and of the phase $\Phi(t)$ (Eq.(IV.28)) have to be well separated (amplitude modulation restricted to low frequencies range, and phase modulation to high frequencies range), otherwise, the computed phase would depend on both, losing physical sense. Bedrosian proposed in [15] a product theorem for the Hilbert transform for band-limited functions. Writing this theorem with the signal $s(t)$ of Eq.(IV.28) and with Eq.(IV.26) leads to :

$$\mathcal{H}[s(t)] = \beta(t) \cdot \mathcal{H}[\cos \Phi(t)] = -\beta(t) \cdot \sin \Phi(t) \quad (\text{IV.29})$$

The last part of Eq.(IV.29) is not strictly speaking the Bedrosian theorem, and is not valid for any $\Phi(t)$ (see discussion below about the Nuttall theorem ([137])). It is nonetheless true in the quasi-monochromatic case (narrow-band condition expressed hereafter). The phase is then easily extracted with Eq.(IV.27).

5.3.3.2 Null local mean The analytical method fails in the case of real-valued signals with non zero mean. Indeed the HT of such a signal is given by:

$$\mathcal{H}[\beta \cos \Phi(t) + \alpha] = -\beta \sin \Phi(t) \quad (\text{IV.30})$$

The extracted phase is then (see Fig.IV.13 representing $\Psi(t)$ in the complex plane):

$$\Phi_{AS}(t) = \arctan\left(\frac{\beta \sin \Phi(t)}{\beta \cos \Phi(t) + \alpha}\right) \neq \Phi(t) \quad (\text{IV.31})$$

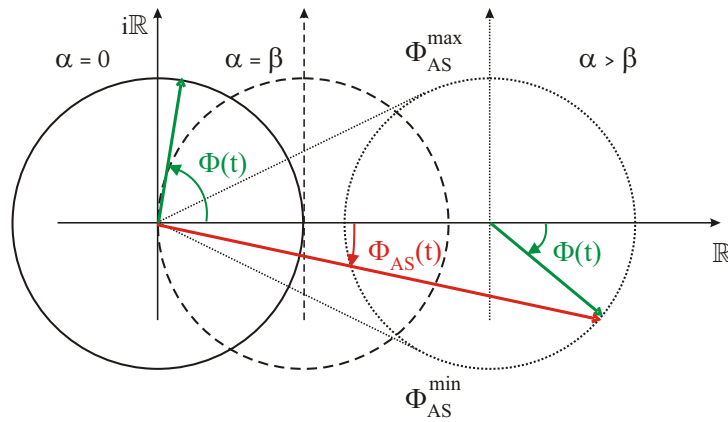


Figure IV.13: Representation of the analytic signal in the complex plane.

For the dashed curve, the phase moves fast near the origin, with a π jump in the limit case where the modulation depth equals the mean, leading to a singularity. As soon as the modulation depth is lower than the mean (dotted line), the phase computed with the HT, $\Phi_{AS}(t)$, is distributed in a narrow range, namely $[\Phi_{AS}^{min}(t), \Phi_{AS}^{max}(t)]$, and is indeed very different from the meaningful quantity of interest $\Phi(t)$. The phase error, when the local mean is not zero but nonetheless smaller than the local modulation depth, can be easily estimated. Let us first rewrite Eq.(IV.31) to simplify the notations:

$$\Phi_{AS}(t) = \arctan\left(\frac{\sin \Phi(t)}{\cos \Phi(t) + \gamma}\right), \quad (\text{IV.32})$$

where γ , positive and smaller than 1, represents the ratio mean over modulation. The error between the actual phase $\Phi(t)$, and the unwrapped extracted one $\Phi_{AS}(t)$, is null at $k\pi$ (k integer), and is thus bounded elsewhere. A Taylor expansion of Eq.(IV.32) limited to the first order readily shows that the error upper bound is equal to γ itself. Thus, if the residual mean remains smaller than the modulation depth in the whole data set, the phase error is bounded and does not propagate.

5.3.3.3 Narrow-band signal condition The HT is perfectly defined for wide-band signals. As soon as its FT exists, there is no difficulty to compute its HT with Eq.(IV.24). The problem lies actually in the physical sense to give to the evaluated phase. To illustrate this difficulty, let us consider the two-tone signal $s(t)$ with fixed amplitude and constant frequencies:

$$s(t) = A_1 \cos \nu_1 t + A_2 \cos \nu_2 t, \text{ where } \nu_2 = \nu_1 + \Delta\nu \quad (\text{IV.33})$$

The two-tone case has already been extensively studied, even in the non-stationary situation ([19, 118, 122]). If A_1 is equal to A_2 , the IF $\nu_{AS}(t)$ as computed with Eq.(IV.23) is found to be the average of ν_1 and ν_2 . For unequal strength of the two tones, the IF can even extend beyond the range $[\nu_1, \nu_2]$. What is true for signals containing two frequencies separated by $\Delta\nu$ is especially true for signals with a continuous distribution of the same width. This example is used by some authors to illustrate the weaknesses of the analytic method, whereas it simply illustrates the fact that it is not possible to correctly characterize with one single quantity, the IF $\nu_{AS}(t)$, a signal with a broad frequency content at one time.

The Nuttall theorem ([137]) stipulates that the HT of $\cos \phi(t)$ is not necessarily $\sin \phi(t)$, for any arbitrary $\phi(t)$. This theorem and the Bedrosian one demonstrate that in certain cases, the HT is only approximately a quadrature operator. It is however important to say, that if the conditions expressed previously are satisfied, the HT allows an accurate computation of the quadrature signal.

5.4 How to compute the HT?

We considered so far continuous-domain functions with an ideal definition of the Hilbert transform to obtain the quadrature signal. In practise again, only discrete-time signals are available, and one has thus to design Hilbert transformers which must be the best approximation of the ideal one. The definitions in Eq.(IV.24) and Eq.(IV.25) straightforwardly suggest to compute the HT in the Fourier domain ([126]). The idea is thus simply to compute the FT of the original signal and zero the half part of the complex spectrum. The discrete quadrature signal is then obtained by an inverse FT of the so-filtered complex spectrum. This approach seems to be ideal at first glance but it has the usual drawback of the DFT use, to wit, new frequencies creation due to border effects. This is the well-known leakage error ([178]). Applying a smooth window to the data set greatly alleviates the induced errors, which manifest themselves in spurious oscillations in the extracted IF. An alternative to the FT-based approach is to conceive an all-pass phase filter which approaches the ideal HT filter (see Eq.(IV.25)). There has been a considerable matter of interest in the 1970s to efficiently design digital Hilbert transformers with finite impulse response (FIR phase filter) ([151]). The idea is actually to approximate the function $1/(\pi t)$ with a finite number of coefficients, while the frequency response both in amplitude and

phase are as close as possible to the ideal case ⁴. The main drawback of this approach is that only the imaginary part of the signal has been filtered, and consequently, outside the approximation band, the quadrature operation is not well performed (loss of orthogonality between the real and the imaginary part of the signal).

A third approach is proposed in [153] and compared to the direct DFT method (without signal windowing) and the FIR filter method. The authors actually propose to design first a low-pass filter and shift it to the positive frequencies by an appropriate carrier. The authors demonstrate that the methods based on FIR filter use show better results than the direct DFT technique, even if it would have been valuable to compare it when appropriate windowing is applied prior to the FFT computation([81]).

In the following, we will use the DFT-based methods to compute the HT. As said before, the sampling window greatly reduces the spurious oscillations around the correct IF without any bias. The lack of bias implies that no error greater than 2π will be made. However, the DFT-based method, even if a sampling window is used, is not suitable if the sought quantity is the IF, rather than the phase. A tracking technique with better noise rejection should be preferred. For long experiments, overlapping data sets have been considered so as to alleviate those leakage errors.

5.5 Behavior of the analytic method with different types of signals

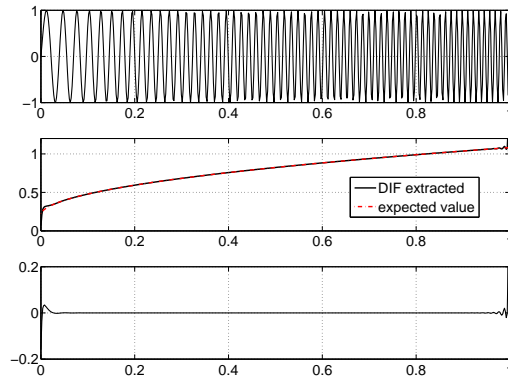
We now come to basic examples to see how the analytic method behaves in cases we might encounter in SI, like signals with varying frequency, with phase and/or frequency step, and signals polluted with different amounts of noise. In each case, a Hanning window is used to minimize the border effects due to HT implementation in the Fourier domain.

5.5.1 Frequency modulated signal

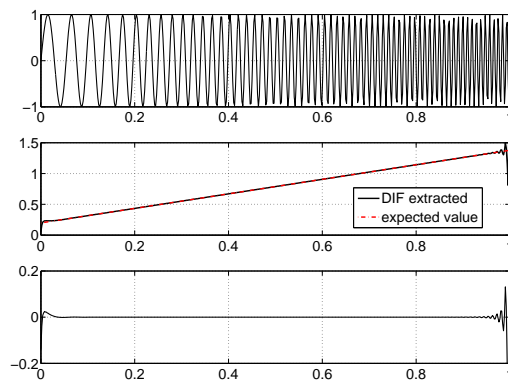
We consider here a signal whose frequency increases in time, ranging from $2\pi/32$ up to $2\pi/8$, with three different laws of variation. We report the results of the HT-based phase extraction for the three different cases in Fig.IV.14. So as to reduce the boundaries errors, due to the use of the DFT, we windowed the signal with a Hanning window.

⁴given a filter length, a trade-off must be found between the cut-off frequencies (low and high) and the ripple error in the approximation band (frequency band between the two cut-off frequencies) ([151])

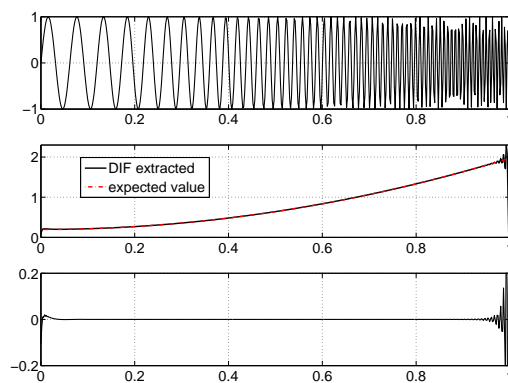
5. The analytic signal and the analytic method: back to basics



(a) Square root law (from top to bottom: signal, extracted and theoretical DIF and discrepancy between the two).



(b) Linear law (from top to bottom: signal, extracted and theoretical DIF and discrepancy between the two).



(c) Power of two law (from top to bottom: signal, extracted and theoretical DIF and discrepancy between the two).

Figure IV.14: HT-based phase extraction method from a chirped signal with different frequency laws.

5.5.2 Signal with phase or frequency step

To evaluate the behavior of the HT when a phase step occurs in the signal history, we simulate a single tone with an added phase step at the center of the signal support. We have considered a phase step of $\pi/8$, $\pi/4$, $\pi/2$ and π . The difference between the extracted phase and the original phase is reported in Fig.IV.15.

In the same way as before, a single tone with a frequency step at the center of the signal

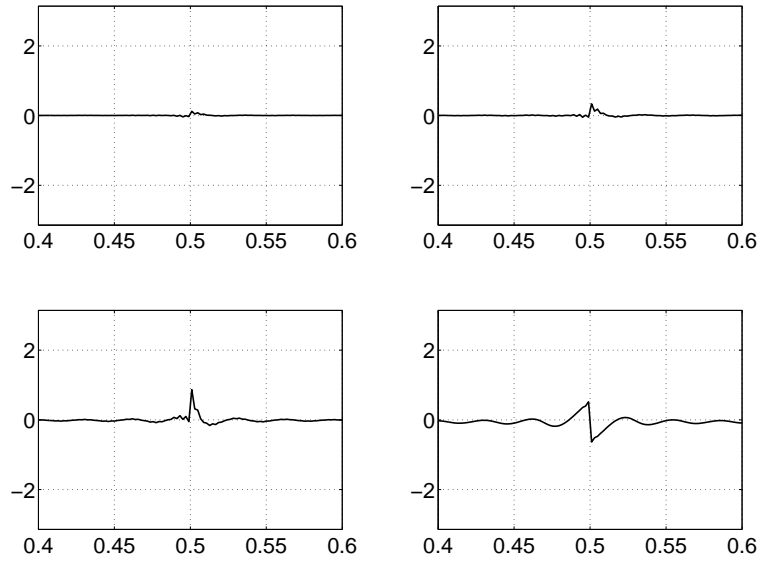


Figure IV.15: Discrepancy between the original phase and the extracted one for phase step of $\pi/8$, $\pi/4$, $\pi/2$ and π .

support is simulated. We have considered a frequency step from $2\pi/32$ to respectively $2\pi/16$, $2\pi/8$ and $2\pi/4$. The extracted IF and the original one are jointly shown in Fig.IV.16.

5.5.3 Noise sensitivity

The analytic method is not well-suited for IF computation as it is very sensitive to noise (derivative filters are high-pass filters, enhancing thus the noise). We consider a sine wave with additive gaussian noise of standard deviation σ_n . We compute the standard deviation of the phase error for different values of σ_n , and the so-obtained curve average on 100 realizations is shown in Fig.IV.17.

An error on the phase greater than 2π is made as soon as the SNR becomes lower than approximately 3 dB.

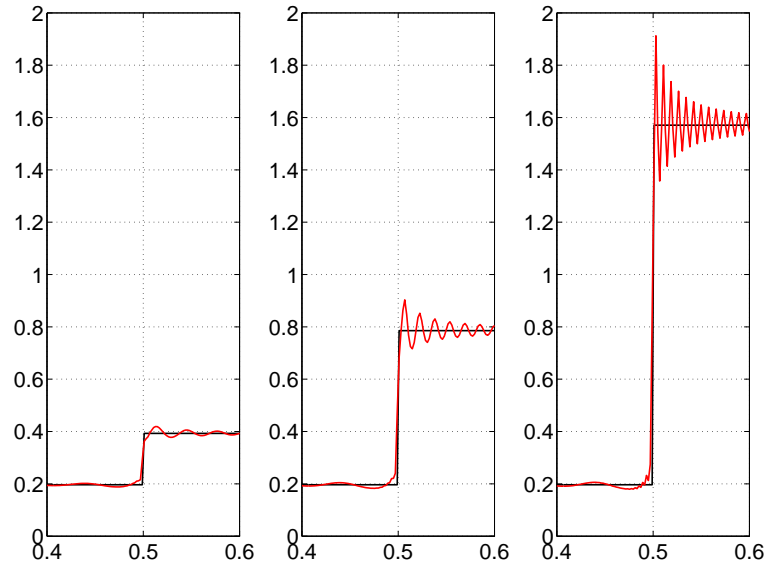


Figure IV.16: Gibbs phenomenon around a frequency step in a signal (from $2\pi/32$ to respectively $2\pi/16$, $2\pi/8$ and $2\pi/4$).

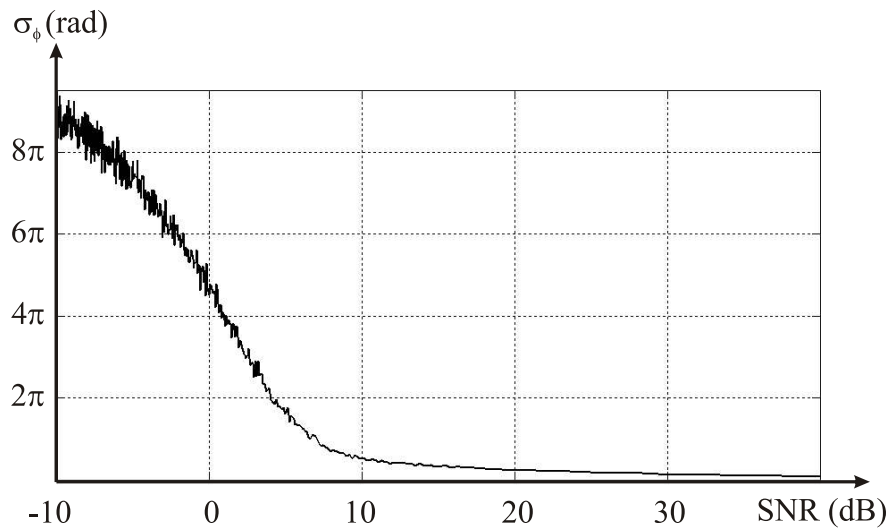


Figure IV.17: Standard deviation of the phase error as function of the SNR.

5.6 A preprocessing tool is missing for detrending SI signals

In fact, the quantity of interest carried by SI signals is unique at one time as soon as the setup is mechanically, optically and electronically isolated from external disturbances. Hence the narrow-band signal condition is fulfilled for the signals we are interested in. We have spent some space to review the requirements that the signal must fulfil to allow a meaningful phase extraction. We focused on the analytical method but the requirements are actually general and apply to any phase extraction or tracking method. We will show now how the EMD method is a perfect candidate to put the signal in the ad-hoc shape for subsequent phase evaluation.

In SI, the spectra separation condition is actually intrinsically fulfilled. In a suitable experiment, the modulation variations are much slower than the oscillation periods of the phase term. Modulation depth variations are ruled by the statistical spatial properties of the speckle fields and decorrelation effects, while the phase variations depend on the sensitivity of the interferometer. Though they form the subject of rather involved mathematical descriptions, the fluctuations of the modulation have been thoroughly studied ([108]), leading to a set of quite simple operational rules the principal parameters of the optical system - the aperture of the recording system, the pixel size, the sensitivity of the interferometer, the frame frequency, and the rate of phase change - should obey. It is just reminded here that an inappropriate choice of this set of parameters would lead to a complete failure of the experiment, irrespective of the processing method. On the contrary, with adequately selected system parameters, pixel signals take *ipso facto* the form of rapid oscillations (of the cosine term) with random, slowly varying modulation and mean values, as exemplified in Fig.V.22.

Chapter V

The Empirical Mode Decomposition dedicated to SI

1 Basic principles of the decomposition

The Empirical Mode Decomposition (EMD) has been developed a decade ago to address ([85]), jointly with the Hilbert spectral analysis, the thorny problem of the characterization of signals which are fulfilling neither the stationarity nor the linearity conditions. Actually, we are not devoid of means to analyze signals stemming from non-stationary but linear processes, and wavelet analysis ([121]) is certainly one of the most famous one, due to a neat mathematical formalism, some efficient implementations through filter banks ([184]), and numerous and successful applications ([39]). The Wigner-Ville distribution ([36]) is another classical way to process such non-stationary signals, notably for the IF tracking issue ([21, 62]). It has nonetheless the drawback of cross-term interferences which pollute the useful time-frequency pattern. Some improvement have been brought to reduce those interference artifacts while keeping the desirable properties of the distribution.

For non-stationary and non-linear signals, the mathematical paradigm of signal analysis, which is to decompose the signal over an *a priori* established basis, has to be circumvented. The EMD method is a completely new approach in the sense that it is a data-driven method. It actually decomposes any non-stationary signal $s(t)$ into its intrinsic oscillation modes, acting basically like a filtering process from higher to lower frequencies, but with self-adaptive band-filters.

This chapter is organized as follows: first the EMD method will be presented and some examples will illustrate its way of working with more and more intricate signals. A quick overview of the range of application will demonstrate its potentials and its versatility. After this overview of the decomposition, a deeper analysis is necessary. We will focus thus

on the sifting process influence, the sampling effect and the boundaries ending. Their impact on the decomposition will be discussed, notably in terms of orthogonality, uniqueness and completeness. Those three properties are generally highly valuable features that a decomposition should have. We will present here known results and new ones as well, especially to check and quantify the orthogonality of the decomposition and recover it if it has been lost during the process. This comprehensive study of each step of the EMD will show the strengths and the limitations of the method. A fast implementation of the EMD will finally be proposed and assessed to process SI signals.

1.1 Algorithm

1.1.1 The concept of the intrinsic mode function

As said before, the EMD technique, fed with any non-stationary signal, yields a sparse set of functions, which are the intrinsic oscillation modes of the signal. The modes that could be non-stationary too, are acceptable modes, namely the intrinsic mode functions (IMF), if they satisfy the two following conditions:

- i) in the whole data set, the number of *extrema* and the number of zero-crossings differ from each other at most by one, and
- ii) the mean envelope is zero at any point.

The first condition is equivalent to the narrow-band condition (see previous chapter on the HT). The second one is a good approximation of the zero local mean condition, and less constraining as it does not need a definition of a local time scale. Indeed, to compute a local mean we need to define a range containing a sufficient integer number of local periods. For non-stationary signals, the width of this range (local time scale) has to be adjusted all along the time axis. It is directly done by the EMD algorithm through the *extrema* finding and the subsequent envelopes computation. The last condition, namely the spectra separation condition for amplitude and phase, must be fulfilled by the nature of the experiment itself. Thus, by construction, the IMFs have a well-behaved Hilbert transform, and more generally they allow good phase extraction. Let us now see how the EMD yields this collection of IMFs, which have the ideal shape for subsequent phase extraction.

1.1.2 The way the decomposition works

The starting idea is to consider the signal constituted by a detail part (local high frequency) $d(t)$, and a residue part (local low frequency) $m(t)$. The detail part is sifted out

from the raw signal by removing the mean envelope, whose computation is based on a cubic spline ([179])¹ fitting between the signal *extrema*. The interpolation with a cubic spline kernel is acknowledged to have the best performances in most cases. The residue is then considered itself as a signal to process and thus split into a detail and a residue part as well. We obtain *in fine* the following decomposition:

$$s(t) = \sum_{k=1}^K d_k(t) + m_K(t), \quad (\text{V.1})$$

where the $d_k(t)$ are the extracted IMFs and $m_K(t)$ is the final residue. The decomposition can be stopped at any rank K depending on the purpose, or in other words, depending on the frequency band the sought-after information belongs to (detrending, denoising, texture extraction and so on). If a total decomposition is wished, the procedure is ended when the current residue contains less than three *extrema*.

Let us see now how the algorithm works by relying on some simple examples involving harmonic signals, chirps and also piecewise polynomial signals. The power of the method will be particularly obvious for the two latter classes of signals. The algorithm, in its basic form ([60]), consists in the following steps:

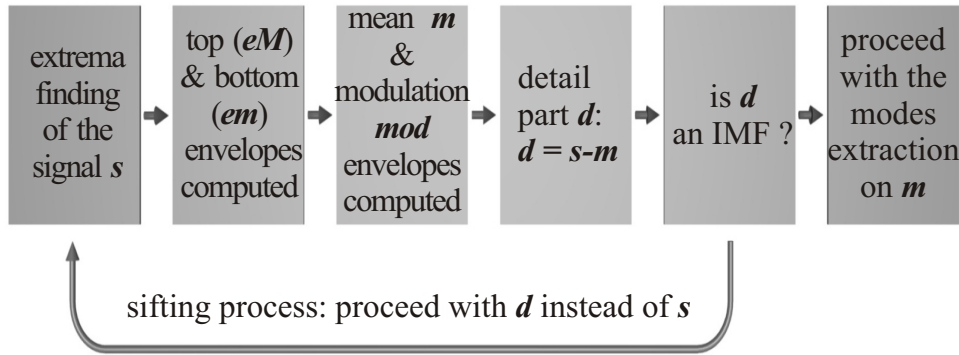


Figure V.1: The standard EMD algorithm.

- i) Sum of harmonic signals: For the trivial case of a signal composed by a linear combination of harmonic signals, we obtain a decomposition, which is identical to what Fourier analysis gives, except near the data set boundaries. All the issues (sampling, *extrema* finding, interpolation and so on) raised by the implementation of EMD and the processing of discrete-time signals will be addressed in the next section.

¹The cubic spline kernel is acknowledged to perform well for the envelopes computation, but the real impact of choosing higher order splines is still unknown (see the paragraph on the *extrema* finding for further discussion on the use of higher order splines).

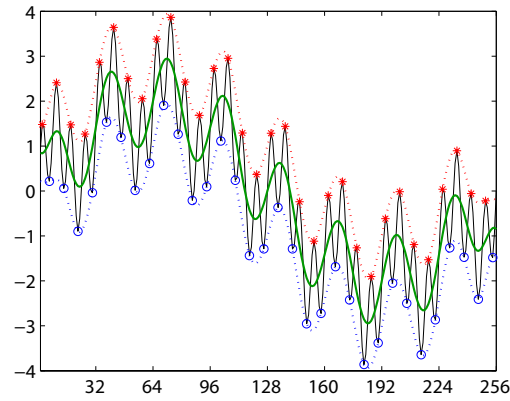
The signal considered below is the sum of 3 sines:

$$s(t) = \sin\left(\frac{2\pi}{8}t\right) + \sin\left(\frac{2\pi}{32}t\right) + \sin\left(\frac{2\pi}{256}t\right) \quad (\text{V.2})$$

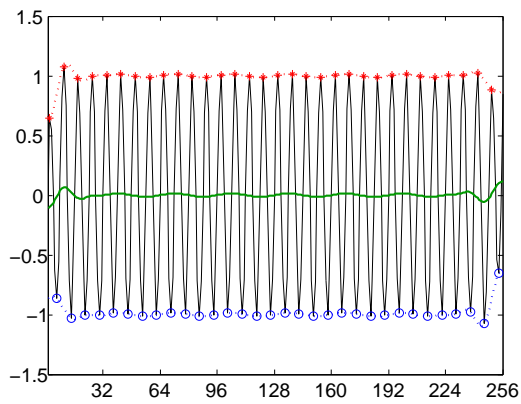
After having found the *extrema*, the upper and lower envelopes are computed with a cubic spline kernel. The mean envelope is then simply evaluated as the average of the two previous interpolated curves (see Fig. V.2(a)). The mean envelope is then subtracted from the original signal $s(t)$ to obtain the detail part $d(t)$. If the obtained mode is not an acceptable IMF, *i.e.* the condition on the number of zero-crossings and *extrema* and the condition on the local mean envelope are not fulfilled, the sifting process must be pursued (see Fig. V.2(b)) until a certain or several criterions are fulfilled. There are different ways to end the sifting process: it might be, a maximum number of iterations, or a certain similarity measurement between consecutive extracted modes. The sifting process influence will be seen later in details, and for now, we will just keep in mind that the sifting process goal is to remove riding waves and make the mode as symmetrical as possible, but it may also make boundaries errors spreading inward the data set and thus lead to over-decomposition and mode-mixing. A trade-off must be found ([83, 156]).

Once the mode is compliant with our expectations (see Fig. V.2(c)), it is subtracted from the original signal and the same procedure is applied to the first residue, which yields the second IMF (see Fig. V.3(a) and Fig. V.3(b)).

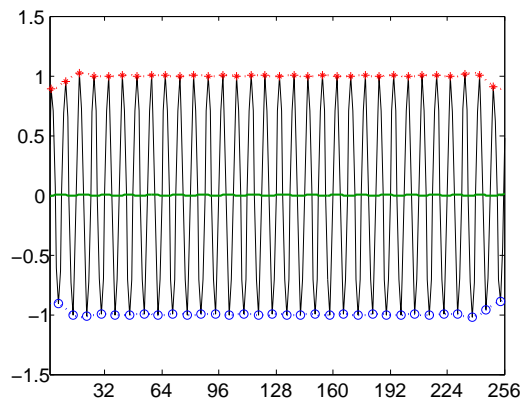
The final decomposition is shown in Fig. V.4, jointly with each mathematical harmonic signal. Except for issues near the boundaries, we recover quite well the three original sines. In those examples, the boundaries ending strategy is to keep the 1st and the last *extremum* value for the 1st and the last point of the data set used for the envelopes computation. The modes are not expected or forced to have an harmonic nature, and what we get for each IMF is actually the approximation of a sine by a cubic spline. Due to the basic boundaries management strategy, we have slightly distorted sine signals in the final decomposition.



(a) *Extrema* finding and envelopes computation

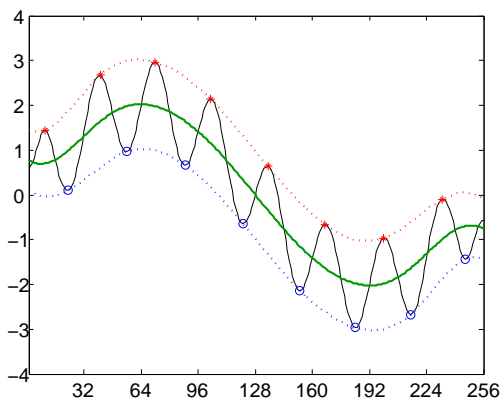


(b) First extracted mode after the first iteration of sifting process

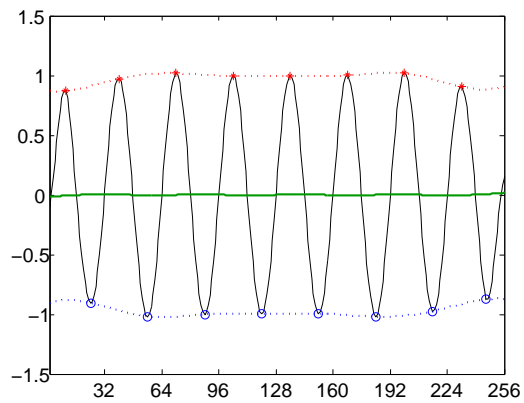


(c) First IMF

Figure V.2: The EMD algorithm: first IMF extraction.



(a) Mode extraction pursued on the first residue



(b) Second IMF

Figure V.3: The EMD algorithm: second IMF extraction.

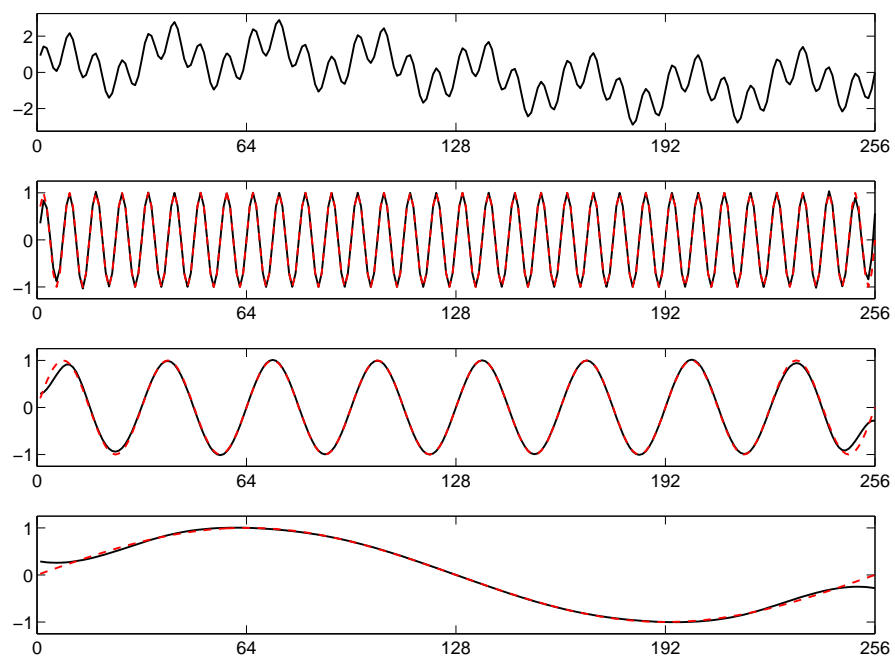


Figure V.4: Final decomposition of the sum of three sines (from top to bottom: original signal, first IMF with first component, second IMF with second component, and finally, residue with third component).

- ii) Sum of parabolic chirps: It is when dealing with non-stationary signals that the EMD is really valuable. The following example illustrates the sparseness of the decomposition when the considered signal is the sum of two parabolic chirps of equal strength, whose instantaneous frequencies increase linearly and are well-separated at each instant but span overlapping ranges:

$$s(t) = \sin(\omega_1 \cdot t) + \sin(\omega_2 \cdot t) , \quad (\text{V.3})$$

where ω_1 and ω_2 span respectively the ranges $[\frac{2\pi}{64}; \frac{2\pi}{16}]$ and $[\frac{2\pi}{32}; \frac{2\pi}{8}]$.

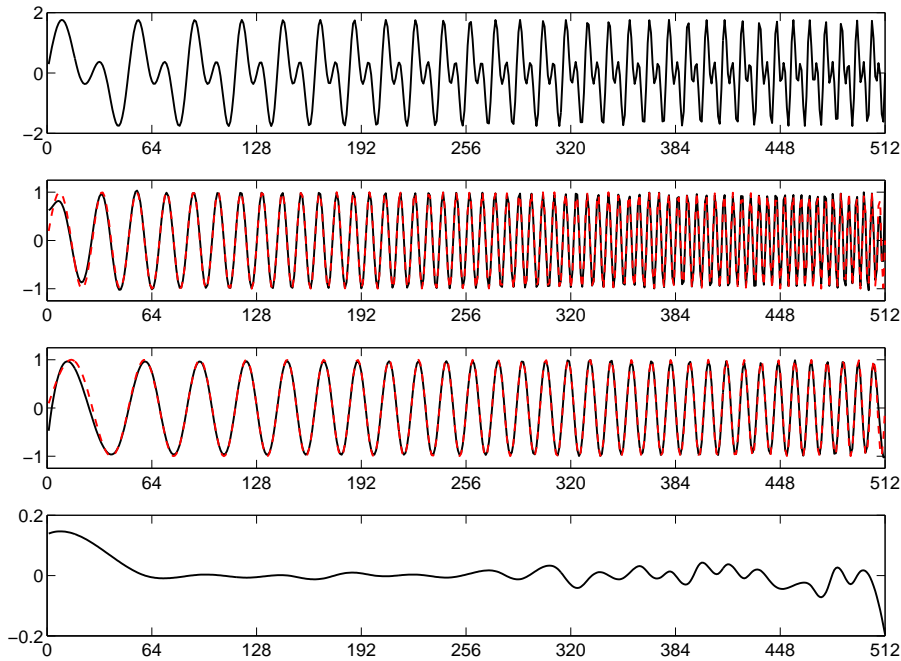


Figure V.5: The EMD of the sum of two parabolic chirps (from top to bottom: original signal, first IMF with first chirp component, second IMF with second chirp component, and final residue).

This example will be used later to illustrate the concept of local orthogonality. The separation of the two components is perfect, apart again some issues near the data set boundaries (see Fig. V.5). The final residue is shown in the bottom graphic of (see Fig. V.5). The sparseness of the decomposition appears in an obvious manner.

- iii) Piecewise polynomial signals: We consider here the sum of a sine and a triangle, *i.e.* a continuous piecewise linear signal. Except at points of non derivability, the reconstruction is pretty good (see Fig. V.6). In this particular example, a linear interpolation would probably better fit, at least for the piecewise linear IMF.

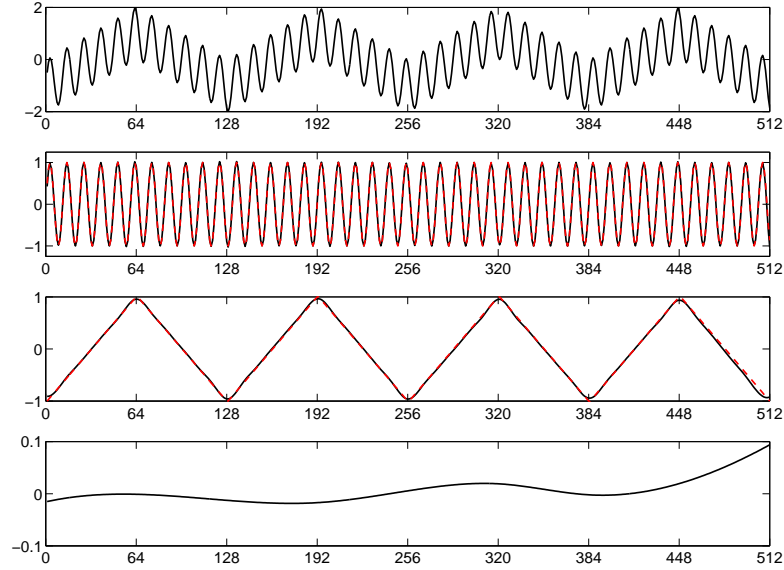


Figure V.6: The EMD of the sum of a sine and a piecewise linear signal (from top to bottom: original signal, first IMF with sinewave component, second IMF with piecewise linear component, and final residue).

- iv) Sine wave with a mean value step: We consider here a pure sine wave with a mean value which experiences a step in the middle of the signal support. This is a situation which might occur in SI, due to a brutal mode jump of the laser source. What we will get is simply the response of the cubic spline kernel to a step function. An example is shown in Fig.V.7.

The ratio overshoot over step value is constant, and the overall induced phase error is null, unless the oscillations created by the interpolating polynomial create riding waves. It will then create a 2π error for each so-created riding wave (see Fig.V.8).

We observe that depending on when the event occurs, an overall phase error might exist (the phase error experiences oscillations around the event date). This error bound is nonetheless inferior to $\pi/10$ if the mean value step takes reasonable values; laser intensity jumps are in practice smaller than 10% (see Fig.V.9).

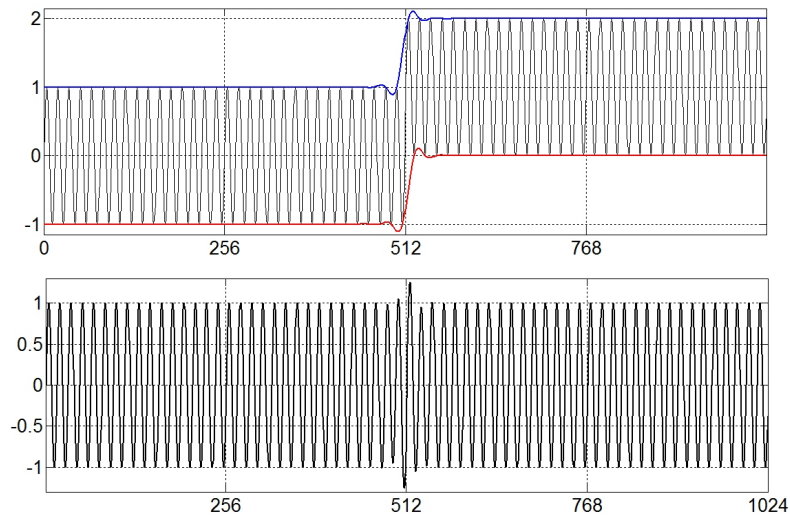


Figure V.7: The first IMF (bottom) of the EMD of a sine wave with a mean value step in the middle of its support (the signal is jointly shown on top with its upper and lower envelopes).

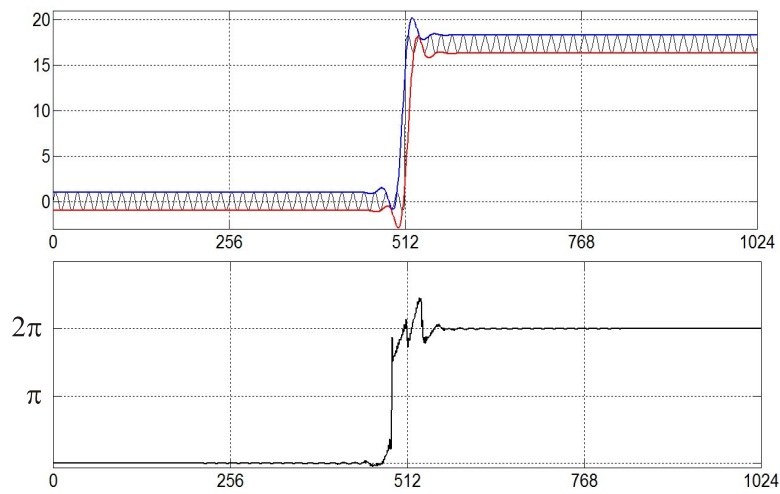


Figure V.8: Induced phase error by a mean value step (bottom). The EMD outcome is given on top.

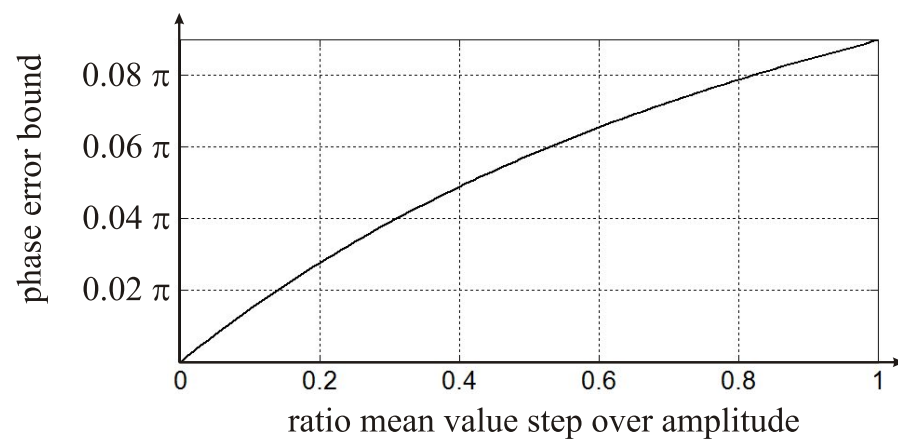


Figure V.9: Error bound for a mean value step ranging from 0 to 1; the amplitude is equal to 1.

- v) Sine wave with a phase jump: With not equal-path setups, the mode jump would probably introduce both intensity and phase jumps. The influence of the phase jump on the extracted phase has been studied in paragraph 5.5.2. We consider here a pure sine wave with a phase step of π in the middle of the signal support. We compare the results of the phase extraction with HT from the first IMF and from the raw signal in Fig.V.10. There is no real impact of the EMD on the phase extraction accuracy when a phase jump occurs.

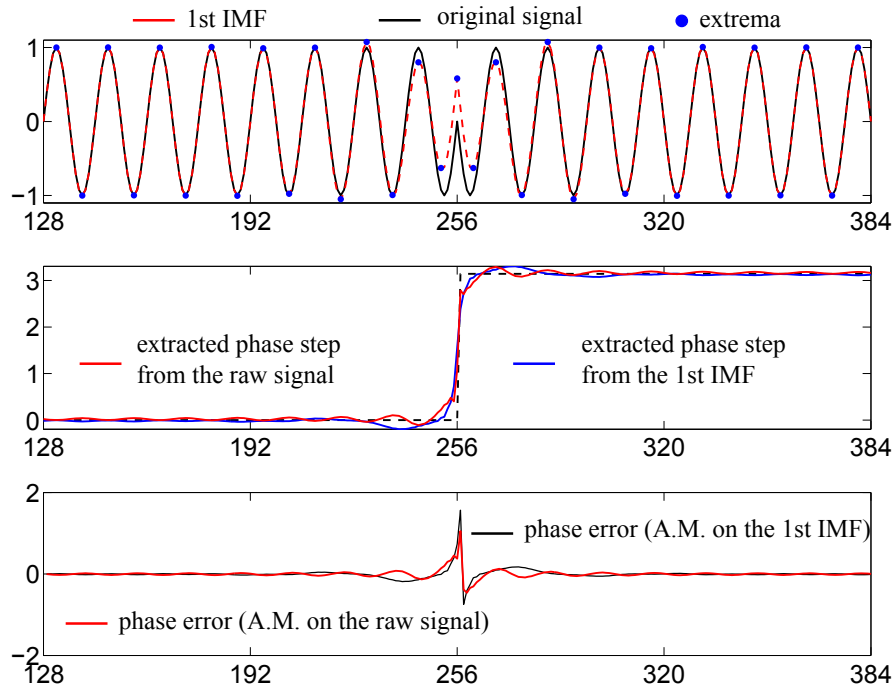


Figure V.10: Outcome of the EMD for a sine wave with a π phase jump in the middle of its support. The original signal and the first IMF are jointly shown on top, while the extracted phase steps are compared in the middle graph. The discrepancy between the original phase and the extracted ones are given in bottom (with EMD in black and without EMD in red).

1.2 Applications

The EMD has been proven to be highly valuable in any case where non-stationary signals are considered. Among the fields of applications, there is the processing of seismic, ECG, weather forecast signals, financial series, the extraction of textures in 2D ([135, 136]), and lately the denoising and processing of SI signals [16, 53–55, 58, 124, 125]. The interested reader is encouraged to go to [84] for further applications.

1.3 Strengths and weaknesses of the method

EMD is a powerful method which finds a larger and larger range of applications, not surprisingly given its simplicity of implementation and its valuable features. However, some mathematical issues are still pending and the method is still waiting for theoretical foundations. In this connection, Oliver Heaviside said: *"Mathematics is an experimental science, and definitions do not come first, but later on"* and in a more pictorial manner, *"Why should I refuse a good dinner simply because I don't understand the digestive processes involved?"* ([84]). The wavelet analysis waited for Daubechies ([46]) and Mallat ([121]) to rely on the strong mathematical basis that is available nowadays. EMD has not revealed all its secrets yet, and thus represents a great challenge for mathematicians and data analysis experts, being at the same time, a most welcome signal analysis method for researchers in many fields. On that subject, Chen *et al* propose in [33, 84] an answer to the issue of the mathematical definition of suitable envelopes. Hence, the authors propose a new sifting process algorithm which circumvents the upper and lower envelopes computation, and directly computes the mean envelope with B-splines. Flandrin *et al* reported in [63] that when the EMD is fed with stochastic process realizations, it acts as a dyadic filter bank, as those used in wavelet analysis.

As clearly shown by the few basic examples in the previous section, one of the main assets of the EMD is its sparseness: an arbitrary signal is decomposed in fewer components than with classical Fourier or even wavelet analysis, especially because we usually do not know if any vector of the predefined basis represents more or less reliably the intrinsic behavior of the analyzed data. Another important asset is the completeness: by design, the algorithm guarantees a lossless decomposition. However, one of the main drawbacks is the non-uniqueness of the final decomposition. It is indeed strongly dependent on the different algorithm parameters and choices, like the sifting stoppage criterion, the boundaries ending technique (signal continuation), the interpolation method, and so on. The boundary ending is also a sensitive part of the mean estimation: an interpolation kernel is chosen to link the *extrema* with smooth curves and some extrapolation is needed near the boundaries to take benefit of the whole data set. The cubic spline kernel is acknowledged to be the best trade-off between computation load, IMF smoothness and

preserving the adaptiveness of the method ([84, 85, 195]).

Bad choices for the aforementioned issues could lead to errors in the entire decomposition, like over-decomposition but also mode-mixing (for instance, higher frequencies oscillations are not caught locally by a given mode but by a successive one that should contain lower frequencies oscillations). It simply follows from the non-uniqueness of the decomposition. From the mathematical point of view, this is the most annoying issue, but in practice the previous errors can be straightforwardly identified by simple visual check of the decomposition or by more involved means, as e.g. the quantification of the orthogonality between modes ([53]). Some readjustments can then be brought to the algorithm, to avoid the errors or compensate them ([83, 84, 156]). At the end, a trade-off has to be found between imposing signal-dependent safeguards to give more robustness to the algorithm and preserving the self-adaptiveness of the method.

The outcome of a well-controlled EMD algorithm is actually multiple, ranging from signal detrending to specific features extraction. In addition of the centered signal on which phase extraction, estimation or tracking can be carried out, the location of the signal *extrema* can provide a rough estimation of the "instantaneous" phase - rather the mean of the instantaneous phase over every half-period. Moreover, the envelopes computation gives also the modulation depth which is helpful to appraise the reliability of the phase computation, and can also be of use to phase tracking techniques (for instance Digital Phase Lock Loop).

2 Deeper analysis of the decomposition

2.1 The *extrema* finding and the sampling influence

In the real world, we deal with discrete-time signals, and, as briefly mentioned, the first step of the EMD, *i.e.* the *extrema* identification, is error-prone especially in the case of signals critically sampled. The EMD outcomes depend thus strongly on sampling conditions ([60, 171]).

The authors in [171] have shown that a slight misalignment of the *extrema* with the sampling points results in a wrong estimation of the amplitude and then in over-decomposition and mode leakage. The error is actually maximum when the extremum of the continuous time function is equally spaced from two samples. It emerges from this study that the amplitude difference between the continuous time signal and its sampled version becomes below five percent as soon as the signal is sampled ten times finer than required by the Shannon sampling theorem. Their criterion provides indeed an indication on the wrong estimation of the amplitude, but the connection with a possible error on the extracted phase has not been addressed. We might lose indeed, the orthogonality of the extracted modes, leading to an energy spreading over successive modes, but the key point for our

application is definitely the phase conservation.

In [154], the authors consider a single tone and define the error as the deviation of the EMD outcome from the original signal. Here, with an original signal defined in Eq.(V.4), we quantify the phase error due to sampling with the averaging over φ (a uniform distribution of random phase pertaining to the speckle effect) of the standard deviation of the difference between the original phase and the phase ϕ_{imf} extracted from the 1st IMF:

$$x_{f_s, \varphi}[k] = \cos(2\pi \cdot f_s \cdot k + \varphi) \quad (V.4)$$

$$\langle \sigma_\phi \rangle_\varphi = \left\langle \sqrt{\frac{1}{N} \sum_{k=1}^N ((\phi_{imf}(k) - 2\pi f_s k - \varphi) - \langle \phi_{imf}(k) - 2\pi f_s k - \varphi \rangle_N)^2} \right\rangle_\varphi, \quad (V.5)$$

where f_s is the signal frequency and $2\pi f_s k + \varphi$ is the theoretical phase. The phase extraction is carried out through the analytic method as explained in the previous chapter. To reduce boundaries errors due to the discrete FT, a Gaussian window is used to pre-filter the dataset. Simulations have been conducted over 100 realizations of the signal defined in Eq.(V.4) and the dependence of the phase error with the signal frequency $1/2^r$ (r being a real number) is shown in Fig.V.11.

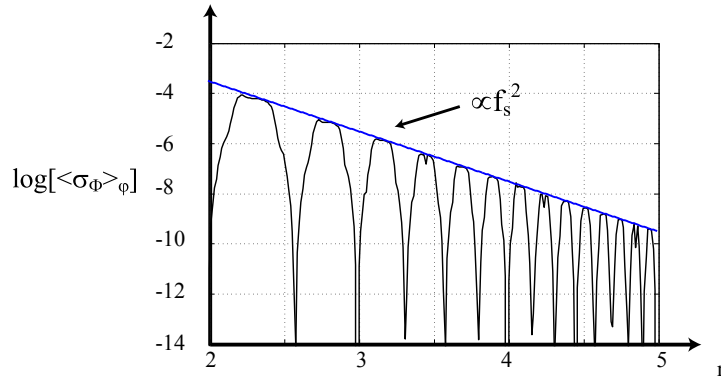


Figure V.11: Standard deviation of the difference between the extracted phase from the first IMF and the theoretical phase with an upper bound.

It appears clearly that the EMD behaves better when 2^r is an even integer greater than 3, and especially a power of 2. The largest error is made when 2^r is an odd integer. In the latter case the odd number of samples per period leads indeed to a detrimental asymmetry for the upper and lower envelopes computation. The maximum standard deviation is in average about one hundredth of period and an upper bound varying with the square of the signal frequency gives the global trend of the error (see Fig.V.11). Finally, the sampling error is much lower than what we could have expected from the

study in [171], and our results are actually closer to the ones presented in [60, 154]. We end this part on the sampling influence with the comforting conclusion that sampling has indeed an influence on the phase extraction but that we can neglect the error as long as the sampling frequency is at least 3 times smaller than the Nyquist frequency.

The extrema finding step is another key step of the decomposition. It is actually the step where some fine tuning can be done to enhance for instance the robustness of the algorithm, as usual at the cost of the self-adaptiveness. With discrete signals, the common way to identify the *extrema* is shown in Fig.V.12 in a pseudo-filter manner.

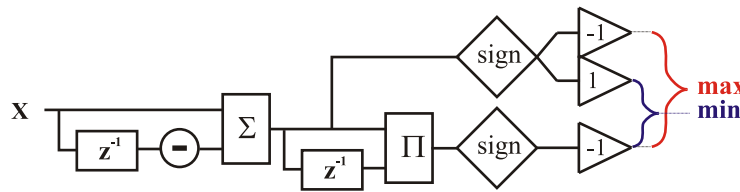


Figure V.12: Pseudo-filter view of basic *extrema* finding.

This procedure applied on noise free signals does what it is expected to do, but things change with realistic signals which contain unavoidably some noise, as shown in FigV.13.

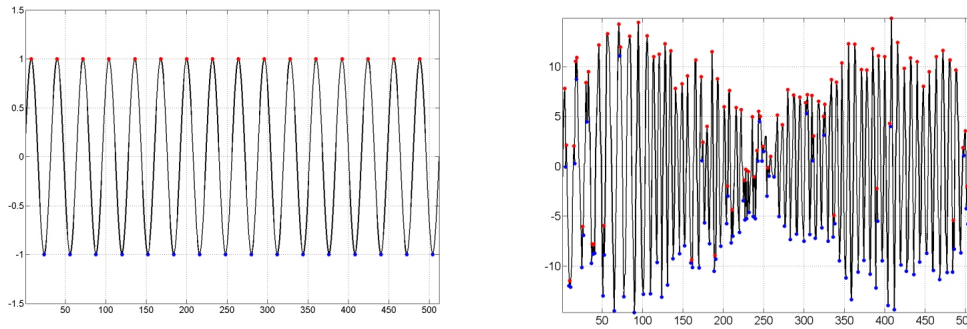


Figure V.13: Basic *extrema* finding with a noise-free signal (left) and an experimental SI signal (right). *Maxima* and *minima* are respectively highlighted by red and blue circles.

It is obvious that a more elaborate *extrema* finding algorithm is required. One first point to care about is to be sure that there are no consecutive *minima* or *maxima*. Furthermore, we already mentioned that the riding waves must be sifted out, to make of an extracted mode an acceptable IMF. This is one of the purposes of the sifting process. But noise may artificially create such riding waves, which may create, if taken as actual oscillations, errors of 2π . One solution, suggested in [84], is to forbid a maximum to be too close to a

minimum, based again on a preset limit of allowed proximity. It is actually what we did for the fast implementation described in section 3. With a revisited *extrema* finding step, we could obtain the result shown in Fig.V.14.

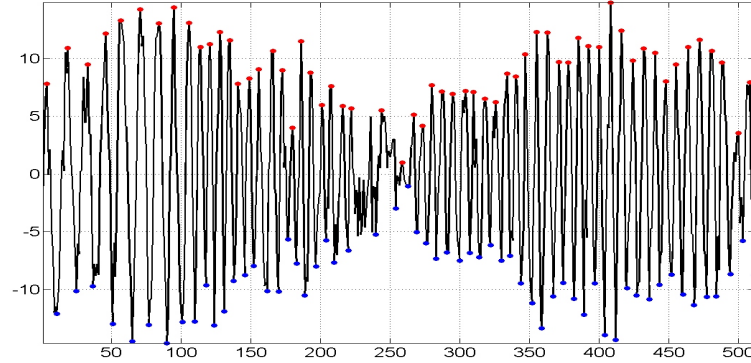


Figure V.14: Improved *extrema* finding step to avoid taking into account riding waves created by noise.

Recently, a new EMD algorithm has been proposed and named doubly-iterative EMD ([97]). The starting point of this new method is the observation that, at a certain point of the procedure - say the extraction of the k th mode is ongoing at the j th iteration of the sifting process -, the local *extrema* of the signal under consideration $s_j^{(k)}$ are not necessarily the best interpolation points to take into account for the envelope computation. The authors showed that it is preferable to rather take the *extrema* of the highest frequency content subsignal, that is the signal $s_{j+1}^{(k)}$. The sought interpolation points are estimated through an additional sifting process interwoven in the regular one, as the signal $s_{j+1}^{(k)}$ is not known in advance being the forthcoming outcome of the current iteration of the regular sifting process. The authors used higher order splines for this secondary sifting process and they showed that the frequency separation power of the EMD has been slightly enhanced, at the cost of a substantially increased complexity.

2.2 The sifting process influence

Another key step of EMD algorithm is the sifting process and the criterion to stop it. We will briefly say some words on which basis it is reasonable to stop or run further the sifting process. First of all, its goal is to extract from the original signal an acceptable IMF, as already said, and thus by definition, whose HT will behave well. In [83], several ways are considered to end this iterative process, because if it might be necessary in some cases to iterate a certain number of times to extract the IMF, it is definitely mandatory not to run it too many times, otherwise over-decomposition will surely occur. The first

proposed criterion ([85]) was the Cauchy-type convergence criterion, where the sifting process is carried out until two consecutive sifted modes are close enough according to a certain preset limit. This way of determining the sifting process end does actually not rely on the definition of the IMF. It requires a certain closeness between consecutive sifted modes but nothing on the nature itself of the mode. A better criterion was then proposed in [83] more empirical but closer to the core definition of IMFs. It requires that the number of zero-crossings and *extrema* remain the same after a couple of iterations (typically between three and five). Another valid criterion would be to proceed with the sifting process to the point when the mean envelope is sufficiently small, again according to a preset threshold. The main problem with this latter approach is that the aimed result may not be obtained without a proper management of the boundaries. Because it is a global criterion, it may be satisfied at different rates within the data set, which means in other words, that applying this criterion globally, may lead to over-sifting in some areas of the signal. That is why the authors in [156] propose a stopping criterion which acts locally: the idea is thus to isolate the regions where the error remains high and to carry out the sifting process only on those regions. In our specific application, we have in view a high accuracy in the phase extraction and it may thus be delicate to concatenate the different regions without creating or missing fringes of displacement.

We now turn to a deeper analysis of the sifting process influence on the separation power of the EMD. The authors in [155] consider the following sum of two tones:

$$x(t) = \cos(2\pi t) + \alpha \cdot \cos(2\pi \nu t + \varphi), \quad (\text{V.6})$$

where α is a normalized amplitude ratio ranging from say 10^{-2} up to 10^2 , ν is a normalized frequency ratio ranging from say 10^{-2} to 1 and φ is a random phase uniformly distributed in $[-\pi, \pi]$. Their performance criterion measures the deviation of the outcome of the EMD algorithm for the first IMF from the expected mode, i.e. the high frequency term in Eq.(V.6):

$$\delta_1^i(\alpha, \nu, \varphi) = \frac{\|d_1^i(\alpha, \nu) - \cos(2\pi t)\|_{l_2}}{\|\alpha \cdot \cos(2\pi \nu t + \varphi)\|_{l_2}}, \quad (\text{V.7})$$

where d_i^1 stands for the first IMF obtained after i iterations of the sifting process, and $\|\dots\|_{l_2}$ stands for the l_2 norm (square root of the sum of the square values). When the two tones frequencies are close to each other, i.e. $\nu \approx 1$, we guess the separation will fail and the EMD outcome will be the signal itself leading to a performance criterion close to 1. However, if the two tones frequencies are well separated, i.e. $\nu \ll 1$, the EMD will perform a perfect separation, and thus leads to a criterion value close to 0. For intermediate cases, the guess is not trivial. We report a result from [155] in Fig.V.15, where the average criterion over 100 realizations of φ is mapped for ten iterations of sifting process.

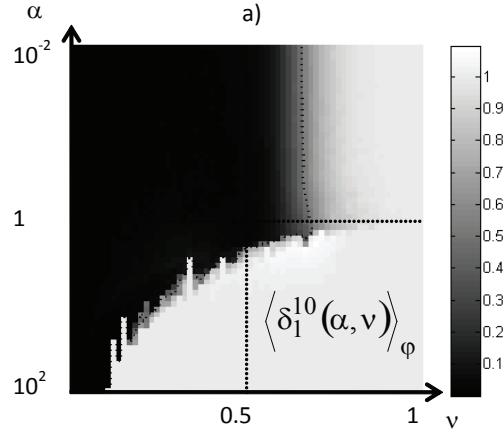


Figure V.15: averaged criterion δ for 10 iterations of sifting process.

Those results actually provide a wealth of insights. We observe two very distinct areas basically for $\alpha < 1$ and for $\alpha > 1$. It has been shown in [155] that the area where $\alpha < 1$ can be modeled by a filtering process (see Fig.V.16) with the kernel K used for the interpolation (loosely cubic spline). The first IMF obtained after i iterations of the sifting process takes the form:

$$d_1^i(\alpha, \nu) = \cos(2\pi t) + [1 - K(\nu)]^i \cdot \alpha \cdot \cos(2\pi \nu t), \quad (\text{V.8})$$

where $K(\nu)$ takes the following form in the cubic spline interpolation case ([179]):

$$K(\nu) = \left(\frac{\sin(\pi \nu)}{\pi \nu} \right)^4 \cdot \frac{3}{2 + \cos(2\pi \nu)} \quad (\text{V.9})$$

In Fig.V.16, we reproduced another result from [155] with some cross-sections of the $\langle \delta_1^i(\alpha, \nu) \rangle_\varphi$ distribution for $i = 1, 5$ and 10 sifting process iterations, obtained through simulations and jointly shown with curves obtained from Eq.(V.8):

However, the filter model is no longer appropriate for the area where $\alpha > 1$. It appears indeed that the sharp boundary between no separation at all and complete separation does not depend on the number of sifting process iterations. Before drawing any conclusion we must study the non-stationary case, but it is a good omen for a fast implementation for SI temporal signals. Indeed, as our signals have necessarily an amplitude ratio greater than 1 and well-separated spectra, we are most likely to be in an area where perfect separation will be achieved in one single iteration. As previously said, the signals we are interested in are strongly non-stationary, and it would be valuable to define a criterion similar to the one in Eq.(V.6) for SI signals defined by the classical two-beam equation. To this aim, we simulate temporal SI signals with the model described in [52] and detailed in Appendix B. As a quick reminder, our model actually relies on the convolution equation between a

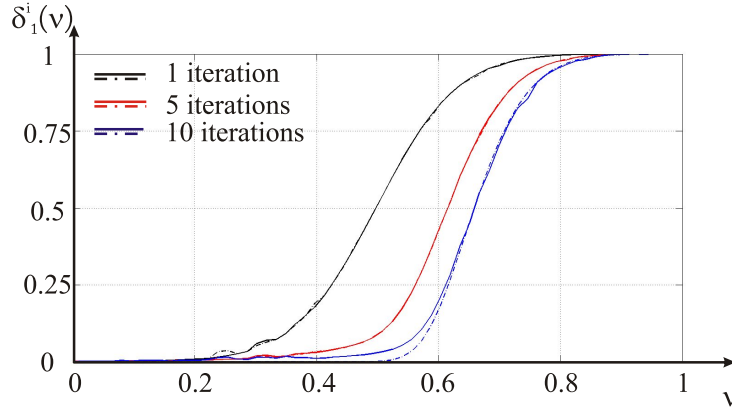


Figure V.16: EMD filter model (cubic spline kernel) with simulations in solid line and predictions in dashed line.

given impulse response and a complex field of random argument and unitary amplitude, according to both the diffraction theory in the Fresnel approximation and the mechanism of speckle formation. Our purpose here is to show that for SI signals, the separation is actually perfect between the AM-FM term and the varying bias after one single iteration. For each temporal signal we compute the following criterion:

$$\delta_1^i = \frac{\| d_1^i - 2\sqrt{I_1 \cdot I_2} \cos \Phi \|}{\| I_1 + I_2 \|} \quad (\text{V.10})$$

A simulated signal is shown in Fig.V.17, while the histograms of the criterion δ_1^i computed for 4096 temporal signals are depicted for $i = 1, 5$ and 10 in Fig.V.18. We impose a non-linear digital instantaneous frequency (IF) evolution distributed in the $[2\pi/16, 2\pi/8]$ range.

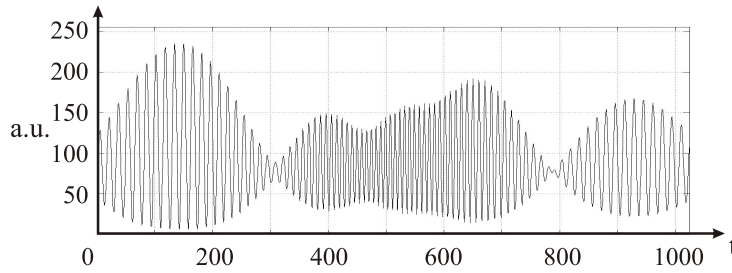


Figure V.17: A simulated temporal SI signal.

It finally turns out from the simulations that, whatever is the number of sifting process iterations, the criterion defined in Eq.(V.10) is below 0.015: the similarity between the EMD-processed temporal signal and the true sought-after AM-FM signal is better than

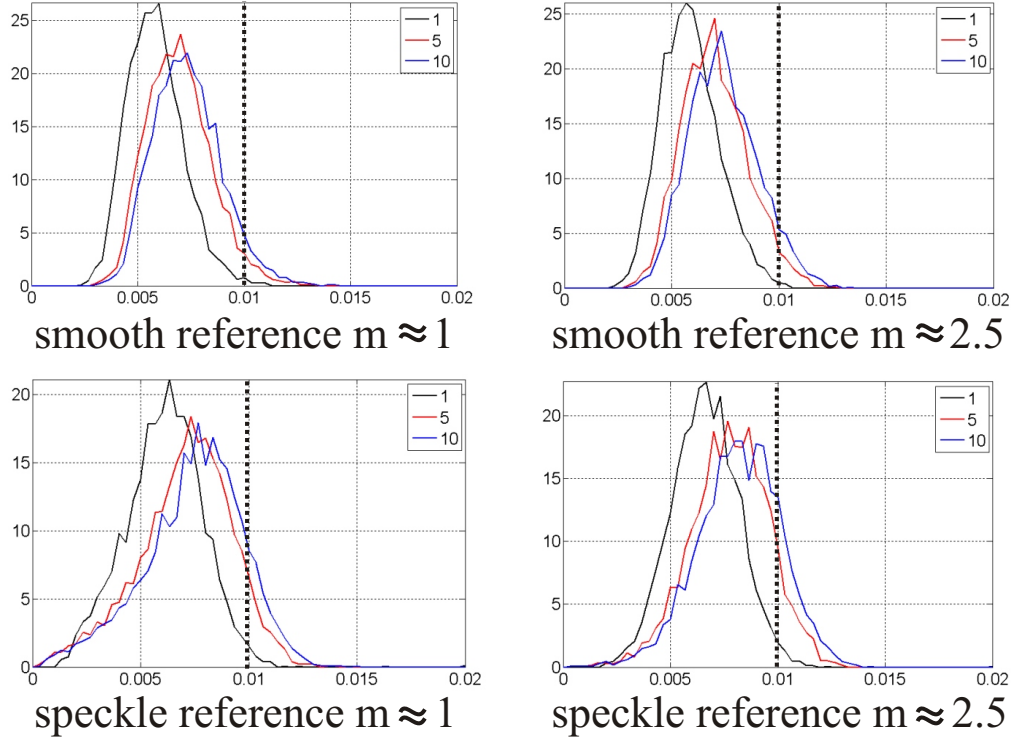


Figure V.18: Histograms of criterion defined in Eq.(V.10) for 4096 simulated SI temporal signals with 1, 5 and 10 iterations of sifting process (the dotted line represents the similarity criterion of 99%). m is the fit parameter of the Gamma distribution (see Chap 3, Eq.(III.4)).

98.5%. We observe that the sifting process actually degrades rather than improves the components separation. It is likely to be due to the boundary choice and to the fact that the sifting process makes the boundaries errors propagating within the data set. Not surprisingly, we observe finally from Fig.V.18 that the separation is achieved with a very high confidence independently from the spatial integration regime and from the type of reference (smooth or speckle).

2.3 The boundaries ending

As briefly stated before, the boundaries ending is important as it may create artificial oscillations in the interpolated curves, and thus generate errors which will propagate inward through the sifting process. This point is well-known by users of the EMD and several methods have been conceived to solve this issue. The authors in [156] propose to mirrorize the *extrema* close to the edges. Zeng in [195], as for him, suggests to perform separately an odd and an even extension of the signal, and the final mean envelope is

computed by taking the average of the two upper and the two lower envelopes. The authors precised that the mean must be beforehand removed from the signal to avoid large jumps and as a consequence large swings in the cubic spline interpolation. This precaution is a serious drawback and deteriorates the adaptiveness of the EMD method. An interesting technique is exposed in [43]. The authors extend the signal at both ends by constructing a sine wave, whose amplitude, frequency, phase and mean value are directly computed respectively from the first and the last couple of (*minimum, maximum*). This way, the slope of the envelopes tend toward zero, eliminating large swings of the cubic spline. The Gerchberg algorithm is also a well-known technique to extend signals within their support (typically in interferometry when the object has holes or a non-convex shape) or beyond. Another way of doing could be extending the signals by relying on the trend near the borders. More explicitly, it would consist in imposing respectively *maxima* and *minima* which belong to the best linear fitting curve of the respectively *maxima* and *minima* close to the edges.

In this thesis work and the related articles ([53–55]), we chose to repeat the first and the last couple of (*minimum, maximum*) to bound the vectors of interpolation points. This way of doing is fast, does not need to extend the signal support or to compute some local trends, but is certainly not optimal in all the cases. However, it proved to be efficient in ours.

2.4 Orthogonality

At this point, we shall discuss the orthogonality and the completeness of the EMD. Completeness is actually straightforward from the decomposition itself. Orthogonality is a little bit trickier. Let's first rewrite the decomposition in (V.1) ([85]):

$$s(t) = \sum_{k=1}^{K+1} C_k(t), \quad (\text{V.11})$$

where we consider the final residue as a component. Taking the square of equation (V.11) yields:

$$s^2(t) = \sum_{k=1}^{K+1} C_k^2(t) + 2 \sum_{i=1}^{K+1} \sum_{j=1}^{K+1} C_i(t) C_j(t) \quad (\text{V.12})$$

If the basis vectors form an orthogonal set, the second term of the right member is null. So, we can assess the obtained decomposition orthogonality by estimating the following global index:

$$IO = \frac{\sum_{t=0}^T (\sum_{i=1}^{K+1} \sum_{j=1}^{K+1} C_i(t) C_j(t))}{\sum_{t=0}^T s^2(t)}, \quad (\text{V.13})$$

which, for two modes, becomes:

$$IO = \frac{\sum_{t=0}^T (C_1(t) C_2(t))}{\sum_{t=0}^T s^2(t)} \quad (\text{V.14})$$

We can even build $(K + 1) \times (K + 1)$ matrices defined by:

$$OM_{i,j} = \frac{\sum_{t=0}^T (C_i(t)C_j(t))}{\sum_{t=0}^T s^2(t)} \quad OMn_{i,j} = 2 \frac{\sum_{t=0}^T (C_i(t)C_j(t))}{\sum_{t=0}^T (C_i^2(t) + C_j^2(t))} \quad (V.15)$$

These matrices of orthogonality are symmetric, and even diagonal if the decomposition is orthogonal. On one hand, the matrix OM allows a quick identification of the number of modes of significant energy, and on the other hand, OMn is handy to see qualitatively the leakage between modes.

It is important to note that the orthogonality concept becomes local when dealing with non-stationary signals. This is illustrated with the example of a signal, which is the sum of two parabolic chirp signals plus a centered sine wave. The frequency trajectories of each chirp never cross but the ranges covered do have overlap. As seen in Fig.V.5, there is no problem for the EMD to separate the two signals with varying frequency, whichever is the law of variation by the way. The matrices of orthogonality clearly show the orthogonality of the two components (Fig.V.19). It also demonstrates their usefulness to compensate over-decomposition, by direct inspection of the correlated modes (we have been able to rebuild the last mode with a quite good reliability).

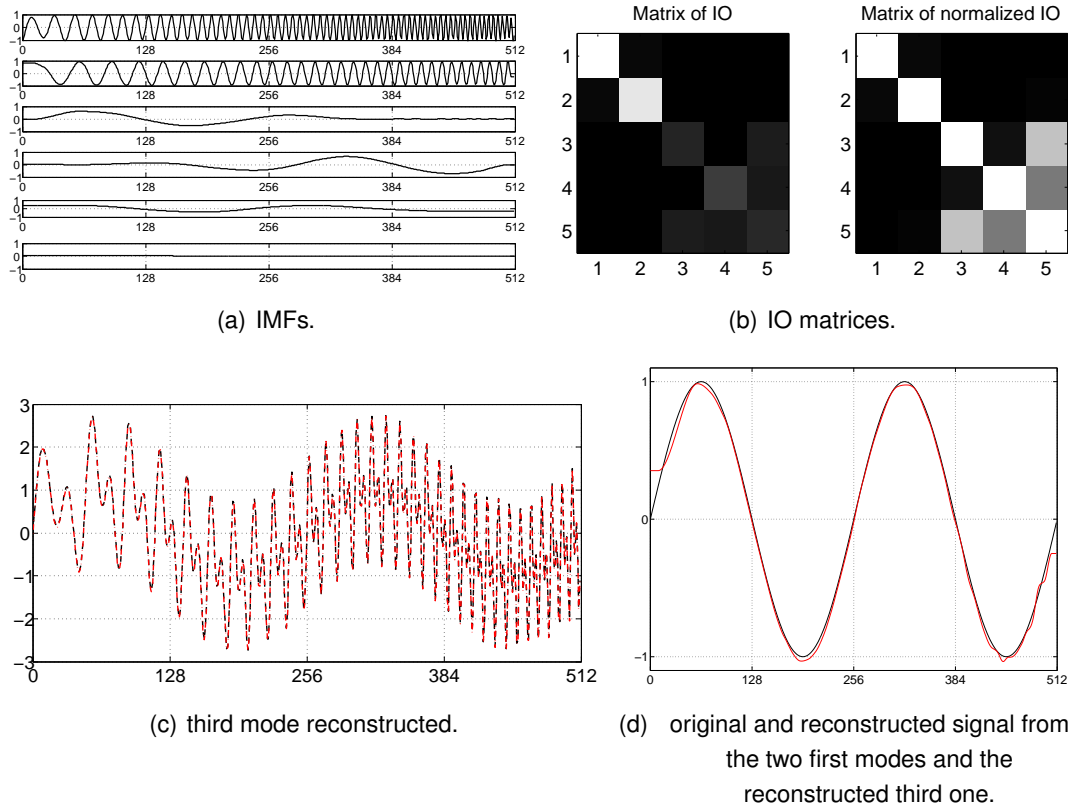


Figure V.19: Reconstruction of an orthogonal decomposition by direct inspection of the orthogonality matrices.

3 A fast implementation of the EMD for SI signals processing

3.1 Advocating the fast implementation

For a pixel signal with enough modulation and as soon as the illumination is well adapted to the sensor dynamic, the relevant information is carried by the high frequency part of the signal (the cosine term in the two-beam equation). This information is thus contained in the first IMF, and it becomes useless to proceed further in the modes extraction. We have moreover seen in details that the EMD is effective after one single iteration of the sifting process with non-stationary, narrow-band signals containing two well-separated IFs. We can extract the first IMF (or pseudo-IMF for the sake of rigorosness) through a single iteration of the EMD algorithm. At this point, it is worth mentioning the method developed by Vikhagen ([185]) and improved by Carlsson and Wei ([191]) for deformation measurement in dynamic SI experiments. The phase evaluation method ([185]) consists in scanning the pixel history signal within a local oscillation to detect a maximum and a minimum value: $(I_o + I_m)$ and $(I_o - I_m)$ with the notations of Eq.(II.10). There is only one unknown left, the phase Φ_{OPD} that is finally easily computed modulo 2π at each instant using again Eq.(II.10). The improvement of the method ([191]) consists in a better evaluation of the initial speckle phase, i.e. before deformation, and in a least-squares estimation of the phase during the deformation allowing at the same time the resolution of the sign ambiguity. Even if the methods come from very different starting points, we arrive to a quite similar technique, likely to be nonetheless much faster in our case. Indeed, the EMD does not need to analyze the signal at the oscillation level. We have thus implemented the EMD in a light way, though with numerous changes to improve the robustness - details are given in the next section.

3.2 Additional free features of the EMD

From the *extrema* finding step, we can readily extract a useful knowledge, though of an approximate nature, on the IF and thus the phase. In continuous time domain with narrow-band noise-free signal, if we consider a local maximum at $t = t_1$ and a local minimum at $t = t_1 + \tau$, a rough estimate of the IF in the range $[t_1, t_1 + \tau]$ is simply (see Fig.V.20):

$$\bar{f} = \frac{1}{2\tau} \quad (\text{V.16})$$

The previous estimation is simply the average IF over each half period of the original signal. With discrete time signals, especially in the non-stationary case, the *extrema* are very unlikely to be located at sampling points, adding thus some quantization noise to the computation. The higher the FM is, the better the temporal resolution will be, as usual to

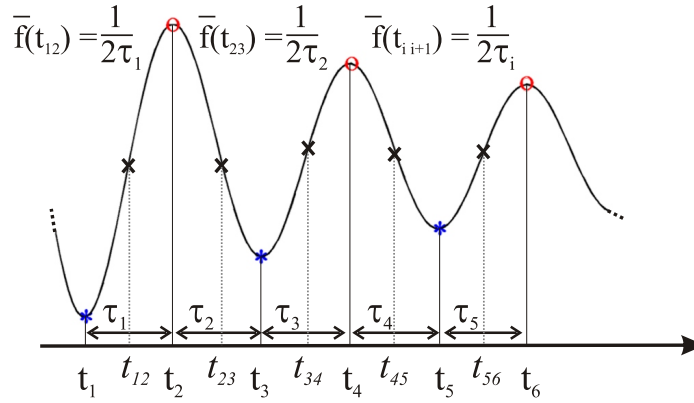


Figure V.20: Rough estimation of the signal IF and phase.

the detriment of the frequency resolution and, in corollary, of the quantization noise. Notwithstanding the strong limitations of this method, we will use it as it is, either to provide a fast evaluation of the phase in long experiments for instance, or to provide an initial guess for phase tracking methods.

The key step of the EMD procedure is the envelopes computation so as to be able to build a mean envelope, supposed to be as close as possible to the local mean value everywhere. Once the upper (eM) and the lower (em) envelope are computed, we have also access to the modulation (mod) of the signal:

$$\begin{aligned} m &= \frac{em + eM}{2} \\ mod &= eM - em \end{aligned} \quad (V.17)$$

The modulation can be also of great use for gain normalization purpose in IF and phase tracking methods, as PLL and linear predictive filtering. A filtering technique inspired by [79], exposed in the last chapter, will take advantage of the modulation computation.

3.3 Algorithm and evaluation

We now come to a detailed description of our implementation of the EMD. The flow-chart of the algorithm is given in Fig.V.21 (the code is given in Appendix C).

The algorithm is fed with the original signal of length n and the threshold value used for the reliability index computation. This latter quantity simply indicates whether the pixel modulation is higher or lower than a certain threshold. This information will be exploited by the 3DPP procedure, which will be the matter of the forthcoming chapter. The first step is the extraction of the *extrema*. Once a rough estimate of their location has been found (see Fig.V.12), three operations are carried out to refine their position:

3. A fast implementation of the EMD for SI signals processing

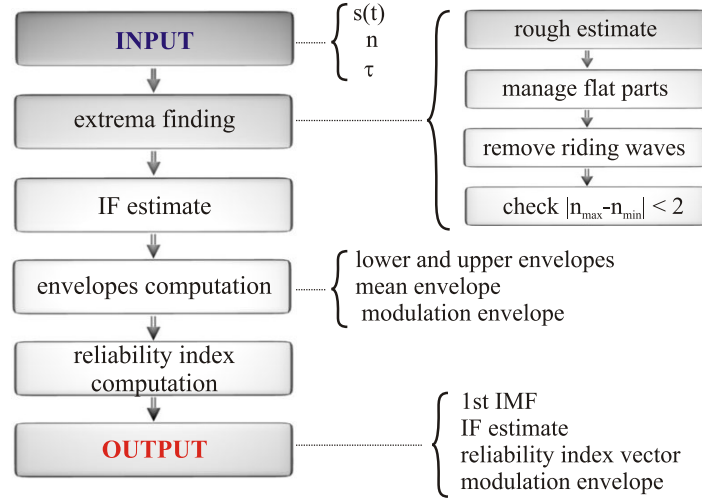
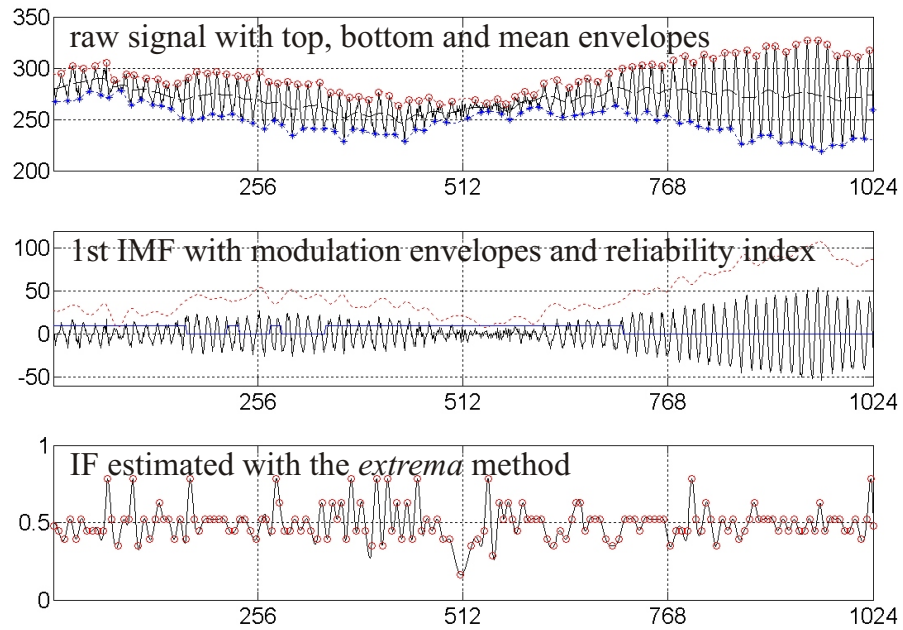


Figure V.21: Structure of the fast implementation of EMD for SI signals processing.

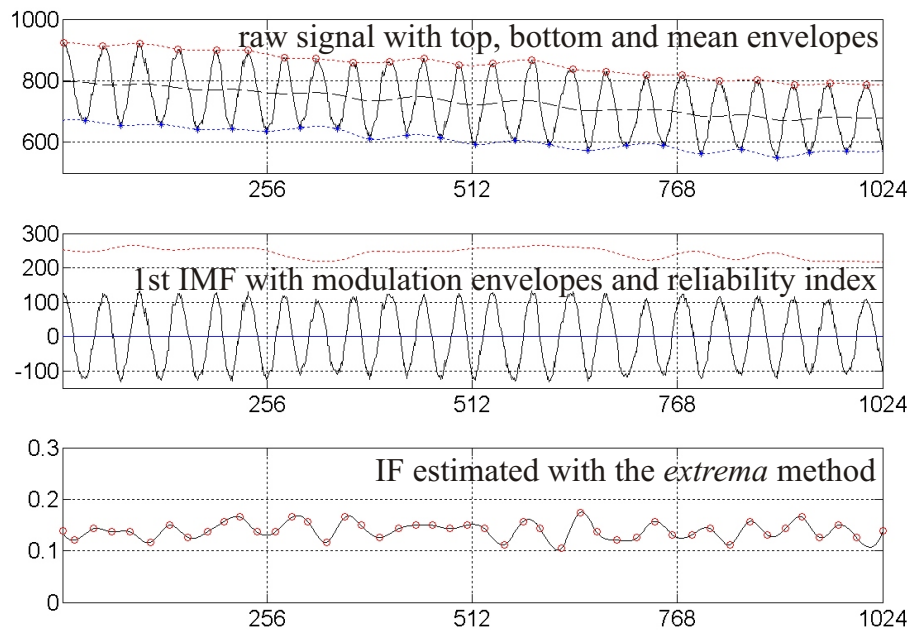
- i) We first take care of the possible flat parts of the signal. Instead of taking into account all the consecutive *extrema*, we consider a single one located at the middle of the considered flat part.
- ii) We then remove the riding waves. As discussed earlier, we want to extract the useful information in the first IMF and it is thus important not to count a noise-induced riding wave as a fringe. We forbid thus extrema to be closer than 3 time samples.
- iii) We finally check that the number of *maxima* and *minima* differs from each other at most by one. We remove, this way, spurious *extrema* and possible ones which have been counted twice or more.

With the finer locations of the *extrema*, we compute the IF of the signal as it has been described in the previous paragraph. Based on the rough estimate of the IF for each half-period, a smooth curve is computed (with a cubic spline kernel) which can be further numerically integrated to obtain an estimate of the phase law of the temporal pixel signal. The next step is the envelopes computation. The lower and the upper envelopes are then computed so as to obtain the mean envelope and, as also said in the previous paragraph, the modulation envelope. The algorithm eventually yields the sought centered signal, the rough IF estimate, the reliability index vector and the modulation envelope.

We provide in Fig.V.22, genuine temporal SI signals processed by our algorithm, with its different outcomes (1st IMF, envelopes, reliability index and rough IF estimate).



(a) Pixel signal with a high phase rate.



(b) Pixel signal with a low phase rate.

Figure V.22: Genuine SI pixel signals processed with the fast-EMD algorithm.

3.4 Outlook: construction of an hybrid mode

In the next chapter, we will address the problem of decorrelation-induced random phase errors in a completely new manner. Those phase errors are inherent to speckle fields and cannot be avoided, but it does not mean that nothing can be done to reduce their impact on the final result. This is the object of the next chapter with concrete results in the seventh chapter. It is well-known that the under-modulated pixels are the scene of the largest phase errors (see chapter 3 and 6). The SNR is indeed lower in there. Whichever safeguards are taken for the EMD implementation, especially at the *extrema* finding stage, we cannot avoid some mode-mixing to occur in those areas, and the mode contains thus essentially noise. The phenomenon is even more pronounced when the activity is low (very large amount of over-sampling). The idea is then to regain some information, which is contained in the first residue. The hybrid mode is actually defined by:

$$IMF_{hyb}[k] = IMF^{(1)}[k] + RI[k] * IMF^{(2)}[k] \quad \text{for } k \in [1, N], \quad (\text{V.18})$$

where $IMF^{(1)}$ and $IMF^{(2)}$ designate respectively the first and the second IMF, and RI the reliability index. The idea is thus to take into account the information contained in the second IMF only in the regions where the pixel modulation has been declared as too low, because it is within those regions that mode-mixing is the most likely to occur. The choice of the threshold value will be discussed in chapters 6 and 7.

We show in Fig.V.23 an experimental temporal SI signal which experiences roughly 15 fringes of displacement. The extrema finding step is doomed to failure in such a case, and the first IMF is indeed mainly constituted by noise in the under-modulated regions. Some precious information is recovered in the hybrid mode.

If the construction of such hybrid modes can be valuable in some cases, the under-modulation issue will be treated in a more robust and elegant way in the next chapter.

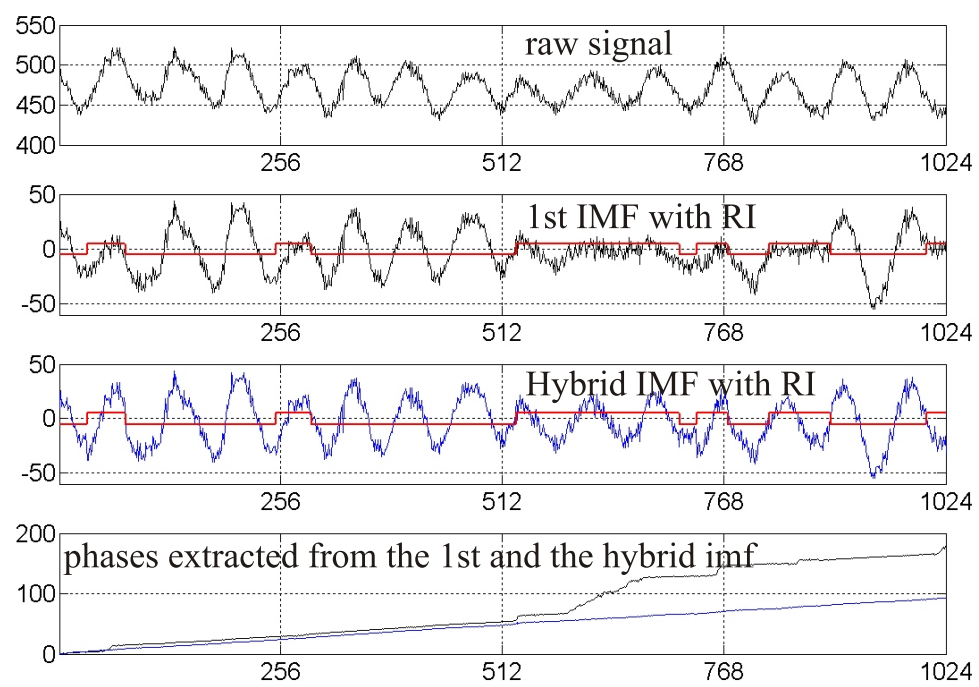


Figure V.23: Construction of an hybrid mode.

Chapter VI

A novel approach to address the modulation drops issue with the Delaunay triangulation

The randomness of the background and modulation intensities and of the speckle phase make tricky and prone to errors phase extraction procedures. Several strategies aiming at reducing or eliminating the phase errors are available. The first one consists in compensating the decorrelations by appropriate adjustments of the setup. It is also possible to split the recorded data set into several batches, in each of which the displacement is confined to a fraction of the correlation length, and to finally concatenate the results. Another successful way is to use filtering methods, where the kernel coefficients depend on the confidence levels of the measurements ([109]). The method we propose here, namely the 3DPP method - standing for 3 dimensional piecewise processing - is a still completely different approach ([55, 56]). It consists in discarding, purely and simply, the regions, within each temporal pixel history, where the phase extraction is likely to be unreliable, according to a predefined criterion. The so-built regions of missing data, of random length and location, are filled by the information carried by reliable well-modulated neighboring pixels, using an interpolation operation based on the Delaunay triangulation (DT). The two main steps are detailed below:

- i) the classification of the pixel signals based on their modulation which provides non-uniformly sampled maps of phase increment at each instant, and
- ii) the DT of the so-built scattered data associated to a triangle-based interpolation procedure to obtain the phase maps at each instant of the experiment.

Even if the core of this thesis work is the characterization of dynamic regimes, it is obviously possible to define the pixel modulation intensity in static phase-shifting interferometry ([39, 109]). We already briefly discussed this point in the section dealing with SI

statistics in chapter 3, where it is recalled that the reliability of a pixel is well represented by a factor inversely proportional to its modulation. We nevertheless said that a binary classification might be interesting and that we chose this direction to enhance the quality of phase maps. We will thus present a novel phase map filtering technique, well-suited for static regimes, and by essence regimes where the displacement does not extend beyond the correlation cell.

1 Data classification and the concept of pixel reliability

1.1 The dynamic regime

As seen in Chap.3, the lower the pixel modulation, the higher the induced random phase error ([109]). It is reasonable to consider the modulation of the temporal pixel signal as a good indicator of reliability (see Fig. VI.1).

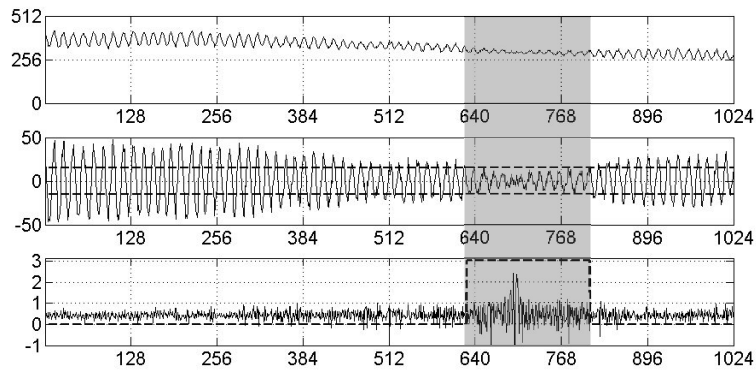


Figure VI.1: A temporal SI signal (top) with 1024 time samples, experimentally obtained and processed with the EMD, yields a centered signal (middle) with a fluctuating modulation (the chosen threshold is shown in dashed line in the middle graph), whose IF (bottom in plain line) obtained through the use of the Hilbert transform ([55]) exhibits high noise level in the low-modulation discarded region (highlighted by the gray strip in the three graphs).

In the reliable areas, *i.e.* where the pixel modulation is higher than a chosen threshold, the phase will be obtained up to an additive constant. The computation of the discrete IF - temporal derivative of the phase allows of course to get rid of this constant, leaving a meaningful exploitable result. The IF values in the under-modulated regions are discarded. Each pixel being independent, when we gather again the temporal sets to form frames (see Fig. VI.2), we obtain arrays of valid discrete IF sampled on a fluctuating non-uniform grid. An interpolation step has then to take place to obtain arrays of discrete

IFs uniformly sampled. A final discrete integration step yields the phase maps at each instant.

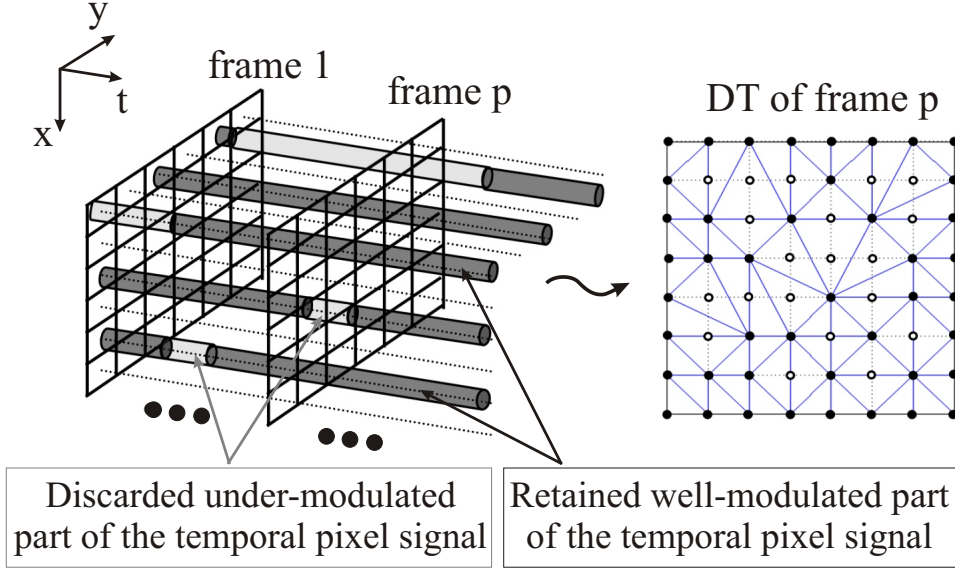


Figure VI.2: Data classification: (left) the irrelevant parts of the temporal signals are highlighted by bright tubes while the dark ones show the parts on which the interpolation step will rely; (right) the non-uniform sampling grid computed for an arbitrary frame with the associated DT.

1.2 The static regime

The situation here is quite different as we consider the case where a map of phase difference between two static states has been computed, for instance with a phase-stepping algorithm. We have thus in hand a phase map in the range $[-\pi, \pi]$ with a large amount of noise, which we want to remove as much as possible, whereas the sharpness of the 2π jumps has to be preserved for the subsequent unwrapping step. This problem is well-known. The widely adopted strategy is to apply filtering techniques on the cosine and the sine of the phase map and recompute afterwards the phase (see chapter 4 and [3]). The novel approach we bring here to tackle this issue is to replace the filtering step with classical convolution by a certain kernel, by an interpolation procedure on the cosine and the sine of the phase from which the pixels with insufficient modulation have been again purely and simply discarded. The interpolation procedure will be exactly the same as in the dynamic regime and is schematically shown in Fig.VI.3. We will designate this filter by the sine-cosine-DT filter.

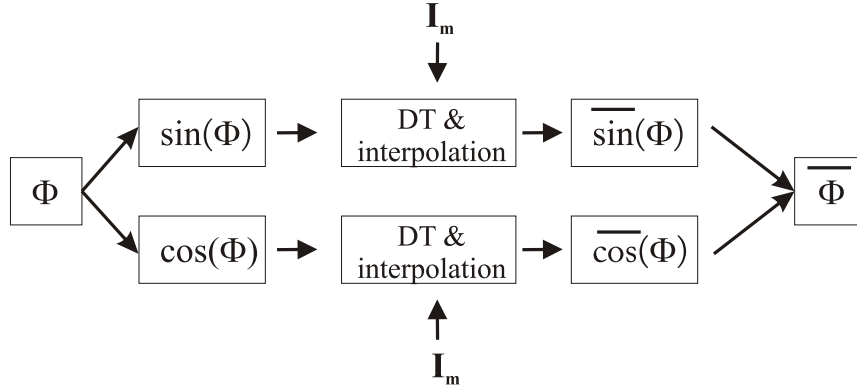


Figure VI.3: Sine-cosine filter with the DT.

Comparing to the procedure of [3], the iterative loop becomes useless and is thus removed, and the required modulation map is simply used as a mean to classify the pixels in a black and white manner, similarly to what has been explained for the dynamic regime. The method will be tested and discussed in the forthcoming chapter.

2 The Delaunay triangulation: a new approach to the modulation loss issue

Given a set of points, randomly spread over a portion of space, it is convenient in many instances (from terrain surveying to graphics rendering, robotics, and crystal structures modeling [13]) to construct a smooth surface, containing these points and obeying definite properties, which can be furthermore sampled on a uniform mesh. With this aim in view, a natural approach is to construct first a triangulation in the plane, then assign a weight to each point of the mesh, *i.e.* the IF value here, and finally, build a piecewise polynomial surface over it. The purpose of this section is to give the theoretical background of this scattered data interpolation which uses the DT. This procedure will then be included in the 3DPP procedure which will be thoroughly described and discussed in the next section.

2.1 Convex hull, Delaunay triangulation and Voronoi diagram

2.1.1 Definition and computation of the convex hull of a data set

We already mentioned that, given a random set of points in the plane, the first step of the whole triangulation-interpolation process is to compute the convex hull of the data set in

question. The convex hull in 2D might be seen as a rubber band surrounding a set of nails driven in a wooden board, the latter ones representing our mesh of valid data (see Fig.VI.4).

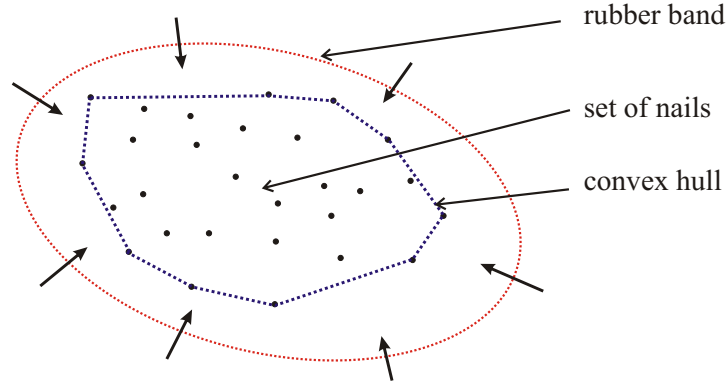


Figure VI.4: Convex hull of a set of points.

More formally, a subset S of the plane is said convex if and only if for any pair of points $(p, q) \in S$ the line segment \bar{pq} is completely contained in S . The convex hull $\mathcal{CH}(S)$ of a set S is the smallest convex that contains S ([48]).

Now that we have some basic knowledge on convex hull, we of course have to worry about its computation. We can see that from Fig.VI.4, given the points p and q such that \bar{pq} is an edge of $\mathcal{CH}(S)$, all the points of the set are one side of the line (pq) , say right if the line is oriented. So if one can identify the pairs of our set - containing say n points - for which the other points are all located on one side, one is able to compute the convex hull. The problem of this straightforward algorithm is its complexity: $n^2 - n$ pairs have to be checked and for each of them, there are $n - 2$ points to look at to see whether they lie on one side or the other. It results in a complexity in $\mathcal{O}(n^3)$, preventing the use of such an algorithm for large point sets. Another strategy is mandatory and it can be shown that an incremental algorithm can be designed with a total computation time of $\mathcal{O}(n \log n)$ ([48]). The idea is to first compute separately the upper and the lower hull. For each of them, only a lexicographic sorting of the points and a test whether three consecutive points make a right turn (right because we chose arbitrarily to walk around the set clockwise) are required (see Fig.VI.5). To be a little bit more specific, the points are sorted by x -coordinate, and if several points share the same x -coordinate, then they are sorted by y -coordinate: this is the lexicographic sorting (see Fig.VI.5). The construction of the upper hull starts from the point with the smaller x -coordinate and the greater y -coordinate, i.e. p_1 in the array of Fig.VI.5. We proceed then with p_3 and p_6 . If this triplet make a right turn, we can proceed with the triplet (p_3, p_6, p_7) , otherwise, we delete the middle point

and check the triplet (p_1, p_6, p_7) . The same procedure is applied for the lower hull except that now the array of sorted points is perused in the other direction (from high to low x -coordinate and with the smaller y -coordinate each time).

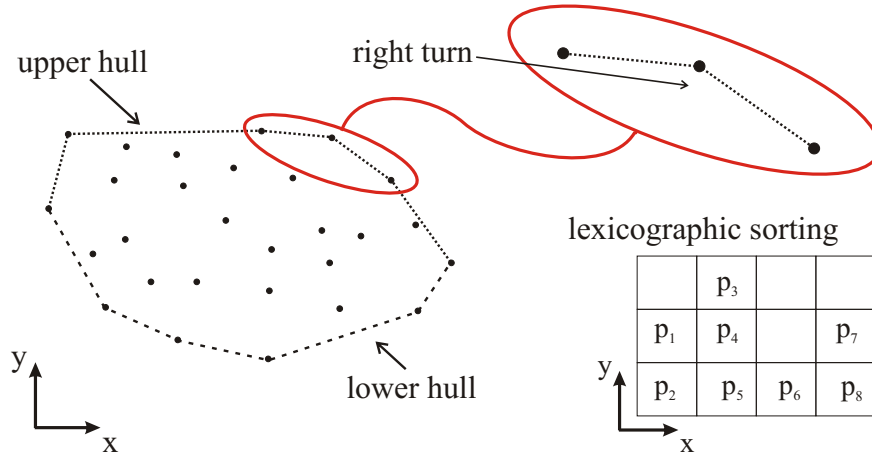


Figure VI.5: Upper and lower hulls, and fast algorithm to compute them.

We have mentioned that the triangulation is constructed inside the convex hull of the data set, which does not guarantee a constant definition of the boundaries of our area of interest (AOI). It is thus mandatory to have at each instant fixed points on which the convex hull will be constructed. The triangulation will then be computed within this fixed framework, and the interpolating surface as well. To do so, we simply make sure that the AOI is always surrounded by pixels, naturally or artificially, labeled as valid with values of IF, either imposed by a priori knowledge or computed by averaging and/or fitting the values of the AOI border. We will detail the adopted strategy for each specific experiment in the next chapter.

2.1.2 The DT and its dual graph: the Voronoi diagram

Once the convex hull of the point set is defined, facets have to be built following some criteria. It is actually desirable to build a triangulation which minimizes the size of the facets. In other words, we should obtain a triangulation where each facet is as close as possible to an equilateral triangle. Indeed, it sounds natural to expect from the triangulation-interpolation process that each interpolated point is computed by relying on the closest data. The DT actually fulfils this criterion by maximizing the smallest angle of all the triangles of the mesh, avoiding this way skinny triangles. So equivalently said, the DT generates the least stretched facets and thus best preserves the spatial resolution. A bit more formally, a DT for a set S of points in the plane is a triangulation $DT(S)$ such that

no point in S is inside the circumcircle of any triangle in $DT(S)$. The question of the DT uniqueness is interesting, and the answer is that, the DT is indeed unique for point sets containing no sets of four co-circular points. Solutions have been proposed to resolve this non-uniqueness problem ([51]), but if it is valuable in some applications, it is clearly not our case.

There is another well-known geometrical entity, worthy of interest for practical implementation of the DT: the Voronoi diagram (VD) ([13]). Given a set of points in the plane, each point - or site - is associated with a Voronoi cell, consisting of all points closer to this point than to any other one. The frontiers of those Voronoi cells are all segments of the plane equidistant to two sites and also the perpendicular bisectors of the triangles sides of the associated DT. The VD is actually the dual graph of the DT (Fig.VI.6).

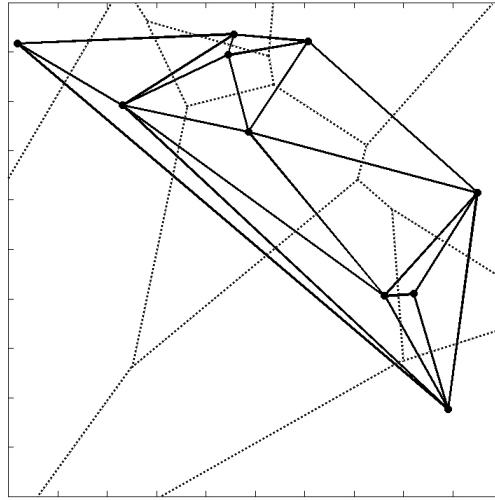


Figure VI.6: The Voronoi diagram (thin dashed lines) of a random point set (black circles), jointly shown with the DT (thick lines).

Due to this bijective relationship between DT and VD, the computation of one of them leads to the other (see [48] for a review of algorithms).

2.2 The Quickhull algorithm

There is a close relationship between planar VD and convex hulls in space. This connection between those geometrical structures led to the design of improved algorithms for fast computations of VD or equivalently DT. Let us consider, in a 2D Euclidean space, a point set randomly distributed on a line and the unit parabola (see Fig.VI.7). The tangent lines at the orthogonal projection of each point of the point set on the parabola are drawn. It can be shown ([48]), that the projection of the vertices of the upper polygonal enve-

lope of the tangent lines to the parabola on the original 1D space is actually the Voronoi diagram of the point set. The generalization of this construction to 3D is straightforward, except that now we have to deal with tangent planes.

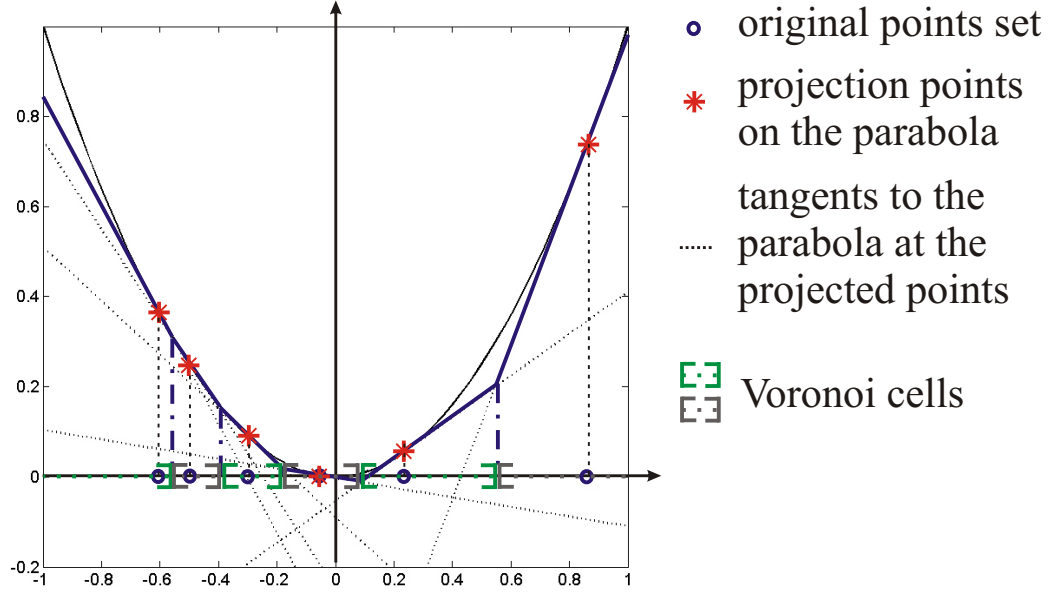


Figure VI.7: Given a set of points distributed in a 1D space embedded in a 2D Euclidean space, the VD is the projection of the upper envelope of the tangent line set.

In our case, the DT is implemented using the Quickhull algorithm [14, 147] and followed by a triangle-based cubic spline interpolation (Clough-Toucher method [11]) step to obtain the wanted uniformly sampled smooth IF frames.

3 The 3DPP procedure

3.1 Description of the method

The flow-chart of the algorithm is given in Fig.VI.8 for the dynamic cases (the procedure in the static regime is schematically shown in Fig.VI.3).

At time $k \in [1, N]$, relying on the reliability index matrix $RI[k]$, a non-uniformly sampled frame of IF values $IF^{(v)}[k]$ is built. With a convex hull properly defined, the DT is computed followed by an interpolation/resampling step, so as to obtain a smooth uniformly sampled frame of IF values $IF^{(s)}[k]$. This latter one is simply added to the phase frame

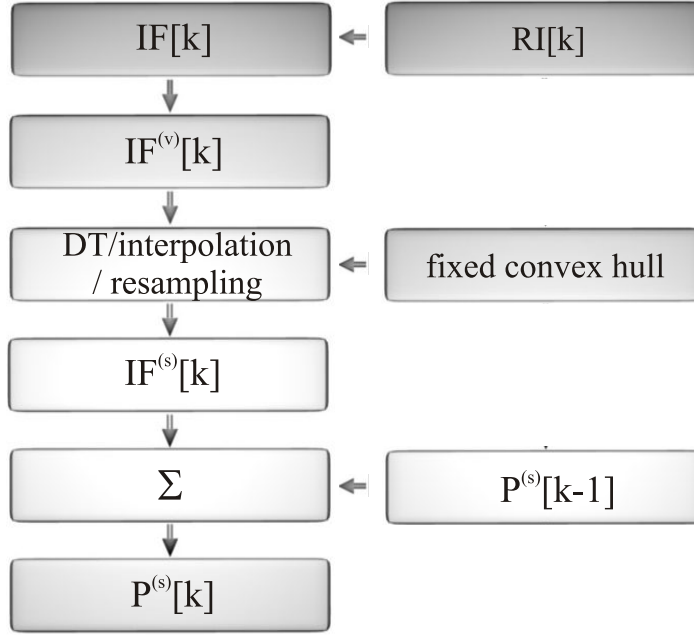


Figure VI.8: Processing scheme of the 3DPP procedure with SI signals.

obtained at time $k - 1$, $P^{(s)}[k - 1]$, to finally get $P^{(s)}[k]$. The phase map $P^{(s)}[N]$ of the total displacement is eventually obtained once the former procedure has been conducted at each instant.

3.2 Assessment of the 3DPP method

The measurement accuracy of the extracted phase will be evaluated on a well-controlled rigid-body motion (see Chapter 7). It is not straightforward to accurately quantify the spatial resolution loss, as the sampling grids are fluctuating. Indeed, at one point of the probed surface, the spatial resolution, or in other words the density of relevant pixels, changes at each frame and except for areas with almost no activity, a pixel always features enough modulation somewhere in its history to allow meaningful IF extraction. What is clear, is that at one time, the spatial resolution can be directly linked to the representative dimension of the local area. The fact that the non-uniform sampling grids are fluctuating reduces the spatial resolution loss, in the style of superresolution where a batch of images of the same scene are taken while shifted by a random fraction of pixel from one to the next to obtain a final image with a higher spatial resolution than the detector - or the individual spatial resolution of each image if some filtering has to be conducted. We will evaluate the average facet size at each point for the experiments detailed in the next chapter, and the average edge length as well.

3.3 Choice of the modulation threshold

The quality of the outcome of the 3DPP technique obviously depends on the choice of the modulation threshold used to classify the pixel signals. A too low threshold will not discard regions of pixel signals with poor modulation intensity which are prone to the highest random phase error. Of course a too high threshold will lead to a very discriminate test and the triangulation-interpolation step will rely on very few points, which induces a great loss of spatial resolution, without in addition a significant improvement of the result quality. The threshold has also to be high enough to filter out the noise of the whole imaging and acquisition chain. The very point of the 3DPP method is to discard the aberrant pixels while the spatial resolution is best preserved.

3.4 Computation load reduction with the sparse-3DPP

Even if efficient algorithms have been conceived for the whole processing scheme, a lot of data manipulations are involved and it is often valuable and appreciated by end-users to have procedures that are as fast as possible. The fewer discarded points, the heavier DT/interpolation/resampling operation. A straightforward way to reduce this load ¹ is to process only one frame every D frames. With the notations of Fig.VI.8, the scheme is slightly changed as followed:

$$P^{(s)}[Dk] = P^{(s)}[D(k-1)] + D \times IF^{(s)}[Dk] \quad (\text{VI.1})$$

3.5 Definition of convex hull with constraints

The 3DPP technique is able to address the issue of under-modulated pixels (which again are the scene of the largest phase errors) accurately and efficiently, should we define correctly the convex hull. This fixed convex hull guarantees that the same framework is used for each IF frame. It is moreover likely that we have additional knowledge on the shape and the type of deformation or displacement under study. We can take advantage of this additional *a priori* knowledge by imposing constraints within the fixed framework, defined beforehand. It is important to notice that "the convex hull with constraints" we are talking about is completely different from the constrained DT, which is not supported by the Quickhull algorithm. Adding constraints within the fixed convex hull simply means to force pixels to be valid and assign them a certain IF value, determined either by averaging, fitting or modeling. We give below an example of such a convex hull with constraints (see Fig.VI.9). This allows notably to best preserve the sharpness of edges.

¹The reduction of the 3DPP computation load only is considered here. It is thus implied that the temporal phase laws are available at each time.

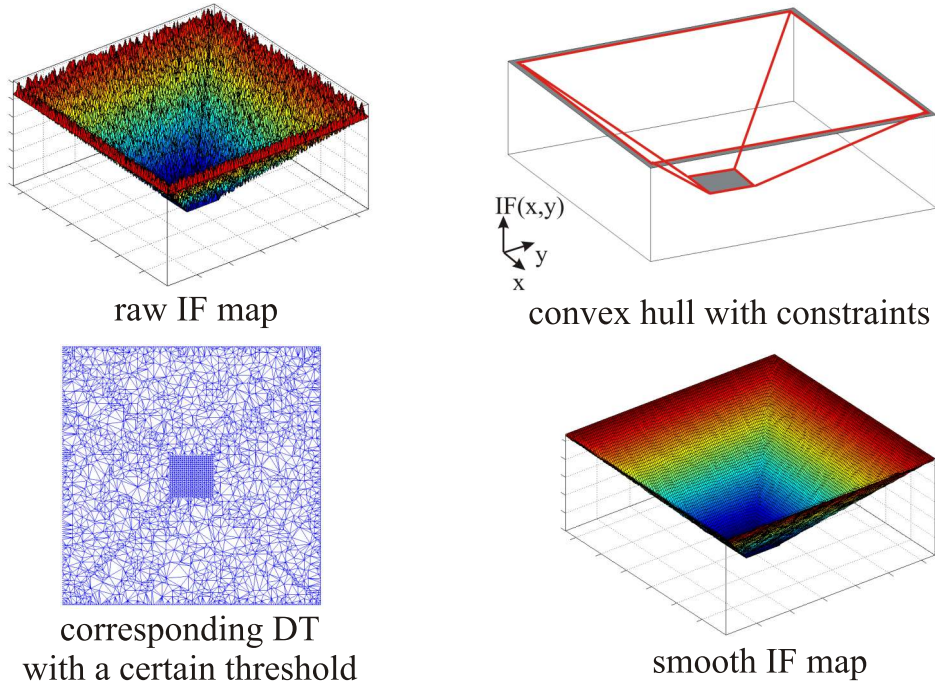


Figure VI.9: An example of convex hull with constraints to best preserve edges.

3.6 Outlook: an improved 3DPP procedure for phase discontinuities management

In the previous paragraph, we were wondering how to evaluate the spatial resolution of the 3DPP method. We mentioned the computation of the representative dimension of the facet stemming from the DT and its area at one instant of the dynamic experiment. We know that due to the fluctuations of the sampling grid, the resulting resolution loss will be less than what could have been expected from the previous considerations, as long as the motion is smooth within the whole convex hull. However, if a discontinuity is present in the image (apparition of a crack, slide between two parts or layers of a given material, and so on), the triangulation will clearly smooth out the sharpness of this discontinuity, which is not desirable. A solution would be to use constrained DT ([13]), but such geometrical construction is not supported by the Quickhull algorithm.

Another quite obvious solution would be to tile the area of interest into regions where the motion is known to be smooth and in the same manner as stitching interferometry, the phase for the whole object is obtained by gathering the results for each region. The main issues here will be to define properly the convex hull for each subregion, and to

properly connect the phases maps so as to avoid the creation of artificial steps. Efficient techniques have been developed to detect features in images - like edges - and segment images into sub-images (see e.g. anisotropic diffusion methods [113]).

Chapter VII

Application of the EMD-HT-3DPP to experimental signals

This chapter is dedicated to the experimental evaluation of our processing procedures which we designed for the characterization of mechanical behaviors in dynamic regimes. The bulk of this chapter is thus dedicated to this regime. The last section will be however dedicated to static regime and the evaluation of the novel phase map filtering technique relying on the DT. This organization has been done so as not to split the chapter into two very unbalanced parts.

1 Experimental setup

A SI setup with an in-plane sensitivity (Leendertz configuration) has been built to assess our phase extraction procedures. The object is illuminated by two divergent laser beams of equal intensity, each of them making an angle θ with the normal to the object surface (see Fig.VII.1). The light source is a CW Argon laser emitting at 514.2 nm with a maximum power of 1.5 W.

In Fig.VII.1, S_1 and S_2 designate the two unit vectors of the illumination directions, while the observation direction coincides with the object surface normal. The overall phase change between the two arms when a displacement L occurs is given by:

$$\Delta\phi = \frac{2\pi}{\lambda} (\mathbf{S}_1 - \mathbf{S}_2) \cdot \mathbf{L} = \mathcal{S} \cdot L_x , \quad (\text{VII.1})$$

where S and L_x are respectively the sensitivity of the interferometer and the projection of the motion on the x -axis. Due to its symmetry, the sensitivity is actually simply related to the physical parameters of the setup by the following relation:

$$\mathcal{S} = \frac{4\pi}{\lambda} \sin \theta \quad (\text{VII.2})$$

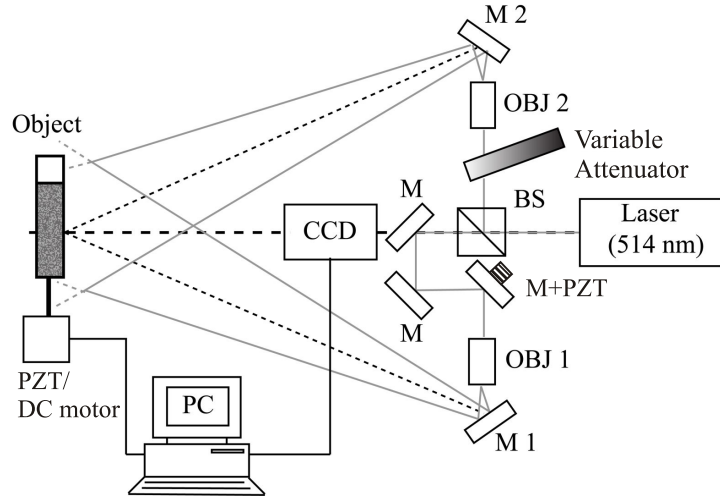


Figure VII.1: SI arrangement with in-plane sensitivity.

In our experiment, the sensitivity S is equal to $8.7 \text{ rad}/\mu\text{m}$. For off-axis points, due to the divergence of the illumination beams, the interferometer has slight sensitivity to L_y , and L_z . Those sensitivities are more than one order of magnitude lower than S , and will be thus neglected. The divergent illumination leads also to variations of the sensitivity S within the field that appear to be negligible (less than 0, 2%). The setup has been used to follow different in-plane deformations and/or rigid body motions:

- the rigid body translation of a rough piece of aluminium, achieved through the use of the DC motor,
- the in-plane rotation of a rough metallic plate of 0.25° , achieved through the use of the DC motor,
- the compression of a piece of rubber, achieved through the use of the DC motor,

The acquisition and processing chain will be described in details in the next section. The speckle fields involved in the different experiments are integrated by the CCD sensor, and the value of m (see Eq.(III.4)) is in the order of 20.

1.1 Experiment I: rigid body translation

The purpose of the experiment is the assessment of the method in terms of measurement accuracy and repeatability. We thus performed experiments with and without temporal carrier - added through the use of the mirror mounted on a PZT in one arm of the interferometer (see Fig.VII.1) - on smooth rigid body motions performed with the DC motor. The probed object is a white diffusing plate which is fixed on a ball-bearing carriage and is smoothly translating in a reproducible and well-known manner (see Fig.VII.2).

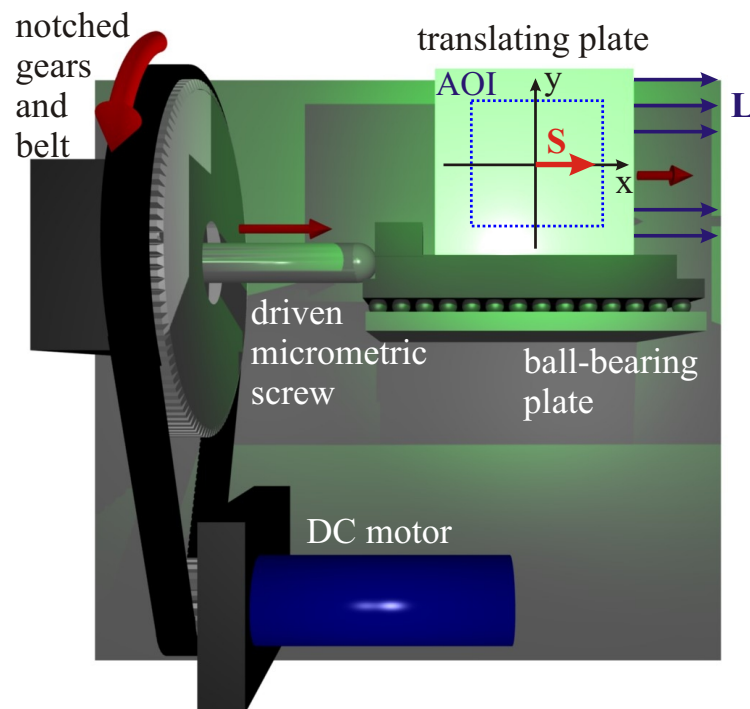


Figure VII.2: Rigid body translation of a rough metallic plate.

1.2 Experiment II: rigid body rotation

During the motion, 4640 frames are taken at a rate of $48fps$, and processed by blocks of 1024 frames with an overlapping of 120 frames between them to reduce the boundaries errors. The total rotation, equal to 0.25° , represents for the points of the higher displacement along the x -axis ($270\mu m$) twice the pixel size, i.e. the correlation length. In this experiment, we do not use an optical temporal carrier - mandatory to find out the direction of the deformation - in order to have the largest measurement bandwidth (which otherwise would have to be shared with the carrier frequency) and to assess the method with a very wide range of deformation rates. It is thus enough to process the temporal pixels of half the plate (see Fig.VII.3).

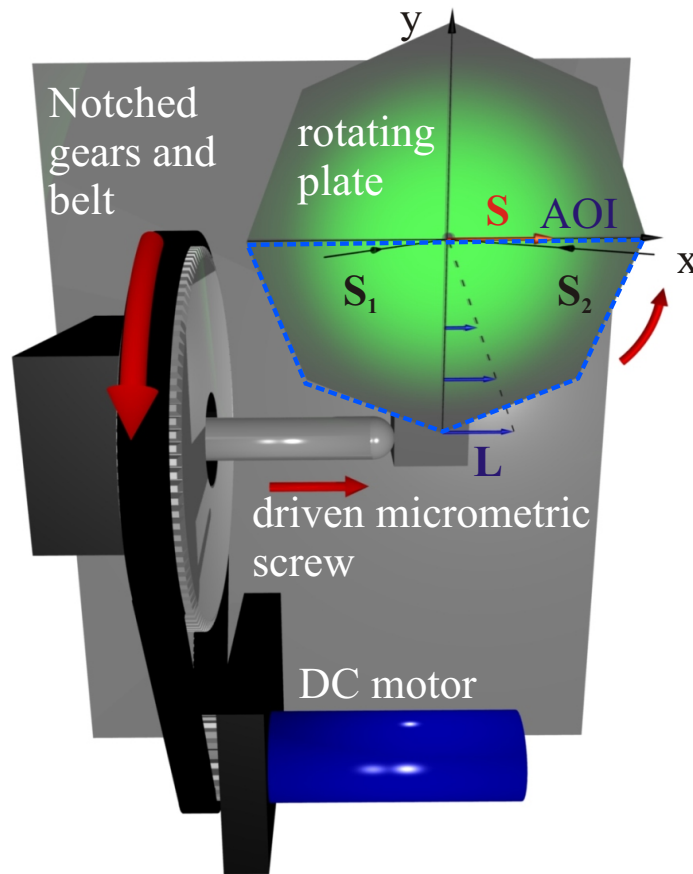


Figure VII.3: Rigid body rotation of a rough metallic plate.

1.3 Experiment III: rubber compression

During the compression, 1024 frames are saved on the computer while a smooth motion is performed by the DC motor in constant velocity mode (1500 rpm). A total displacement of $90\ \mu\text{m}$ is achieved this way.

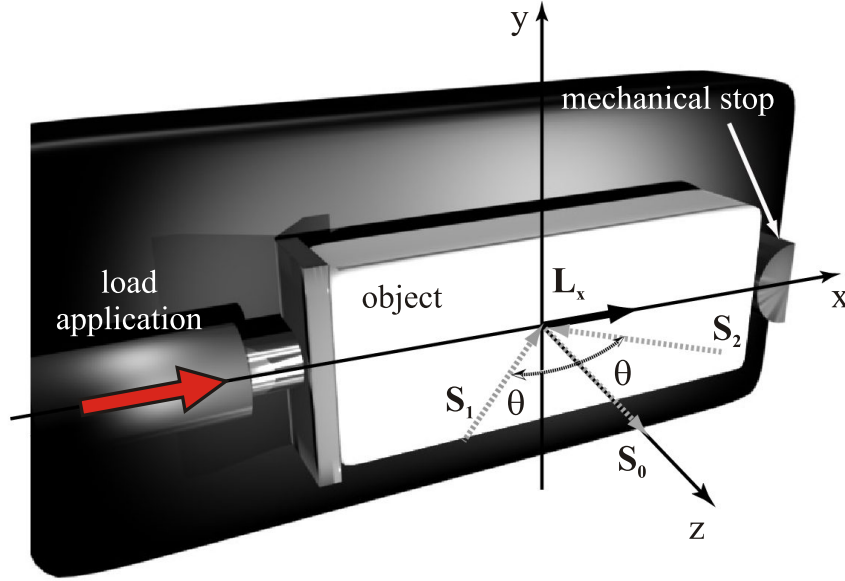


Figure VII.4: Compression of a piece of rubber.

2 Acquisition and processing chain

2.1 Acquisition system

The acquisition system is constituted by the camera, the DC motor (motor with reduction gear) and the computer for the hardware part and some softwares for recording and processing.

2.1.1 Hardware

The camera used to acquire the interferograms is the *A202k* model from Basler with CameraLink interface. The sensing array is composed by 1000×1000 pixels encoded on 10 bits, and measuring each $7.4 \times 7.4\ \mu\text{m}^2$. The maximum frame rate in full resolution is 48 frames per second, which can be speeded up by enabling the binning option. The

frame rate is this way doubled as the resolution is divided by 2 (frames of 500×1000 pixels). Our goal has always been to perform long dynamic experiments which implies large quantities of data to process, but first to record, and ensuring a constant recording rate on the HDD of our computer was thus of primary importance. Keeping all the frames in RAM and transferring them on the HDD after the motion under study is done was of course out of question as we have often to deal with several tens of GB of data. We thus opted for a computer with HDD in RAID configuration able to maintain a recording rate higher than 100 MB per second. The bay is also able to control a high-voltage power supply to actuate the PZT device for temporal carrier generation, the whole thing being of course synchronized with the camera internal shutter. The assessment of our processing schemes requires reproducible and well-controlled motions, which is not possible with PZT actuators for two reasons. Depending on the voltage profile applied to the PZT, the total range may vary (hysteresis effect when moving back and forth, and possible locking effect ¹). In addition, the total available range of displacement is in the order of few tens of microns rather than hundreds of microns as wished. We thus chose to use a DC motor with notched gears and belt. The ensemble is shown in Fig.VII.5 with the corresponding reducing ratio of the gears.

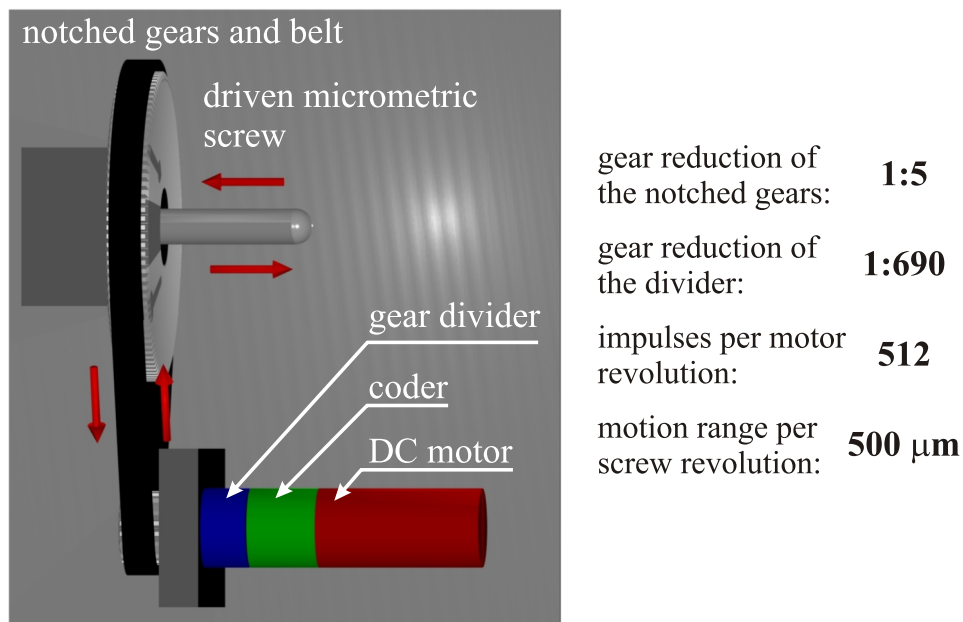


Figure VII.5: DC motor with reducer and coder.

¹The displacement of the outer face of a PZT stack depends strongly on the slope of the command voltage.

2.1.2 Acquisition software

The acquisition software, realized on a Labview platform and tailored for our application, has been delivered with the system. The main features of this software are the following:

- calibration of the PZT actuator used for the temporal carrier generation,
- continuous acquisition with the possibility to visualize the correlation fringes in real-time and also to follow the temporal behavior of two pixels whose emplacement can be chosen,
- cyclic acquisition for experiments with a carrier, with the same possibilities as for the continuous mode.

The frames are recorded in TIF format. The software architecture is schematically shown in Fig.VII.6.

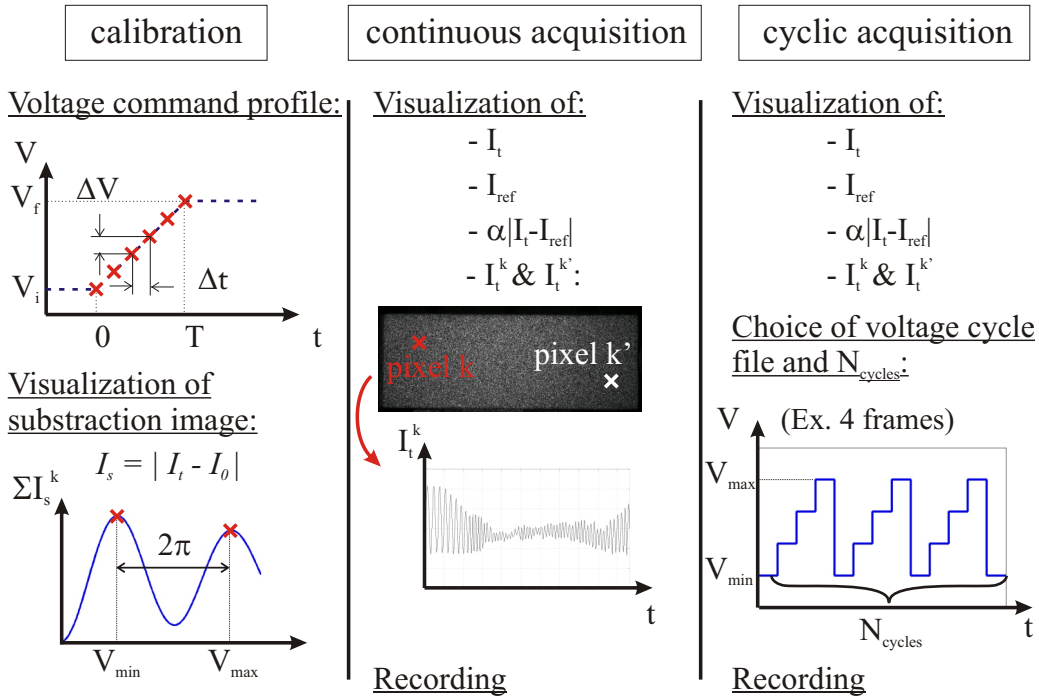


Figure VII.6: The acquisition software architecture.

2.2 Processing scheme

The processing routines are implemented under MATLAB and LABVIEW and the whole processing procedure is schematically shown in Fig.VII.7.

Once the SI raw frames are recorded on the computer, the data are reshaped in stacks

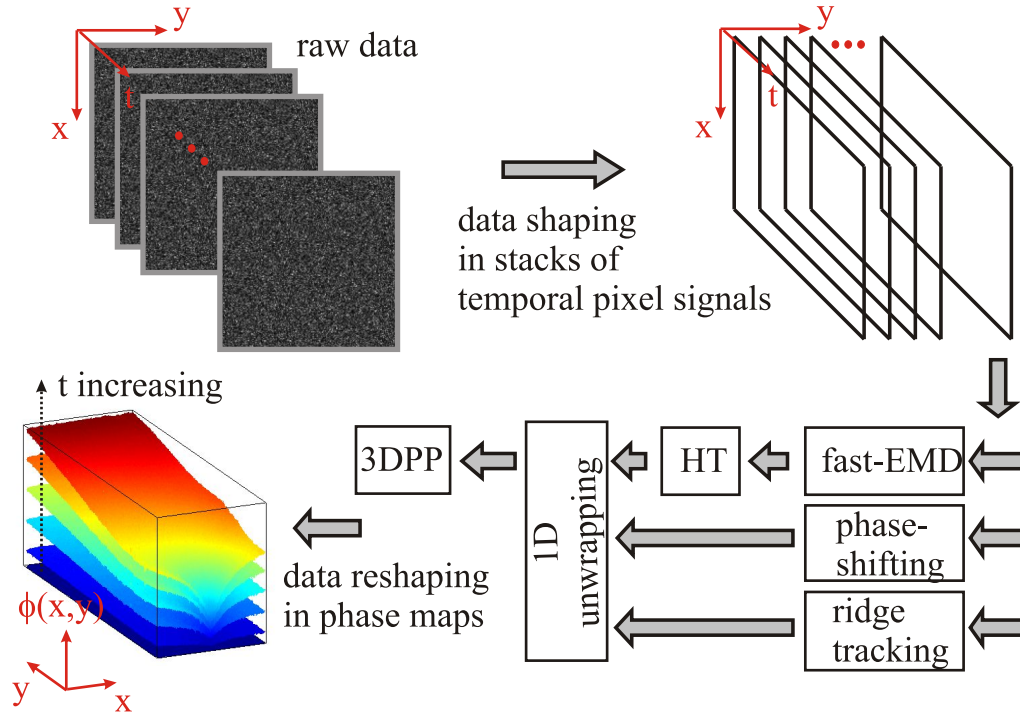


Figure VII.7: Flowchart of the processing schemes assessed on data experimentally obtained.

of temporal signals. This way of reshaping the data allows to reduce the computation load of this operation by a factor of ten. It also minimizes the reading/writing operations on the HDD during the processing tasks and thus greatly lightens the computation burden again. The so-built raw stacks are then processed in four manners:

- i) fast implementation of EMD followed by phase extraction with the HT and 1D-phase unwrapping ([54]),
- ii) same operation as previously but enhanced by the 3DPP procedure ([55]),
- iii) Morlet wavelet ridge tracking algorithm followed by 1D-phase unwrapping ([39]),
- iv) five-frames dynamic phase-shifting algorithm followed by 1D-phase unwrapping ([40]).

It is important to precise that a further improvement of the ridge tracking algorithm has been made in [39]. It consisted in considering a fixed window of $N \times N$ (originally 3×3) pixels to which a weight, depending on the squared modulation value, is assigned. This way, if the ridge tracking algorithm fails, a relevant IF value can be assigned to the pixel by inspecting its neighbors within the $N \times N$ window. This improvement has not been implemented and considered in the forthcoming discussions.

3 Results and discussion

3.1 Experiment I: rigid body translation

As mentioned earlier, we use this basic experiment to fully characterize our processing scheme. We thus perform different kinds of motion with and without temporal carrier, to evaluate the absolute accuracy and the robustness to full decorrelation when the motion covers distances larger than the correlation length.

3.1.1 Accurate computation of the temporal carrier frequency

Without any displacement, 1024 images (128 cycles of 8 frames) are recorded. The phase is computed simply through the use of the HT without any subsequent filtering and the frequency carrier is simply computed by a classical least-square method applied on 100×100 temporal pixel signals. We obtained a distribution whose mean value and standard deviation are given below:

$$f_{carrier} = 0.788 \pm 0.01 \quad \text{instead of } \frac{2\pi}{8} = 0.785, \quad (\text{VII.3})$$

which means an error less than half a percent from the wanted frequency tuned after the PZT calibration step.

3.1.2 Phase extraction and discussion of the results

The DC motor is enabled in the profile position mode, and a motion with constant velocity is performed over a distance of $9\mu m$. The input velocity profile and the associated displacement profile are shown in Fig.VII.8.

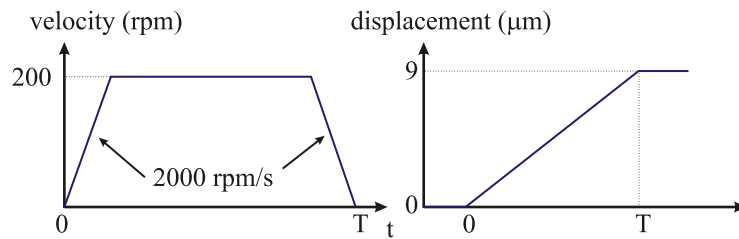


Figure VII.8: Input velocity profile and displacement profile for the experiment with a carrier at $2\pi/8$.

3.1.2.1 Result of EMD + HT: The final phase map is jointly shown with phase maps at intermediate states in Fig.VII.9.

The raw phase maps are highly polluted by salt and pepper noise, and the median filter

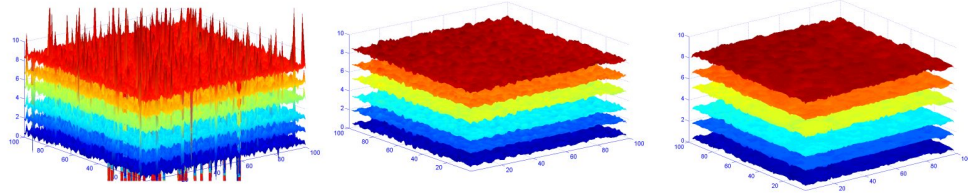


Figure VII.9: Result from the fast EMD followed by the HT based phase extraction method (left). Raw phase maps filtered with a median filter with a box kernel of size 3×3 (middle) and 5×5 (right). The displacement maps are given in microns.

is well-known to be efficient in such situation. The raw phase maps filtered by median filter with 3×3 and 5×5 box kernels are also presented in Fig.VII.9. The temporal evolution of the phase on a good pixel and an aberrant one are shown in Fig.VII.10, jointly with the original interferometric signal and the outcome of the EMD.

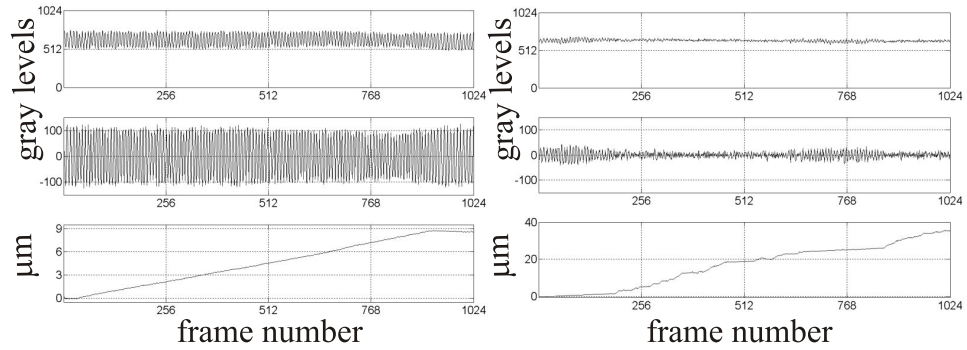


Figure VII.10: Result from the fast-EMD followed by the HT-base phase extraction method. The result for a well-modulated pixel is shown (left), and for an under-modulated pixel as well (right).

We can note that there is a little discrepancy between the performed motion and the expected linear one. Despite the PID feedback with optimized parameters, the motor speed is not perfectly constant. This has however no impact on the measure and the processing. The expected displacement is $9\mu m$ and the obtained value from this processing is in average of $9.25\mu m$. This value is actually biased by the errors generated by the under-modulated pixels. The maximum likelihood value (taken as the maximum of the probability density function of the displacement map) is closer to the expected value with

8.90 μm . The standard deviation of the displacement map is equal to 4.64 μm . This result will be compared and discussed later.

3.1.2.2 Result of 3DPP: We now come to the results from the 3DPP method with different threshold values (see Fig.VII.12 for threshold values ranging from 10 gray levels up to 450 gray levels). The imposed convex hull is constituted by the border pixels, which have been assigned as IF value, the average IF value of the pixels considered as reliable (see Fig.VII.11). The average displacement and the maximum likelihood displacement are also given for each threshold value.

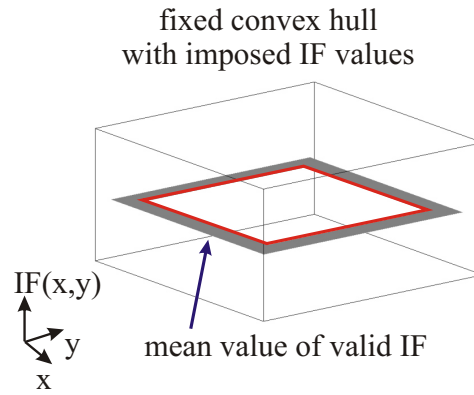


Figure VII.11: Fixed convex hull for the rigid body translation experiment.

The DT, as detailed in the previous chapter, has to be computed at each instant, and we show in Fig.VII.13, the DT of the scattered data at one instant of the motion. The percentage of valid points, the facet area map (given in pixel^2), and the edge length map (given in pixel), with average values, are given for the threshold values of 10, 100, 200 and 450 gray levels.

Where the triangulation yields large facets, the spatial resolution is consequently degraded. A trade-off has thus to be found between noise removal and spatial resolution conservation. For the threshold value of 10 gray levels, we discard only few pixels and the triangles areas are mainly equal to 0.5 pixel^2 . However, it is not straightforward to accurately quantify the spatial resolution loss, as the grids are fluctuating. Indeed, at one point of the probed surface, the spatial resolution, or in other words the density of relevant pixels, changes at each frame and a pixel always features enough modulation somewhere in its history to allow meaningful IF extraction.

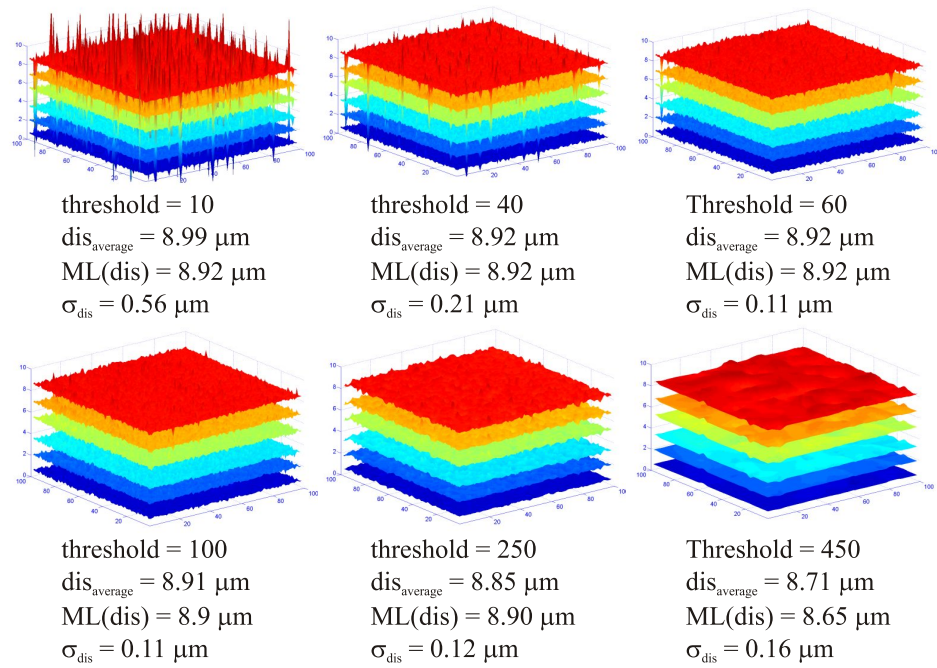


Figure VII.12: Outcome of the 3DPP procedure with different thresholds values. The average displacement and the maximum likelihood displacement are also given. The displacement maps are given in microns.

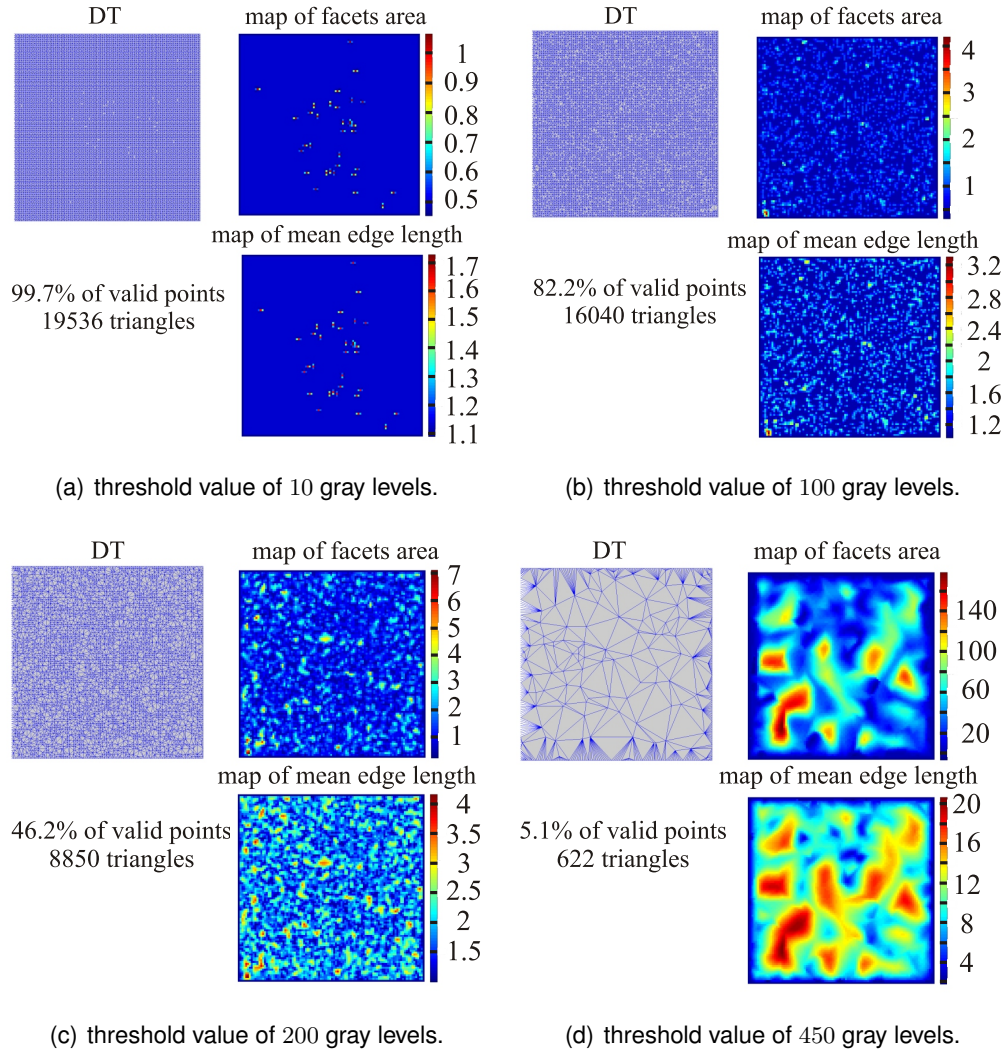


Figure VII.13: DT of the nonuniform sampling grids at one instant of the motion.

So as to connect the threshold value with a physical quantity of the experiment, we compute the modulation histogram for the whole data set acquired for the frequency carrier computation and obtain the curve shown in Fig.VII.14. The curve of the proportion of pixels with a higher modulation than a certain value is jointly shown in Fig.VII.14. As an example, the probability to find a pixel with a modulation of 100 gray levels is 0.85 times the maximum likelihood, whereas 82.4% of the pixels have a modulation higher than 100 gray levels. The thresholds of 10, 40, 60, 100, 250 and 450 gray levels are highlighted by dashed lines with the corresponding values.

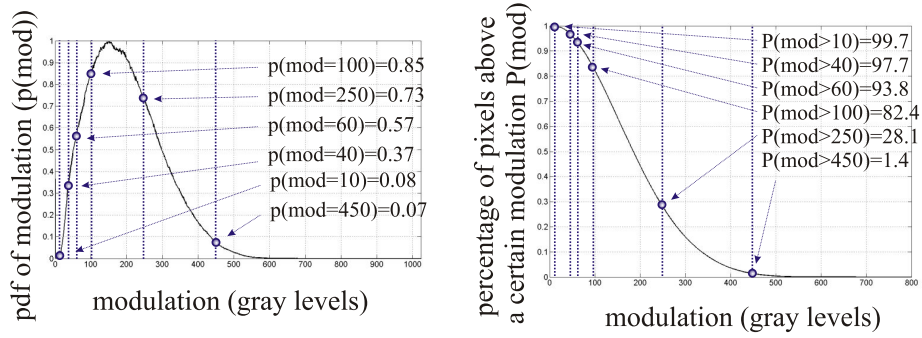


Figure VII.14: Probability density function of the modulation intensity with the threshold values highlighted.

Those results teach us different things. There is first of all, a clear - and expected - improvement of the results whereas the threshold value is increasing, from 10 to 100 gray levels. Beyond those values, we have clearly a bias in the method, as the facets become larger and larger. The main reason of this trend reversal is probably due to the cubic interpolation. The large facets lead indeed to large - though smooth - peaks and valleys in the phase map, which are totally artificial and produce not only a bias in the final result but also increase the standard deviation. Interestingly, the trend reversal seems to be around the most likely modulation value, around 150 gray levels.

3.1.2.3 Discussion: In order to compare the results obtained so far, we use the wavelet ridge extraction algorithm ([35, 39]) and we implement also a five frames dynamic phase-shifting algorithm, as presented in [40], where the phase-shift amount $\delta\phi$ is recomputed at each instant in order to take into account the phase-shift induced by the motion. There are several manners to include the refining computation step of $\delta\phi$ along time, and we adopted the one which is proven to be robust for a phase-shift amount around $\pi/2$ ([39]). As the frequency carrier is equal to $2\pi/8$, the phase at time k is simply given by Eq.(VII.4).

$$\begin{aligned}\hat{\Phi}(k) &= \arctan\left[2 \frac{I(k+2)-I(k-2)}{I(k+4)+I(k-4)-2I(k)} \sin(\delta\phi)\right] \\ \cos(\delta\phi) &= \frac{1}{2} \frac{I(k+4)-I(k-4)}{I(k+2)-I(k-2)}\end{aligned}\quad (\text{VII.4})$$

The final phase map is jointly shown with phase maps at intermediate states in Fig.VII.15.

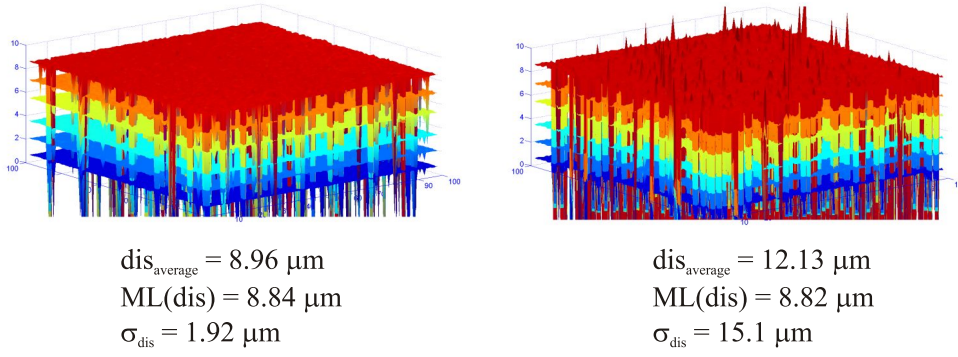


Figure VII.15: Result from the five-frame algorithm (left) and from the ridge extraction algorithm (right). The displacement maps are given in microns.

As for the results from the 3DPP procedure, the average and the maximum likelihood displacements are given while the standard deviation of the final phase map is also given for the two methods. The values of the average displacement and the standard deviation of the final phase map are highly biased by the salt and pepper noise of the phase map, and the right value to take into account is the maximum likelihood (ML) value. Those latter displacement values are nonetheless also a bit shifted from the results obtained with the analytic method and with the 3DPP technique. Despite its great smoothing ability, the ridge extraction algorithm fails to track the ridge in low-SNR areas and does not converge. An iterations counter must thus be added so as to exit the loop and produce a result, generally of poor reliability. The histograms of the total displacement map are given in Fig.VII.16 for the EMD/HT method, the EMD/HT/3DPP method (with a threshold value of 100 gray levels), the five-frame algorithm and the ridge extraction algorithm.

We present in Fig.VII.17, the temporal evolution of the phase on a good pixel and an aberrant one, jointly with the original interferometric signal and the outcome of the EMD, for the four methods compared in this paragraph.

We summarize the obtained results for the rigid body translation motion in Table VII.1.

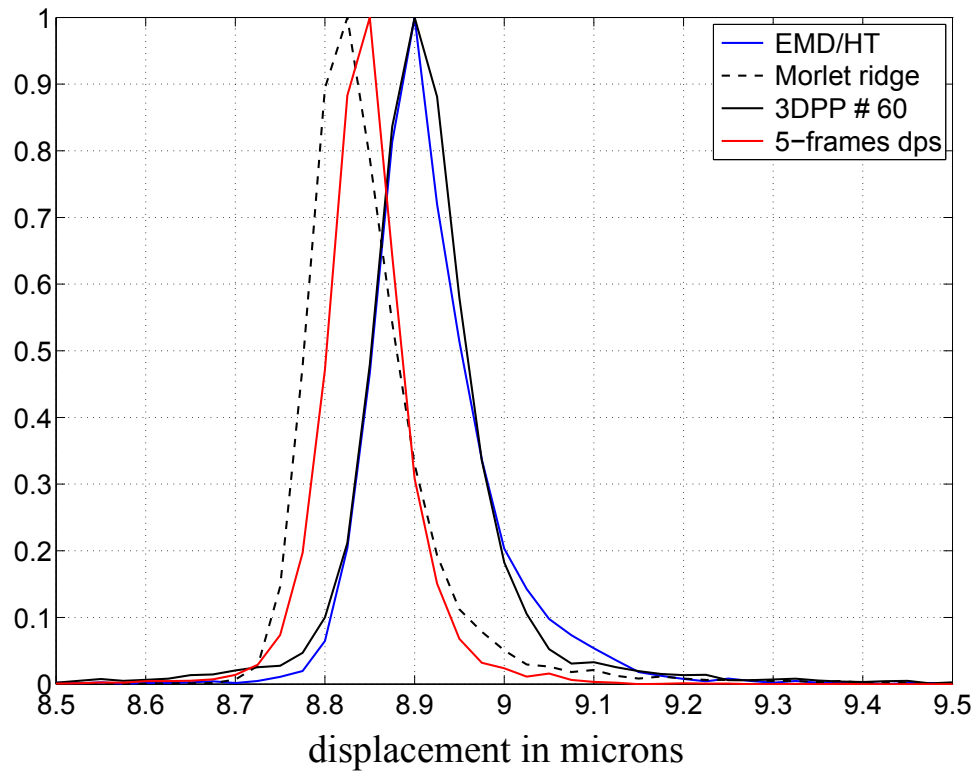
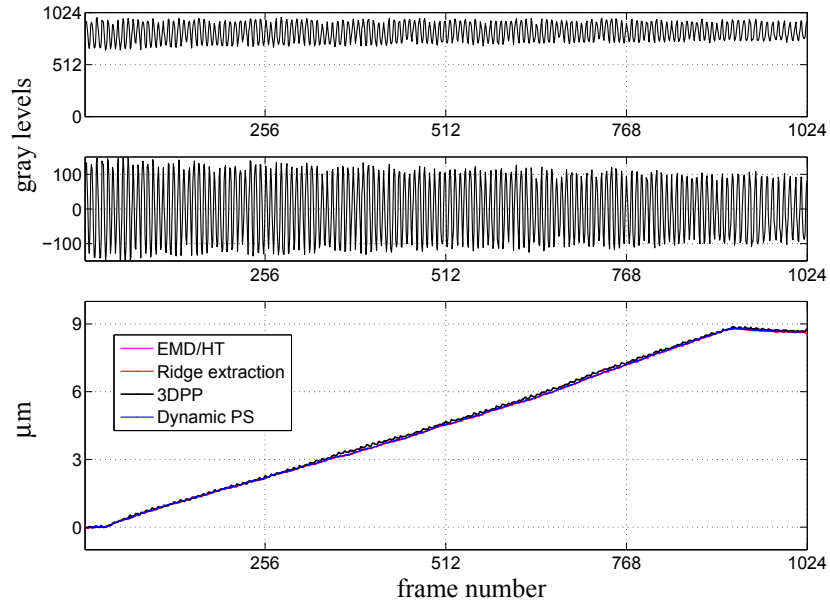


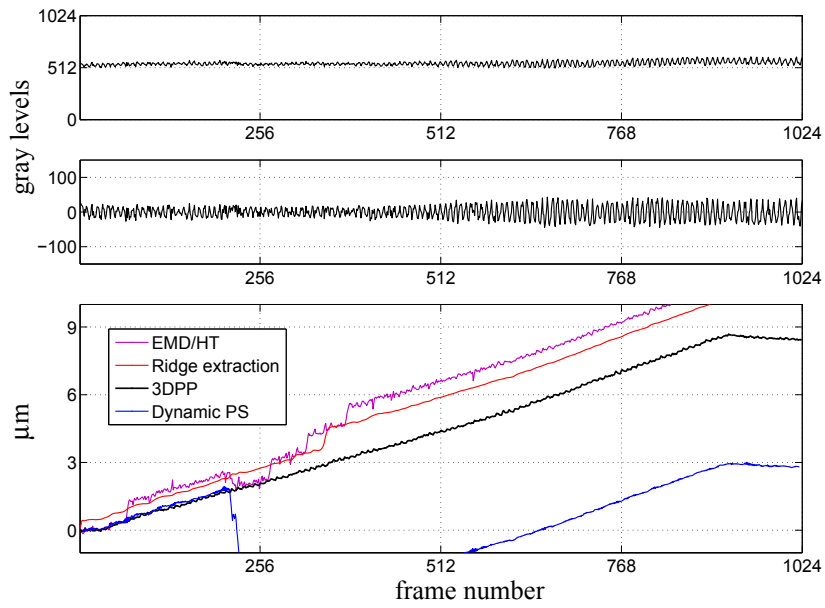
Figure VII.16: Normalized histograms of the displacement maps obtained with the different methods.

Table VII.1: maximum displacement obtained during a batch of 1024 frames grabbed at 48fps rate for the translation motion.

Method	HT	Ridge	Dyn. PS	3DPP#60
Average displacement (μm)	9.25	12.13	8.96	8.92
ML displacement (μm)	8.90	8.82	8.84	8.92
Standard deviation (μm)	4.64	15.1	1.92	0.11



(a) Comparison of temporal phase history for a well-modulated pixel.



(b) Comparison of temporal phase history for an under-modulated pixel.

Figure VII.17: Temporal evolution of the phase for a well-modulated pixel, and for an under-modulated pixel as well.

3.2 Experiment II: rigid body rotation

3.2.1 Result of EMD + HT

As already explained, so as to assess the method with a large range of deformation rates, we did not introduce a temporal carrier for this basic experiment and it is thus sufficient to process the pixels of half the plate. We present first the results for the phase map representing the total displacement, which we additionally process with a classical median filter with different kernel sizes (see Fig.VII.19). We first show the subtraction fringe at intermediate instants of the displacement and at the term of the motion in Fig.VII.18.

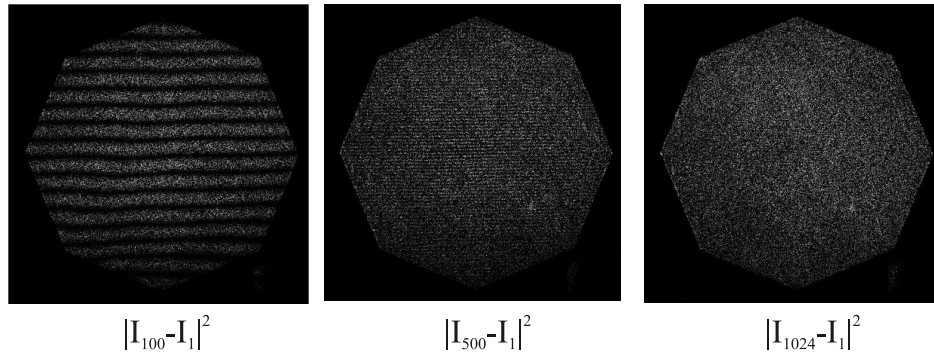


Figure VII.18: Correlation fringe between different couples of grabbed frames.

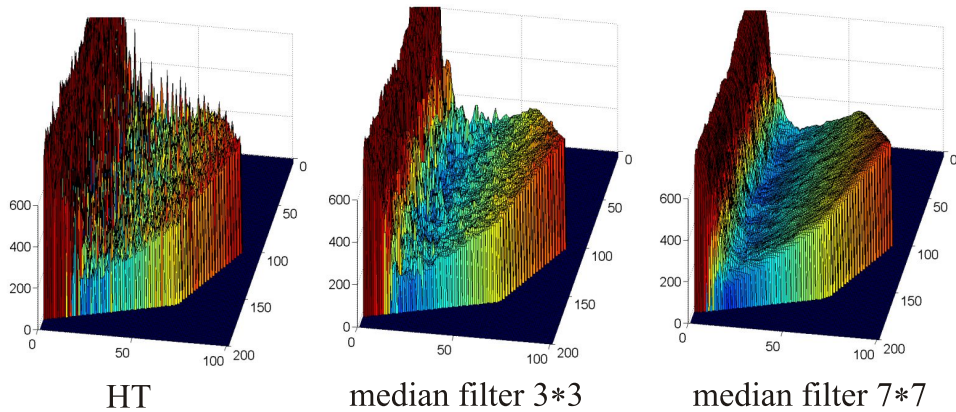


Figure VII.19: Phase map of displacement, carried out after 1024 frames grabbed at $48fps$ rate, resulting from the fast-EMD/HT procedure, with from left to right, no subsequent filtering, filtering by a median filter with a 3×3 box kernel, and filtering by a median filter with a 7×7 box kernel.

The phase computed through the use of the fast EMD followed by the analytic method is very noisy and very quickly unexploitable for pixels experiencing less and less fringes of displacement (toward the central part of the plate). This area is denoted as the blindness area as the algorithm does not allow measuring accurately what happens inside. There are actually two main cases to distinguish: the case where there are few fringes of displacement and the case where there is almost none. The latter one corresponds to the very central part of the metal plate and cannot be solved without a temporal carrier. When there is very low activity during the pixel history, the presence of noise and the sparsity of fringe *extrema* make the *extrema* finding step very inaccurate. The outcome of the EMD algorithm contains then long areas of only noise. Applying the analytic method to such signals leads to a result where the useful phase information is overwhelmed by large and meaningless phase values. In those areas, a large proportion of pixels are declared as invalid and the median filter clearly fails to filter out this salt noise, whichever is the kernel size - especially toward the center of the plate - with an additional spoiling of the boundaries sharpness.

3.2.2 Result of 3DPP

We present now the result of the 3DPP procedure in Fig.VII.21 with three different thresholds. The imposed convex hull has been defined as shown in Fig.VII.20, whereas the imposed IF values have been attributed from a theoretical IF plane. We have represented also the case where an additional constraint of null IF is imposed in the center of the metal plate.

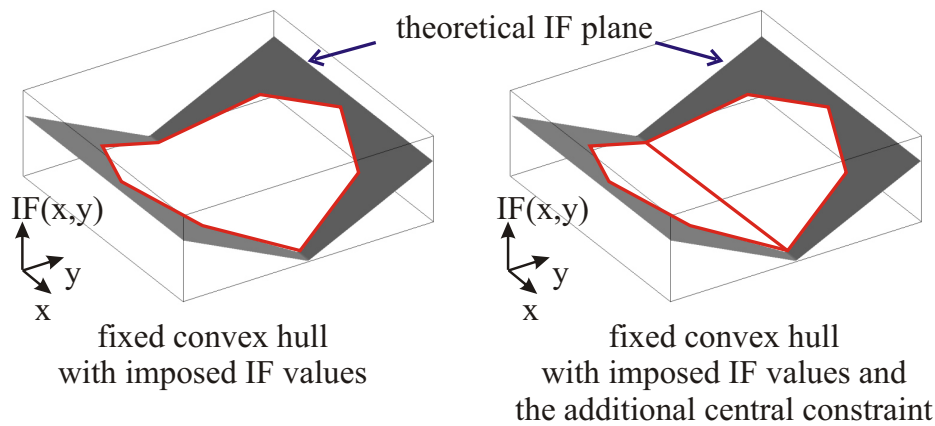


Figure VII.20: Definition of the imposed convex hull for the rigid body rotation experiment.

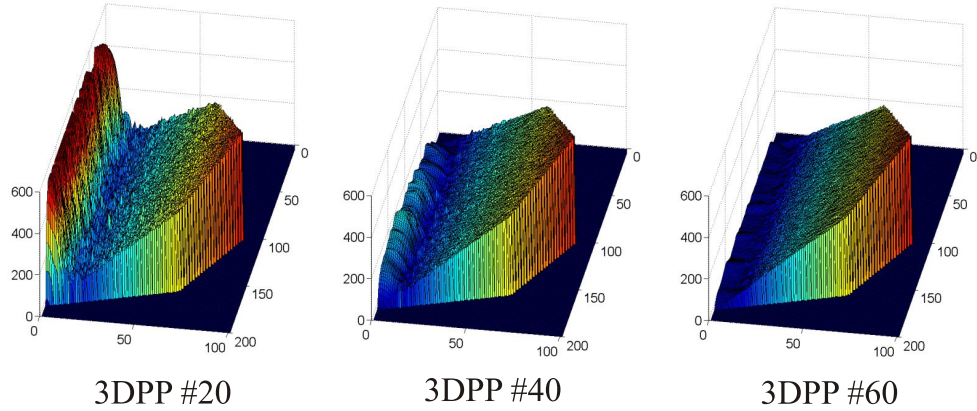


Figure VII.21: Phase map of displacement, carried out after 1024 frames grabbed at 48fps rate, resulting from the 3DPP procedure with a threshold of 20, 40 and 60 gray levels (from left to right).

The benefit of the 3DPP technique is obvious and greatly extends the measurement bandwidth.

3.2.3 Discussion

In the same manner as for the rigid body translation, we compare our results with the ones obtained with the ridge extraction algorithm. We actually compare the results for one of the five batches of data and for the total displacement, to see the influence of full decorrelation. Due to the lack of temporal carrier, the five-frame dynamic phase-shifting algorithm would need to be adapted with respect to the local IF. The motion is supposed to be smooth, and thus, the algorithm would simply need to be adjusted for each pixel in this case - in fact as the motion is a pure rigid body translation, the algorithm would simply necessitate to be adapted for each row of pixels, or even for group of rows, in the direction of the interferometer sensitivity vector. The local IF used to tailor the dynamic phase-shifting algorithm could perfectly be the estimation provided by the *extrema* method. We chose nonetheless to discard this method to only compare our procedures with the ridge tracking algorithm.

Despite the feedback loop of the motor, the motor velocity experienced some fluctuations, and it is thus difficult to evaluate with a high accuracy the total displacement. We have nonetheless estimated it to be around $270\text{ }\mu\text{m}$.

We now compare the phase maps for one batch of 1024 frames, during which the displacement is equal to about $59\text{ }\mu\text{m}$. We present below the final phase map after this displacement with the associated maximum displacement for the *extrema* method, the HT-based method, the dynamic phase-shifting method, the ridge tracking method and

finally the 3DPP method with a threshold equal to 20, 40 and 60 gray levels, recalled here for comparison purposes (see Table VII.2 and Fig.VII.22).

Table VII.2: Maximum displacement obtained during a batch of 1024 frames grabbed at $48fps$ rate.

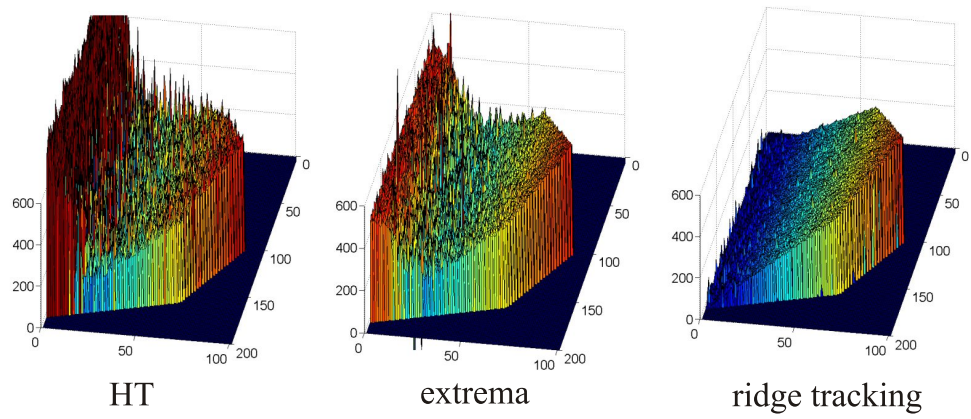
Method	Extrema	HT	Ridge	3DPP#20	3DPP#40	3DPP#60
Displacement (μm)	60.14	58.22	57.17	58.25	58.22	58.40

Not surprisingly, the phase map coming from the analytical method is severely polluted by salt noise. The blindness area is highly reduced by the 3DPP procedure. The ridge extraction algorithm performs very well also. The cross-sections of the different phase maps are compared in Fig.VII.23.

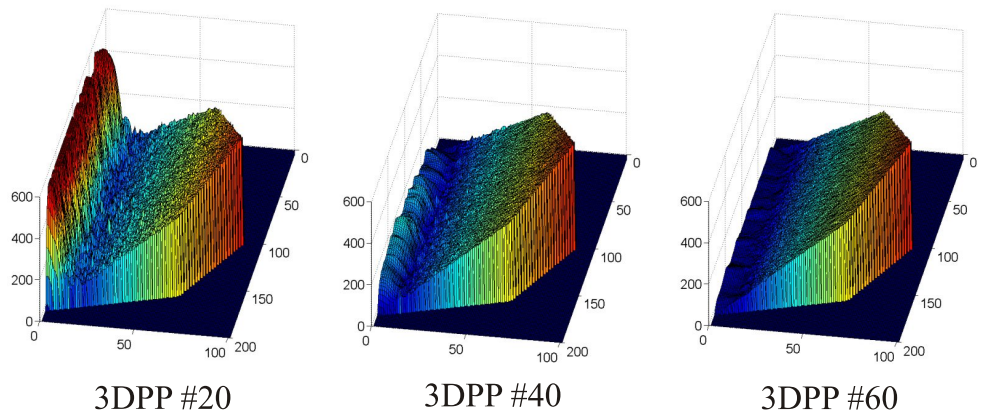
We finally show the discrepancy of the obtained phase maps with the theoretical phase plane in Fig.VII.24, where the scales of colors are given in each case in μm .

An additional knowledge about the motion has not been exploited so far: this is the fact that the phase must be exactly null in the center of the metal plate (see Fig.VII.20). We thus add this constraint in the definition of the convex hull and the so-obtained results, for a threshold value of 40 and 60 gray levels, are shown in Fig.VII.25, where the result from the ridge tracking algorithm is recalled for comparison purposes. The cross-sections of the different phase maps are compared in Fig.VII.26.

We finally show the discrepancy of the obtained phase maps, with this additional central constraint with the theoretical phase plane in Fig.VII.27, where the scales of colors are still given in each case in μm . The maximum phase difference between the theoretical phase plane and the phase map obtained with this additional constraint has been reduced by roughly a factor of two.



(a) Phase map of displacement, carried out after 1024 frames grabbed at 48fps rate, resulting from the HT-based, the *extrema* and the ridge tracking methods (from left to right).



(b) Phase map of displacement, carried out after 1024 frames grabbed at 48fps rate, resulting from the 3DPP procedure with a threshold of 20, 40 and 60 gray levels (from left to right).

Figure VII.22

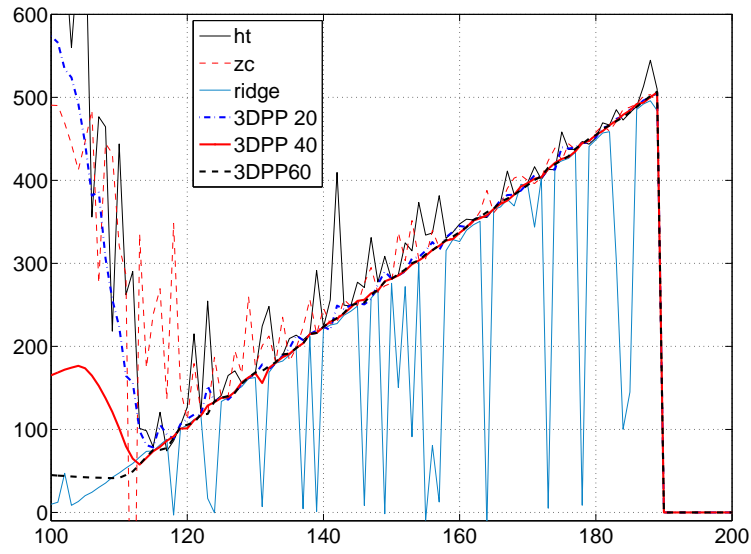


Figure VII.23: Cross-section of the phase maps given in Fig.VII.22.

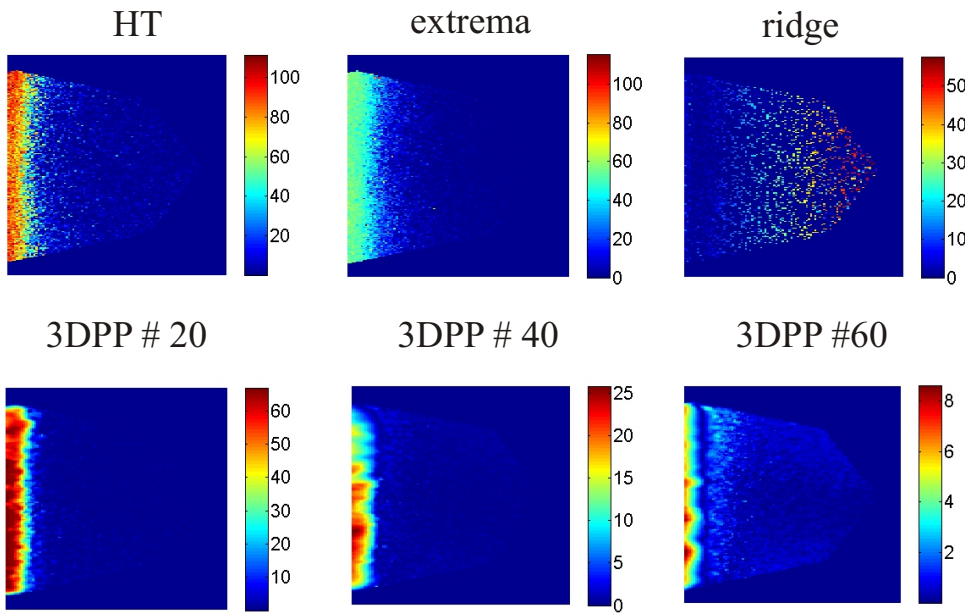


Figure VII.24: Discrepancy from the theoretical displacement plane for the different methods shown in Fig.VII.22. The color bars are given in microns.

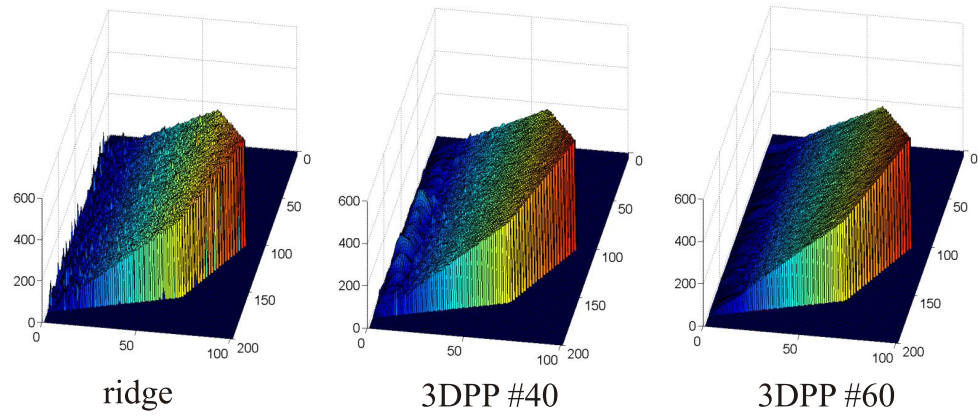


Figure VII.25: Phase map resulting from the 3DPP algorithm with the additional central constraint.

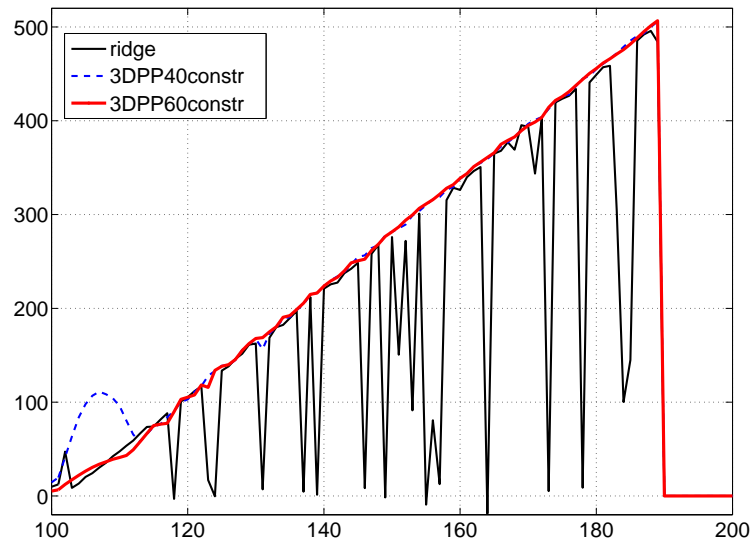


Figure VII.26: Cross-section of the phase maps given in Fig.VII.25.

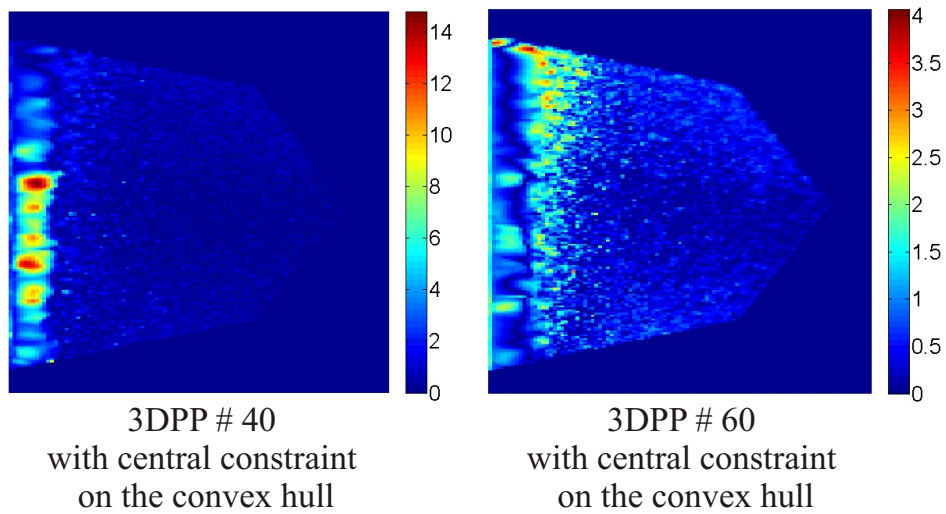
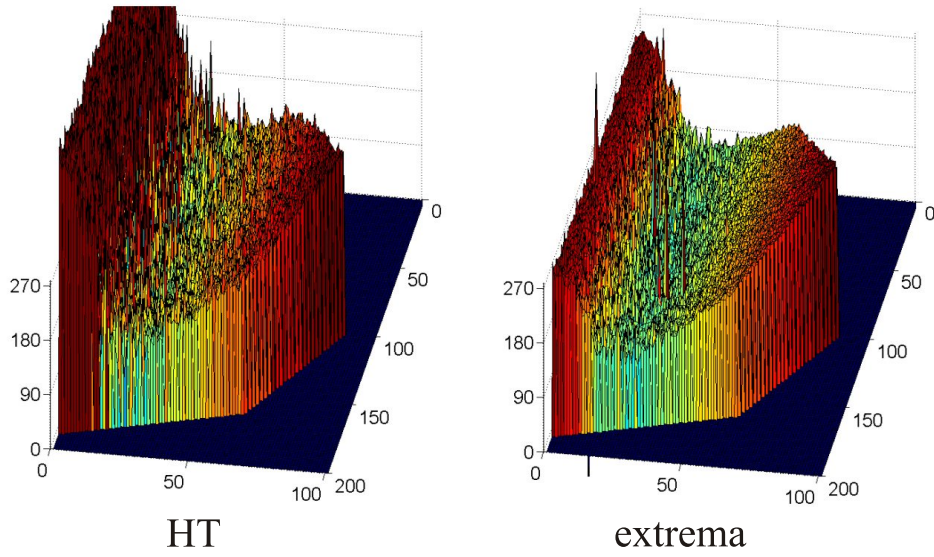


Figure VII.27: Reduction of the discrepancy from the theoretical displacement plane by the additional central constraint. Those results are to be compared with those shown in Fig.VII.24. The color bars are given in microns.

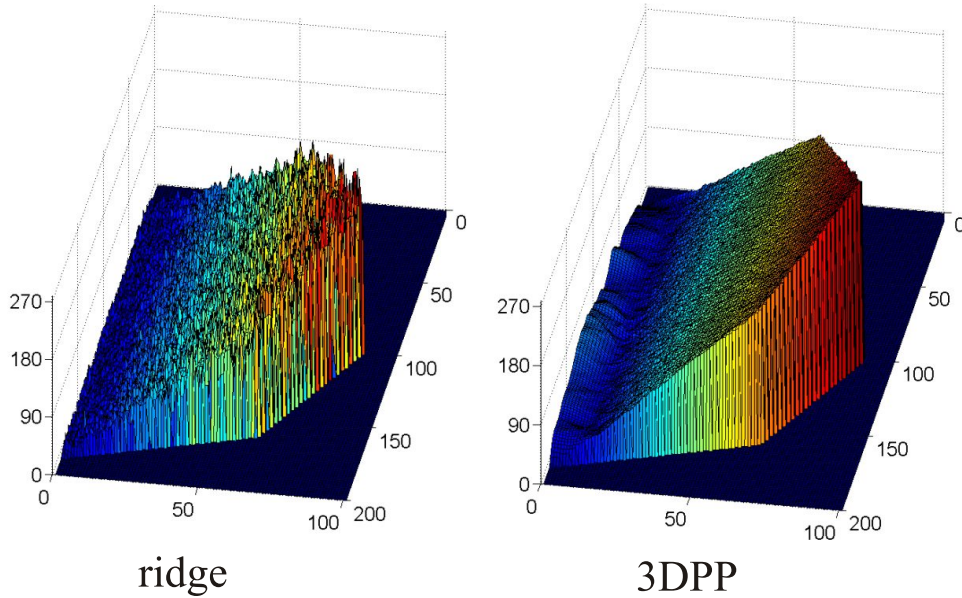
3.2.4 Results for the total displacement

The phase maps for the total displacement of $270\ \mu m$ are shown in Fig.VII.28, with the cross-sections in Fig.VII.29.

We can observe that the ridge extraction algorithm does not perform well everywhere. It is due to the choice of the mother wavelet frequency. A low value for ω_o (see section 2.1.3 in chapter 4) will lead to narrow temporal analysis windows and thus provide a fine temporal resolution, but a poor frequency resolution. In this specific experiment, pixels experience very different deformation rates (the IF ranges from 0 to typically $2\pi/8$). To avoid interference with the DC term, a value of ω_o of 2π or more should be chosen. However, we observed that the higher the mother wavelet frequency, the more sensitive the algorithm to the initial scale value. As a trade-off between ridge sharpness (and thus noise rejection power) and tracking convergence, we chose $\omega_o = \pi$. Not surprisingly, the largest errors are made with the analytic method, due to its bad behavior with noisy signals. The 3DPP procedure allows nonetheless to recover a smooth and accurate phase map.



(a) Phase maps after the total displacement of $270\ \mu m$ obtained with the analytic method and the *extrema* method.



(b) Phase maps after the total displacement of $270\ \mu m$ obtained with the wavelet ridge tracking algorithm and the 3DPP method with a threshold value of 40 gray levels.

Figure VII.28: Phase map of total displacement, carried out after 4640 frames grabbed at $48fps$ rate, resulting from the HT-based, the *extrema*, the ridge tracking and the 3DPP methods.

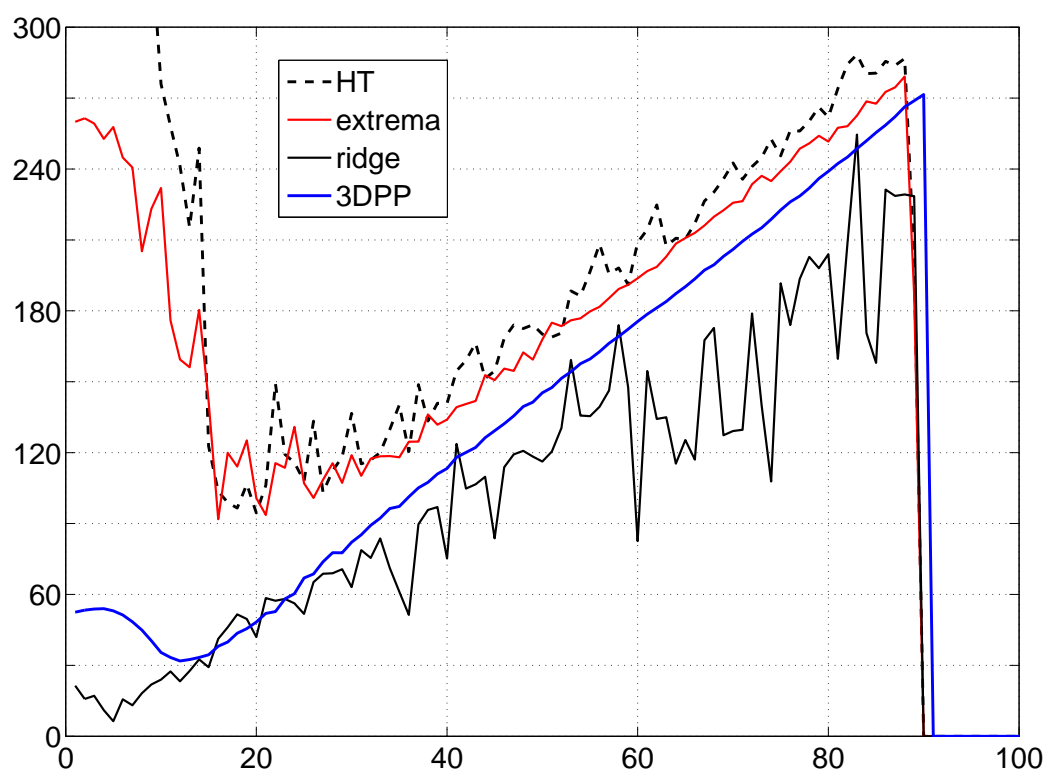


Figure VII.29: Cross-section of the phase maps given in Fig.VII.28.

3.3 Experiment III: rubber compression

We show now the results for the in-plane compression of a piece of rubber with two different mechanical stop shapes. The idea is actually to observe the behavior of the method, and more specifically its real impact on the spatial resolution, when high gradients of deformation are involved. It will be also the opportunity to assess the impact of the sparse 3DPP on the final result. Examples of correlation fringes in the two cases are shown in Fig.VII.30. Once again, it appears clearly that the fringe visibility quickly disappears, illustrating speckle decorrelation mainly induced here by structural change.

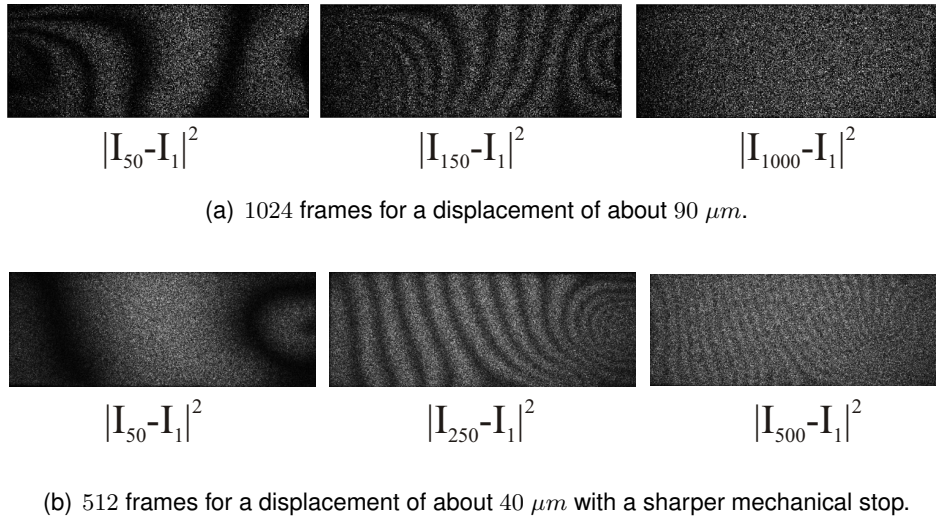


Figure VII.30: Correlation fringe between different couples of grabbed frames.

3.3.1 Results and discussion

As done in the previous analysis of experimental cases, we compare the phase maps obtained with the ridge extraction, the fast-EMD/HT, the extrema-based and the fast-EMD/HT/3DPP algorithms in Fig.VII.33 and in Fig.VII.32, for the two cases illustrated in Fig.VII.30. The fixed convex hulls for the two cases are shown in Fig.VII.31.

We observe on this particular example that the 3DPP procedure yields the smoother phase map without endangering the spatial resolution especially near the mechanical stop.

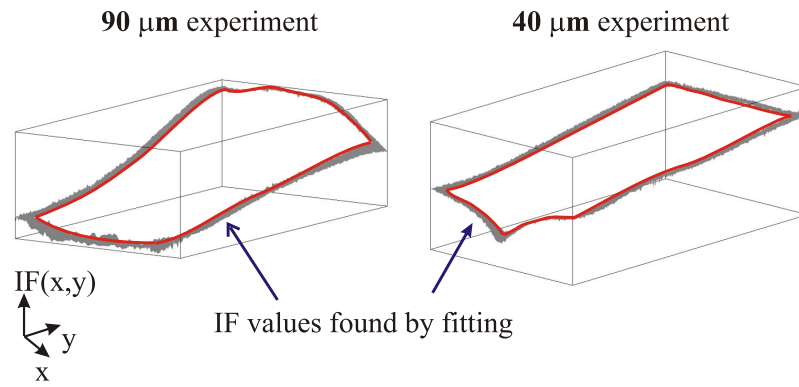


Figure VII.31: Fixed convex hull with imposed IF values for the 90 μm and the 40 μm experiments.

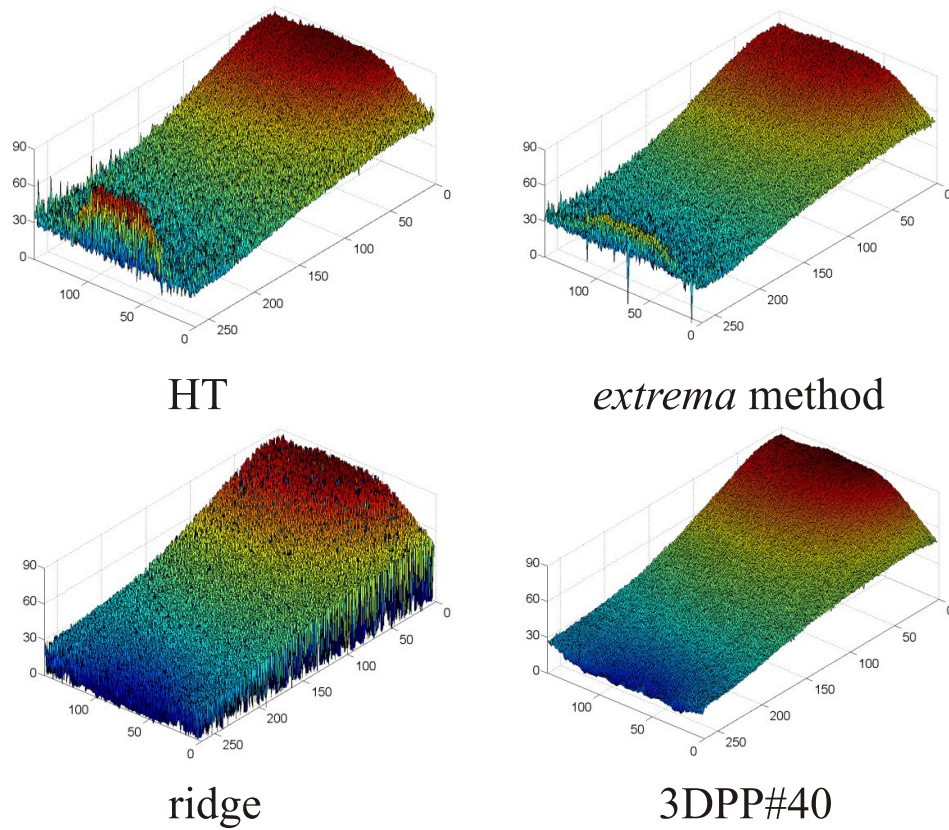


Figure VII.32: Final phase maps for the different methods in the 90 μm experiment.

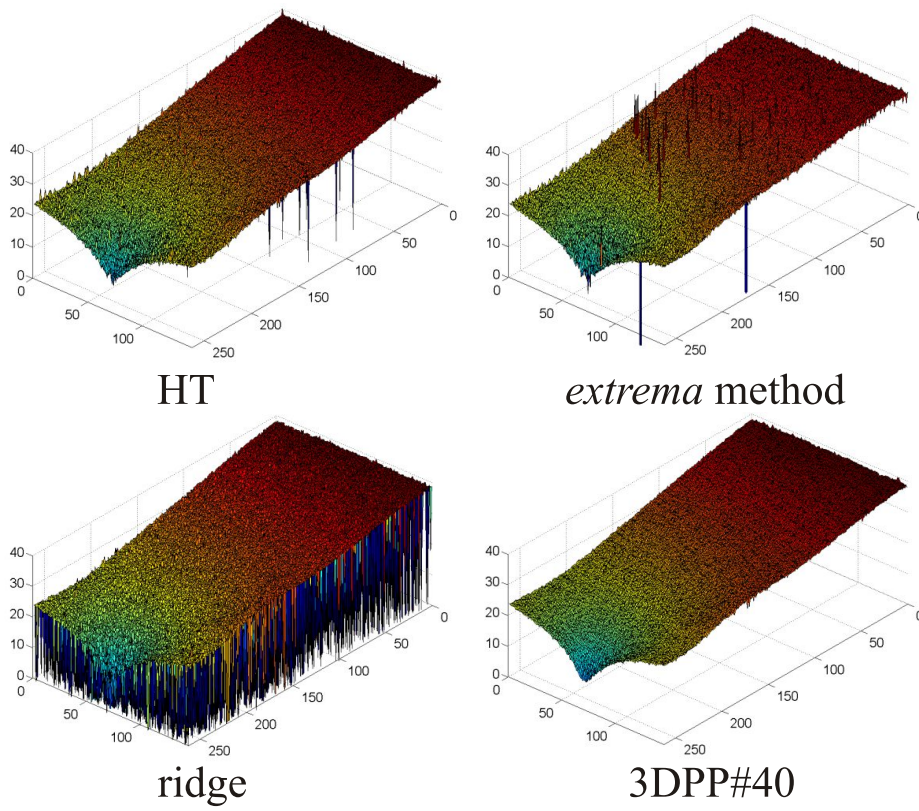


Figure VII.33: Final phase maps for the different methods in the $40\ \mu m$ experiment.

3.3.2 Results of sparse-3DPP

As briefly said in the previous chapter, it is often valuable for a method to feature a computation load which can be tailored by the end-user, depending on the sought accuracy of the result. We know that the temporal approach lends itself perfectly to this as we can choose to process or not any pixel. For the 3DPP procedure, the computation load can also be lightened at will, by processing one frame every D . We present in Fig.VII.34 the results for different "temporal downsampling" factors for the rubber compression experiment with the $90\ \mu m$ displacement. The phase map obtained after having processed all of the 1024 frames has been shown in Fig.VII.32, and we consider a factor D equal to 4, 8, 16 and 32.

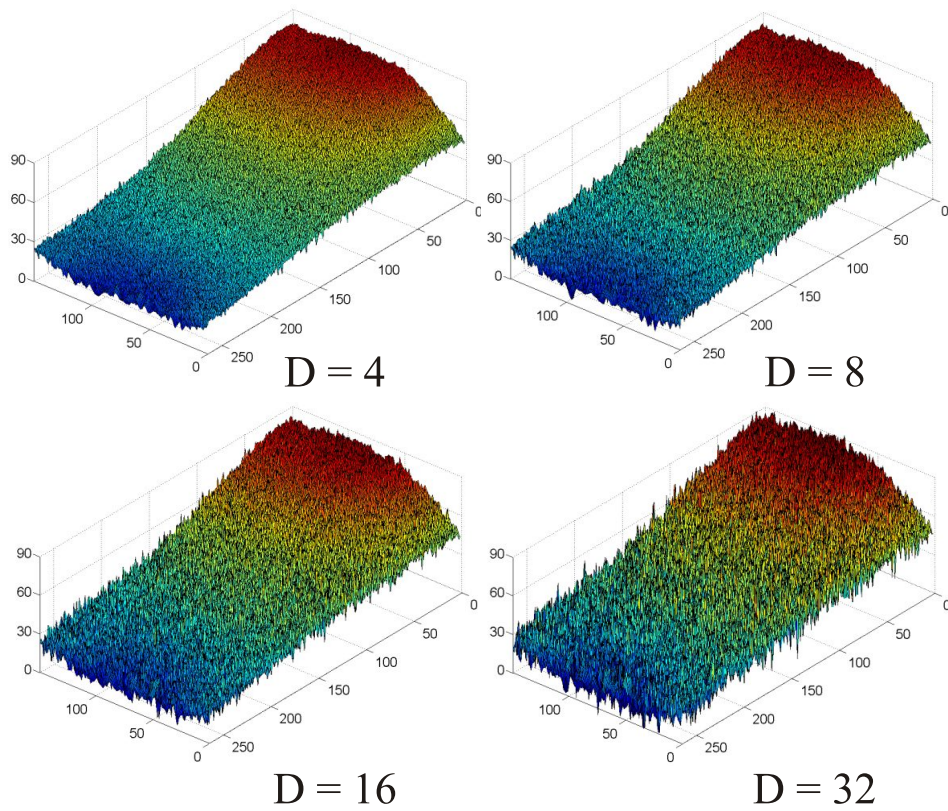


Figure VII.34: Final phase maps in the $90\ \mu m$ experiment for the sparse-3DPP technique when 1 frame every respectively 4, 8, 16 and 32 is treated.

4 Evaluation of the sine-cosine DT filter

A SI setup with out-of-plane sensitivity (Michelson configuration) has been used to measure the deformation of a rough aluminium plate along the z -axis (see Fig.VII.35).

The five-frames algorithm has been used to compute the raw phase map and the mod-

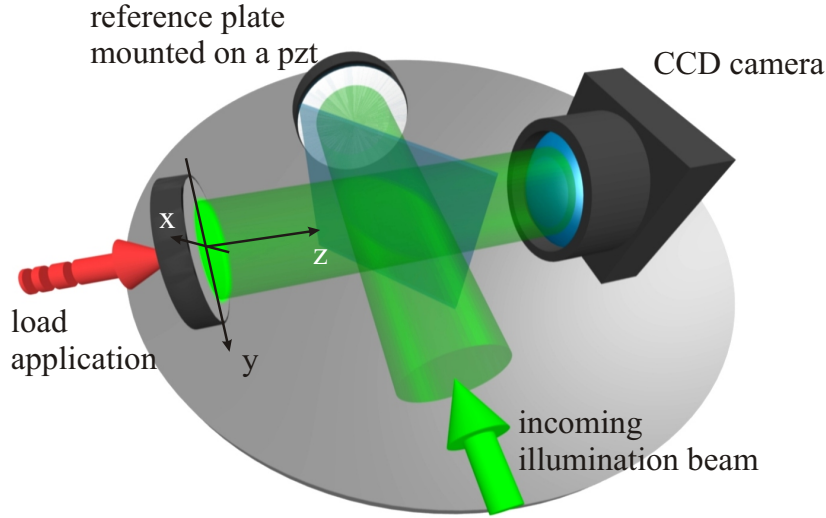


Figure VII.35: Michelson-type setup for out-of-plane measurement.

ulation map as well. To obtain the latter, we simply combine in a slightly different way the original phase-shifted frames (see Eq.VII.5) as shown in Eq.(VII.6), where the phase shift is assumed to be equal to $\pi/2$.

$$\begin{aligned}
 I_1 &= I_o + I_m \cos(\Phi - 2\delta\phi) \\
 I_2 &= I_o + I_m \cos(\Phi - \delta\phi) \\
 I_3 &= I_o + I_m \cos(\Phi) \\
 I_4 &= I_o + I_m \cos(\Phi + \delta\phi) \\
 I_5 &= I_o + I_m \cos(\Phi + 2\delta\phi)
 \end{aligned} \tag{VII.5}$$

$$\hat{\Phi} = \arctan \frac{2(I_3 - I_1)}{I_4 + I_0 - 2I_2} \tag{VII.6}$$

$$\hat{I}_m = \sqrt{(I_3 - I_1)^2 + \frac{1}{2}(I_4 + I_0 - 2I_2)^2} = \sqrt{I_m^2 \sin^2(\Phi) + I_m^2 \cos^2(\Phi)}$$

We first show the wrapped raw phase map, *i.e.* the 2π difference of the phases from the two states, each of them computed with the five-frame algorithm (Fig.VII.36). It is jointly shown with the modulation map computed with Eq.(VII.6). As stated in the previous chapter, the principle of our sine-cosine DT filter is to firstly classify the pixels for the sine and the cosine maps of the original wrapped phase based on this modulation map newly

built. Then, the DT is computed for each of the two sparse arrays of reliable data and a smooth surface is finally computed on a uniform grid. The smoothed phase is then classically computed with the \arctan function in $[-\pi, \pi]$. Maps of pixel validity, simply

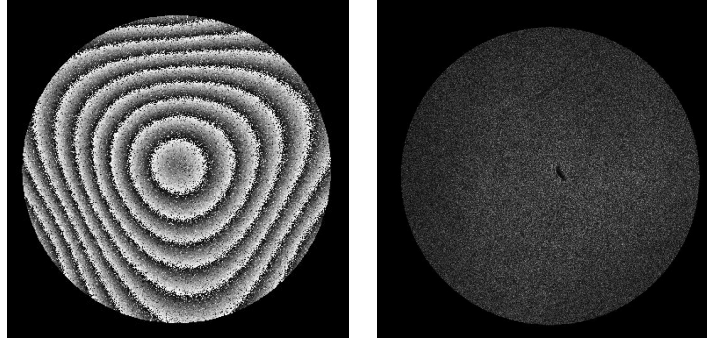


Figure VII.36: Wrapped raw phase map (left) and modulation map (right).

built by thresholding the modulation map for three different threshold values, are shown in Fig.VII.37, with the corresponding filtered phase maps (see Fig.VII.38).

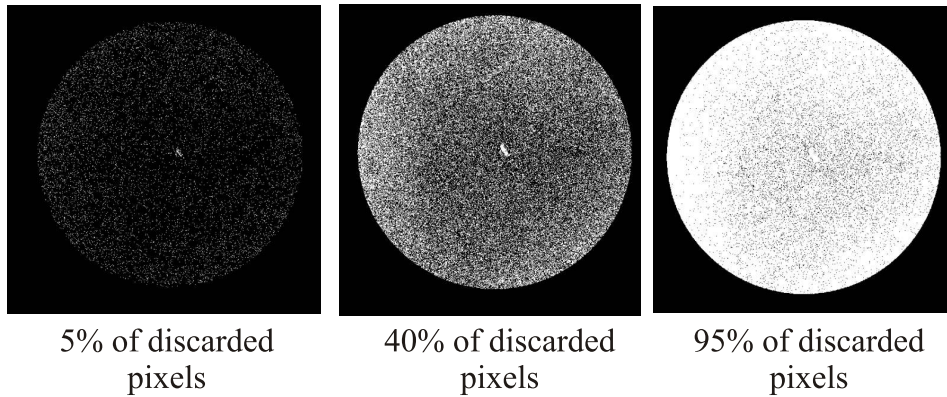


Figure VII.37: Maps of pixel validity for different threshold values. The number of discarded pixels in the area of interest is indicated as a percentage.

It appears clearly on the filtered phase maps that the higher the threshold, the better the noise rejection. A problem however appears near the boundaries of the AOI. It is simply due to the fact, that the illumination is not uniform across the field of view of the camera. The test is thus more discriminate near the boundaries than in the middle. The solution is simply to take into account the illumination profile and to tailor the threshold accordingly. The best result we have been able to obtain with this method is shown in Fig.VII.39. For information only, we reported also the result of the classical iterative sine-cosine filter, applied 20 times with a box kernel of 3×3 pixels. The unwrapped phase maps are shown in Fig.VII.40

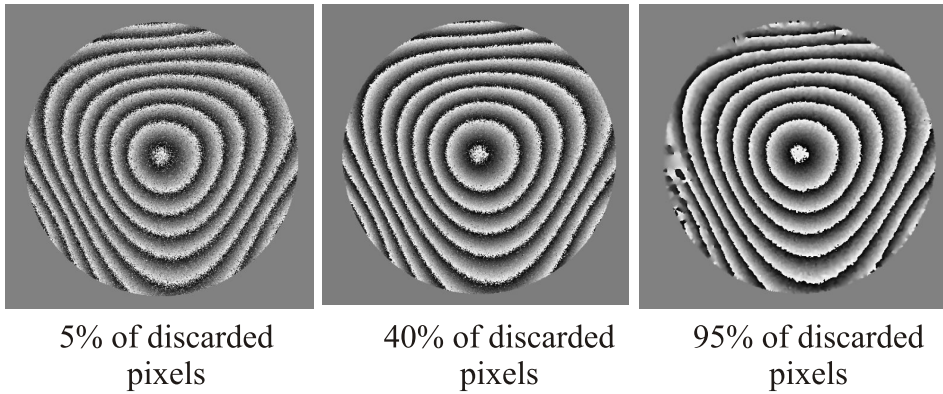


Figure VII.38: Results of the sine-cosine DT filter for different threshold values.

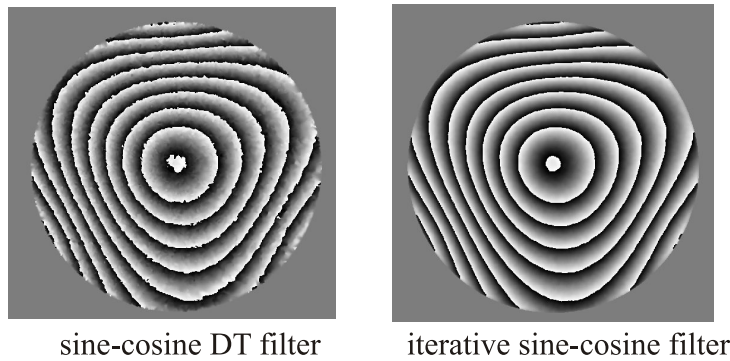
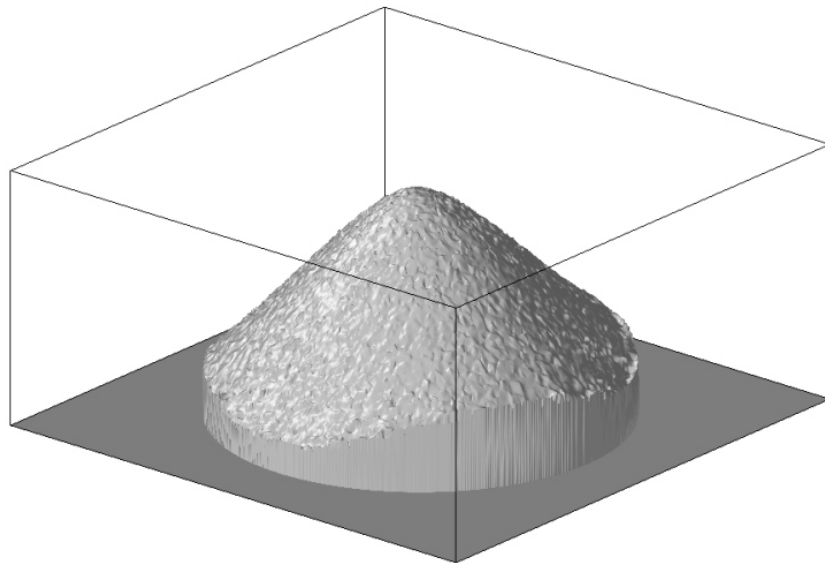
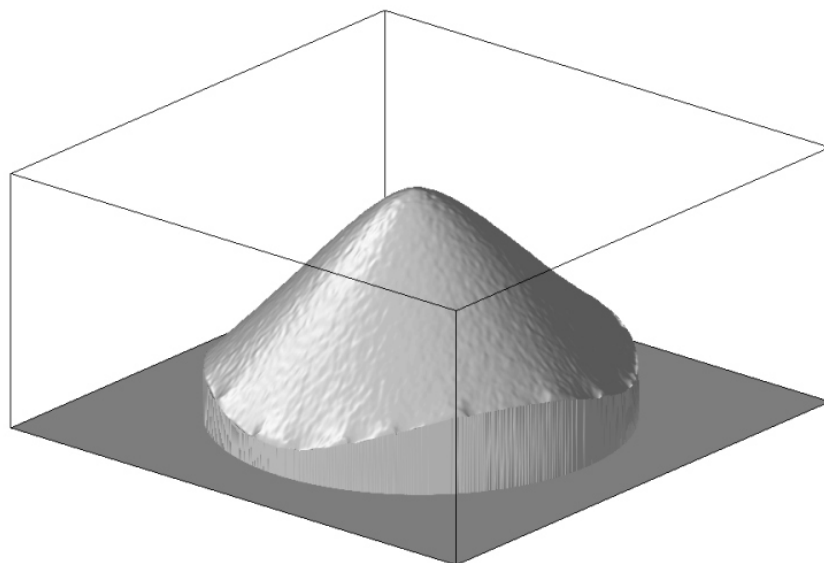


Figure VII.39: Result of the sine-cosine DT filter with an optimum threshold value which depends on the illumination profile (left). Result of the classical iterative sine-cosine filter after 20 iterations (right).

It is undeniable that the result from the iterative sine-cosine filter appears smoother than the outcome of the sine-cosine DT filter. In addition, it has been demonstrated that with a convenient kernel ([3]), the spatial resolution is not degraded by the iterative process, while the result of the sine-cosine DT filter shown in Fig.VII.39 has been obtained by discarding more than 97% of the pixels, resulting in an average length of the DT facets of 10 to 15 pixels. However, the most annoying drawback of the classical sine-cosine filter is that it pollutes the reliable data with the unreliable ones - as usual filtering methods do. This can be improved by choosing appropriate filter coefficients, but it might be interesting to combine the two methods: firstly, discarding the most aberrant pixels with the sine-cosine DT filter and finally improving the result with the iterative sine-cosine filter. Moreover, it should allow to reduce the number of iterations for the same requirement on the phase smoothness.



sine-cosine DT filter



iterative sine-cosine filter

Figure VII.40: 3D view of the phase maps shown in Fig.VII.39 after unwrapping.

Chapter VIII

The stochastic signal processing world: a mine of phase extraction methods within reach thanks to the EMD

1 Estimation or tracking techniques?

What we have seen so far, is that thanks to the EMD method, we obtain a signal that is in an appropriate shape for subsequent accurate phase extraction. It is then up to the user to choose the phase/IF extraction method according to the application. We have seen in the past with the work of Colonna de Lega, that the SI community (developers and as a consequence users) could benefit from advances in other fields like acoustics, speech processing, *etc.* We do believe there is a mine of phase and IF computation methods which are developed, notably in the speech processing domain, that could be of benefit to our field, and the reciprocal might even be true.

Frequency tracking and estimation is an old issue, as it became quickly necessary to accurately estimate frequencies embedded in noise, especially in radio waves domain. The book from Quinn and Hannan ([148]) offers a review of methods aiming at retrieving the spectral content of a signal in different SNR conditions ranging from the Wiener filter, to ARMA (auto-regressive moving-average) modeling, Kalman filtering and Hidden Markov models.

The Wiener filter is the optimal filter to estimate a signal embedded in noise, in the stationary case. The Kalman filter is a recursive formulation of the Wiener filter and assumes thus that the system which produces the observed process is linear. To deal with non-stationary situations, we need to move to the extended Kalman filter, which has been

applied to the frequency tracking issue ([142]). It has notably be shown that the extended Kalman filter is closely related to the phase-locked loop ([142]), another widely used technique, firstly analogically and later digitally ([114]). ARMA models are among the most relevant signal models, thanks to their ease of use, their ability to model a wide range of physical signals. For instance, GSM communications are actually based on an ARMA modeling of voice signals. The task of signal estimation reduces then to estimating the ARMA parameters, and the Yule-Walker equations and the Levinson algorithm are the basic methods to compute those parameters. Labarre *et al* proposed in [99] a two-Kalman filters scheme to estimate AR parameters of speech signals, with the purpose to enhance them. Besson proposed in [18] the ARCOS model, which is basically a sine wave where the amplitude is modeled by an AR process. This model addresses the issue of signal estimation in multiplicative noise, while this is principally the additive noise case which is studied. The last model mentioned here is the Hidden Markov model ([150]), which has been applied to the frequency tracking issue notably in [172].

The purpose of this section does obviously not constitute an exhaustive review of frequency trackers and estimators, but should convince that a rich collection of techniques is available to model and estimate signals, with statistics that we are familiar with in SI, AM-FM signals with different amounts of noise.

2 Example: Linear predictive filtering for signal modeling

This section is strongly inspired, at least for the starting point, from the the work of Griffiths ([79]). The original method is actually composed by three steps: *i*) a linear filter prediction, *ii*) the LMS (least mean square noisy gradient descent) algorithm to update the filter coefficients, and *iii*) a spectral estimation. If we consider first a sequence $x[k]$ perfectly predictable using a linear filter, the prediction at time k is thus a linear combination of the previous values weighted by the coefficient of the filter:

$$\hat{x}[k] = \sum_{l=1}^L g_l \cdot x[k-l] , \quad (\text{VIII.1})$$

where L is the filter length and g_l is the l th filter coefficient. The coefficients are then updated as stated above by a LMS algorithm whose formulation is recalled hereafter (see [79] for the complete development):

$$G[k+1] = G[k] + \mu(x[k] - \hat{x}[k]) \cdot X[k-l] , \quad (\text{VIII.2})$$

where G is the filter coefficients vector at instant k , *i.e.* $[g_1(k), g_2(k), \dots, g_L(k)]$, X is the vector of data upon which the prediction is based again at time k , *i.e.* $[x[k-1], x[k-2], \dots, x[k-L]]$, and μ is the step-size, which regulates the convergence speed of the algorithm. The

2. Example: Linear predictive filtering for signal modeling

filter length L and the LMS algorithm step-size are parameters we impose empirically here. This classical formulation works for signals with constant amplitude, and some adjustments are required to be able to process our AM-FM signals. It is enough to weight the data sample at time k with the modulation value (see chapter 5) of the SI signal. It leads finally to the following formulation:

$$\hat{x}[k] = \sum_{l=1}^L g_l \cdot \tilde{x}[k-l]G[k+1] = G[k] + \mu(\tilde{x}[k] - \hat{x}[k]) \cdot \tilde{X}[k-l], \quad (\text{VIII.3})$$

where $\tilde{\cdot}$ denotes the operation of normalizing by the modulation envelope value. Considering our perfectly predictable signal and taking the discrete Fourier transform of both sides of equation Eq.(VIII.3), we obtain:

$$X(\omega) \cdot [1 - \sum_{l=1}^L g_l e^{-i\omega l}] = 0 \quad (\text{VIII.4})$$

Thus, for frequencies where the signal spectrum is not null, the second term of Eq.(VIII.4) must be equal to 0. The spectral estimate defined below exhibits thus peaks at the input signal frequencies:

$$Q(\omega) = \frac{1}{|1 - \sum_{l=1}^L g_l e^{-i\omega l}|^2} \quad (\text{VIII.5})$$

The problem here is that we have to compute at each time the spectral estimate over a range of frequencies. The estimation will thus suffer some quantization noise due to the finite number of frequencies where it is evaluated. A good way to reduce the computation cost would be to evaluate the estimate over a close range around a rough frequency estimate, that is actually easily available with the *extrema* method presented in chapter 5. It is also a pity to build an iterative estimator to model the signal to finally estimate the IF over a certain range, wasting this way some computation resources.

The idea of the linear predictive filter (LPF) is nonetheless a good idea as SI temporal signals - pre-processed with the EMD, *i.e.* centered and normalized - lend themselves to such models and require few filter coefficients ¹. Two coefficients are necessary for a sine wave with constant amplitude, and four or five coefficients are in practice enough for AM-FM signals encountered in SI. It is nonetheless interesting to increase the number of coefficients as, the higher the number of coefficients, the better the noise rejection. We show below two experimental pixel signals, experiencing different - but constant - displacement rates, smoothed with this LPF approach. The phase of the so-built model is then extracted with the analytic method, and the IF of the signals are then computed and compared. We eventually compute the distribution of the IF values in the different cases to highlight the influence of the filter length on the noise rejection (see Fig.VIII.1 and Fig.VIII.2).

¹The signal model used here is in other words an autoregressive model (AR) whose components are simply found by a steepest descent algorithm.

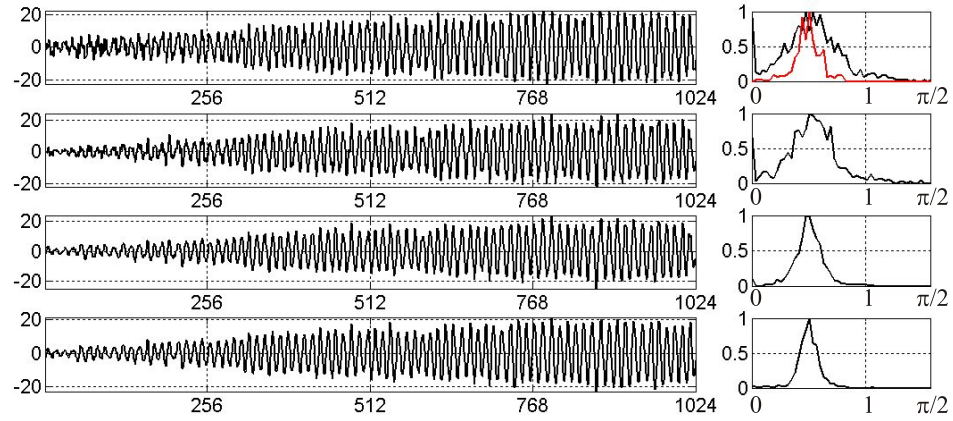


Figure VIII.1: 1st IMF extracted from an experimental temporal SI signal (top) experiencing around 80 fringe of displacement, and modeled with the LPF approach with (from top to bottom) a 4-tap, 8-tap and 16-tap filter. On the right, the distribution of the IF values along time are shown for each signal (the red curve on top designates the distribution for the *extrema* method).

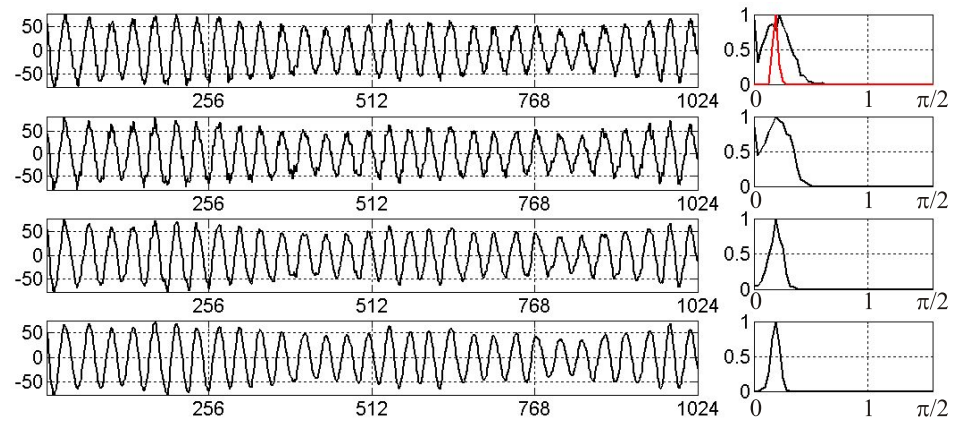


Figure VIII.2: 1st IMF extracted from an experimental temporal SI signal (top) experiencing around 30 fringe of displacement, and modeled with the LPF approach with (from top to bottom) a 4-tap, 8-tap and 16-tap filter. On the right, the distribution of the IF values along time are shown for each signal (the red curve on top designates the distribution for the *extrema* method).

Chapter IX

Conclusion

1 Achievements

The goal of this work was the conceiving of robust and accurate procedures for the characterization of dynamic behaviors of mechanical surfaces, using speckle interferometry or related full-field optical methods.

We first came up with a numerical model whose validity domain has been clearly defined, and which is very convenient for creating complex speckle fields, a valuable tool to test new processing schemes. We tackle the phase extraction problem by going back to the basics of phase extraction from non-stationary signals. The idea was to clearly identify the requirements of a meaningful phase computation.

It was then shown that a pre-processing tool was missing to efficiently detrend SI signals, which are by nature strongly non-stationary. The Empirical Mode Decomposition, an appealing candidate to fill the gap at first glance, proved to be efficient and accurate to remove SI signal background intensity. The method is however iterative, which is not an ideal feature for dynamic regimes, and in addition, remains delicate to control. An algorithm has thus been written with safe-guards to make the decomposition more robust without deteriorating its self-adaptiveness, its very asset. The Hilbert transform and its use as a quadrature operator, has been studied and assessed for the phase computation. The so-called analytic method proved to be efficient but highly sensitive to noise. Other phase extraction and/or tracking methods - subsequently to EMD preprocessing - have been investigated and tested for comparison purposes.

A novel and powerful approach to the under-modulation issue has been proposed which actually fits for phase (Φ) map filtering in static ($\Phi(r)$) and dynamic regimes ($\Phi(r, t)$). For the static case, where two states are recorded and compared, the method showed some pretty good noise rejection power without nonetheless reaching the level of the classical iterative sine-cosine filter. A trade-off must be found between noise rejection and spatial

resolution, but unlike the latter classical filter, the outcome depends only on the reliable data. For the dynamic case, the first step is the binary classification of the pixels signals according to a certain threshold. The key point is that this classification is made along time. Within its history, a pixel signal is very likely to carry useful information for a certain period of time and to be completely unreliable at other instants. The useful information considered here is the instantaneous frequency (IF) - the IF is the numerical derivative of the phase - as the phase is very likely to be wrong up to a constant when such a loss of modulation occurs in the temporal signal. Once the classification has been made at each instant, an interpolation step, based on the Delaunay triangulation, takes place so as to recover a uniform smooth phase map from the so-build non-uniformly sampled frames of IF. The key point of the proposed technique is that its outcome depends on the most reliable data as it discards the data which are the most prone to phase errors, unlike classical filtering techniques. The method has no bias and greatly reduces the decorrelation-induced random phase errors, intrinsically linked to speckle interferometry. The dynamic characterization of large displacements requires tackling the problem of computation load. In addition, if a temporal carrier is required, the amount of data to record is even higher. Our method proved to increase the measurement bandwidth without damaging the measurement accuracy as it permits to do without temporal carrier, which greatly compensates the oversampling needed by the EMD to perform well.

2 Further work

We already gave along this dissertation some possible improvements of the developed methods. First, at the background intensity removal level, the use of the EMD method has been advocated. In the under-modulated areas of the temporal pixel signals, mode-mixing occurs despite the implemented safe-guards. Constraining more the decomposition is not appreciable as it would damage its self-adaptiveness, which is the very strength of EMD. The construction of an hybrid mode, which basically regains useful information from the second IMF only in the regions with low modulation, yields a more information-saving EMD. A careful implementation might be of use, especially when the broadest measurement bandwidth is sought, *i.e.* with no temporal carrier.

The world of stochastic methods for frequency estimation and tracking has been briefly investigated and it can definitely help to conceive accurate, fast phase computation methods with a better noise immunity than the analytic method. Signal models have been briefly discussed, and a predictive filtering based model has been proposed with some good noise rejection ability on the first mode.

Our answer to the under-modulation issue proved to be powerful, versatile and very ac-

curate. Some improvements can be done to be able to treat the case of objects with non-convex shapes, and the case of spatial discontinuities as well. Another point that would deserve to be pursued is the surface tiling to lighten the computation burden ([34]). A tiling depending on the activity with criteria derived from the temporal and spatial phase gradients would permit to process the pixels, sparsely spread over the surface, which are the most relevant to treat (around a crack, in a high spatial displacement gradient area, and so on...).

Appendix A

A reminder on Fourier analysis

The definitions and the basic theorems are recalled in this paragraph and the forthcoming one without any proof. This would be beyond the scope of this chapter and this thesis. The purpose of this section is to recall the basics of Fourier analysis to properly introduce the FT-based processing methods in SI.

1 The continuous Fourier transform (FT)

1.1 Definition

The FT $F(s)$ of the function $f(x)$ is defined as ([24]):

$$F(s) = \int_{-\infty}^{\infty} f(x) e^{-i2\pi xs} dx \quad (\text{A.1})$$

The inverse FT is simply defined as:

$$f(x) = \int_{-\infty}^{\infty} F(s) e^{i2\pi xs} ds \quad (\text{A.2})$$

1.2 Basic theorems

We recall in the following the basic theorems, without proof, which are useful in fringe analysis and diffraction patterns computation. Again, the interested reader is invited to look in [24] for a thorough review of FT theorems.

1.2.1 Similarity theorem

Considering the Fourier pair $\{f(x), F(s)\}$, the FT of $f(ax)$, a being any real number, is:

$$\mathcal{F}(f(ax)) = \frac{1}{|a|} F\left(\frac{s}{a}\right) \quad (\text{A.3})$$

1.2.2 Shift theorem

Considering again the Fourier pair $\{f(x), F(s)\}$, a shift in the real domain does not change the amplitude of the Fourier components and are confined to their phase as following:

$$\mathcal{F}(f(x - a)) = e^{-i2\pi as} F(s) \quad (\text{A.4})$$

1.2.3 Modulation theorem

This is the well-known theorem behind Fourier-based methods of fringe analysis. Adding a carrier of frequency $\nu_o = 2\pi\omega_o$ in the real domain results in a shift in the reciprocal domain. The spectrum of the function $f(x)$ is shifted around the frequencies ν_o and $-\nu_o$:

$$\mathcal{F}(f(x) \cos 2\pi\omega_o x) = \frac{1}{2}F(s - \omega_o) + \frac{1}{2}F(s + \omega_o) \quad (\text{A.5})$$

1.2.4 Convolution theorem

This theorem is of primary importance as it enables fast computations of convolution products, which are very time-consuming. The convolution product reduces indeed to a simple product in the Fourier domain. Considering the Fourier pairs $\{f(x), F(s)\}$ and $\{g(x), G(s)\}$, then:

$$\mathcal{F}(f \otimes g(x)) = F(s) \cdot G(s) \quad (\text{A.6})$$

This theorem enables to compute diffraction patterns very efficiently (see the forthcoming Annex).

2 The discrete Fourier transform (DFT)

2.1 Definition and theorems

We will not insist on the case of discrete signals of infinite extend. We recall simply the definitions before talking about the FT of discrete sequences of bounded temporal support. We do not consider the case of non-uniform sampling either. The sampling operation causes the Fourier transform to become periodic and the FT and the inverse FT of infinite sequences are defined as following:

$$\mathcal{X}(e^{i\omega}) = \sum_{n \in \mathbb{Z}} x_n e^{-i\omega n} x_n = \frac{1}{2\pi} \int_{-\pi}^{\pi} \mathcal{X}(e^{i\omega}) e^{i\omega n} d\omega \quad (\text{A.7})$$

The theorems recalled above for the continuous case apply in the discrete one. It is customary to specify the dependency of the discrete-domain FT as $\mathcal{X}(e^{i\omega})$ instead of

simply $\mathcal{X}(\omega)$, to make a point that the FT of infinite sequences is 2π -periodic function (the continuity is implicit). It is common and convenient to look at this 2π -periodicity, by saying that the DFT is defined on the unit circle (interpreting physically the results and thus considering a sampling period different from 1 is simply a matter of scale).

2.2 The Shannon's sampling theorem

The sampling frequency must be properly chosen to avoid aliasing, *i.e.* irremediable loss of information. To avoid this loss of information, the sampling frequency must be chosen so that for any local period of the signal, there are at least two sampling points. This is a "hand-waving" reformulation of the Shannon sampling theorem which stipulates: If $f(t)$ is continuous and bandlimited to ω_o , then $f(t)$ is uniquely defined by its samples taken at $\omega_s = 2\omega_o$ (Nyquist criterion. We talk also of critical sampling). $f(t)$ can then be recovered by the interpolation formula (T is the sampling period):

$$f(t) = \sum_{n=-\infty}^{\infty} f(nT) \text{sinc}_T(t - nT) \quad , \text{ with } \quad \text{sinc}_T(t) = \frac{\sin(\pi t/T)}{\pi t/T} \quad (\text{A.8})$$

It means, in practice, that before sampling, it is mandatory to filter. The interpolation kernel, in the original formulation of the Shannon theorem, is the function *sinc*, and being not of finite support, it is not very convenient for computer implementation. Sampling theory has aroused the interest of many researchers among the signal processing community. The interpretation of the Shannon's sampling theorem as an orthogonal projection onto the Hilbert subspace of band-limited functions allows for more realistic and easy to implement interpolation models ([180]).

2.3 FT of finite sequences

2.3.1 Definition

In our real world, the data set we want to somehow process are inevitably of finite extent. We have seen that sampling the original signal makes the spectrum 2π -periodic but continuous. Truncating the signal means multiplying the infinite sequence by a window of finite length. The spectrum, in accordance with the convolution theorem, is thus the result of the convolution of the original spectrum with the FT of the window. The spectrum is thus degraded. The FT for such a finite sequence is defined by:

$$\mathcal{X}_k = \frac{1}{\sqrt{N}} \sum_{n=0}^{N-1} x_n W_N^{nk} = \frac{1}{\sqrt{N}} \sum_{k=0}^{N-1} \mathcal{X}_k W_N^{-nk} , \quad (\text{A.9})$$

where $W_N^{nk} = \exp(-i2\pi nk/N)$. We have considered here sequences of finite length N , but the same definition of the FT applies for N -periodic sequences. The DFT can

be implemented in a very fast way thanks to the Fast Fourier Transform (FFT) algorithm ([42]). The algorithm complexity is $O(n \log(n))$, while the direct computation complexity is $O(n^2)$. Typically, for a data set of 1024 samples, the FFT algorithm is 100 times faster than the direct computation. It is also well-known, that the algorithm, due to its structure, is much more efficient for data set of length N equal to a power of two.

2.3.2 Windowing and DFT

This point is a crucial matter of concern in spectral analysis of finite sequences, as when the analysis window is not commensurate with the natural period of the signal, discontinuities appear in the periodic extension of the signal at its boundaries. It generates spectral contributions which have nothing to do with the intrinsic spectral content of the signal ([178]). One mean to avoid this so-called spectral leakage is to apply a window of a certain shape to the signal, and thus smoothly bring the windowed data to zero at the boundaries. This point is detailed in [81].

2.3.3 Zero-padding

The DFT of a finite sequence of N samples is itself a complex-valued vector of length equal to N . The spectrum is sampled with a step of $1/N$. If some zeros are added to the data sequence to form a sequence of length P ($P > N$), it is clear that the resulting DFT will not be changed as the zeros bring no contributions. However the spectrum is this time sampled with a finer step of $1/P$. It is worthwhile to specify how to interpret correctly this result:

- i) if the signal is of impulse nature and is fully contained in the original window of length N , zero-padding might be interesting to compute a finer spectral estimation, which could be, by the way, equivalently achieved by an interpolation process directly in the Fourier domain.
- ii) if the sequence results from the truncation of a signal on which we have no knowledge beyond the window, it is illusive to look for a finer spectral estimation by adding zeros.
- iii) if the sequence represents a period of a signal, zero-padding will certainly give a finer spectral representation but still degraded by the FT of the sampling window. It is preferable in that case to look toward the direction of signal continuation (signal mirroring techniques or Gerchberg algorithm).

Appendix B

Diffraction patterns computation

1 In which way a numerical model is valuable?

Experiments involving speckle distributions are indeed frequently carried out firstly on a simulation basis. The underlying reasons are in the impossibility to exercise a perfect material control of all the parameters governing the speckle formation, especially the roughness parameters and their possible alterations. A great number of numerical models have therefore been built. These models most often are of an ad hoc nature, limited to the validation of particular findings. Such approaches span an horizon as wide as the analysis of surface roughness versus speckle contrast ([67]), the statistical study of intensity and phase in the vicinity of singularities ([167]), the intrinsic speckle noise in Gabor particle holography ([130]), the effectiveness of a wavelet filtering technique in speckle interferometry ([57]), the noise evaluation in coherent fringe projection techniques ([116]), the subjective significance of a given SNR in speckle interferometry ([109]), the testing of unwrapping algorithms ([72]), *etc.*

Sometimes, it is sufficient to introduce some sort of noise, additive or multiplicative, into the standard two-beam interference formula in order to give a speckle appearance to the fringe patterns under examination ([158]). Artificial speckle patterns are also in use outside the visible part of the electromagnetic spectrum. Rare publications, on the contrary, are tackling the question of the elaboration of an explicit and realistic digital representation of a speckle field, mimicking as closely as possible the concerned physical processes ([57, 128]). Moreover, apart from elementary tests, very few in-depth validations have been attempted in order to guarantee the adequacy of the modeling. On the contrary, this has been the goal of this preliminary work to the core topic of the thesis ([52]). We will recall in a first paragraph some basic matter of the diffraction theory from its fundamental form, the Rayleigh-Sommerfeld integral, to the well-known Fresnel approximation. We will discuss numerical computation of diffraction patterns and use sampling considerations to determinate the validity range of different acknowledged methods. The use of

the linear model to simulate complex speckle fields and SI signals will then be advocated, while its limits will be discussed.

2 Diffraction theory: from Rayleigh-Sommerfeld to Fresnel

The base of Fourier Optics is the Rayleigh-Sommerfeld diffraction model. Considering Fig.B.1(a), its formulation is given by:

$$U(P') = -\frac{i}{\lambda} \iint_{\Sigma_o} U(P) \frac{e^{ikp}}{p} \cos(\vec{n}, \vec{p}) ds, \quad (\text{B.1})$$

where ds is an elementary surface of the diffracting aperture Σ_o , $k = 2\pi/\lambda$, $\vec{p} = \overrightarrow{PP'}$ and \vec{n} is the outward normal to the surface.

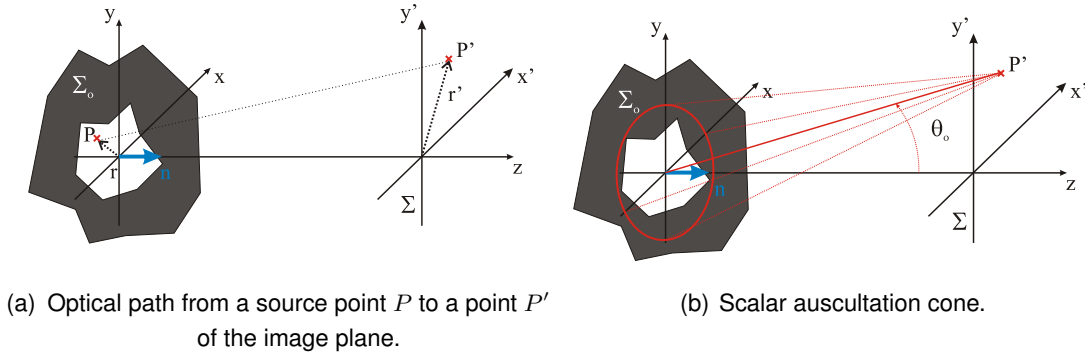


Figure B.1: Computation of the electromagnetic field diffracted by a given aperture.

The only condition to establish Eq.(B.1) is to consider that the surface where we want to compute the field (Σ) is sufficiently far from the diffracting surface (Σ_o). This formulation is very general and rigorous. The scalar approximation of electromagnetic waves requires that the contribution in P' are all parallel in a first approximation. In other words, the diffracting surface Σ_o must be seen under a narrow solid angle called the scalar auscultation cone. The term $\cos(\vec{n}, \overrightarrow{PP'})$ can thus be approximated by $\cos(\theta_o)$, known as the obliquity factor, where θ_o is the field angle (see Fig.B.1(b)), and can be removed from the integral. The Rayleigh-Sommerfeld integral becomes:

$$U(P') = -\frac{i}{\lambda} \cos(\theta_o) \iint_{\Sigma_o} U(P) \frac{e^{ikp}}{p} ds \quad (\text{B.2})$$

In the paraxial domain, the obliqueness can even be considered as equal to 1. When the system aperture is too large to fulfill the paraxial approximation, it means that, in the resulting field computation, we overestimate some contributions and this relative error is

2. Diffraction theory: from Rayleigh-Sommerfeld to Fresnel

typically equal to 1% and 5% when the aperture angle is respectively 8° and 18° . Despite the approximations made so far, the Rayleigh-Sommerfeld integral of Eq.(B.2) remains hard to compute, and it takes a much simpler form in the Fresnel approximation. Indeed in the paraxial domain, the distance PP' exhibits very low variations. It can thus be removed also from the integral computation and developed to the first order in the phase term; it yields the Fresnel integral or Fresnel transform:

$$U(P') = -\frac{i}{\lambda z} e^{ikz} \iint_{\Sigma_o} U(P) e^{i\pi \frac{(r-r')^2}{\lambda z}} ds \quad (\text{B.3})$$

The Fresnel approximation consists, in other words, to approximate the spherical wavelets of Huygens by quadratic ones. We can evaluate the phase error made within this approximation by considering the second order term of the Taylor expansion of the phase:

$$\delta\phi \approx -\frac{\pi z}{4\lambda} \tan^4 \theta, \quad (\text{B.4})$$

where θ being again the aperture angle. Accepting a maximum error of $\pi/2$ yields the following relation between the aperture angle and the ration z/λ :

$$\theta^4 < \frac{2\lambda}{z} \quad (\text{B.5})$$

In Fig.B.2, the validity domains of the approximations made so far are shown.

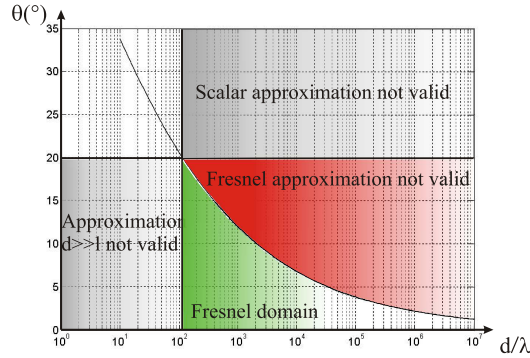


Figure B.2: Acceptable range for Fresnel approximation.

Under the Fresnel approximation, the resulting field $U(P')$ is actually simply the convolution of the field in the pupil plane of the diffracting surface with a function $h(r)$ which corresponds to the response of a certain filter:

$$h(r, z) = -\frac{i}{\lambda z} e^{ikz} e^{i\pi \frac{r^2}{\lambda z}} \quad (\text{B.6})$$

This linear time invariant filter view is very suitable, especially to introduce fast computation matters, through FFT algorithm. The FT of $h(r)$ is given by:

$$\mathcal{F}(h(r, z)) = \tilde{H}(\omega, z) = e^{ikz} e^{-i\pi \lambda z \omega^2} \quad (\text{B.7})$$

This computation trick finds a physical meaning within the model of the plane waves. The FT of the field is its decomposition in plane waves whose spatial frequency is $\omega = \sin(\theta)/\lambda$, θ being the inclination of the plane wave with respect to the z axis. Without recalling all the well-known development, resolving the Helmholtz equation with the Fourier domain expansion of the field yields the following filtering model with the free-space kernel:

$$\tilde{U}(\omega, z) = \tilde{U}(\omega, 0) e^{ikz\sqrt{1-\lambda^2\omega^2}} \quad (\text{B.8})$$

The simplification of the square root to the 1st order gives the Fresnel kernel in the Fourier domain. Fig.B.3 summarizes diffraction patterns computation both from the point of view of scalar waves diffraction theory, and from the one of plane waves decomposition and homogeneous free-space transfer function as well. The two approaches are obviously theoretically equivalent but lead to very different results numerically.

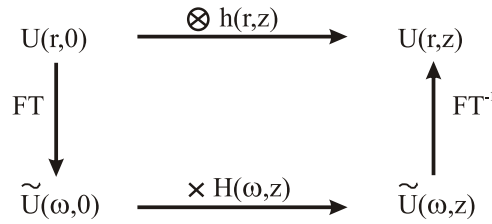


Figure B.3: Spectrum propagation method and integral computation method.

3 Computation of diffraction patterns: sampling considerations

We now focus on the numerical implementation of the two approaches summarized in Fig.B.3. Without any loss of meaning, we limit ourselves in this section to 1D signals. The Rayleigh-Sommerfeld integral cannot be computed efficiently, except in the Fourier domain thanks to the filtering model with the free-space kernel. However, the diffraction pattern computation in the Fresnel domain of validity can be conducted efficiently in both spaces. The Fresnel transform in eq.(B.3) can indeed be rewritten as following where the diffracted field computation reduces to the FT of the input field multiplied with a quadratic phase term:

$$U(x', z) = -\frac{i}{\lambda z} e^{ikz} e^{i\pi \frac{x'^2}{\lambda z}} \int_{-\infty}^{\infty} [U(x, 0) e^{i\pi \frac{x^2}{\lambda z}}] e^{-i2\pi \frac{xx'}{\lambda z}} dx \quad (\text{B.9})$$

3. Computation of diffraction patterns: sampling considerations

In the far field, in the so-called Fraunhofer regime, the output field simply reduces to the scaled FT of the input field:

$$U(x', z) = -\frac{i}{\lambda z} e^{ikz} \int_{-\infty}^{\infty} U(x, 0) e^{-i2\pi \frac{xx'}{\lambda z}} dx \quad (\text{B.10})$$

To achieve physically meaningful computation with the FFT algorithm, *ad hoc* sampling must be done. Considering a function $f(x)$ and its N points sampled version $f[k]$, its DFT is defined by:

$$\mathcal{F}(\tilde{k}) = \sum_{-N/2}^{N/2-1} f[k] e^{-i2\pi \frac{k\tilde{k}}{N}} \quad (\text{B.11})$$

The sampling intervals are assumed to be Δx and $\Delta x'$ for the input and the output matrices, and the sampling steps are thus $\delta x = \Delta x/N$ and $\delta x' = \Delta x'/N$. We have the following relation between both coordinates in the reciprocal spaces:

$$N \cdot \delta x \cdot \delta x' = 1 \quad (\text{B.12})$$

In Eq.(B.9) and Eq.(B.10), it appears that the scaling factor is not equal to 1 but to λz , and we obtain the following scaling relations between the input and output planes:

$$N \cdot \delta x \cdot \delta x' = \lambda z \quad (\text{B.13})$$

To clarify what we've done so far, we have shown that the integral computation can be efficiently done thanks to the FFT algorithm, keeping in mind the scaling relation (Eq.(B.13)) existing between the planes at $z = 0$ and z . Hence, for a given sampling number of points and a sampling step in the input plane, the sampling step in the output plane will increase linearly with the distance z , allowing the complete computation of the wider and wider diffracting field. The computation of the diffracted field can be also done by the spectrum propagation method. The double use of Fourier operator impedes any rescaling relation which means that the sampling step will remain the same in the output plane at any z . Whichever method is chosen, an appropriate sampling of the kernel, either in the Rayleigh-Sommerfeld model or in the Fresnel approximation is mandatory. A critical sampling, *i.e.* according to the Nyquist criterion, of the phase term of the Fresnel kernel in the real domain leads to the following condition on z ([76, 128, 129]):

$$k \frac{\delta^2}{\lambda z} < 1 \quad \forall k \quad \text{and so, } z > \frac{\Delta^2}{\lambda N}, \quad (\text{B.14})$$

where Δ is the field extension $\Delta = N\delta$. While keeping this classical sampling criterion, we find another condition depending on z for the Fresnel kernel in the Fourier domain:

$$z < \frac{\Delta^2}{\lambda N} \quad (\text{B.15})$$

In Fig.B.4, the real part of the kernels in the Fresnel approximation are shown with respect to (ω, z) and (r, z) . Thus, the spectrum propagation method is only appropriate to

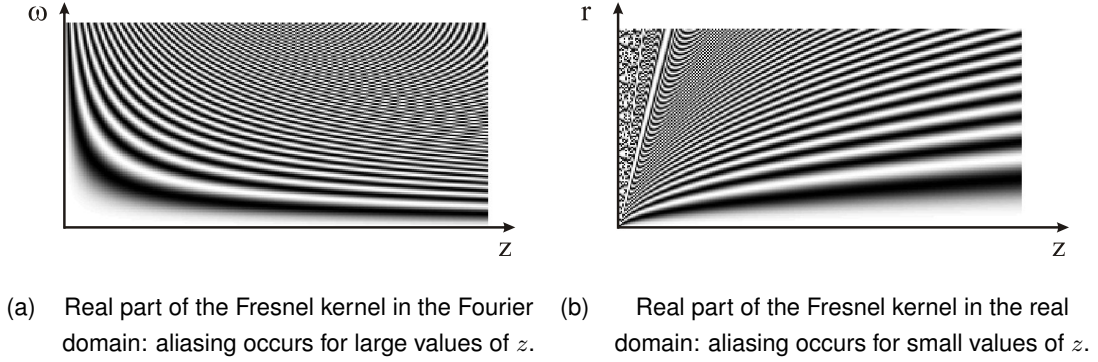


Figure B.4: Real part of the kernels in the Fresnel approximation in the Fourier domain (left) and in the real domain (right)..

compute the complex field in the near-field, while the direct computation in the real domain apply only in the far-field. Outside the ranges of application of each method, strong aliasing takes place. The conditions given above to properly sample the Fresnel kernel phase show clearly the limits of the quadratic approximation, but it must be said, that the spectrum propagation method with the free-space kernel comes up against exactly the same sampling issue, with nonetheless slightly different domains of validity. In fact, the greatest discrepancies between the two kernels are linked to the $1/\lambda$ limit for propagating fields k vectors. This limit does not hold mathematically for the Fresnel approximation, but it is meaningless not to impose it.

4 The fractional FT: a versatile tool for near-field and far-field diffraction computation

Operators originally defined for integers orders can be generalized to fractional orders featuring this way interesting properties. The definition of the a th power of a function $f(x)$ as the multiplication of $f(x)$ by itself a times makes sense only for a integer, but its extension to any a , real or even complex, is elementary. The same occurs with the derivative. Letting $\mathcal{F}(\nu)$ denote the FT of a real-valued function $f(x)$ (see Appendix A), the time differentiation theorem allows the extension of the definition of derivative to real orders:

$$\frac{d^a}{dx^a}[f(x)] \leftrightarrow (i\nu)^a \mathcal{F}(\nu) \quad (\text{B.16})$$

In Optics, in setups involving free-space propagation and focusing devices such as GRIN fibers, lenses, *etc* the field distributions in some specific planes are related with the FT. But as the definition of power and derivative of functions extend naturally to real order, it is worthwhile to wonder if:

4. The fractional FT: a versatile tool for near-field and far-field diffraction computation

- i) Can we define a Fourier transform of fractional order?
- ii) What would be the link between such a transform and the Rayleigh - Sommerfeld diffraction theory?

The answer at the first question is yes. Lohmann in [117] introduces the fractional Fourier transform (frFT) as a rotation operator of the Wigner distribution. A compilation of the definitions of the frFT can be found in [140], with notably one which involves the Green theorem. It can be shown that, under the paraxial approximation, the frFT is a solution of the wave equation and thus appears as a natural operator to compute fields propagation in the Fresnel domain ([8, 140]). The basic diffraction patterns in Fig.B.5 show that the frFT-based method allows to unify the near-field and far-field domains with a non-linear scaling relation between the input and output planes. Designating by a the fractional order of the frFT, the scaling relations of the sampling steps, δx and $\delta x'$, associated to the planes respectively located at $z = 0$ and at z , is written as followed ([139]).

$$\delta x' \delta x = \frac{\lambda z}{\sin a\pi/2} \quad (\text{B.17})$$

The fractional order a is equal to 0 at the input plane and is equal to 1 in the focal plane of a lens, as the frFT of order 1 is the common FT.

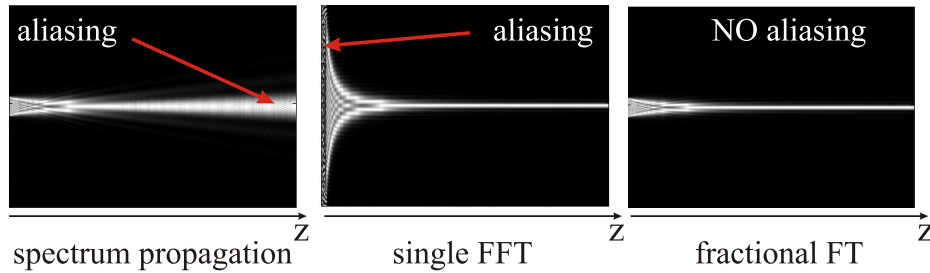


Figure B.5: Computer simulations of the diffracted field by an infinite slit with the spectrum propagation method(left), the single-FFT method (center) and the fractional FT (right).

The methods involving a scaling relation are actually not suitable to complex speckle patterns computation, as fields computed at different locations along the z -axis cannot be directly superimposed, and interpolating an integrated speckle pattern to appropriately resample it afterwards is obviously out of question - especially in the integrated case. The spectrum propagation method remains the only meaningful way to compute complex speckle patterns.

5 Which computation method for speckle and SI signals computation?

The linear amplitude imaging model is chosen here for creating numerical speckles. This model is dubbed for simplicity "linear model". It starts from the basic and well-known convolution integral between object complex amplitude and impulse response for obtaining the output amplitude. It is described in Fig.B.6.

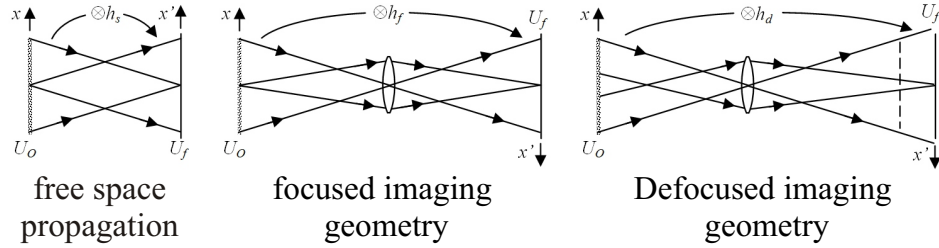


Figure B.6: Schematic representation of the input and output complex amplitude distributions in different geometries.

The diffuser is usually assumed to be a pure phase object, whose phase is uniformly distributed over a 2π interval:

$$U_0(r) = \exp(i\phi(r)) \quad (\text{B.18})$$

With λ , D and f being respectively the wavelength, the pupil diameter and the focal length of the imaging lens, and with the pupil function defined by $\text{circ}(\rho) = 1$ for $0 < \rho < D/2$ and 0 otherwise, the functions h_s , h_f and h_d are simply written as following.

$$\begin{aligned} h_s(r, z) &= \exp\left(\frac{i2\pi}{\lambda} \frac{r^2}{2z}\right) \\ h_f(r) &= FT\text{circ}(\rho) = \frac{J_1(q)}{q}, \quad \text{with } q = \frac{\pi r D}{2\lambda f} \\ &\text{and } J_1 : \text{Bessel function of the first kind of order 1} \\ h_d(r) &= FT\text{circ}(\rho) \exp(i\phi_a(\rho)) \quad \text{where } \phi_a(\rho) \text{ is the defocus aberration function} \end{aligned} \quad (\text{B.19})$$

The Matlab program is given at the end of the chapter.

6 Potentials, limits and applications of the model

Generating speckle fields with the linear model is valuable for testing and benchmarking automatic fringe processing methods developed for SI. Strongly grounded to the first principles, computationally efficient when the convolution integral is calculated by two FFT, this model creates pertinent complex speckle distributions. The linear model is relevant

for both objective and subjective speckle amplitudes: it is just a matter of choosing the appropriate impulse response, which assumes respectively either the form of the FT of the pupil function or the Fresnel function. In an imaging geometry, arbitrary amounts of defocusing are also very easily modeled. When confronting the statistical properties of the numerically created speckle fields to the theoretical distributions a Gaussian speckle should obey, very good statistical agreements between theory and model are obtained for the intensity and phase probability density functions, and hence for the moments of these random variables, in particular the contrast. More elaborate statistical properties, as the intensity autocorrelation functions, the average speckle size, the occurrence of singularities, are also correctly verified. Moreover, interesting results have been obtained in the fine structure of phase maps as shown in Chapter 3.

The linear model has nonetheless obvious limits linked to sampling considerations of the phase of the Kernel in the Fourier domain, either it be in the Fresnel approximation or not. Decorrelation induced phase errors are thus rather connected to the undersampling of the kernel phase than to the physical reason that would have been closely simulated.

7 Matlab program

```
%Simulation of Speckle Patterns
%-----
lambda = 532E-9;%lambda
a = 15E-3;%lens radius
f = 100E-3;%focal length
nuc = a/(lambda*2*f);%cut frequency of the imaging lens
N = 512;%number of sampling points
%-----
%Pupil matrix creating.
D = ones(N,N)*diag(-N/2:N/2-1);
D = (4/(N)^2)*(D.*D+D'.*D');
P = ones(N,N)-im2bw(D,0.1);
P0 = ones(N,N)-im2bw(D,1);
gammaP = sqrt(sum(sum(P0))/sum(sum(P)));
T = 0.5*(1/nuc)/gammaP;%sampling rate in the object and image plane
%-----
phase = rand(N,N);
Ui = exp(i*2*pi*phase);
Ufd = fftshift(fft2(Ui));
```

Appendix B. Diffraction patterns computation

```
%-----
%Fourier shift theorem
vE = upsample(2*ones(1,N/2),2)-1;
vF = upsample(2*ones(N/2,1),2)-1;
FSTM = vE(ones(N,1),:).*vF(:,ones(1,N));
%-----

Mx = ones(N,N)*diag((-N/2+1):(N/2));
My = Mx';
k0 = (gammaP*a)^2*((2/N)^2*(Mx.*Mx)+(2/N)^2*(My.*My));
delta = -N/2+1:N/2;
beta = 3E-6;
Atemp = zeros(N,N);
Itemp = zeros(N,N);
Hd = zeros(N,N);
%-----
%possibility to simulate the integrating effect of the sensor array
nint = 8;
Ni = floor(N/nint);%number of pixels of the sensor
Op = zeros(N,N);
bloc = [ones(nint,1),zeros(nint,nint-1)];
for kop=1:Ni
    Op((nint*(kop-1)+1):((nint*(kop-1)+1)+(nint-1)),...
        (nint*(kop-1)+1):((nint*(kop-1)+1)+(nint-1))) = bloc;
end

for k = 1:length(delta)
    z = delta(k)*beta;
    Hd = exp(i*pi*z*k0/(4*lambda*f^2));
    Ud = ifft2(Uf.*Hd.*P*exp(i*2*pi/lambda*z)).*FSTM;
    Id = Ud.*conj(Ud);
    Idmean = mean(mean(Id));
    Temp = (Id*Op)'.*Op;
    Idint = (1/nint^2)*Temp(1:nint:end,1:nint:end);
    Idmeanint = mean(mean(Idint));
    k
end
%-----
```


Appendix C

Fast-EMD algorithm

```
%Empirical Mode Decomposition implementation to process signals obtained
in SI. The algorithm is fed with stacks of temporal signals.
%-----
function [mode_out,mean_est,envmax,envmin,valid_env,if_em] = dec_emd_v6(y,N,th)
%-----
%OUTPUT:
%mode_out : 1st IMF.
%mean_est : 1st residue.
%envmax & envmin : upper and lower envelopes.
%valid_env : designates the temporal regions of the signal which have been
%   classified as valid or not valid, based on th.
%if_em : estimate of the IF of the signal with the extrema method.
%-----
%INPUT:
%y : temporal signal under analysis.
%N : number of time samples.
%th : thrsehold value used for the pixels classification for 3DPP.
%-----
t = 0:N-1;
%-----
signal = y;
[envmin,envmax,if_em] = extrema(signal,t,N);
mean_est = 0.5*(envmin+envmax);
valid_env = define_envmodul(envmax-envmin,th);
signal = signal-mean_est;
mode_out = signal;
%-----
```

Appendix C. Fast-EMD algorithm

```
%-----
function [envmin,envmax,if_em] = extrema(x,t,n)
% find the position of the extrema of the signal
m = length(x);
if (nargin == 1)
    t = 1:m;
end
dx = diff(x);
dx1 = dx(1:m-2);
dx2 = dx(2:m-1);
posmin = find(dx1.*dx2 < 0 & dx1 < 0)+1;
posmax = find(dx1.*dx2 < 0 & dx1 > 0)+1;
seuil_flat = 1E-10*abs(max(x)-min(x));
dxoo = (abs(dx) > seuil_flat);
dxo = dx.*dxoo;

if isempty(posmin) == 1 || isempty(posmax) == 1
    posmin = 256;
    posmax = 256;
else
    %+++++
    if (any(dxo == 0))
        dxopos = find(dxo == 0);
        ldxopos = length(dxopos);
        dxocount = [];
        dxoposf = [];
        ko = 1;
        vec_flat = [];
        if (ldxopos > 1)
            dxopos = [dxopos 0];
            while (ko < ldxopos)
                dposo = dxopos(ko+1)-dxopos(ko);
                while (dposo == 1) && (ko < ldxopos)
                    vec_flat = [vec_flat dxopos(ko)];
                    ko = ko+1;
                    dposo = dxopos(ko+1)-dxopos(ko);
                end
                vec_flat = [vec_flat dxopos(ko)];
                dxocount = [dxocount length(vec_flat)];
            end
        end
    end
end
```

```

        dxoposf = [dxoposf floor(sum(vec_flat)/length(vec_flat))];
        vec_flat = [];
        ko = ko+1;
    end
    ldxoposf = length(dxoposf);
    for ko = 1:ldxoposf
        kot = dxoposf(ko);
        if (floor(kot-dxocount(ko)/2) > 0) && ...
            (floor(kot+dxocount(ko)/2) < n-1)
            ind1 = kot-dxocount(ko)/2;
            ind2 = kot+dxocount(ko)/2+1;
            xo_ext = x(floor(ind1):floor(ind2)+1);
        elseif (floor(kot-dxocount(ko)/2) < 1)
            ind = kot+dxocount(ko)/2+1;
            xo_ext = x(kot:min(floor(ind)+1,n));
        elseif (floor(kot+dxocount(ko)/2)+1 > n-1)
            ind = kot-dxocount(ko)/2;
            xo_ext = x(floor(ind):kot+1);
        end
        probe = diff(xo_ext);
        lxo = length(probe);
        if (sign(probe(1))*sign(probe(lxo)) == -1) &&...
            (sign(probe(1)) == -1)
            posmin = sort([posmin dxoposf(ko)]);
        elseif (sign(probe(1))*sign(probe(lxo)) == -1) &&...
            (sign(probe(1)) == 1)
            posmax = sort([posmax dxoposf(ko)]);
        else
            clear xo_ext
        end
    end
elseif (ldxopos == 1)
    if (dxopos == 1 && sign(dx(2)) == 1)
        posmin = [2 posmin];
    elseif (dxopos == 1 && sign(dx(2)) == -1)
        posmax = [2 posmax];
    elseif (dxopos == n-1 && sign(dx(n-2)) == 1)
        posmin = [posmin n-1];
    elseif (dxopos == n-1 && sign(dx(n-2)) == -1)

```

```

        posmax = [posmax n-1];
    elseif (sign(dx(dxopos-1))*sign(dx(dxopos+1)) == -1) &&...
        (sign(dx(dxopos+1)) == 1)
        posmin = sort([posmin dxopos]);
    elseif (sign(dx(dxopos-1))*sign(dx(dxopos+1)) == -1) &&...
        (sign(dx(dxopos+1)) == -1)
        posmax = sort([posmax dxopos]);
    end
end
end %end dx == 0
%+++++
%removing riding waves
posex = sort([posmin,posmax]);
dposex = diff(posex);
deltan = 3;
if any(dposex <= deltan)
    dposexo = find(dposex <= deltan);
    lposrw = length(dposexo);
    for krw = 1:lposrw-1
        posexk1 = posex(dposexo(krw));
        posexk2 = posex(dposexo(krw)+1);
        dxb = dx(posexk1-1);
        dxa = dx(posexk2);
        if (dxb*dxa >= 0)
            indinf = max((posexk1-deltan),1);
            indsup = min((posexk2+deltan),n);
            if ((max([x(posexk1),x(posexk2)]) < max(x(indinf:indsup))) &&...
                (min([x(posexk1),x(posexk2)]) > min(x(indinf:indsup))))
                posmax(posmax == posexk1) = [];
                posmax(posmax == posexk2) = [];
                posmin(posmin == posexk1) = [];
                posmin(posmin == posexk2) = [];
            end
        end
    end
end
end
posex = sort([posmin,posmax]);
dposex = diff(posex);
dposexo = find(dposex == 1);

```

```

lposrw = length(dposexo);
while lposrw > 0
    posexk1 = posex(dposexo(1));
    posexk2 = posex(dposexo(1)+1);
    posmax(posmax == posexk1) = [];
    posmax(posmax == posexk2) = [];
    posmin(posmin == posexk1) = [];
    posmin(posmin == posexk2) = [];
    posex = sort([posmin,posmax]);
    dposex = diff(posex);
    dposexo = find(dposex == 1);
    lposrw = length(dposexo);
end
%+++++
%nmax and nmin must differ by at most 1
posex = sort([posmin,posmax]);
nex = length(posex);
for kex = 1:nex-1
    posextr1 = posex(kex);
    posextr2 = posex(kex+1);
    indexmax1 = find(posmax == posextr1);
    indexmax2 = find(posmax == posextr2);
    indexmin1 = find(posmin == posextr1);
    indexmin2 = find(posmin == posextr2);
    if length([indexmax1,indexmax2]) == 2
        %'2 CONSECUTIVE MAXIMA'
        if x(posextr1) > x(posextr2)
            posmax(indexmax2) = [];
        else
            posmax(indexmax1) = [];
        end
    elseif length([indexmin1,indexmin2]) == 2
        %'2 CONSECUTIVE MINIMA'
        if x(posextr1) < x(posextr2)
            posmin(indexmin2) = [];
        else
            posmin(indexmin1) = [];
        end
    end
end
end

```

```

end
%+++++
posex = sort([posmin,posmax]);
nex = length(posex);
for kex = 1:nex-1
    posextr1 = posex(kex);
    posextr2 = posex(kex+1);
    indexmax1 = find(posmax == posextr1);
    indexmax2 = find(posmax == posextr2);
    indexmin1 = find(posmin == posextr1);
    indexmin2 = find(posmin == posextr2);
    if length([indexmax1,indexmax2]) == 2
        %'2 MAXIMA CONSECUTIFS'
        if x(posextr1) > x(posextr2)
            posmax(indexmax2) = [];
        else
            posmax(indexmax1) = [];
        end
    elseif length([indexmin1,indexmin2]) == 2
        %'2 MINIMA CONSECUTIFS'
        if x(posextr1) < x(posextr2)
            posmin(indexmin2) = [];
        else
            posmin(indexmin1) = [];
        end
    end
end
end
%+++++
end
ne = length(posmax)+length(posmin);
[envmin,envmax] = envelinterp(posmin,posmax,x,t,n,ne);

%extrema method
posex = sort([posmin,posmax]);
dn_locper = diff(posex);
dn_locper(dn_locper < 4) = 4;
rough_if = pi/(mean(dn_locper)+0.01);
x_rif = posex(1:end-1)+dn_locper/2;
if_locper = pi./dn_locper;

```

```

if any(x_rif == n)
    x_rif(x_rif == n) = []; %#ok<NASGU>
    l_rif = length(x_rif);
    if_locper = if_locper(1:l_rif);
end
x_rif = [1,x_rif,n];
if_em = interp1(x_rif,[rough_if,if_locper,rough_if],(t+1),'spline');
%-----
%-----

function [envmin,envmax] = envelinterp(posmin,posmax,x,t,n,ne)
methint = 'spline';%Cubic spline interpolation
lmin = length(posmin);
lmax = length(posmax);
kex = 0;
if (ne > 2 )
    %make sure that all the data all between the two enveloppes
    while (lmin ~= 0 || lmax ~= 0) && (kex < 10)
        %check errors in extrema vectors used for interpolation
        [posmin,posmax] = check_ext(posmin,posmax,t,n);
        posminp = [t(1) t(posmin) t(n)];
        posmaxp = [t(1) t(posmax) t(n)];
        xmin = x(posmin);
        xminp = [xmin(1) xmin xmin(length(posmin))];
        xmax = x(posmax);
        xmaxp = [xmax(1) xmax xmax(length(posmax))];
        %interpolation
        envmin = interp1(posminp,xminp,t,methint);
        envmax = interp1(posmaxp,xmaxp,t,methint);
        kex = kex+1;
    end
else
    envmin = x;
    envmax = x;
end
%-----
%-----

function [posmin,posmax] = check_ext(posmin,posmax,t,n)
%check that there is no position gathered several times
dvmin = diff(posmin);

```

```

dvmax = diff(posmax);
if (any(dvmin == 0))
    posmin(dvmin == 0) = [];
    posmin = sort(posmin);
else
    posmin = sort(posmin);
end
clear pos;
if (any(dvmax == 0))
    posmax(dvmax == 0) = [];
    posmax = sort(posmax);
else
    posmax = sort(posmax);
end
clear pos;
%check there is no position 1, t(1), t(n) or n already mentioned
if (any(posmin == 1)) || (any(posmin == t(1))) || (any(posmin == n)) ||...
    (any(posmin == t(n)))
    pos1 = find(posmin == 1);
    pos2 = find(posmin == t(1));
    pos3 = find(posmin == n);
    pos4 = find(posmin == t(n));
    pos = [pos1 pos2 pos3 pos4];
    posmin(pos) = [];
    clear pos1 pos2 pos3 pos4 pos;
end
clear pos;
if (any(posmax == 1)) || (any(posmax == t(1))) || (any(posmax == n)) ||...
    (any(posmax == t(n)))
    pos1 = find(posmax == 1);
    pos2 = find(posmax == t(1));
    pos3 = find(posmax == n);
    pos4 = find(posmax == t(n));
    pos = [pos1 pos2 pos3 pos4];
    posmax(pos) = [];
    clear pos1 pos2 pos3 pos4 pos;
end
%-----
%-----

```

```

function valid_env = define_envmodul(env,threshold)
%discard parts of voxels where phase cannot be accurately extracted.
modul_env1 = (env < threshold);
modul_env1 = [0,modul_env1,0];
postot = find(abs(diff(modul_env1)) == 1);
posp = find(diff(modul_env1) == 1);
posm = find(diff(modul_env1) == -1);
nint = length(posp);
if nint < 2
    modul_env2 = modul_env1;
else
    modul_env2 = modul_env1;
    lengthint = diff(postot);
    for k = 1:nint-1
        if lengthint(2*k) < 20
            modul_env2(posm(k):posp(k+1)) = 1;
        end
    end
end

postot = find(abs(diff(modul_env2)) == 1);
posp = find(diff(modul_env2) == 1);
posm = find(diff(modul_env2) == -1);
nint = length(posp);
lengthint = diff(postot);
if nint > 0
    for k = 1:nint
        if lengthint(2*k-1) < 10
            modul_env2(posp(k):posm(k)) = 0;
        end
    end
end
valid_env = modul_env2;

```


Bibliography

- [1] <http://www.lynceetec.com>.
- [2] H.A. Aebischer and S. Waldner. Strain distributions made visible with image shearing speckle pattern interferometry. *Optics and Lasers in Engineering*, 26(4-5):407–20, 1997.
- [3] H.A. Aebischer and S. Waldner. Simple and effective method for filtering speckle-interferometric phase fringe patterns. *Optics Communications*, 162(4-6):205–10, 1999.
- [4] C. Ai and J.C. Wyant. Effect of piezoelectric transducer nonlinearity on phase shift interferometry. *Applied Optics*, 26(6):1112–6, 1987.
- [5] A.Jr. Albertazzi. Radial metrology with electronic speckle pattern interferometry. *Journal of Holography and Speckle*, 3(2):117–24, 2006.
- [6] Jr.A. Albertazzi, M.R. Viotti, and W.A. Kapp. A radial in-plane dspe interferometer using diffractive optics for residual stresses measurement. volume 715525 of *Proceedings of the SPIE*, pages 1–10, 2008.
- [7] T.L. Alexander, J.E. Harvey, and A.R. Weeks. Average speckle size as a function of intensity threshold level: comparison of experimental measurements with theory. *Applied Optics*, 33(35):8240–50, 1994.
- [8] T.T. Alieva. The fractional Fourier transform in optical propagation problems. *Journal of Modern Optics*, 41(5):1037–44, 1994.
- [9] P. Almero, A.M.S. Maallo, and S.G. Hanson. Fast-convergent algorithm for speckle-based phase retrieval and a design for dynamic wavefront sensing. *Applied Optics*, 48(8):1485–93, 2009.
- [10] P. Almero, G. Pedrini, and W. Osten. Complete wavefront reconstruction using sequential intensity measurements of a volume speckle field. *Applied Optics*, 45(34):8596–605, 2006.

- [11] I. Amidror. Scattered data interpolation methods for electronic imaging systems: a survey. *Journal of Electronic Imaging*, 11(2):157–76, 2002.
- [12] A. Anand, G. Pedrini, W. Osten, and P. Almero. Wavefront sensing with random amplitude mask and phase retrieval. *Optics Letters*, 32(11):1584–6, 2007.
- [13] F. Aurenhammer. Voronoi diagrams - a survey of a fundamental geometric data structure. *ACM computing surveys*, 23(3):345–405, 1991.
- [14] C.B. Barber, D.P. Dobkin, and H. Huhdanpaa. The quickhull algorithm for convex hulls. *ACM transactions on mathematical software*, 22(4):469–83, 1996.
- [15] E. Bedrosian. A product theorem for Hilbert transforms. *Proceedings of the IEEE*, 51(5):868–9, 1963.
- [16] M.B. Bernini, G.E. Galizzi, A. Federico, and G.H. Kaufmann. Evaluation of the 1D empirical mode decomposition method to smooth digital speckle pattern interferometry fringes. *Optics and Lasers in Engineering*, 45(6):723–9, 2007.
- [17] M.V. Berry. Disruptions of wavefronts: statistics of dislocations in incoherent Gaussian random waves. *Journal of Physics A*, 11(1):27–37, 1978.
- [18] O. Besson and F. Castanie. On estimating the frequency of a sinusoid in autoregressive multiplicative noise. *Signal Processing*, 30:65–83, 1993.
- [19] B. Boashash. Estimating and interpreting the instantaneous frequency of a signal. I. Fundamentals. *Proceedings of the IEEE*, 80(4):520–38, 1992.
- [20] B. Boashash. Estimating and interpreting the instantaneous frequency of a signal. II. Algorithms and applications. *Proceedings of the IEEE*, 80(4):540–68, 1992.
- [21] B. Boashash and P. O’Shea. Use of the cross Wigner-Ville distribution for estimation of instantaneous frequency. *IEEE Transactions on Signal Processing*, 41(3):1439–45, 1993.
- [22] D.J. Bone, H.A. Bachor, and R.J. Sandeman. Fringe-pattern analysis using a 2D Fourier transform. *Applied Optics*, 25(10):1653–60, 1986.
- [23] M. Born and E. Wolf. *Principle of Optics*. Pergamon Press, Oxford, 1999.
- [24] R. Bracewell. *The Fourier transform and its applications*. Electrical and electronic engineering series. McGraw-Hill, New York, 1965.
- [25] J.H. Bruning, D.R. Herriott, J.E. Gallagher, D.P. Rosenfeld, A.D. White, and D.J. Brangaccio. Digital wavefront measuring interferometer for testing optical surfaces and lenses. *Applied Optics*, 13(11):2693–703, 1974.

-
- [26] L. Bruno. Global approach for fitting 2D interferometric data. *Optics Express*, 15(8):4835–47, 2007.
- [27] L. Bruno. A novel operating system in speckle interferometry: the double-focusing. *Optics Express*, 15(14):8787–96, 2007.
- [28] L. Bruno and A. Poggialini. Phase shifting speckle interferometry for dynamic phenomena. *Optics Express*, 16(7):4665–70, 2008.
- [29] J.N. Butters and J.A. Leendertz. A double exposure technique for speckle pattern interferometry. *Journal of Physics E*, 4(4):277–9, 1971.
- [30] J.N. Butters and J.A. Leendertz. Speckle pattern and holographic techniques in engineering metrology. *Optics and Laser Technology*, 3(1):26–30, 1971.
- [31] F. Charriere, J. Kuhn, T. Colomb, F. Montfort, E. Cuhe, Y. Emery, K. Weible, P. Marquet, and C. Depeursinge. Characterization of microlenses by digital holographic microscopy. *Applied Optics*, 45(5):829–35, 2006.
- [32] F. Charriere, N. Pavillon, T. Colomb, T. Heger, E. Mitchell, P. Marquet, B. Rappaz, and C. Depeursinge. Living specimen tomography by digital holographic microscopy: morphometry of testate amoeba. *Optics Express*, 14(16):7005–13, 2006.
- [33] Q. Chen, N. Huang, S. Riemenschneider, and Y. Xu. A B-spline approach for empirical mode decompositions. *Advances in computational mathematics*, 24:171–95, 2006.
- [34] M. Cherbuliez. *Wavelet analysis of interference patterns and signals: development of fast and efficient processing techniques*. PhD thesis, EPFL - 2377, 2001.
- [35] M. Cherbuliez, P. Jacquot, and X. Colonna De Lega. Wavelet processing of interferometric signals and fringe patterns. volume 3813 of *Proceedings of the SPIE*, pages 692–702, 1999.
- [36] L. Cohen. Time-frequency distributions - a review. *Proceedings of the IEEE*, 77(7):941–81, 1989.
- [37] L. Cohen, P. Loughlin, and D. Vakman. On an ambiguity in the definition of the amplitude and phase of a signal. *Signal Processing*, 79:301–7, 1999.
- [38] T. Colomb, F. Montfort, J. Kuhn, N. Aspert, E. Cuhe, A. Marian, F. Charriere, S. Bourquin, P. Marquet, and C. Depeursinge. Numerical parametric lens for shifting, magnification and complete aberration compensation in digital holographic microscopy. *Journal of the Optical Society of America A*, 23(12):3177–90, 2006.

- [39] X. Colonna De Lega. *Processing of non-stationary interference patterns: adapted phase-shifting algorithms and wavelet analysis. Application to dynamic deformation measurements by holographic and speckle interferometry*. PhD thesis, EPFL - 1666, 1997.
- [40] X. Colonna De Lega and P. Jacquot. Deformation measurement with object-induced dynamic phase shifting. *Applied Optics*, 35(25):5115–21, 1996.
- [41] T.J. Cookson, J.N. Butters, and H.C. Pollard. Pulsed lasers in electronic speckle pattern interferometry. *Optics and Laser Technology*, 10(3):119–24, 1978.
- [42] J.W. Cooley and J.W. Tukey. An algorithm for the machine calculation of complex Fourier series. *Mathematics of Computation*, 19(90):297–301, 1965.
- [43] K.L. Coughlin and K.K. Tung. 11-year solar cycle in the stratosphere extracted by the empirical mode decomposition method. *Advances in space research*, 34:323–9, 2004.
- [44] K. Creath. Phase-shifting speckle interferometry. *Applied Optics*, 24(18):3053–8, 1985.
- [45] K. Creath. Temporal phase measurements methods. In D.W. Robinson and G.T. Reid, editors, *Interferogram Analysis*, pages 94–140. Institute of Physics Publishing, Bristol, UK, 1993.
- [46] I. Daubechies. The wavelet tranform, time-frequency localization and signal analysis. *IEEE Transactions on information theory*, 36(5):961–1005, 1990.
- [47] I. Daubechies. Where do wavelets come from? - a personal point of view. *Proceedings of the IEEE*, 84(4):510–3, 1996.
- [48] M. De Berg, M. van Kreveld, M. Overmars, and O. Schwarzkopf. *Computational geometry: algorithms and applications*. Springer, Berlin, 2008.
- [49] P. De Groot. Derivation of algorithms for phase-shifting interferometry using the concept of a data-sampling window. *Applied Optics*, 34(22):4723–30, 1995.
- [50] N. Delprat, B. Escudie, P. Guillemain, R. Kronland-Martinet, P. Tchamitchian, and B. Torresani. Asymptotic wavelet and Gabor analysis: extraction of instantaneous frequency. *IEEE Transactions on information theory*, 38(2):644–64, 1992.
- [51] C. Dyken and M.S. S. Floater. Preferred directions for resolving the non-uniqueness of Delaunay triangulations. *Computational Geometry*, 34:96–101, 2006.
- [52] S. Equis and P. Jacquot. Simulation of speckle complex amplitude: advocating the linear model. volume 6341 of *Proceedings of the SPIE*, pages 634138–1, 2006.

-
- [53] S. Equis and P. Jacquot. Phase extraction in dynamic speckle interferometry by empirical mode decomposition. ICEM 13, International Conference in Experimental Mechanics, Gdoutos E.E. Ed., pages 719–720. Springer, Dordrecht, The Netherlands, 2007.
- [54] S. Equis and P. Jacquot. Phase extraction in dynamic speckle interferometry by empirical mode decomposition and Hilbert transform. *Strain*, 2008.
- [55] S. Equis and P. Jacquot. The empirical mode decomposition: a must-have tool in speckle interferometry? *Optics Express*, 17(2):611–23, 2009.
- [56] S. Equis and P. Jacquot. A new application of the Delaunay triangulation: the processing of speckle interferometry signals. Proceedings of Fringe, the international workshop on automatic processing of fringe patterns, Osten W. and Kujawinska M. Eds, pages 123–31. Springer, Berlin, Germany, 2009.
- [57] A. Federico and G.H. Kaufmann. Comparative study of wavelet thresholding methods for denoising electronic speckle pattern interferometry fringes. *Optical Engineering*, 40(11):2598–604, 2001.
- [58] A. Federico and G.H. Kaufmann. Evaluation of dynamic speckle activity using the empirical mode decomposition method. *Optics Communications*, 267(2):287–94, 2006.
- [59] J.R. Fienup. Phase retrieval algorithms: a comparison. *Applied Optics*, 21(15):2758–69, 1982.
- [60] P. Flandrin. <http://perso.ens-lyon.fr/patrick.flandrin/emd.html>.
- [61] P. Flandrin and P. Borgnat. Revisiting and testing stationarity. Euro American Workshop on Information Optics, 2008.
- [62] P. Flandrin and B. Escudie. An interpretation of the pseudo-Wigner-Ville distribution. *Signal Processing*, 6(1):27–36, 1984.
- [63] P. Flandrin, G. Rilling, and P. Goncalves. Empirical mode decomposition as a filter bank. *IEEE Signal Processing Letters*, 11(2):112–14, 2004.
- [64] I. Freund and N. Shvartsman. Wave-field phase singularities: the sign principle. *Physical review A*, 50(6):5164–74, 1994.
- [65] I. Freund, N. Shvartsman, and V. Freilikher. Optical dislocation networks in highly random media. *Optics Communications*, 101(2):247–64, 1993.
- [66] Y.Y. Fu, C.J. Tay, C. Quan, and H. Miao. Wavelet analysis of speckle patterns with a temporal carrier. *Applied Optics*, 44(6):959–65, 2005.

- [67] H. Fujii, J. Uozumi, and T. Asakura. Computer simulation study of image speckle patterns with relation to object surface profile. *Journal of the Optical Society of America*, 66:1222–36, 1976.
- [68] D. Gabor. Theory of communication. *Journal of the IEE*, 93(26):429–57, 1946.
- [69] B. Gautier. *Etude et réalisation d'un interféromètre speckle à mesure de formes intégrée*. PhD thesis, Ecole des Mines de Paris, 2005.
- [70] M.A. Gdeisat. Spatial carrier fringe pattern demodulation by use of a two-dimensional continuous wavelet transform. *Applied Optics*, 45(34):8722–32, 2006.
- [71] M.A. Gdeisat, D.R. Burton, and M.J. Lalor. Real-time hybrid fringe pattern analysis using a linear digital phase locked loop for demodulation and unwrapping. *Measurement Science and Technology*, 11(10):1480–92, 2000.
- [72] D.C. Ghiglia and M.D. Pritt. *Two-dimensional phase unwrapping : theory, algorithms, and software*. Wiley, New York, 1998.
- [73] J.W Goodman. Digital image formation from electronically detected holograms. *Applied Physics Letters*, 11(3):77–9, 1967.
- [74] J.W Goodman. Dependence of image speckle contrast on surface roughness. *Optics Communications*, 14(3):324–7, 1975.
- [75] J.W Goodman. Statistical properties of laser speckle patterns. In J.C. Dainty, editor, *Laser speckle and related phenomena*, pages 9–75. Springer-Verlag, Berlin, 1975.
- [76] J.W. Goodman. *Introduction to Fourier optics*. Roberts, Englewood, Colorado, 2005.
- [77] J.W. Goodman. *Speckle phenomena in optics : theory and applications*. Roberts and Company, Englewood, Colorado, 2007.
- [78] N. Goudemand. *3D-3C speckle interferometry: Optical Device for Measuring Complex Structures*. PhD thesis, ETHZ - 15961, 2005.
- [79] L.J. Griffiths. Rapid measurement of digital instantaneous frequency. *IEEE Transactions on Acoustics, Speech, and Signal Processing*, 23(2):207–22, 1975.
- [80] S.L. Hahn. On the uniqueness of the definition of the amplitude and phase of the analytic signal. *Signal Processing*, 83:1815–20, 2003.
- [81] F.J. Harris. On the use of windows for harmonic analysis with the discrete Fourier transform. *Proceedings of the IEEE*, 66(1):51–83, 1978.

-
- [82] E. Hecht. *Optics*. Addison Wesley, San Francisco, California, 2002.
- [83] N.E. Huang. A confidence limit for the empirical mode decomposition and Hilbert spectral analysis. *Proc. of the Royal Society A*, 459(2037):2317–45, 2003.
- [84] N.E. Huang and S.S.P. Shen. *Hilbert-Huang transform and its application*. Interdisciplinary mathematical sciences. World scientific, Singapore, 2005.
- [85] N.E. Huang, Z. Shen, S.R. Long, M.C. Wu, H.H. Shih, Q. Zheng, N.C. Yuen, C.-C. Tung, and H.H. Liu. The empirical mode decomposition and the Hilbert spectrum for nonlinear and nonstationary time series analysis. *Proc. of the Royal Society A*, 454A(1971):903–95, 1998.
- [86] Y.Y. Hung. A speckle shearing interferometer: a tool for measuring derivatives of surfaces displacements. *Optics Communications*, 11(2):132–5, 1974.
- [87] J.M. Huntley. Temporal phase-unwrapping algorithm for automated interferogram analysis. *Applied Optics*, 32(17):3047–52, 1993.
- [88] J.M. Huntley. Random phase measurement errors in digital speckle pattern interferometry. *Optics and Lasers in Engineering*, 26:131–50, 1997.
- [89] P. Jacquot. Speckle interferometry: a review of the principal methods in use for experimental mechanics applications. *Strain*, 44(1):57–69, 2008.
- [90] R. Jones and C. Wykes. *Holographic and speckle interferometry: a discussion of the theory, practice and application of the techniques*. Cambridge series in modern optics. Cambridge University Press, Cambridge, 1989.
- [91] H. Kadono and T. Asakura. Statistical properties of the speckle phase in the optical imaging system. *Journal of the Optical Society of America A*, 2(10):1787–92, 1985.
- [92] G.H. Kaufmann. Speckle noise reduction in television holography fringes using wavelet thresholding. *Optics Express*, 35(1):9–14, 1996.
- [93] G.H. Kaufmann. Phase measurement in temporal speckle pattern interferometry using the Fourier transform method with and without a temporal carrier. *Optics Communications*, 217(1-6):141–9, 2003.
- [94] G.H. Kaufmann, D. Kerr, and N.A. Halliwell. Contrast enhancement of pulsed ESPI addition fringes. *Optics and Lasers in Engineering*, 20(1):25–34, 1994.
- [95] K. Kemao. Two-dimensional windowed Fourier transform for fringe pattern analysis: principles, applications and implementations. *Optics and Lasers in Engineering*, 45(2):304–17, 2007.

- [96] K. Kinstetter, A.W. Lohmann, J. Schwider, and N. Streibl. Accuracy of phase shifting interferometry. *Applied Optics*, 27(24):5082–9, 1988.
- [97] Y. Kopsinis and S. McLaughlin. Improved EMD using doubly-iterative sifting and high order spline interpolation. *EURASIP Journal on advances in signal processing*, 2008(128293):1–8, 2008.
- [98] M.F. Küchel. Some progress in phase measurement techniques. Proceedings of Fringe, the international workshop on automatic processing of fringe patterns, Osten W. and Kujawinska M. Eds, pages 27–44, 1997.
- [99] D. Labarre. Two-Kalman filters based instrumental variable techniques for speech enhancement. *2004 IEEE 6th Workshop on Multimedia Signal Processing*, pages 375–8, 2004.
- [100] K.G. Larkin. Natural demodulation of two-dimensional fringe patterns. II. Stationary phase analysis of the spiral phase quadrature transform. *Journal of the Optical Society of America A*, 18(8):1871–81, 2001.
- [101] K.G. Larkin. Uniform estimation of orientation using local and nonlocal 2D energy operators. *Optics Express*, 13(20):8097–121, 2005.
- [102] K.G. Larkin, D.J. Bone, and M.A. Oldfield. Natural demodulation of two-dimensional fringe patterns. I. General background of the spiral phase quadrature transform. *Journal of the Optical Society of America A*, 18(8):1862–70, 2001.
- [103] J.A. Leendertz. An image-shearing speckle-pattern interferometer for measuring bending moments. *Journal of Physics E*, 6(11):1107–10, 1973.
- [104] J.A. Leendertz and J.N. Butters. Interferometric displacement measurement on scattering surfaces utilizing speckle effect. *Journal of Physics E*, 3(3):214–8, 1970.
- [105] R. Legarda-Saenz, W. Osten, and W. Jüptner. Improvement of the regularized phase-tracking technique for the processing of nonnormalized fringe patterns. *Applied Optics*, 41(26):5519–26, 2002.
- [106] M. Lehmann. Optimization of wavefield intensities in phase-shifting speckle interferometry. *Optics Communications*, 118(3-4):199–206, 1995.
- [107] M. Lehmann. Phase-shifting speckle interferometry with unresolved speckles: a theoretical investigation. *Optics Communications*, 128(4-6):325–40, 1996.
- [108] M. Lehmann. *Statistical theory of two-wave speckle interferometry and its application to the optimization of deformation measurements*. PhD thesis, EPFL - 1797, 1998.

-
- [109] M. Lehmann. Speckle statistics in the context of digital speckle interferometry. In P.K. Rastogi, editor, *Digital Speckle Pattern Interferometry and Related Techniques*, pages 1–58. John Wiley and Sons, Ltd, Chichester, 2001.
- [110] L. Leushacke and M. Kirchner. Three-dimensional correlation coefficient of speckle intensity for rectangular and circular apertures. *Journal of the Optical Society of America A*, 7(5):827–32, 1990.
- [111] Q.B. Li and F.P. Chiang. Three-dimensional dimension of laser speckle. *Applied Optics*, 31(29):6287–91, 1992.
- [112] M. Liebling. *On Fresnelets, interference fringes and digital holography*. PhD thesis, EPFL - 2977, 2004.
- [113] T. Lindeberg. *Scale-space theory in computer vision*. Kluwer Academic Publishers, Boston, 1994.
- [114] W.C. Lindsey and M.K. Simon. *Phase-locked loops and their application*. IEEE Press, John Wiley and Sons, New-York, 1978.
- [115] C. Liu, Z. Liu, F. Bo, Y. Wang, and J. Zhu. Super-resolution digital holographic imaging method. *Applied Physics Letters*, 81(17):3143–45, 2002.
- [116] H. Liu, G. Lu, S. Wu, S. Yin, and F.T.S. Yu. Speckle-induced phase error in laser-based phase-shifting projected fringe profilometry. *Journal of the Optical Society of America A*, 16(6):1484–95, 1999.
- [117] A.W. Lohmann. Image rotation, Wigner rotation, and the fractional Fourier transform. *Journal of the Optical Society of America A*, 10(10):2181–6, 1993.
- [118] P.J. Loughlin and B. Tacer. On the amplitude - and frequency - modulation decomposition of signals. *Journal of the Acoustical Society of America*, 100(3):1594–601, 1996.
- [119] W.W.Jr. Macy. Two-dimensional fringe-pattern analysis. *Applied Optics*, 22(23):3898–901, 1983.
- [120] V.D. Madjarova, H. Kadono, and S. Toyooka. Dynamic electronic speckle pattern interferometry (DESPI) phase analyses with temporal Hilbert transform. *Optics Express*, 11(6):617–23, 2003.
- [121] S.G. Mallat. A theory for multiresolution signal decomposition: the wavelet representation. *Transactions on Pattern Analysis and Machine Intelligence*, 11(7):674–93, 1989.

- [122] L. Mandel. Interpretation of instantaneous frequencies. *American Journal of Physics*, 42(10):840–6, 1974.
- [123] A. Maréchal and M. Françon. *Diffraction. Structures des images*. McGraw-Hill electrical and electronic engineering series. La Revue d’Optique Theorique et Experimentale, Paris, 1960.
- [124] F.A. Marengo Rodriguez. Hilbert transform analysis of a time series of speckle interferograms with a temporal carrier. *Applied Optics*, 47(9):1310–16, 2008.
- [125] F.A. Marengo Rodriguez, A. Federico, and G.H. Kaufmann. Phase measurement improvement in temporal speckle pattern interferometry using empirical mode decomposition. *Optics Communications*, 275(1):38–41, 2007.
- [126] S.L.Jr. Marple. Computing the discrete-time “analytic” signal via FFT. *IEEE Transactions on Signal Processing*, 47(9):2600–3, 1999.
- [127] J. L. Marroquin, M. Rivera, S. Botello, R. Rodriguez-Vera, and M. Servin. Regularization methods for processing fringe-pattern images. *Applied Optics*, 38(5):788–94, 1999.
- [128] D.D. Mas. Fast algorithms for free-space diffraction patterns calculation. *Optics Communications*, 164(4):233–45, 1999.
- [129] D.D. Mendlovic. Computation considerations and fast algorithms for calculating the diffraction integral. *Journal of Modern Optics*, 44(2):407–14, 1997.
- [130] H. Meng, W.L. Anderson, F. Hussain, and D.D. Liu. Intrinsic speckle noise in in-line particle holography. *Journal of the Optical Society of America A*, 10:2046–58, 1993.
- [131] A.J. Moore, J.R. Tyrer, and F.M. Santoyo. Phase extraction from electronic speckle pattern interferometry addition fringes. *Applied Optics*, 33(31):7312–20, 1994.
- [132] P.K. Murphy, J.P. Allebach, and N.C. Gallagher. Effect of optical aberrations on laser speckle. *Journal of the Optical Society of America A*, 3(2):215–22, 1986.
- [133] K. Nakagawa, N. Nagamatsu, T. Asakura, and Y. Shindo. An effect of the extended detecting aperture on the contrast of monochromatic and white-light speckles. *J. Optics*, 13(3):147–53, 1982.
- [134] J. Novak, P. Novak, and A. Miks. Multi-step phase-shifting algorithms insensitive to linear phase shift errors. *Optics Communications*, 281(1):5302–9, 2008.

-
- [135] J.C. Nunes, Y. Bouaoune, E. Delechelle, O. Niang, and P. Bunel. Image analysis by bidimensional empirical mode decomposition. *Image and Vision Computing*, 21(12):1019–26, 2003.
- [136] J.C. Nunes, S. Guyot, and E. Delechelle. Texture analysis based on local analysis of the bidimensional empirical mode decomposition. *Machine vision and application*, 16:177–88, 2005.
- [137] A.H. Nuttall. On the quadrature approximation to the Hilbert transform of modulated signals. *Proceedings of the IEEE*, 54:1458–9, 1966.
- [138] J.F. Nye and M.V. Berry. Dislocations in wave trains. *Proc. of the Royal Society A*, 336(1):165–90, 1974.
- [139] H.H.M. Ozaktas. Fractional Fourier optics. *Journal of the Optical Society of America A*, 12(4):743–51, 1995.
- [140] H.M. Ozaktas, Z. Zalevsky, and M.A Kutay. *The fractional Fourier transform with applications in optics and signal processing*. Wiley series in pure and applied optics. John Wiley and Sons, LTD, 2001.
- [141] B. Pan, K. Qian, H. Xie, and A. Asundi. Two-dimensional digital image correlation for in-plane displacement and strain measurement: a review. *Measurement Science and Technology*, 20(6):1–17, 2009.
- [142] P.J. Parker and B.D.O. Anderson. Frequency tracking of nonsinusoidal periodic signals in noise. *Signal Processing*, 20(2):127–52, 1990.
- [143] M. Paturzo, F. Merola, S. Grilli, S. De Nicola, A. Finizio, and P. Ferraro. Super-resolution in digital holography by a two-dimensional dynamic phase grating. *Optics Express*, 16(21):17107–18, 2008.
- [144] G. Pedrini, W. Osten, and Y. Zhang. Wave-front reconstruction from a sequence of interferograms recorded at different planes. *Optics Letters*, 30(8):833–5, 2005.
- [145] D.W. Phillion. General methods for generating phase-shifting interferometry algorithms. *Applied Optics*, 36(31):8098–115, 1997.
- [146] P. Picart and J. Leval. General theoretical formulation of image formation in digital Fresnel holography. *Journal of the Optical Society of America A*, 25(7):1744–61, 2008.
- [147] QuickHull. www.qhull.org.

- [148] B.G. Quinn and E.J. Hannan. *The estimation and tracking of frequency*. Cambridge series in statistical and probabilistic mathematics. Cambridge university press, Cambridge, U.K., 2001.
- [149] J.A. Quiroga, M. Servin, and F. Cuevas. Modulo 2π fringe orientation angle estimation by phase unwrapping with a regularized phase tracking algorithm. *Journal of the Optical Society of America A*, 19(8):1524–31, 2002.
- [150] L.R. Rabiner and B.H. Juang. An introduction to hidden Markov models. *IEEE ASSP magazine*, 3(1):4–16, 1986.
- [151] L.R. Rabiner and R.W. Schafer. On the behavior of minimax FIR digital Hilbert transformers. *The Bell System Technical Journal*, 53(2):363–90, 1974.
- [152] P.K. Rastogi. *Digital speckle pattern interferometry and related techniques*. John Wiley and Sons, Ltd, Chichester, 2001.
- [153] A. Reilly, G. Frazer, and B. Boashash. Analytic signal generation: tips and traps. *IEEE Transactions on Signal Processing*, 42(11):3241–5, 1994.
- [154] G. Rilling and P. Flandrin. On the influence of sampling on the empirical mode decomposition. IEEE International Conference on Acoustics, Speech, and Signal Processing, pages 444–7, 2006.
- [155] G. Rilling and P. Flandrin. One or two frequencies? the empirical mode decomposition answers. *IEEE Transactions on Signal Processing*, 56(1):85–95, 2008.
- [156] G. Rilling, P. Flandrin, and P. Goncalves. On empirical mode decomposition and its algorithms. IEEE-EURASEP, Workshop on Nonlinear Signal and Image Processing NSIP-03, 2003.
- [157] E. Robin. Phase demodulation from a single fringe pattern based on a correlation technique. *Applied Optics*, 43(22):4355–61, 2004.
- [158] E. Robin, V. Valle, and F. Bremand. Phase demodulation method from a single fringe pattern based on correlation with a polynomial form. *Applied Optics*, 44(34):7261–9, 2005.
- [159] D.W. Robinson. *Interferogram analysis : digital fringe pattern measurement techniques*. Institute of Physics Publishing, Bristol, 1993.
- [160] P.D. Ruiz, J.M. Huntley, and G.H. Kaufmann. Adaptive phase-shifting algorithm for temporal phase evaluation. *Journal of the Optical Society of America A*, 20(2):325–32, 2003.

-
- [161] T. Santhanakrishnan, P.K. Palanisamy, N. Krishna, and R.S. Sirohi. A new configuration in speckle interferometry for contouring of three-dimensional objects. *Optics Communications*, 152:19–22, 1998.
- [162] U. Schnars and W. Jüptner. Direct recording of holograms by a CCD target and numerical reconstruction. *Applied Optics*, 33(2):179–81, 1994.
- [163] U. Schnars and W. Jüptner. Digital recording and numerical reconstruction of holograms. *Measurement Science and Technology*, 13(9):R85–R101, 2002.
- [164] M. Servin, J.L. Marroquin, and Cuevas F.J. Demodulation of a single interferogram by use of a two-dimensional regularized phase-tracking technique. *Applied Optics*, 36(19):4540–8, 1997.
- [165] M. Servin and R. Rodriguez-Vera. Two-dimensional phase locked loop demodulation of interferograms. *Journal of Modern Optics*, 40(11):2087–94, 1993.
- [166] M. Servin, R. Rodriguez-Vera, and D. Malacara. Noisy fringe pattern demodulation by an iterative phase locked loop. *Optics and Lasers in Engineering*, 23(5):355–65, 1995.
- [167] N. Shvartsman and I. Freund. Speckle spots ride phase saddles sidesaddle. *Optics Communications*, 117(3-4):228–34, 1995.
- [168] R.S. Sirohi and F. Siong Chau. *Optical methods of measurement. Wholefield techniques*. Marcel Dekker, Inc., New York, Basel, 1999.
- [169] P.A.A.M. Somers and N. Bhattacharya. Maintaining sub-pixel alignment for a single-camera two-buckets shearing speckle interferometer. *Journal of optics A: pure and applied optics*, 7:385–91, 2005.
- [170] W. Steinchen and L. Yang. *Digital Shearography*. SPIE Press, Bellingham, WA, 2003.
- [171] N. Stevenson. A sampling limit for the empirical mode decomposition. Proceedings - 8th International Symposium on Signal Processing and its Applications, ISSPA, pages 647–650, 2005.
- [172] R.L. Streit. Frequency line tracking using hidden Markov models. *IEEE Transactions on Acoustics, Speech, and Signal Processing*, 38(4):586–98, 1990.
- [173] Y. Sirel. Phase stepping: a new self-calibrating algorithm. *Applied Optics*, 32(19):3598–3600, 1993.
- [174] Y. Sirel. Design of algorithms for phase measurements by the use of phase stepping. *Applied Optics*, 35(1):51–60, 1996.

- [175] M.A. Sutton, J.-J. Orteu, and H.W. Schreier. *Image Correlation for Shape, Motion and Deformation Measurements*. Springer, Boston, Massachusetts, 2009.
- [176] M.A. Sutton, W.J. Wolters, W.H. Peters, W.F. Ranson, and S.R. McNeill. Determination of displacements using an improved digital correlation method. *Image and vision computing*, 1(3):133–9, 1983.
- [177] M. Takeda, H. Ina, and S. Kobayashi. Fourier-transform method of fringe-pattern analysis for computer-based topography and interferometry. *Journal of the Optical Society of America*, 72(1):156–60, 1982.
- [178] J.K. Thompson and D.R. Tree. Leakage error in fast Fourier analysis. *Journal of Sounds and Vibration*, 71(4):531–544, 1980.
- [179] M. Unser. Splines: a perfect fit for signal and image processing. *IEEE Signal Processing Magazine*, 16(6):22–38, 1999.
- [180] M. Unser. Sampling - 50 years after Shannon. *Proceedings of the IEEE*, 88(4):569–87, 2000.
- [181] M. Unser and T. Blu. Wavelet theory demystified. *IEEE Transactions on Signal Processing*, 51(2):470–83, 2003.
- [182] D. Vakman. On the analytic signal, the Teager-Kaiser energy algorithm, and other methods for defining amplitude and frequency. *IEEE Transactions on Signal Processing*, 44(4):791–7, 1996.
- [183] D. Venet. Techniques automatiques de raccordement de phase. Master's thesis, Université de Bruxelles, et laboratoire IMAC-EPFL Lausanne, 1996.
- [184] M. Vetterli. Wavelets and filter banks: theory and design. *IEEE Transactions on Signal Processing*, 40(9):2207–32, 1992.
- [185] E. Vikhagen. Nondestructive testing by use of TV holography and deformation phase gradient calculation. *Applied Optics*, 29(1):137–44, 1990.
- [186] J. Ville. Theorie et application de la notion de signal analytique. *Cables et Transmissions*, 2(1):61–74, 1948.
- [187] W. Wang, N. Ishii, S.G. Hanson, Y. Miyamoto, and M. Takeda. Phase singularities in analytic signal of white-light speckle pattern with application to micro-displacement measurement. *Optics Communications*, 248:59–68, 2005.
- [188] W. Wang, T. Yokozeki, R. Ishijima, and M. Takeda. Optical vortex metrology based on the core structures of phase singularities in Laguerre-Gauss transform of a speckle pattern. *Optics Express*, 14(22):10195–206, 2006.

-
- [189] W. Wang, T. Yokozeki, R. Ishijima, and M. Takeda. Constellation of phase singularities in a speckle-like pattern of optical vortex metrology applied to biological kinematic analysis. *Optics Express*, 16c(18c):13908–17c, 2008.
- [190] Z. Wang and B. Han. Advanced iterative algorithm for phase extraction of randomly phase-shifted interferograms. *Optics Letters*, 29(14):1671–3, 2004.
- [191] D. Wei and A. C. Bovik. On the instantaneous frequencies of multicomponent AM-FM signals. *IEEE Signal Processing Letters*, 5c(4c):84–6c, 1998.
- [192] J. Xiao, P. Borgnat, and P. Flandrin. Testing stationarity with time-frequency surrogates. 15th European Signal Processing Conference EUSIPCO, pages 1268–1270, 2007.
- [193] I. Yamaguchi and T. Zhang. Phase-shifting digital holography. *Optics Letters*, 22(16):1268–70, 1997.
- [194] G.-Z. Yang, B.-Z. Dong, B.-Y. Gu, J.-Y. Zhuang, and O.K. Ersoy. Gerchberg-Saxton and Yang-Gu algorithms for phase retrieval in a nonunitary transform system: a comparison. *Applied Optics*, 33(2):209–18, 1994.
- [195] K. Zeng and M.-X. He. A simple boundary process technique for empirical mode decomposition. volume 6 of *IEEE International Geoscience and Remote Sensing*, pages 4258–61, 2004.
- [196] Y. Zou, G. Diao, X. Peng, and Tiziani H. Geometry for contouring by electronic speckle interferometry based on shifting illumination beams. *Applied Optics*, 31(31):6616–21, 1992.

Curriculum Vitae

personal data

Name: Sébastien Philippe Marc EQUIS.
Date of birth: November 11th, 1977.
Nationality: French.
Address: Chemin de la côte Malherbe, CH-1188 Saint-George.
E-mail: *sebastien_equis@yahoo.fr*
Mobile: +41 76 239 58 71.

professional experience

Swiss Federal Institute of Technology, Lausanne, Switzerland

2006 – present *PhD student*

- Postgraduate formation in advanced signal and image processing, EPFL doctoral school (**14** credits),
- Teaching assistant for undergraduate courses in optics,
- Examination expert for undergraduate courses.

BCD Microtechnique, Prévèrènges, Switzerland

2004 – 2005 *In charge of the development in industrial optics*

- Conception and development of optical measurement devices: mechanical and optical design.

- 2003 – 2004** **General Electric Medical Systems**, Buc-(78), France
Industrialization engineer
- Manufacturing Component Leader in charge of a subsystem of an X-ray digital imaging medical system,
 - Responsible of the production transfer abroad (new suppliers in Ireland and Hungary),
 - Installation of production lines,
 - Validation policy according to **Six Sigma** methodology.
- 2000 – 2002** **Alcatel Optronics**, Nozay-(91), France
Development engineer
- Modeling of the physical behavior of EDFA (Erbium Doped Fiber Amplifier) in dynamic regime with the aim of designing a pump lasers servo-control,
 - In close collaboration with software and hardware electronics engineers for the design of the first optical amplifier with in-board numerical electronics of Alcatel,
 - Installation of test benches for laser diodes (EXCEL VB / GPIB).
- 2000** **Laboratoire Central de Recherches de THOMSON-CSF (THALES)**, Palaiseau-(91), France
Master internship
- Modeling and assembly of an optical fiber amplifier integrated in a LIDAR.

education

- 2006 – 2009** **Swiss Federal Institute of Technology**, Lausanne, Switzerland
PhD student
- Thesis advisor: Professor Pierre Jacquot.
- 1997 – 2000** **Ecole Supérieure d'Optique (I.O.T.A.)**, Orsay-(91), France
Master student
- 3rd year option: Optronics.
 - D.E.A. (Diplôme d'Etudes Approfondies) in Optics and Photonics.

1995 – 1997 **Lycée Claude Fauriel**, Saint-Etienne-(42), France
Classes Prépartoires aux Grandes Ecoles
- Physics and Chemistry: PCSI - PC*.

1995 **Lycée Saint-Louis**, Saint-Etienne, France
Bachelor S
- Scientific section with option in Mathematics.

languages

French : mother tongue
English : fluent
German : basic skills

computer skills

Programming : Matlab, Labview, Zemax, Autocad, Mathcad, Visual C++.
Publishing : L^AT_EX, Office, CorelDRAW, Adobe Illustrator, Blender, Adobe Photo-shop.

hobbies and interest

Sport: Motocross, ski and mountain-bike enthusiast, scuba diver (PADI Advanced Open Water Diver),
Literature: History, fantastic and SF.

Publication List

Peer-reviewed journal publications

- i) Equis S. and Jacquot P. (2009) The Empirical Mode Decomposition: a must-have tool in Speckle Interferometry? *Optics Express*, 17 (2), 611-623.
- ii) Equis S. and Jacquot P. (2008) Phase Extraction In Dynamic Speckle Interferometry By Empirical Mode Decomposition and Hilbert transform. *Strain*.

Peer-reviewed conference proceedings publications

- i) Equis S. and Jacquot P. (2009) A new application of the Delaunay triangulation: the processing of speckle interferometry signals *Fringe 2009*, Stuttgart, Germany (14th-16th September), Osten W. and Kujawinska M. Ed., Springer-Berlin.
- ii) Equis S., Baldi A. and Jacquot P. (2007) Phase extraction in dynamic speckle interferometry by empirical mode decomposition. *Proc. of ICEM 13*, Alexandroupolis, Greece (1st-6th July), Gdoutos E.E. Ed., Springer-Dordrecht.
- iii) Jacquot P. and Equis S. (2006) Simulation numérique de champs speckle par filtrage linéaire. *Actes du septième colloque international francophone CMOI*, 17, pp 1-7, 20th-24th Nov.
- iv) Equis S. and Jacquot P. (2006) Simulation of speckle complex amplitude: advocating the linear model. *Proc. SPIE 6341*, pp 6341381-6, International Conference Speckle06.
- v) CD of the talks given at the international conference Photomechanics08 (2008), Loughborough, UK (7th-9th July).

Conferences abstracts

- i) Equis S. and Jacquot P. (2008) A phase extraction procedure for dynamic regimes in speckle interferometry. Abstract Proceedings *Photomechanics2008*.

Oral presentations

- i) **Equis S.** and Jacquot P. (2009) A new application of the Delaunay triangulation: the processing of speckle interferometry signals. *Fringe 2009*.
- ii) **Equis S.** and Jacquot P. (2008) Speckle Interferometry addressed to Transient Phenomena Characterization, *Photonics Day 2008*, EPFL, Lausanne, 17th Oct.
- iii) **Equis S.** and Jacquot P. (2008) a phase extraction procedure for dynamic regimes in speckle interferometry. *PhotoMechanics 2008*.
- iv) **Equis S.**, Baldi A. and Jacquot P. (2007) Phase Extraction In Dynamic Speckle Interferometry By Empirical Mode Decomposition. *ICEM 13*.

Posters

- i) Equis S. and Jacquot P. (2008) Speckle Interferometry for Deformation Analysis, *SSOM - Optics Section Day at EPMT (Environnement Professionnel MicroTechnologies)*, 3rd - 6th June.
- ii) Equis S. and Jacquot P. (2007) Phase Extraction In Dynamic Speckle Interferometry By Empirical Mode Decomposition and Hilbert transform, *Photonics Day 2007*, EPFL, Lausanne, 19th Oct.
- iii) Equis S. and Jacquot P. (2006) Phase extraction in dynamic speckle interferometry, *Research Day 2006*, EPFL, Lausanne, 16th Nov and *Photonics day 2006*, EPFL, Lausanne, 24th Nov.
- iv) Jacquot P. and Equis S. (2006) Simulation numérique de champs speckle par filtrage linéaire, *CMOI*.
- v) Equis S. and Jacquot P. (2006) Simulation of speckle complex amplitude: advocating the linear model, *Speckle06*.